

**AN EVALUATION OF THE IOSIPESCU SPECIMEN FOR COMPOSITE
MATERIALS SHEAR PROPERTY MEASUREMENT**

by

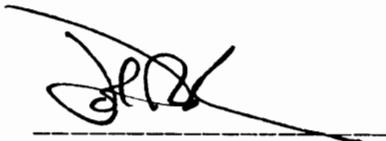
Henjen Ho
Department of Engineering Science and Mechanics
Virginia Polytechnic Institute and State University
in partial fulfillment of the requirements for the degree of

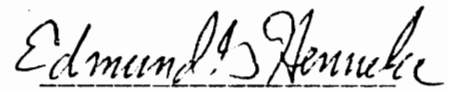
DOCTOR OF PHILOSOPHY

in

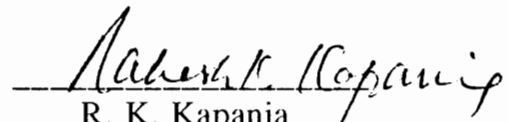
Engineering Mechanics


APPROVED:


J. Morton, Chairman


E. G. Henneke


W. W. Stinchcomb


R. K. Kapania


S. Kellas

July, 1991
Blacksburg, Virginia

AN EVALUATION OF THE IOSIPESCU SPECIMEN FOR COMPOSITE MATERIALS SHEAR PROPERTY MEASUREMENT

by

Henjen Ho

Professor John Morton, Chairman

Department of Engineering Science and Mechanics

(ABSTRACT)

A detailed evaluation of the suitability of the Iosipescu specimen tested in the modified Wyoming fixture is presented. An experimental investigation using conventional strain gage instrumentation and moire interferometry is performed. A finite element analysis of the Iosipescu shear test for unidirectional and cross-ply composites is used to assess the uniformity of the shear stress field in the vicinity of the notch, and demonstrate the effect of the nonuniform stress field upon the strain gage measurements used for the determination of composite shear moduli.

From the test results for graphite-epoxy laminates, it is shown that the proximity of the load introduction point to the test section greatly influences the individual gage readings for certain fiber orientations but the effect upon shear modulus measurement is relatively unimportant. A numerical study of the load contact effect shows the sensitivity of some fiber configurations to the specimen/fixture contact mechanism and may account for the variations in the measured shear moduli. A comparison of the strain gage readings from one surface of a specimen with corresponding data from moire interferometry on the opposite face documented an extreme sensitivity of some fiber orientations to eccentric loading which induced twisting and yielded spurious shear stress-strain curves.

In the numerical analysis, it is shown that the Iosipescu specimens for different fiber orientations have to be modeled differently in order to closely approximate the true loading conditions. Correction factors are needed to allow for the nonuniformity of the strain field and the use of the average shear stress in the shear modulus evaluation. The correction factors, which are determined for the region occupied by the strain gage rosette, are found to be dependent upon the material orthotropic ratio and the finite element models.

Based upon the experimental and numerical results, recommendations for improving the reliability and accuracy of the shear modulus values are made, and the implications for shear strength measurement discussed.

Further application of the Iosipescu shear test to woven fabric composites is presented. The limitations of the traditional strain gage instrumentation on the satin weave and high tow plain weave fabrics is discussed. Test result of a epoxy based aluminum particulate composite is also presented.

A modification of the Iosipescu specimen is proposed and investigated experimentally and numerically. It is shown that the proposed new specimen design provides a more uniform shear stress field in the test section and greatly reduces the normal and shear stress concentrations in the vicinity of the notches. While the fabrication and the material cost of the proposed specimen is tremendously reduced, it is shown the accuracy of the shear modulus measurement is not sacrificed.

ACKNOWLEDGEMENTS

I would like to express my sincere gratitude to Dr. John Morton, the chairman of my graduate committee, for his guidance and encouragement throughout the Ph.D. program. I am also very grateful to Dr. Gary L. Farley at NASA LaRC for his support and fruitful suggestions of this research. I am thankful to the other members of my graduate committee, Dr. E. G. Henneke, Dr. W. W. Stinchcomb, Dr. R. K. Kapania and Dr. S. Kellas for their review and comments of this dissertation. The sponsorship from Virginia Tech NSF Center for High Performance Polymeric Adhesives and Composites and the US Aerostructures Directorate under NASA Research Grant NAG-1-1053 is very much appreciated. In addition, thanks:

- My fellow group members, Dr. Ming-Yi Tsai, Dr. Publio Pintato, Todd Wieland, Kuen Tat Teh, Hary Budiman, Ellen Zhang, David Johnson and Catherine Traffanstedt, for the great time we shared together.
- The photomechanics lab personel, Dr. Robert Czarnek, Dr. Joosik Lee, Shih-Yung Lin and Jau-Je Wu, for their help in the moire experiments.
- Chari Morton for her hospitality and friendship.
- My wife, Jackie, and my daughter, Sarah, for their patience and love.

TABLE OF CONTENTS

CHAPTER 1. INTRODUCTION	1
1.1 Introduction.....	1
1.2 Objectives.....	2
1.3 Approach.....	3
1.4 Dissertation outline	3
CHAPTER 2. STRAIN GAGED SPECIMENS.....	4
2.1 Materials and specimen details	4
2.2 Shear modulus calculation	5
2.3 Experimental results	6
2.3.1 Individual strain gage readings	6
2.3.2 Typical shear stress-strain behavior	6
2.4 Summary.....	7
CHAPTER 3. MOIRE EXPERIMENT	9
3.1 Moire interferometry	9
3.2 Specimen preparation and testing	10
3.3 Moire fringe patterns	11
3.4 Shear strain distributions across the notches	12
3.5 Shear stress-strain data.....	13
3.6 Localized hybrid analysis	13
3.7 Summary.....	16
CHAPTER 4. NUMERICAL ANALYSIS	18
4.1 Introduction.....	18
4.2 Finite element models	19
4.3 Results and discussion	20
4.3.1 Force distribution on the specimen	20
4.3.2 Strain state in the specimen	21
4.4 Correction factor	23
4.5 Simulated gage reading	25
4.6 Load-point effect.....	27
4.7 Summary.....	28

CHAPTER 5. MECHANICS OF THE IOSIPESCU SPECIMEN.....	29
5.1 Introduction.....	29
5.2 One dimensional mechanics	29
5.3 Two dimensional mechanics	29
5.3.1 Asymmetric gage readings for 0° specimen.....	30
5.3.2 Apparent shear moduli for 0° and 90° specimens are different	30
5.3.3 Spread of measured shear moduli for 0° specimen	31
5.4 Three dimensional mechanics	32
5.4.1 Inconsistent modulus in a 90° specimen	32
5.4.2 Twisting model	33
5.4.3 Supplementary experiments	34
5.4.4 Effect of twisting	36
5.5 Shear modulus measurement.....	37
5.6 Shear strength measurement.....	38
5.7 Summary.....	40
CHAPTER 6. APPLICATION OF IOSIPESCU SHEAR TEST IN PARAMETRIC STUDIES	41
6.1 Introduction.....	41
6.2 Interfacial study	41
6.2.1 Material and specimen details	41
6.2.2 Experimental results and discussion.....	42
6.3 Cure cycle study	43
6.3.1 Material and specimen details	43
6.3.2 Experimental results.....	44
6.4 Summary.....	44
CHAPTER 7. APPLICATION OF IOSIPESCU SHEAR TEST TO WOVEN FABRIC, PARTICULATE COMPOSITES.....	46
7.1 Introduction.....	46
7.2 Woven fabric composites	47
7.2.1 Materials and specimen details	47
7.2.2 Experimental results.....	47
7.2.3 Discussion.....	48
7.3 Particulate composites.....	50

7.3.1	Materials and specimen details	51
7.3.2	Experimental results and discussion.....	51
7.4	Summary.....	52
CHAPTER 8. EVALUATION OF U-NOTCH IOSIPESCU SPECIMENS		53
8.1	Introduction.....	53
8.2	3" U-notch specimen	54
8.2.1	Numerical analysis	54
8.2.2	Materials and specimen details	56
8.2.3	Experimental results and discussion.....	56
8.3	2" U-notch specimen	58
8.3.1	Numerical analysis	58
8.3.2	Experimental results and discussion.....	59
8.4	Summary.....	61
CHAPTER 9. CONCLUSIONS AND FUTURE WORK		63
9.1	Conclusions and recommendations.....	63
9.2	Future work.....	65
REFERENCES.....		66
TABLE AND FIGURE CAPTIONS.....		70
TABLES AND FIGURES.....		80
VITA.....		195

CHAPTER 1. INTRODUCTION

1.1 Introduction

The in-plane shear modulus G_{12} for unidirectional composite materials is an essential quantity for the design of multidirectional composite laminates. It can also provide a useful parameter for the assessment of the effects of processing variables upon the performance of new composite material systems. A considerable number of test configurations have been proposed to determine G_{12} for unidirectional composite materials. The most popular of these are the $\pm 45^\circ$ tension test [1,2], the off-axis test [3], the rail test [4], and the Iosipescu V-notched beam specimen loaded in the modified Wyoming test fixture [5].

The Iosipescu specimen was originally proposed for the shear strength measurement of metals by Nicolae Iosipescu [6] in the 1960's. The specimen is rectangular with two opposing V-notches centered on the top and bottom edges. In addition to Iosipescu's original design, numerous loading fixtures have been developed for use with the V-notch specimen. Arcan *et al.* [7] developed the Arcan V-notch specimen and loading fixture in the late 1970's. Slepetz *et al.* [8] developed an antisymmetric four point bend loading fixture. In the late 1970's, Walrath and Adams [9] developed a Wyoming fixture (W1) and specimen, Figure 1.1. Since then the Iosipescu specimen has received wide attention in the composites community. The W1 fixture had small fixture-to-specimen contact regions with the inner contact regions located very close to the edge of the notch and thus created a small region in the test section where a near uniform shear stress was produced. Significant normal strains, ϵ_y , were observed in the test section for the 0° specimen. Adams and Walrath [5,10] continued to investigate how parameters such as the notch angle, notch depth, notch root radius and proximity of the loading point (region) to the test section influenced the test results and, thereafter, refined the specimen geometry, and modified the test fixture and specimen, Figure 1.2. The modified Wyoming fixture (W2) and specimen produced a larger test section and larger fixture-to-specimen contact regions than the original Wyoming fixture (W1) and the innermost load points are moved farther away from the test section. Composite specimen thicknesses between 2.5 and 5.0mm can be tested.

Most of the reported tests on unidirectional composites have been performed on specimens in which the fibers are parallel to the specimen longitudinal (x) axis; such specimens are designated 0° specimens in the present work. Less frequently, unidirectional

specimens are tested with the fibers parallel to the loading (y) axis; these are designated 90° specimens. The 0° specimen configuration is preferred by most researchers because it provides more of the shear stress-strain response than is achievable with 90° specimens. The investigation conducted hereafter focuses on the evaluation of the V-notch specimen tested in the modified Wyoming fixture.

While most existing shear testing methods are usually specialized for the measurement of shear properties in a single plane, the Iosipescu shear test distinguishes itself with the following features: (1) small specimen size with the ability to test a range of specimen thicknesses, (2) the ability to test unidirectional and multidirectional laminates, woven fabric, sheet molding compound and particulate composites, (3) the capability for measuring shear properties in the 1-2, 1-3 and 2-3 material planes and (4) the potential to measure shear modulus and strength.

Due to its attractive features, the Iosipescu shear test method has been widely used in recent years. Inconsistencies in measured strength and stiffness of composite materials have, however, been identified [11-13]. For example, the shear modulus for unidirectional AS4/3501-6 graphite-epoxy measured by a number of investigators using the Iosipescu specimen geometry and the modified Wyoming test fixture are shown in Figure 1.3. The data shown in Figure 1.3 have been normalized with respect to $G=5.12$ MPa which is the average shear modulus obtained from the $\pm 45^\circ$ tension and 10° off-axis tests [14]. From the data in Figure 1.3 it is found that shear moduli obtained from the 0° and 90° fiber orientations are different and there is a very large degree of scatter associated with the data.

The main problems for the Iosipescu shear test method can be categorized into three observations : (1) a pure shear state in the test section cannot be obtained for 0° specimen [15,16], (2) apparent shear moduli for 0° and 90° specimens are different [17], and (3) large variations occur in the shear stress-strain response for both 0° specimen and 90° specimen [11-13].

1.2 Objectives

Many [5,10,18] of the investigations about Iosipescu shear test focused on the parametric studies, such as the effects of notch depth, notch angle and notch radius on uniformities of the strain fields. The effect of load application scheme on the shear field in the test section has also been discussed [19,20]. Recently, Abdallah *et al.* [12] investigated

the influence of the test fixture design on Iosipescu shear specimen by direct comparison on the W1, W2 and antisymmetric four point bend fixtures. Wilson [13] conducted a round robin test for Iosipescu specimens tested in the W2 and antisymmetric four point bend fixtures and evaluated the repeatability and reproducibility of the two fixtures. In all these researches, variations of the measured shear moduli have been reported and some of the problems associated with the Iosipescu shear test have been identified. But the mechanics and the causes of the problems and apparent inconsistencies associated with the Iosipescu shear test have never been studied. The objective of this study is to explore the mechanics of the experimental procedure for the determination of composite material in-plane shear moduli of Iosipescu specimens loaded in the modified Wyoming fixture in order to resolve the existing controversies in the literature.

1.3 Approach

An experimental investigation is performed on unidirectional and cross-ply graphite-epoxy composites. Conventional strain measuring techniques are combined with whole-field moire interferometry. The resulting shear stress-strain curves are compared for the two techniques. A two-dimensional finite element analysis is performed to simulate the loading mechanics and assess the uniformity and purity of the shear stress distributions in the test section. The complementary numerical and experimental approach is used to separate factors involving instrumentation, specimen geometry, material properties, fixture effects and operator sensitivity.

1.4 Dissertation outline

In Chapter 2, general details of the V-notch specimen tested in the Wyoming fixture are given. An experimental study using traditional strain gage technique is presented. A full-field study using moire interferometry is carried out in Chapter 3. In Chapter 4, a two dimensional finite element analysis is performed and some of the existing controversies are resolved. A detailed mechanics study is presented in Chapter 5 and recommendations for performing the Iosipescu shear test are proposed. In Chapter 6, an application of the Iosipescu shear test to parametric studies of composite manufacturing processes is presented. In Chapter 7, an application of the Iosipescu shear test to woven fabric and particulate composites is investigated. Traditional strain gage techniques and moire interferometry are used. In Chapter 8, an U-notch Iosipescu specimen design is evaluated numerically and experimentally. Finally, Chapter 9 concludes this dissertation.

CHAPTER 2. STRAIN GAGED SPECIMENS

2.1 Materials and specimen details

Iosipescu specimens were cut from 20-ply unidirectional and cross-ply graphite-epoxy panels (AS4/3501-6) according to the dimensions suggested by Adams and Walrath [5], Figure 1.2b. These panels were supplied by NASA LaRC and were prepared according to the manufacturer's recommendation. The unidirectional specimens were prepared with the fibers in the 0° and 90° fiber orientations. The specimens had a nominal thickness of 2.8mm (0.11 in). In cutting the V-notches, a diamond-tipped end mill was used. Each specimen was then ground flat on the long edges. The specimen test section (the region between the top and bottom notches) was carefully sanded flat with very fine sand papers and the test section dimensions (test section thickness t , test section width w , and test cross-section area $A=tw$) were measured. The specimens were instrumented with stacked three-gage rosettes (Micro-measurements WK-06-060WR-350), as shown in Figure 1.2b. The rosette was attached to the center of the specimen, centered mid-way between the notches. One rosette was used on each specimen.

The instrumented specimens were tested in a modified Wyoming test fixture. Two versions of the fixture were used, one purchased from Wyoming Test Fixtures Inc., and the other produced for NASA LaRC according to Adams & Walrath's original drawings of the fixture. The two fixtures were used initially as a result of concerns about fixture-dependency in this shear testing method. It was later found that there was no significant difference in the performance of the fixtures for the measurement of the shear modulus. The specimen is centered using an alignment pin. The alignment pin is lifted to engage the lower notch in the specimen, and the specimen is then secured in the fixture with adjustable wedge clamps. Load is applied to a yoke (the movable portion of the fixture) which is constrained to move vertically along a guide shaft. During testing, the movable portion of the fixture moved downward and imposed displacement constraints to the specimen. The resultant force, P , from the specimen, which is also the equivalent applied shear force in the test section, was obtained from the load cell connected to the fixture.

In a preliminary series of tests the specimens were loaded to failure in a Tinius Olsen universal testing machine using a cross-head rate of 2mm per minute. During testing the load and individual gage readings were logged using an Apple Macintosh SE computer

equipped with a Strawberry Tree Inc. data acquisition system. Over 200 specimens were tested in this research program.

2.2 Shear modulus calculation

The measurement of shear modulus requires determining the shear strain corresponding to the average shear stress across the test section, for a given applied load. Shear strains are usually measured with a strain gage rosette which averages the strains over a finite area in the test section. If two gages, SG1 and SG2, are arranged at $\pm 45^\circ$ to the longitudinal axis of the specimen, as shown in Figure 1.2b, the shear strain γ_{xy} determined from the strain gages is

$$\gamma_{xy}^{SG} = \epsilon_{+45} - \epsilon_{-45} \quad (2.1)$$

The strain in SG1 (ϵ_{+45}) is compressive, and that in SG2 (ϵ_{-45}) is tensile, so the shear strain is negative. Occasionally, a third gage is used to record the strains in the longitudinal (x) direction to provide an estimation of out-of-plane bending (moment about the y axis). Note that the third gage provides information of the purity of the shear field but does not affect the shear strain calculation. The shear modulus G_{xy} is then calculated by dividing the average shear stress ($\tau_{avg} = P/A$) on the specimen cross-section by the measured shear strain.

$$G_{xy}^{SG} = \frac{\tau_{avg}}{\gamma_{xy}^{SG}} \quad (2.2)$$

In the current study, secant shear modulus is calculated at 0.5% shear strain. Under 0.5% shear strain, the shear stress-strain responses are linear for 0° , 90° and $0^\circ/90^\circ$ specimens. The secant and initial tangential shear moduli are essentially the same. Common practice is to use a two-gage rosette on one face of the specimen. Gage sizes of 1mm to 2mm are commonly used. The rosettes may be stacked or unstacked. If the gages are not stacked then they record the strains at two locations. If the shear strain field in the test section is uniform, then shear modulus and shear stress-strain response are independent of gage size and whether the gages are stacked.

2.3 Experimental results

2.3.1 Individual strain gage readings

The normal strains measured by the individual gages of the rosette are plotted as a function of the *average shear stress* in Figure 2.1. The absence of strain in the gage oriented parallel to the longitudinal axis of the 0° specimen, shown in Figure 2.1a, indicates that little or no out-of-plane bending (bending about the y-axis) occurred. The symmetrically placed off-axis gages ($\pm 45^\circ$) document a significant degree of nonlinear behavior. Also the strains recorded in these gages are not equal in magnitude and opposite in sign. This is contrary to the observation of Sullivan [15] who stated that "In a properly loaded Iosipescu specimen, the two strains at $\pm 45^\circ$ deg should be equal in magnitude and opposite in sign to a reasonable approximation." The 90° specimen also showed little out-of-plane bending. The stress-strain response of the specimen was nearly linear to failure and the measured $\pm 45^\circ$ strains were equal in magnitude and opposite in sign. The stress-strain response of the $0^\circ/90^\circ$ specimen is shown in Figure 2.1c. The behavior of this specimen is essentially between those of the 0° and 90° specimens.

If the specimen test section is in a state of pure shear, the $\pm 45^\circ$ directions would be the principal directions and the normal strains recorded by the two gages at $\pm 45^\circ$ directions should be equal in magnitude and opposite in sign, Figure 2.2. Therefore, the 0° specimen is not under pure shear but the 90° specimen is. This is observation (1) associated with Iosipescu shear test as stated in section 1.1.

2.3.2 Typical shear stress-strain behavior

In Figure 2.3, average shear stresses are plotted as a function of shear strains determined from the strain gages for the 0° , 90° and $0^\circ/90^\circ$ graphite-epoxy composites. These curves are for individual specimens loaded to failure and are representative of typical behavior. The apparent shear moduli (initial, secant and tangent) are lower for the 90° specimen than for the 0° specimen. The behavior of the $0^\circ/90^\circ$ specimen is approximately midway between the two unidirectional cases. This phenomenon is denoted observation (2) associated with the Iosipescu shear test in section 1.1. The shear strengths of the specimens are shown in Figure 2.3. The strength of the 90° specimen is much less than those of the other two cases.

The 90° specimen failed through the propagation of a single crack between the notches, parallel to the fibers. However, failure did not occur at the minimum cross section but at the intersection of the notch root and the right notch flank. The 0° specimen failed with two longitudinal cracks propagating parallel to the fibers and emanating from the intersection of the notch root and the notch flank. The cracks occurred on the left side of the upper notch and on the right side of the lower notch. The $0^\circ/90^\circ$ specimen failed through a network of cracks developing in both fiber directions. Schematic drawings of the failure modes of the 0° , 90° and $0^\circ/90^\circ$ specimens are shown in Figure 2.3. The failure modes mentioned above are commonly observed and are characteristics of the V-notch geometry, which will be further discussed in Chapter 4.

2.4 Summary

In a pure shear stress field, the gage readings at $\pm 45^\circ$ directions should be equal in magnitude and opposite in sign. From this experiment on strain gaged specimens it is found that the individual gages on 0° specimens do not record normal strains equal in magnitude and opposite in signs. This observation indicated the presence of normal strains in the gage section. Note that the use of equation (2.1) for the shear strain calculation is based on the pure shear assumption, therefore, the validity of 0° specimen in the Iosipescu shear test is questioned. The individual gages on the 90° specimen do record equal and opposite strains and provide evidence of the state of pure shear in the gage section.

In practice, the 0° specimen is more frequently used because it provides a wider range of shear stress-strain response as compared to that of the 90° specimen. But the inequality in the magnitude of the strains is either not observed or ignored by most researchers. It has even been suggested that the shear strain can be obtained by doubling the magnitude of the normal strain measured by a single gage at the $+45^\circ$ direction [5]. Lee and Munro [16] showed experimentally that the individual gages at the $\pm 45^\circ$ direction cannot record equal and opposite strains and, hence, concluded that the 0° specimen should not be used for shear modulus measurement.

The second observation from the experiments on strain gaged specimens is that the shear moduli obtained from shear stress-strain curves of 0° , 90° and $0^\circ/90^\circ$ specimens are not consistent even though elementary mechanics indicated that they should be the same.

The two phenomena above will be investigated in detail in the following three chapters.

CHAPTER 3. MOIRE EXPERIMENT

3.1 Moire interferometry

Moire interferometry [21,22] is an optical technique which uses the interference of two coherent beams of light to produce contours, or fringe patterns, of in-plane surface displacement components (u,v). The method employs a high frequency grating which is attached to the surface of the specimen and deforms with the specimen surface. When the deformed specimen is interrogated in an interferometer, fringe patterns corresponding to the u or v fields are obtained. The sensitivity f (or frequency of the virtual reference grating) of the technique is determined by the frequency of the specimen grating, the wavelength of the light, λ , and the optical arrangement. The basic equation is,

$$f = \frac{2}{\lambda} \sin \alpha \quad (3.1)$$

where α is the angle between the incident beam and the first order diffracted beam, Figure 3.1. The displacement components u and v are related to the fringe orders N_x and N_y by

$$u = \frac{1}{f} N_x \quad \text{and} \quad v = \frac{1}{f} N_y \quad (3.2)$$

and the in-plane strains are related to the gradients of the fringe orders by

$$\begin{aligned} \epsilon_x &= \frac{\partial u}{\partial x} = \frac{1}{f} \frac{\partial N_x}{\partial x} \\ \epsilon_y &= \frac{\partial v}{\partial y} = \frac{1}{f} \frac{\partial N_y}{\partial y} \\ \gamma_{xy} &= \frac{\partial u}{\partial y} + \frac{\partial v}{\partial x} = \frac{1}{f} \left(\frac{\partial N_x}{\partial y} + \frac{\partial N_y}{\partial x} \right) \end{aligned} \quad (3.3)$$

A three mirror, optical system, developed by Czarnek [23], was used in this study. The optical set-up is shown in Figure 3.1a. The determination of the shear strain from the moire experiment requires the differentiation of data from two fringe patterns. In the three mirror system a beam selector, Figure 3.1a, is used to illuminate the specimen grating with

two beams A and B, Figure 3.1b, in the horizontal plane. The horizontal component of the displacement field is then recorded photographically. The beam selector is then adjusted to give beams C and D which, with the aid of the two 45° mirrors in the three-mirror interferometer, illuminate the specimen grating in the vertical plane. This arrangement provides the vertical displacement component fringe pattern. The rotation adjustment screw, Figure 3.1a, allowed rotation of the whole system (about the z-axis) relative to the specimen to introduce carrier fringes.

3.2 Specimen preparation and testing

Two specimens of each fiber orientation were instrumented with a stacked three-gage rosette (Micro-measurements WK-06-060WR-350) at the center of the test section, with two gages at $\pm 45^\circ$ (SG1, SG2) and the third gage (SG3) parallel to the specimen longitudinal axis, as shown in Figure 1.2b. A crossed-line diffraction grating was applied to the face opposite the strain gage rosette. This specimen grating had a frequency of 1200 lines/mm, and covered the width of the specimen and extended approximately 10 mm on either side of the notch. The interferometer used in the experiments gave a fringe pattern sensitivity of 0.417 μm per fringe.

The instrumented specimens were tested in a conventional screw driven test machine. The three-mirror interferometer was positioned in front of the specimen. Before applying load to the specimen, the interferometer was tuned to provide no-load (null field) fringe patterns. The null field fringe patterns consisted of one fringe or less across the field of view. Load was then applied to the specimen until a predetermined value was obtained. Under constant loading, u and v fringe patterns were recorded photographically. A set of patterns was also obtained with rigid body rotation introduced. The shear strain γ_{xy-r} due to the rigid body rotation is given by

$$\gamma_{xy-r} = \left(\frac{\partial u}{\partial y} + \frac{\partial v}{\partial x} \right) = 0. \quad (3.4)$$

The rotation can be adjusted to cancel out the cross derivative term, $\partial u/\partial y$, of the u field. Therefore, the v field (with rotation) contains all the shear information in the uniform region of the test section. This technique is known as applying a carrier pattern of rotation and is a convenience for fringe pattern interpretation and data reduction. This test

procedure was repeated at numerous load levels until the fringe patterns became too dense to analyze.

3.3 Moire fringe patterns

Typical fringe patterns from the 0° , 90° , and $0^\circ/90^\circ$ specimens are shown in Figures 3.2-3.4. The fringes in Figures 3.2a and 3.4a are not smooth but contain a zig-zag pattern. In Figures 3.3b and 3.4b, nonuniform fringe bands are observed. In the test section, where the maximum shear stress occurs, the fringe density is high. At some regions away from the test section, high density fringe bands also exist. The zig-zag pattern in the u -fields of the 0° and $0^\circ/90^\circ$ specimens and the fringe bands in the v -fields of the 90° and $0^\circ/90^\circ$ specimens suggest that the material cannot be regarded as homogeneous. The nonuniform displacement fields due to material nonhomogeneity are shown in the u -fields for specimens with fibers in the longitudinal direction and in the v -fields for specimens with fibers in the transverse direction.

The normal and shear strains at any location in the field of view can be determined by calculating the in-plane displacements and taking the appropriate derivatives of the u and v displacements. The normal strains are readily interpreted in terms of the gradients of the fringe contours, in the u field patterns in the x -direction (horizontal), $\partial u/\partial x$, and, in the v field patterns in the y -direction (vertical), $\partial v/\partial y$. The shear strains require determining the cross derivatives in both fringe patterns.

The normal strain ϵ_x in the 0° and $0^\circ/90^\circ$ specimens is very small in the test section except at the notch roots because the longitudinal stiffness E_x is very large. The small ϵ_x can be readily observed by noting that there are a few fringes located in the test section, Figures 3.2a and 3.4a, and that the gradients of these fringes in the x -direction are small.

Because E_x is small for the 90° specimen, the normal strain ϵ_x could be large near the notch root. This can be interpreted in the relatively closely spaced fringes near the notch roots. In this particular moire experiment, the normal strain ϵ_x at the top notch tip is essentially zero but is of certain magnitude at regions on both sides of the notch tip. At the left notch flank region, the normal strain ϵ_x is tensile while at the right notch flank region the normal strain ϵ_x is compressive. At the bottom notch tip and its right flank region, the normal strain ϵ_x is also tensile. These normal strains and the lack of antisymmetry are a

consequence of the V-notch design and bending of the specimen about the y and z axes as a result of the low flexural stiffness of the 90° specimen about these axes.

The v-displacement field for the 0° specimens consists of dense, almost vertical fringes in the region between the notches, as shown in Figure 3.2b. Since the vertical gradient of the fringe contours in the u-displacement field (Figure 3.2a) is small in comparison with the horizontal gradient in the v-displacement field, most of the shear strain is due to the cross derivative term $\partial v/\partial x$. This is especially the case near the center of the specimens: note that the strain gages are located at the center of the specimen. However, near the notches the term $\partial u/\partial y$ becomes significant and is required to satisfy the stress-free condition. The v-displacement field for the 0° specimen reveals that they are S-shaped. Thus, there is a vertical gradient corresponding to a normal strain ϵ_y . Thus the normal strains recorded by the two strain gages at $\pm 45^\circ$ directions would not be equal in magnitude and opposite in sign. This further confirms the observation in the strain gaged experiment.

The v-displacement field for the 90° specimen, shown in Figure 3.3b, consists of almost straight vertical fringes. The same nonuniformity of fiber distribution is present in the 90° specimens as in the 0° specimens. Along the line between the notches and in the center of the test section where strain gages are normally applied, the normal strain ϵ_y is zero. The 90° specimen does not show any effect of proximity of the applied load in the test section. Similar behavior is evident in the 0°/90° specimen, as shown in Figure 3.4b.

3.4 Shear strain distributions across the notches

One way of assessing the uniformity of the shear strain distribution is to examine the shear strain along a line joining the notch tips. The shear strains, normalized with respect to the average shear strain γ_{avg} , are shown in Figures 3.5a-3.5c for the 0°, 90°, and 0°/90° specimens respectively. Note that γ_{avg} is defined by

$$\gamma_{avg} = \frac{1}{h} \int_{-h/2}^{h/2} \gamma_{xy} dy \quad (3.5)$$

Shear strain distributions are shown for several load levels.

The 0° specimen, Figure 3.5a, has the largest shear strains near the notch tips. At the center, the shear strain is about 90% of the average value across the section. The distribution, particularly near the notch tips, depends upon the magnitude of the applied load. At the higher load level the distribution takes on a more symmetric form. The differences in the shear strain distributions at different load levels indicate that the 0° specimen is sensitive to the actual loading conditions. This will be further discussed in Chapter 4.

The 90° specimen has the peak shear strain at the center, as shown in Figure 3.5b. The peak shear strain distribution varies with load, from between 18% to 29% greater than the average value. The shear strain distribution for the 0°/90° specimen, Figure 3.5c, is similar to that of the 90° specimen. The peak shear strain near the center is about 10 to 18% greater than the average value. Note that the shear strain distribution for the 0°/90° specimen is not smooth, as a result of the local nonuniform deformation documented in Figure 3.4b. From moire data reduction, it is shown that shear stress distributions is not uniform for 0°, 90° and 0°/90° specimens.

3.5 Shear stress-strain data

The moire data can also be used to determine the average shear strain *over an area equivalent to that covered by the strain gages*. The shear stress-strain data for the moire and strain gage rosettes can then be compared directly. In Figure 3.6, the average shear stress (the applied load P /notch section area A) is plotted as a function of the shear strains from moire and the strain gage rosettes. Recall that these represent strains on opposite faces of the same specimen. The shear strains for the rosettes were calculated from the normal strains ϵ_{+45} and ϵ_{-45} in the $\pm 45^\circ$ gages by

$$\gamma_{xy} = \epsilon_{+45} - \epsilon_{-45} \quad (3.6)$$

The shear stress-strain data for the 0° specimen, shown in Figure 3.6a, are almost coincident. However, the data for the 90° and 0°/90° specimens are quite different for the moire and strain gage rosette, as shown in Figures 3.6b and 3.6c.

3.6 Localized hybrid analysis

In practical engineering analyses, strain and stress data are required or produced. Strain can be obtained from taking derivatives of the u- and v-displacement fringes of moire experiment. But manual reduction of the displacement data becomes tedious when the area of interest is large. Thus a localized hybrid analysis is introduced [24] to perform efficient reduction of moire data, producing whole field strain distributions in the specimen test section.

The finite element method was used as part of a localized hybrid analysis of the moire data [24]. In the localized hybrid analysis an arbitrary shaped region in the test section of the specimen is selected. A rectangular region covering most of the zone between the notches was chosen in the current investigation. The chosen region was divided into 384 rectangular plane stress elements for the 0° specimen and 192 rectangular plane stress elements for the 90° and $0^\circ/90^\circ$ specimens. The u and v-displacements (relative to a reference point on the specimen) at the nodes on the boundary of the region were determined manually using linear interpolation of the moire fringe patterns. The ABAQUS finite element program was used to calculate the displacements, strains, and stresses everywhere within the region. The finite element displacement fields within the region were compared with the displacement fields from the moire experiment. If agreement was obtained, then the finite element strains could be used as representative of those in the region of the specimen selected for analysis. This simple technique has the advantage that it forms an efficient and convenient means of moire data reduction.

The displacement contours produced in the localized hybrid analysis are very similar to those obtained from the moire experiment. The nonuniformities in the u-displacement fields (zig-zag shaped fringes) of the 0° and $0^\circ/90^\circ$ specimens, shown in Figures 3.7 and 3.8, and in the v-displacement fields (high density fringe bands) of the $0^\circ/90^\circ$ and 90° specimens, shown in Figures 3.8 and 3.9, cannot be replicated in the localized hybrid patterns. These nonuniformities, attributed to local imperfections in the specimen fiber distribution, are not represented in the localized hybrid analysis which assumes homogeneous material behavior.

For the 90° case, the calculated u-displacement field is two or three fringes less than the moire data, Figures 3.9a and 3.9c. The difference is due to the presence of the null-field fringes and the very small strains associated with the u displacement field. The

calculated v-displacement field (showing every 3rd fringe) in Figure 3.9d is very similar to the moire data. The agreement between the calculated and experimental displacement fields indicates that the localized hybrid analysis provides a good approximation.

When the calculated displacement fields show good agreement with the moire data, further data reduction can be effected. The normal strains, ϵ_x and ϵ_y , and the shear strains, γ_{xy} , together with the deformed shape are obtained from the localized hybrid analysis. Deformed shapes and in-plane strains are shown in Figures 3.10-3.12 for the 0° and 90° and $0^\circ/90^\circ$ specimens. Comparisons of shear strain data along the y and x-axes for the 0° , 90° and $0^\circ/90^\circ$ specimens are shown in Figures 3.13 and 3.14. In Figures 3.13 and 3.14, the strain distributions, calculated from localized hybrid analysis and manual data reduction, agree well except for the local fluctuations in the $0^\circ/90^\circ$ specimen.

Strain fields

The ideal requirement of the Iosipescu specimen is that a state of pure shear should be produced within the test section. The experiments provide a means of evaluating the extent to which this is achieved in the three composites tested. The data, obtained through the localized hybrid technique, are presented as the deformed local mesh shape and contour maps of the three strain components in Figures 3.10-3.12 for the 0° and 90° and $0^\circ/90^\circ$ specimens, respectively. For the 0° specimen the deformed mesh, Figure 3.10a, indicates, superficially, that the deformation corresponds to uniform shear over most of the region analyzed. However, examination of the corresponding normal strain fields reveals a significant compressive strain ϵ_y due to the proximity of the loading to the test section in this specimen (which has a low stiffness E_y in the direction parallel to the applied load, compared to that in the longitudinal (x) direction). At the center of the specimen, where the strain gage would be located in the material property test, the normal strain ϵ_y is about 0.109% compared to the shear strain of 0.71%; that is, the normal strain is about 15% of the shear strain. At two small regions near the notch root-notch flank intersection further from the applied load, tensile normal strain ϵ_y is observed, which is about 11% of the shear strain in the test section. The corresponding shear strains at the two regions are about 85% of the shear strain in the test section. The strain ϵ_x is small everywhere across the test section, with a value of about 0.015% at the center, or about 2% of the shear strain. The above observation implies that the test section in the 0° specimen is not subjected to pure shear, and that the $\pm 45^\circ$ strain gages used in the Iosipescu test would not read equal and opposite strains. The strains near the notches are in a very complex state. The lack of

equal and opposite strains for the $\pm 45^\circ$ gages and the complex strain state in the vicinity of the notch root will be further investigated using a finite element model in the next chapter.

The deformed mesh obtained from the localized hybrid analysis of the 90° specimen, Figure 3.11, shows that significant bending takes place in the test section. This is also shown in the contour map for ϵ_x . A feature of this distribution is that the axial (bending) strain is small near the center of the test section, ϵ_x is about 0.04%. At the top left and bottom right corners of the region, large tensile normal strain ϵ_x is observed. The fringes are not antisymmetrically distributed. The non-antisymmetrical nature of the fringes implies that the specimen is under a combination of in-plane and out-of-plane bending in addition to the applied shear. The strain ϵ_y is small over most of the test section; at the center ϵ_y is about 0.02%. This is a result of the relatively large stiffness E_y in the loading direction, for this fiber orientation. Both of these normal strains are small compared to the value of about 0.59% for the shear strain near the center of the specimen. This is in agreement with the observation that the 90° specimen does give equal and opposite strains in $\pm 45^\circ$ gages. The implication of this is that the 90° specimen is insensitive to the proximity of the load to the test section.

The data for the $0^\circ/90^\circ$ specimen are essentially a combination of those from the 0° and 90° specimens. The bending strains are small across the section; ϵ_x is about 0.01%. The strain ϵ_y is also small near the center; ϵ_y is about 0.01%, when the shear strain at the center is 0.74%.

3.7 Summary

For the Iosipescu specimen tested in the modified Wyoming fixture, the innermost load points are moved farther away from the test section. From the v-field fringe pattern for 0° specimen, it is found that the fringes are S-shaped and the normal strain ϵ_y is still present in the test section. If two strain gages are aligned at $\pm 45^\circ$ directions, they will record normal strains which are not equal in magnitude and opposite in sign. Due to the presence of the normal strain, the shear strain cannot be calculated by doubling the magnitude of one strain gage at $+45^\circ$ direction, as had been suggested by Adams *et al.*, [5].

It was shown that shear strain distributions along the notch axis for 0° , 90° and $0^\circ/90^\circ$ specimens are not uniform and the distribution patterns are not the same for these three

fiber orientations. For the 0° specimen, the distribution depends on the magnitude of the applied load. It was suggested that the 0° specimen is sensitive to the actual loading conditions.

The moire experiment with moire grating on front face and strain gage rosette on the other face of the specimen also provides comparison of the shear stress-strain data on the two faces. It is found that for the 0° specimen the front and back shear stress-strain curves are very nearly coincident but for 90° and $0^\circ/90^\circ$ specimens the shear stress-strain curves for front and back faces are far apart. Hence the shear moduli obtained from the front and back stress-strain curves are not consistent. Though the moduli obtained from front and back faces of a 0° specimen are essentially of the same magnitude, the moduli obtained from several 0° specimens show a significant variation from specimen to specimen.

The moire fringe patterns provide a whole field displacement information in the test section. Strain data are obtained through a localized hybrid analysis. Significant normal strain ϵ_y is found in the test section of 0° specimen while for 90° specimen the test section is essentially under pure shear. The strain state in the vicinity of the notch root is complex. Large tensile strains are found in certain areas around the notch root.

The issues mentioned above will be addressed in the next two chapters.

CHAPTER 4. NUMERICAL ANALYSIS

4.1 Introduction

The development and evaluation of in-plane shear test methods for the determination of shear modulus and strength has not only received considerable experimental but also analytical attention from the composite materials industry. The numerical analysis provides a general and objective study of the shear test, which excludes some factors involved in the experimental work, such as instrumentation, fixture effects and operator sensitivity. An ideal shear test method would produce a pure and uniform shear stress field in the test section of the specimen throughout the linear and nonlinear response regimes. Although the Iosipescu shear test method has gained wide acceptance for measuring the in-plane shear response of composite materials, it has been shown experimentally that it does not possess these ideal characteristics. The purpose of the numerical analysis is to evaluate the purity and uniformity of the shear stress field and its effect on the measurement of shear modulus.

Numerical analyses have been used widely in determining the influence of different geometric variables, such as notch angle [5,10,18], notch radius [5,18] and ply orientation [5,17,18,19,20] on the shear response. Numerical analysis has also provided insight into failure mechanisms and locations [20], uniformity of stress/strain distribution in the test section [5,9,12,17-20,25-27] and the development of shear modulus correction factors [17,19]. However, without an accurate prediction of the strain distribution in the test section, shear modulus correction factors cannot be determined. The strain state in the test section is a function of the manners in which the load is introduced to the specimen, and the applied boundary conditions.

Unfortunately, there seems to be a lack of consensus of how to represent the boundary conditions and load introduction in the Iosipescu specimen. For example, Barnes *et al.* [25] used uniformly distributed applied forces, Sullivan *et al.* [27] used concentrated forces and Walrath *et al.* [10] used prescribed vertical (y) displacement at the specimen-fixture contact regions in their finite element analyses of W1 test fixture and specimen. The use of concentrated forces can cause significant local deformations in the specimen and are unrepresentative of the experimentally observed deformations. A uniform applied force assumes the applied force distribution is known *a priori*. In recent

finite element analyses of the Iosipescu specimen tested in W2 fixture by Adams *et al.* [5] and Pindera *et al.* [17,26], prescribed vertical displacement boundary conditions were used but different type of constraints (hinges and rollers) were applied to the stationary part of the specimen-fixture contact regions. Furthermore, the same finite element model was applied to the 0° and 90° specimens [17,26].

The objective of this study is to conduct a linear-elastic 2-D finite element analysis of the W2 specimen using an iterative analysis approach which more realistically resembles the load transfer between the fixture and specimen and the displacement conditions at the specimen/fixture interface. The force distribution applied to the specimen along the fixture-to-specimen contact region, the strain state in the specimen and the shear modulus correction factors are evaluated. Three fiber orientations (0°, 90° and 0°/90°) are used in the analysis along with three materials having different orthotropic ratios (graphite-, Kevlar- and glass-epoxy).

4.2 Finite element models

In the modified Iosipescu shear test, the left end section of the specimen is clamped into the stationary part of the fixture and the right end section of the specimen is clamped into the movable part of the fixture, see Figure 1.2a. Assuming the clamping process does not introduce any significant strains in the specimen, load is transferred only from the fixture to the specimen along the upper fixture-to-specimen contact region of the movable portion of the fixture. The lower fixture-to-specimen contact region of the movable portion of the fixture cannot "pull" on the specimen because it is not mechanically attached to the specimen. That is, tensile forces cannot be applied along the lower edge of the specimen by the fixture. However, a reaction force is developed between the specimen and fixture along the lower edge of the movable part of the fixture because the lower contact region of the fixture prohibits rotation of the specimen keeping the upper and lower surfaces parallel and horizontal, as depicted in Figure 4.1.

Local in-plane bending of the specimen occurs as load is applied to the specimen, as depicted in Figure 4.1b. Along the upper fixture-to-specimen contact region the outboard region of the specimen and along the lower fixture-to-specimen contact region the inboard region of the specimen (movable portion of the fixture), the specimen can progressively separate from the fixture as a function of the applied load, see Figure 4.1b, which reduces

the length of the contact region. A similar set of deformations occurs on the fixed portion of the specimen.

In this study, the innermost load point distance from the notch axis was 7.0mm. The mechanical properties of the three materials are presented in Table 4.1. The finite element model had 1468 membrane finite elements, see Figure 4.2. At areas close to the notch root, the elements are refined such that the reduction of strains to near zero at the free boundary can be shown. Prescribed displacements, $y = -0.05\text{mm}$, were applied to the fixture-to-specimen contact regions on the movable part of the fixture. The ABAQUS and PATRAN codes were used for calculations and pre-, post processing, respectively. These codes were run on an Apollo DN4000 workstation.

The sequence of steps for application of boundary conditions and applied displacements in this study are as follows:

1. Displacement constraints (roller or hinge) to eliminate rigid body motion of the specimen are applied along the fixture-to-specimen region on the nonmovable (left) part of the specimen, see Figure 4.3.
2. Uniformly applied displacements are applied along the fixture-to-specimen region on the movable (right) part of the specimen, see Figure 4.3.
3. Reaction forces are calculated at the nodes where the applied and constrained displacements are introduced. Displacements along the specimen-to-fixture contact regions are also calculated.
4. If any reaction force were tensile or if the specimen interfered with the fixture (displacement interference) then the displacement constraint or the applied displacement is changed or removed from that finite element node.
5. The analysis is performed with an updated set of displacements and the process is repeated starting with step 3 until convergence occurs.
6. When convergence occurs the load applied to the specimen is the sum of the reaction forces on the movable (right) portion of the specimen.

4.3 Results and discussion

4.3.1 Force distribution on the specimen

After several iterations, it was found that to have no displacement interference and no tensile force at the fixture-to-specimen contact regions, the 0° , 90° and $0^\circ/90^\circ$ specimens had

be modeled differently, as demonstrated in Figures 4.4a-4.4c. On the stationary part of the fixture-to-specimen contact regions, roller constraints should be applied.

The force distributions into the graphite-epoxy specimens along the fixture-to-specimen contact regions for the three different ply orientations using the finite element models from Figure 4.4 are depicted in Figure 4.5. The force distributions are a function of the ply orientation and are representative of neither the concentrated nor uniformly distributed forces. The load distribution along the upper fixture-to-specimen contact region on the movable part of the fixture is highly nonlinear with the highest forces closest to the center of the specimen. The applied force distribution along the upper surface of the movable part is not the same as the reaction force distribution along the lower surface. The applied force distribution at innermost fixture-to-specimen contact regions on the 90° specimen is narrower than for the other ply orientations because considerable in-plane bending occurs causing the specimen to pull away from the fixture. The force distribution of the 0°/90° specimen is approximately the average of the 0° and 90° specimens.

4.3.2 Strain state in the specimen

Test section

The normal and shear strains, normalized with respect to average shear strains computed across the test section, are shown in Figures 4.6-4.8 for 0°, 90° and 0°/90° specimens, respectively. It is shown that the horizontal normal strains, ϵ_x , are negligible for all 0°, 90° and 0°/90° specimens because no horizontal constraints are applied in each model. If hinge constraints were applied, there would be horizontal normal strains, which are not observed in the experimental full-field results. The compressive transverse normal strains, ϵ_y , are negligible for 90° and 0°/90° specimens but are significant for the 0° specimens. As shown in Figure 4.6, ϵ_y reaches maximum at the center of the specimen and decays to zero at the notch root. The normalized transverse normal strain distributions along the notch axis for the 0° specimen are of approximately parabolic shape. At the center of the specimen, ϵ_y is 24.4% of γ_{avg} for graphite-epoxy and are 9.5% and 12.3% of γ_{avg} for Kevlar-epoxy and glass-epoxy respectively. Due to the low transverse stiffness of 0° specimens, the compressive stresses at the contact nodes channel along the fiber direction into the test section and introduce vertical normal strains. For 90° and 0°/90° specimens, the compressive stresses are attenuated locally by the transversely aligned fibers and no ϵ_y due to compressive forces will be present in the specimen gage section.

The shear strain contours of typical 0° , 90° and $0^\circ/90^\circ$ graphite-epoxy specimens are shown in Figure 4.9. The contours are presented for a specimen subjected to a 0.05mm downward displacement on the right side contact nodes. Because our interest is centered on the shear strain distribution at the gage section, only the central part of the contour is shown. The transverse and longitudinal normal strain contours for the proposed models are shown in Figures 4.10-11.

In the center portion of the specimen, where the strain gages would be attached, the shear and normal strains are approximately uniform in all material systems. Strain contours for $0^\circ/90^\circ$ specimen have characteristics of both 0° and 90° specimens and behave essentially midway between.

Fixture-to-specimen contact region

It is shown that in the 0° specimen ϵ_y is largest at inner most contact regions and decay radially from the innermost contact points into the test section, Figure 4.10a. The ϵ_y in the test section is about 16% of the ϵ_y in the innermost contact regions. As shown in Figure 4.11a, ϵ_x is small, about 14% of the ϵ_y , in the innermost contact regions. Shear strain γ_{xy} is of the same order as ϵ_y . For the 90° specimen, the largest transverse normal strains occur at the two antisymmetric inner contact areas next to the notch root and decay vertically only, Figure 4.10b. The test section is not within the decay range. The magnitude of ϵ_x at the innermost contact regions is compressive and is of the same magnitude as ϵ_y and γ_{xy} . For $0^\circ/90^\circ$ specimen, the longitudinal strain ϵ_x contour is more like that of 0° specimen while ϵ_y contour is similar to that of 90° specimen.

Notch region

Ideally, the specimen should fail in shear at the minimum cross section so that the notches should not provide any stress raising effect. Experimental observations indicate that the ideal condition is not achieved and that the failure locations for the 0° and 90° specimens are found at regions close to the intersection of the notch root and notch flank, rather than at the minimum cross section. The linear elastic finite element results obtained here indicate that a complex strain state occurs in the region in which initial failure is generally observed. In Figures 4.9a and 4.10a, it is observed that at the notch root-notch flank intersection further from the applied loading the transverse normal strain ϵ_y is tensile with a value of about 24% of the largest shear strain γ_{xy} in the test section, and the shear

strain γ_{xy} at the notch root-notch flank intersection is about 74% of the largest shear strain in the test section, for the 0° graphite-epoxy specimen.

In the case of the 90° specimen, Figures 4.9b and 4.11b, the longitudinal strain ϵ_x is tensile, at the notch root-notch flank intersections further from the applied loading, with a value of about 18% of the largest shear strain γ_{xy} at the center of the test section. The corresponding shear strain at the notch root-notch flank intersection is about 51% of the γ_{xy} at the center of the test section.

It is beyond the scope of the current work to estimate the failure mode and loads of the Iosipescu specimens. The analysis presented is linear elastic but significant nonlinear material and geometric effects will occur before failure occurs. Also it is of questionable value to apply failure criteria in the present analysis since it is not clear whether the parameters involving shear failures correspond to pure shear or contain some mixed-mode influence. It is clear, however, that the use of the 0° and 90° Iosipescu specimens to measure shear strengths is ill-advised if significant mixed mode effects are observed. The finite elements analysis presented here indicates that such effects are observed, in the linear elastic analysis at least, and experiments indicate that the notch root-notch flank intersections may be critical regions which initiate failure.

4.4 Correction factor

For the 0° specimen, the shear strain distribution is not uniform. Shear strain, γ_{xy} , is less than γ_{avg} , the average shear strain along notch-root axis, in the center portion but increases gradually for areas away from the center and reaches a peak with a magnitude larger than γ_{avg} at areas near the notch roots, then drops at the notch. If the finite element meshes were fine enough, γ_{xy} would drop to zero to satisfy the free boundary condition. The distribution of shear strain for 90° specimen is approximately parabolic in shape with maximum strain located at center of the specimen. Shear strain distribution of $0^\circ/90^\circ$ specimen is more uniform, but the shear strain in the center portion is still greater than γ_{avg} . If the shear modulus, G_{12} , were calculated by dividing the applied shear stress by the measured shear strain (which is obtained from strain gages attached to the center portion of the specimen) then erroneous results would be obtained.

To account for the nonuniformity of the shear strain distribution in shear modulus calculation, correction factors are applied. Correction factors (CF) are obtained by dividing the shear strains, γ_{gage} , at the gage section at the center portion of the specimen by the average shear strain, γ_{avg} , across the notch-root axis.

$$\gamma_{\text{avg}} = \frac{1}{h} \int_{-\frac{h}{2}}^{\frac{h}{2}} \gamma_{xy} dy \quad (4.1)$$

$$\text{CF} = \frac{\gamma_{\text{gage}}}{\gamma_{\text{avg}}} \quad (4.2)$$

$$G_{xy} = \frac{\tau_{\text{avg}}}{\gamma_{\text{avg}}} = \frac{\tau_{\text{avg}}}{\gamma_{\text{gage}}} \times \text{CF} = \text{CF} \times G^* \quad (4.3)$$

where h is the distance between two the notches ($y_{\text{max}}=h/2$) and G^* is the apparent shear modulus ($\tau_{\text{avg}} / \gamma_{\text{gage}}$). A comparison of the shear strain distributions along the notch axis normalized with respect to the average shear strains for 0° , 90° and $0^\circ/90^\circ$ graphite-epoxy, Kevlar-epoxy and glass-epoxy specimens is shown in Figure 4.12. The corresponding correction factors are also shown in Figure 4.12. It is found that the shear modulus correction factors depend on the material orthotropic ratios. For 0° specimen, the correction factor is smaller than unity and the larger the material orthotropic ratio, the smaller the correction factor. As the orthotropic ratio approaches one, the correction factor approaches 1.04. For the 90° specimen, the situation is reversed. Approximately, the correction factors can be expressed as,

$$\text{CF} = 1.036 - 0.125 \times \log\left(\frac{E_x}{E_y}\right) \quad (4.4)$$

where E_x and E_y are extensional stiffnesses in the longitudinal and transverse directions. Figure 4.13 is a plot of the correction factors as a function of material orthotropic ratio.

Note that for the $0^\circ/90^\circ$ specimens, which have unit orthotropic ratio, the normalized shear strain distributions are more uniform in the gage section. But in the calculation of shear modulus, a correction factor is still needed, which is about the average of the correction factors of the 0° and 90° specimens. The application of correction factor to

account for nonuniform shear stress distribution is not desired because numerical analysis is needed beforehand. Sullivan [29] hence suggested that by taking average of the apparent shear moduli obtained from 0° and 90° specimens (G^*_{0} and G^*_{90}), the true shear modulus can be obtained. This approximation scheme will be evaluated in the following paragraph.

The true shear modulus of a material can be obtained by multiplying the apparent shear modulus (either G^*_{0} or G^*_{90}) by the corresponding correction factor (CF_0 or CF_{90}). That is,

$$G = G^*_{0} \times CF_0 = G^*_{90} \times CF_{90} \quad (4.5)$$

or,

$$G = 0.5 (G^*_{0} \times CF_0 + G^*_{90} \times CF_{90}) \quad (4.6)$$

In general, if we define

$$G' = 0.5 (G^*_{0} + G^*_{90}) \quad (4.7)$$

then

$$e = \frac{G' - G}{G} \times 100 = \frac{(1 - CF_0) + (1 - CF_{90}) R}{CF_0 + CF_{90} \times R} \quad (4.8)$$

where $R = G^*_{90}/G^*_{0}$, and e is the induced percentage error in shear modulus estimate using the averaging technique. Using the correction factors obtained from Figure 4.12 and $R = 0.80, 0.92$ for graphite-epoxy and glass-epoxy respectively, the corresponding induced percentage error, e , in shear modulus would be 1.3% and 4.4%, respectively. Thus the accuracy of the approximation scheme depends on the material orthotropic ratio.

4.5 Simulated gage readings

Sullivan [15] stated that "In a properly loaded Iosipescu specimen, the two strains at ± 45 deg should be equal in magnitude and opposite in sign to a reasonable approximation."

Lee and Munro [16] showed recently that this condition cannot be achieved experimentally for 0° specimens. Lee and Munro tried to achieve Sullivan's condition by adding shims to the specimen and having the fixture contact surface carefully ground, but the effort proved to be of no effect. This phenomenon can be attributed to the presence of transverse normal strains in the specimen gage section and is an inherent property of the 0° specimen. The simulated individual gage readings for 0°, 90° and 0°/90° specimens are shown in Figures 4.14-4.16 for graphite-, Kevlar- and glass-epoxy, respectively. It is shown that for 90° and 0°/90° specimens, the +45° gage records compressive strain while the -45° gage records tensile strain and the magnitudes of the strains recorded by the two gages are more or less equal. But for the 0° specimens, the compressive strain recorded by +45° gage is larger in magnitude than that of the tensile strain recorded by the -45° gage. The magnitude of the ratio of the tensile strain to compressive strain, as recorded by the ±45° gages, is found to be 60% for graphite-epoxy and 80% for Kevlar and glass-epoxy specimens.

Though the two gages in the 0° specimen do not record equal and opposite strains, the shear strain calculation is still valid as long as the normal strains are uniformly distributed in the gage section. The two gages in the ±45° directions only give the normal strains in the gage directions. The gage normal strains can be expressed in terms of strains in the specimen coordinate system,

$$SG1 = 0.5 (\gamma_{xy}^{45} + \epsilon_x^{45} + \epsilon_y^{45}) \quad (4.9)$$

$$SG2 = 0.5 (-\gamma_{xy}^{45} + \epsilon_x^{45} + \epsilon_y^{45}) \quad (4.10)$$

$$\gamma_{12} = SG1 - SG2 = 0.5 (\gamma_{xy}^{45} + \gamma_{xy}^{45} + \epsilon_x^{45} - \epsilon_x^{45} + \epsilon_y^{45} - \epsilon_y^{45}) \quad (4.11)$$

where SG's represent strain gage readings, as shown in Figure 1.2b, and γ_{xy} , ϵ_x and ϵ_y represent shear strain, longitudinal and transverse normal strains averaged over the gage length with superscripts +/-45 indicating the gage directions. If stacked rosette is used, the strain components in equation (4.11) represent strains at the same gage section and equation (4.11) will reduce to

$$\gamma_{12} = SG1 - SG2 = 0.5 (\gamma_{xy}^{45} + \gamma_{xy}^{45}) \quad (4.12)$$

If an unstacked rosette is used and the specimen test section is under pure shear, the normal strains are zero and the shear strain can be obtained by equation (4.12). If the specimen is not under pure shear, equation will reduce to equation (4.12) only when the strain fields are uniform. For 90° and $0^\circ/90^\circ$ specimens, the normal strains detected by the strain gage along its length are negligible and equation (4.11) would reduce to equation (4.12). For 0° specimens, the longitudinal normal strain, ϵ_x , is negligible but the transverse normal strain, ϵ_y , is significant, about 9.5% and 24.4 % of γ_{avg} for Kevlar-epoxy and graphite-epoxy respectively; therefore SG1 and SG2 would not record equal and opposite strains. But, the transverse normal strain distribution is found uniform in the region where the strain gages are located, the influence of the transverse normal strain field on the two gages are the same and the calculation of the shear strain also reduces to equation (4.12). Lee and Munro's suggestion [16] that the 0° specimen should not be used for measurement of the in-plane shear properties does not appear to be correct, if it is based solely on the inequality of the $\pm 45^\circ$ strain gage readings.

4.6 Load-point effect

The W2 fixture distinguishes itself from the antisymmetric four-point-bend method by the application of uniform displacement over a large section of the specimen edge and thus avoids the problem of local crushing resulting from concentrated loads. One consequence of this is that the load points are not well defined. The 0° specimen could suffer from the load-point effect due to material nonuniformity or local hardness, which varies from specimen to specimen. The five force boundary models as shown in Figure 4.17 is used to investigate the load-point effect on the shear modulus measurement of 0° and 90° graphite-epoxy specimens. The normalized shear strain distributions are shown in Figures 4.18-4.19. Though these five load cases may be extreme or even unrealistic, it is found that location of the load points has profound effect upon the shear strain distribution along the notch axis for 0° specimen. But for 90° specimen, the load-point effect is negligible. Hence it is possible that the shear modulus obtained experimentally from 0° specimen will have large variations from specimen to specimen.

The W2 fixture has load points which are farther away from the notch axis as compared with those of the W1 fixture, and the induced transverse normal strains in the gage section for the 0° specimen are smaller. Hence it might be suggested that if the fixture were redesigned such that the load points were even farther away from the notch axis, a

closer approximate to pure shear and uniform shear might be obtained along the notch axis for the 0° specimen. However, if the load points are too far away, the concentrated forces would become so large that local crushing of the specimen may occur before shear failure occurs in the test section. It was shown earlier that the transverse normal strain in the test section for the 0° specimen would not affect the calculation of shear modulus. Though a redesigned W2 fixture could not provide pure shear in the test section for 0° specimen, it is not necessary to move the loading points farther away from notch axis.

4.7 Summary

Linear finite element analyses of Iosipescu specimen tested in Wyoming fixtures using different models have been performed and evaluated. The finite element models used by most researchers are considered not representative of the testing mechanism. It is suggested that contact length between the specimen and fixture, constraint type and compatibility should be considered in the finite element modeling. The boundary conditions are not affected by the material systems (graphite-, Kevlar- and glass-epoxy), but are influenced by the elastic stiffnesses due to different fiber orientations (0° , 90° and $0^\circ/90^\circ$) producing different deformation of the specimens in the fixture. Correct models corresponding to the 0° , 90° and $0^\circ/90^\circ$ specimens have been proposed and the results have been analyzed in terms of normalized strain distributions along notch-root axis, strain contours, simulated gage readings and the load-point effect. For the 0° specimen, it is shown that the pure shear state in the test section cannot be achieved. However, the shear strain calculation is not affected due to the uniformity of strain fields. It is shown that correction factors are needed for the calculation of shear modulus and that the correction factor for the 0° specimen is strongly dependent on the finite element model used, but not for 90° specimen. It is also proposed that the variation in measured shear modulus for 0° specimen may be caused by uncertainty of load points in the specimen/fixture contact regions.

CHAPTER 5. MECHANICS OF THE IOSIPESCU SPECIMEN

5.1 Introduction

Though the Iosipescu shear test method has been the topic of much investigation [5,9-20,25-27], little discussion of the mechanics of the shear test method has been presented. In this chapter, the cause and effect of the three observations associated with the Iosipescu shear test will be investigated from the mechanics point of view. The problems associated with the Iosipescu shear test as stated in section 1.1 are: (1) pure shear state in the test section cannot be obtained for 0° specimen, (2) apparent shear moduli for 0° , 90° and $0^\circ/90^\circ$ specimens are different and (3) large variations in the shear stress-strain response for both 0° specimen and 90° specimen. These problems will be reviewed from the experimental observations as well as the numerical results.

5.2 One dimensional mechanics

The original idea as proposed by Iosipescu [6] is that if two pairs of antisymmetric loadings are applied to a beam, the shear force between the two inner load points will be constant and there will be no bending moment along the vertical beam axis, Figure 5.1. Because the moment is zero at its center, the normal stress acting along the vertical beam axis is also zero. Hence, along the vertical center line of the beam, a pure shear condition can be obtained. This occurs regardless of the presence of the notches. The shear stress distribution along the vertical beam axis is not uniform but is of approximately parabolic shape. Iosipescu found that by cutting two notches at the opposite ends of the vertical beam axis, an approximately uniform shear stress distribution along the notch axis can be obtained. Though this simplified one dimensional simulation of the loading mechanics is not representative of the Iosipescu specimen tested in the modified Wyoming fixture, it does provide the fundamental rationale for this shear test

5.3 Two dimensional mechanics

When the Iosipescu specimen is inserted into the modified Wyoming fixture, the specimen is in contact with the fixture in areas rather than the idealized points. One

dimensional beam analysis is, hence, not appropriate. Two dimensional finite element analyses on the Iosipescu specimen have been performed by many researchers [5,10,11,17-20]. However, the finite element models used by most researchers are not representative of the real testing mechanism, as pointed out in Section 4.1. Most of the analyses were focused on the evaluation of the shear stress/strain field in the test section [5,10,11,17-20,25-27], and the calculation of the shear modulus correction factors [17,19,26]. In Chapter 4, the correct models for 0° , 90° and $0^\circ/90^\circ$ specimens are determined and the individual gage behaviors and the load-point effect are investigated. The discussion in Chapter 4 provided most of the answers to the causes and effects of the three categorized observations cited in Section 5.1. These will be reviewed in the following sections.

5.3.1 Asymmetric gage readings for 0° specimen

It was found experimentally in Section 2.3.1 that the two gage readings in the $\pm 45^\circ$ directions are not equal in magnitude and opposite in sign for 0° specimen. The moire fringe pattern for the 0° specimen, Figure 3.2, demonstrated that there is the presence of ϵ_y in the test section, which caused the unequal magnitudes of the two $\pm 45^\circ$ gage readings in the 0° specimen. The finite element analysis in Chapter 4 indicated that the nonsymmetrical strain gage behavior is an inherent property of the 0° specimen but the effect of the presence of ϵ_y on the shear modulus measurement was negligible if the strain fields are uniform. It was found from the finite element analysis that the strain fields are uniform in the gage section; therefore, equation (2.1) still can be used to calculate the shear strain. The 0° specimen still can be used for shear modulus measurement.

5.3.2 Apparent shear moduli for 0° and 90° specimens are different

Typical shear stress-strain behavior for 0° , 90° and $0^\circ/90^\circ$ specimens plotted as average shear stress against measured shear strain are shown in Figure 2.3. It is shown that at the same applied force the 0° specimen will have smaller shear strains while the 90° specimen will have larger shear strains. The shear strains for the cross-ply specimen are essentially between those of the 0° and 90° specimens. Thus the shear moduli calculated from these three stress-strain curves would be different. But, from complementary shear, Figure 5.3, the shear moduli obtained from these three fiber configurations should be the same if the

applied shear stresses are the same. It was, hence, suspected that the shear stress distributions in the test sections of the three fiber orientations are different. This phenomenon has been investigated by several researchers in the W1 and W2 fixtures using different boundary models [5,10,11,17-20,25-27]. In Section 4.3.2, it was shown that the shear strain distributions along the notch line for 0° , 90° and $0^\circ/90^\circ$ specimens are of different shape. The distribution for 90° specimen is of parabolic shape with a peak at the center of the specimen, Figure 4.7, while the distribution for 0° specimen has two peaks close to the notches and at the center the shear stress is a minimum, Figure 4.6. Shear strain distribution of $0^\circ/90^\circ$ specimen is more uniform, Figure 4.8, but, at the center, the shear strain is greater than γ_{avg} . This explains the difference in the measured shear moduli for 0° , 90° and $0^\circ/90^\circ$ specimens. For materials with different orthotropic ratios, the shear strain distribution shapes along the notch line are also different. For those with higher orthotropic ratio, such as graphite epoxy, the shear strain at the center of the specimen is farther away from the averaged shear strain for either 0° or 90° specimens. The nonuniformity of the shear strain distributions is shown experimentally in Section 3.4, Figure 3.5. To account for the nonuniformities of the shear strain distributions in calculating shear modulus, correction factors are needed. The correction factor is defined as the actual shear stress/strain at the gage section divided by the average shear stress/strain across the test section. By applying correction factors, the measured shear moduli are corrected, and, ideally, the shear moduli obtained from the three fiber orientations will be the same.

5.3.3 Spread of measured shear moduli for 0° specimen

For AS4/3501-6 graphite-epoxy, the shear moduli for 0° specimens measured by several researchers spread widely, Figure 1.3. It was shown in Chapter 4 that this phenomenon is caused by the sensitivity to uncertainty of load points for 0° specimen. The Wyoming test fixture has gone through a number of modifications. An important modification has been to move the load points away from the test section and enlarge the specimen-to-fixture contact areas. Based on specimen-to-specimen variations, the positions of the resultant forces for different specimens of same fiber orientation will not necessarily occur at the same points. The 0° specimen could suffer from relatively large variations of the load points (defined by **a** and **b**, as shown in Figure 5.1) with load, and from specimen to specimen. The 0° specimen is sensitive to the particular values of **a** and **b**, in as much as the shear stress distributions, and, therefore, the correction factors will

vary with **a** and **b**. In cases when **a** and **b** vary with load this will give errors in the shear stress-strain data. Such errors cannot be easily compensated.

One consequence of the sensitivity of the 0° specimen to the load points is that the shear moduli of the 0° specimens may vary from specimen to specimen. In the numerical analysis it was demonstrated that different specimen/fixture contact models produced different shear stress distributions in the specimen test section of the 0° specimen (Figure 4.18), but the shear stress distributions for the 90° specimen were independent of the contact models (Figure 4.19). Thus, there will be a specimen to specimen variation in the shear stress-strain behavior recorded for specimens with the 0° fiber orientation. Experimental evidence for the effect of the uncertainty of the load points is readily available. Sullivan [27] reported that, for an isotropic material tested in antisymmetric four point bending, the shear strain distribution became more uniform as the load points were moved away from the notches, and that the shear moduli changed accordingly. Adams and Walrath [10] observed similar effects for 0° specimens in their refinement of the Wyoming test fixture.

It is suggested that the 0° specimen is much more sensitive than the 90° specimen to local nonuniformity in the material (fiber straightness, for example), and to the detailed specimen preparation (grinding of the edges, for example). Thus there can be an intrinsic scatter in the experimental data in the 0° specimen which is not present in the 90° specimen even though it may be cut from the same panel with the specimens prepared, instrumented and tested in the same way. Experimentally there may be large scatter in the shear moduli determined for a 90° specimen. It will be shown later that this is due to specimen twisting. It is important to note that the correction factors are specific to the material orthotropy data used in the analysis and that the correction factor range for the 0° specimen is only approximate, since it depends strongly on how load introduction is modeled in the finite element analysis.

5.4 Three dimensional mechanics

5.4.1 Inconsistent modulus in a 90° specimen

The moire experiments provide strain data equivalent to that of the strain gage rosettes, but over the entire test section. It is of interest to compare the stress-strain data

obtained with a specimen instrumented with a strain gage rosette on one side and a moire grating on the other. This comparison is made in Figure 3.6. It should be noted that the shear strains obtained from the moire fringe patterns were determined by averaging the strains over an area equivalent to that of the strain gage rosette. Therefore, the comparison of the strain gage and moire data is direct. The stress-strain curves, shown in Figure 3.6a, for the 0° graphite-epoxy specimen are almost coincident. A second specimen gave a similar degree of agreement between the strain gage and moire data. The agreement for the 90° specimens was far from perfect, as shown in Figure 3.6b. The data for a 0°/90° specimen, shown in Figure 3.6c, also indicate a strong disagreement between the moire and gage strains on opposite surfaces of the specimen. Rather than regard one measurement as correct, it is suggested that both methods are recording the correct strains, but that there are different strain states on the front and back faces of the specimens.

5.4.2 Twisting model

Twisting can provide an explanation of the differences between the shear-stress strain curves obtained using the strain gage rosette and moire interferometry on opposite faces of the specimens. If twisting were indeed responsible, then the 0° specimen did not twist, but the 90° specimen twisted a great deal. The pure shear condition of equal in magnitude and opposite in sign in the strains in the $\pm 45^\circ$ gages [15] was satisfied by the 90° specimen, but not the 0° specimen. The results of the current experimental investigation suggest that the lack of pure shear will not necessarily imply twisting of the composite Iosipescu specimen, and even when the strain gages indicate pure shear, as in the 90° specimen, twisting may occur.

Consider the causes and effects of twisting of the Iosipescu specimen. Suppose that the cross-section of the specimen between the notch roots is subjected to St. Venant torsion [30], so that the displacement components can be written as

$$u = \theta \psi(y, z) ; \quad v = -\theta xz ; \quad w = \theta xy \quad (5.1)$$

and the in-plane shear strain

$$\gamma_{xy} = \theta \left(\frac{\partial \psi}{\partial y} - z \right) \quad (5.2)$$

where w is the out-of-plane displacement, θ is the angle of twist and $\psi(y,z)$ is the cross-section warping function. Thus equal and opposite shear strains due to twisting will be induced on the faces ($z=\pm t/2$) of the specimen. Midplane shear strains are obtained by averaging the shear strains measured on the front and back faces of the specimen. The shear modulus is calculated using Equation (2.2).

Now consider the relative magnitude of the twisting shear to that due to the applied shear force. A three dimensional representation of the Iosipescu specimen with in- and out-of-plane moments M_z and M_y , and torsional moment M_x is shown in Figure 5.4. Suppose that the loads are eccentric to the midplane by an amount αt ($0 < \alpha < 0.5$). Then the torsional moment M_x is

$$M_x = (F + Q) \alpha t \quad (5.3)$$

Using expressions for F and Q in Figure 5.1, the shear stresses on the face of the specimen can be written as

$$\frac{\tau}{\tau_{ave}} = 1 \pm \frac{\alpha}{e} \frac{a + b}{a - b} \quad (5.4)$$

where e is a geometrical factor. For the specimen used here, $e = 0.2865$ [30]. Thus the relative importance of the twisting effects depends upon the eccentricity α and the locations of the loads a and b . It has been previously observed that the modified Wyoming fixture does not define these load locations precisely. The relative magnitude of the twisting effect is shown in Figure 5.5 for several combinations of a and b . It is apparent that even very small amounts of relative eccentricity α will cause significant shear due to twisting. If such effects occur in an Iosipescu specimen with a rosette on one face only, then an erroneous elastic shear modulus and stress-strain response will be obtained. The problem of twisting is further complicated in the modified Wyoming fixture since a and b may be functions of the applied load, as indeed might be α .

5.4.3 Supplementary experiments

The experiments on specimens instrumented with strain gage rosettes and moiré gratings suggested that the 90° specimen was susceptible to twisting, but the 0° specimen

was not. To investigate this further a series of experiments were performed on specimens which were instrumented with two rosettes, and repeatedly loaded in different positions in the fixture. That is, the specimen was loaded with one rosette facing the front of the fixture and the other facing the back of the fixture. The specimen was then unloaded and rotated 180° about a horizontal or vertical axis, and loaded again. This procedure results in the series of shear stress-strain curves shown in Figure 5.6a in which the average shear stress is plotted against the shear strain from one of the rosettes. All of these data represent apparently valid tests. Clearly very different shear property data could be obtained from this single specimen. If twisting were responsible for this variability, then taking the average of pairs of shear strains recorded from rosettes on the front and back faces would provide data for the shear strain due to the applied shear force. The shear stress-strain data resulting from averaging the shear strains on front and back are shown in Figure 5.6b. The curves in Figure 5.6b are coincident for the different tests. These results are representative of twisting occurring in the specimen. A similar series of experiments performed on a 0° specimen produced the shear stress-strain curves in Figure 5.7a. There is little variation in the stress-strain response between tests. Taking the average of pairs of shear strains from the rosettes on the front and back of the specimen reduced the variability, as shown in Figure 5.7b. A further series of tests on a $0^\circ/90^\circ$ graphite-epoxy specimen showed that this specimen was also prone to twist, though not to the extent of the 90° specimen, see Figure 5.8a. Again averaging front and back gage readings produces consistent shear stress-strain data, as shown in Figure 5.8b.

The previously described test results demonstrate that twisting can cause significant errors in specimens instrumented with a single rosette. However, the test data do not indicate why twisting is more prevalent in the 90° and $0^\circ/90^\circ$ specimens than in the 0° specimen. It has already been remarked that the high value of transverse stiffness E_y in the 90° specimen was responsible for the attenuation of the load proximity effects so that the $\pm 45^\circ$ gages recorded equal and opposite strains. However, it is suspected that a local hardness effect is responsible for the twisting action. Initially contact between the specimen and fixture will occur at highly localized zones (asperities or high spots) and local eccentricity of loading will result. As the load on the specimen is increased these high spots will deform and the load may be distributed more uniformly across the thickness. The 0° specimen may be less prone to twist because of its relatively low hardness. In this case any local high spot along the specimen-fixture load introduction interface would deform readily and the load spread more uniformly to minimize the eccentricity. If the twisting of 90° and $0^\circ/90^\circ$ specimens is due to local conditions between the specimen and the fixture, then

performing the tests with some shim material between the specimen and fixture could result in a different stress-strain response. Masking tape was applied to the edge surfaces of the specimen interfacing with the fixture. The $0^\circ/90^\circ$ specimen which produced the shear stress-strain data in Figure 5.8a was retested with the masking tape on the edge surfaces. When the tests with the specimen in various orientations relative to the fixture were performed, the data shown in Figure 5.8c were obtained. Comparing the results in this Figure 5.8c with those in Figure 5.8a, it is apparent that the soft shim material (masking tape) has reduced the variability between tests and front and back gages, hence twisting. The observations related to twisting were not confined to composite materials. A 7075-T6 aluminum specimen with a thickness of 3.2mm was instrumented with strain gage rosettes on opposite faces and tested in the fixture in the manner described above, but without the soft shims. The shear stress-strain data shown in Figure 5.9a were obtained. Thus even an isotropic material can produce a wide variation in stress-strain response. If the average of shear strains is taken from the rosettes on the front and back faces, then a single, linear shear stress-strain plot is obtained, as shown in Figure 5.9b.

5.4.4 Effect of twisting

It is apparent that the front and back face responses are the same for the 0° specimen but are quite different for the 90° specimen due to the twisting effect. For 90° specimen, the shear strain on each face was a combination of the shear strains due to the applied shear force and torque on the specimen resulting from the fixture irregularity or local hardness of the specimen. On one face the effects add together, on the other they subtract, so that the average of the front and back face responses would eliminate the twisting effect on calculating shear modulus. It should be noted that the difference between the front and back face response is systematic; the shear strains determined on the face farthest away from the fixture linear bearing, the front face, are always higher than those on the back face for the same applied load. This observation has important implications for the values of the shear moduli determined with specimens tested in the 90° configuration since it is common practice to use only one strain gage rosette, and it is probable that the strain gage rosette would be located on the front face of the specimen.

As shown in Figures 5.6-5.9, there are four possible positions a specimen can be installed into the fixture. If we attach a strain gage rosette on front and back faces of a specimen, we will obtain eight possible stress-strain curves for one single specimen. If only one rosette on one face is recorded, there will be eight possible values of measured

shear modulus in one specimen. This may account for the wide variations in the measured shear modulus for 90° specimens. But if we take average of front and back shear strains obtained from the strain gage data, the measured shear moduli corresponding to the four possible positions are essentially the same.

5.5 Shear modulus measurement

The finite element studies have shown that the shear stress distributions are not uniform across the specimen test area, even for isotropic materials. It has also been shown that strain distributions in the test section depend upon the orthotropy ratio for orthotropic materials and upon how the load introduction into the specimen is modelled when the high stiffness direction is parallel to the specimen longitudinal axis. The use of correction factors for the strain-gaged specimens is outlined in Chapter 4. The finite element models suggest that there may be an uncertainty of about $\pm 5\%$ in the correction factor (Figure 4.18) for the 0° graphite-epoxy specimen which could manifest itself as an intrinsic scatter from specimen to specimen in a real experiment. If correction factors, obtained from the data in Figure 4.12, were not applied to the experimental data from the strain-gaged graphite-epoxy specimens then the calculated shear moduli for the 0° specimen will be 10% higher than the true value. When the range of correction factors, obtained from Figure 4.18, are applied the (0.5% secant) shear moduli shown in Figure 5.10 are obtained for the 0° AS4/3501-6 specimens. The shaded areas in Figure 5.10 represent the possible ranges of shear modulus associated with the uncertainty in the correction factors. Adams and Walrath [11] quote a shear modulus of 5.9 GPa (with a standard deviation of 0.5 GPa) for the same specimen geometry, but with a two element unstacked rosette. It appears that no correction factor was applied. Abdallah and Gasgoine [12] have determined a shear modulus of 4.5 GPa with a standard deviation of 0.73 GPa. Swanson *et al.* [31] quote an initial shear modulus of 6.58 GPa for the 0° AS4/3501-6 specimen. While it is possible that the data for AS4/3501-6 may have been obtained from panels with different volume fractions, it is clear that the 0° specimen does produce a very wide scatter in the shear moduli. This is consistent with the observation that a specimen with this fiber orientation is sensitive to the specimen/fixture contact interface which may vary from specimen to specimen.

The experiments reported above showed that specimen twisting could become a severe problem, particularly for the 90° graphite-epoxy specimens. If shear strain data

were taken from one side of the specimen only, then erroneous results can be obtained. Abdallah and Gascoigne [12] recorded a shear modulus of 4.82 GPa with a standard deviation of 0.78 GPa for AS4/3501-6, without the application of correction factors. For the same material system, Wilson [13] reports a value of 5.24 GPa with a repeatability modulus of 0.97 GPa and a reproducibility modulus of 0.98 GPa. The similarity in the repeatability and reproducibility moduli suggest that the large scatter is a characteristic of the specimen, fixture and instrumentation, rather than the laboratory or technician performing the measurement. In the present work shear moduli, for the 90° specimen, between 3.0 GPa and 5.5 GPa could have been reported, if data from only one rosette were used. When the average of front and back readings was taken, and the correction factor applied, the results shown in Figure 5.10 are obtained. A remarkable consistency is obtained. This confirms the predicted insensitivity of this specimen to the position of the applied load. All of the values from the experiments on the 90° specimen are very close to those from $\pm 45^\circ$ tension and 10° off-axis tests performed on the same material [14]. It would seem that the scatter recorded by other workers who tested 90° specimens was indeed due to twisting effects, and the effect of these upon the shear modulus can be minimized by using back-to-back gages and averaging the shear strains.

5.6 Shear strength measurement

Much of the controversy over the Iosipescu specimen lies not only in the measurement of shear modulus but also the measurement of shear strength of composite materials [11]. While the main objective of the current study was to evaluate the test method for shear modulus determination, some observations can be made on strength measurement. The shear stress-strain data presented here also contain the shear strength values. The values given correspond to the first load drop. This was simultaneous with a catastrophic failure in the 90° specimens. However, the 0° and 0°/90° specimens could have sustained further loading and, perhaps, yielded higher strengths. The point to be made here is that the 90° strengths are much lower than those of the 0° and 0°/90° specimens. It seems, from the discussion above that twisting in the 90° specimen may be responsible for the apparently low values of shear strength. It should also be noted that this fiber orientation leaves the specimen susceptible to both in- and out-of-plane moments so that failure will be due to a complex system of stresses and a mixed mode fracture will occur. It would be wrong to describe the average shear stress at which failure occurred as the shear strength of the material, and it would not, of course, correspond to that found in the 0° or

0°/90° specimens. It has been shown that the application of shim material does reduce the twisting. It is probable that, as the twisting is reduced or even eliminated, the *apparent* shear strength will increase. The relative twisting can be estimated by dividing the difference between the front, or back, shear strain and the average shear strain by the average shear strain. The apparent shear strength can then be corrected to account for the twisting. For example, the relative twisting of the specimen in Figure 3.6b is about 33%. Correcting the reported *apparent* shear strength of 37 MPa for twisting yields a value of 56 MPa, much closer to the value of 68 MPa reported for the 0° specimen in Figure 3.6a. Even after the application of the correction for twisting the apparent strength of the 90° specimen is still less than the 0° specimen. The difference is thought to be due in part to the mixed mode fracture which occurs in the 90° specimen. Also, 0° specimens tend to distort at higher loads and the distorted fibers can carry part of the compressive loads and withstand a higher failure load. The 90° has some advantages over the 0° specimen but the low failure strains do not allow an extensive determination of the shear stress-strain behavior in the nonlinear region. It may be speculated, however, that reducing the twisting could make this a preferred configuration.

The 0° specimen had the largest shear stress concentrations near the notch tips. Presumably first failure would occur in that region. The effect of the development of cracks in this region would be to produce a more uniform stress field across the specimen in the test region, and eventually a network of cracks parallel to the fiber direction would be observed across the entire test section. This fiber orientation does suffer from the proximity of the loading to the test section, but this too might be reduced after local damage development. It is debatable as to which load value should be used in defining strength, the load to produce first cracking, with a suitable correction factor to account for the stress concentration near the notches, or the maximum load, without a correction factor [11]. Because the crack initiation is not at the minimum cross section, it is suspected that the 0° specimen is also failed in a combined mode. The failure strength obtained from 0° specimen may also be overestimated due to possible fiber distortion before failure. Nonetheless, the resistance of this fiber configuration to bending and twisting, together with the uniformity of the shear stress field after initial cracking, suggest that meaningful shear strengths may be obtained.

5.7 Summary

Three main observations associated with the Iosipescu shear test method were categorized in Section 1.1. Observation (1): pure shear is not obtainable in the gage section for 0° specimen. It was shown numerically and experimentally that it is caused by presence of ϵ_y in the gage section. The normal strains in the $\pm 45^\circ$ gages are not equal in magnitude and opposite in sign but shear strain calculation is not affected due to the uniformity of strain fields. The 0° specimen still can be used to measure shear modulus. Observation (2): shear moduli obtained from 0° , 90° and $0^\circ/90^\circ$ specimens are not consistent. The inconsistency in shear modulus measurement is caused by nonuniform shear field in the test section and the application of correction factors can bring the difference to a minimum. It was also shown in Chapter 4 that the correction factor depends on the finite element models used. To obtain accurate correction factors, optimal models taking into account of the contact length and constraint types should be used. The correction factors could be a range of values based on specimen-to-specimen variation for 0° specimen. Observation (3): there are wide variations in measured modulus for 0° and 90° specimens. Though this phenomenon is commonly observed, no explanation or solution has yet been provided. It was shown numerically in Chapter 4 that the variation of the measured shear modulus for 0° specimen is caused by the uncertainty of load points and it is an inherent property for this fiber orientation. It was shown experimentally the variation in measured shear modulus for 90° specimen is caused by twisting effect. The effect of twisting on shear modulus measurement can be eliminated by taking average of front and back shear strains.

It was suggested that after considering the relative twisting at failure, the failure strength of 90° specimen can be corrected and the difference of failure strengths obtained from 0° and 90° specimens will become smaller.

CHAPTER 6. APPLICATION OF IOSIPESCU SHEAR TEST IN PARAMETRIC STUDIES

6.1 Introduction

Characterization of in-plane shear properties is a prerequisite to the understanding of the mechanical behavior of a laminated composite structure. For the unidirectional materials, fiber properties dominate the mechanical behavior in the tensile or compressive mode, whereas shear behavior provides a discriminator of matrix and fiber/matrix interfacial properties. Thus shear modulus or strength is a very useful parameter for assessment of the effects of processing variables, such as fiber treatment and laminate consolidation pressure (or temperature), upon the performance of a composite system.

In this chapter, application of Iosipescu shear test in an interfacial study for material systems with and without fiber treatment will be presented. A cure cycle study evaluating the effect of consolidation pressure on shear properties of thermoplastic composites will also be presented.

6.2 Interface study

The fiber-matrix interface transfers the stress in a fiber reinforced composite from the weak and often low modulus matrix to the fiber. Thus, in addition to the material properties of the fiber and matrix, composite behavior is also governed by the chemical-physical interactions occurring at the fiber-matrix interface and encompassing interphase. In this section, the Iosipescu shear test is used to investigate fiber-matrix adhesion and its relation to composite properties.

6.2.1 Material and specimen details

AU4 fibers which are removed from the heat treatment ovens without any further processing, and AS4 fibers which are treated with an electrochemical oxidation step are used. These two set of fibers, AU4 and AS4, are combined with BMI/DIALLYL thermoset matrix with 15% (by weight) polysulfone thermoplastic toughener. The polysulfone thermoplastic is added to the bismaleimide (BMI) thermoset matrix to increase

thermal stability, edge delamination strength and compression after impact strength. The extensional properties are $E_{11}=131$ GPa, $E_{22}=8.65$ GPa for AU4/BMIPES and $E_{11}=140$ GPa, $E_{22}=8.15$ GPa for AS4/BMIPES, respectively. The unidirectional AU4 and AS4 composite panels have an in-plane dimension of 76mm by 127mm (3" x 5") and are 18-ply thick. Six 90° specimens are obtained from each panel and each specimen is numbered according to its panel position (Figure 6.1) for further reference. All specimens are instrumented with two-gage rosettes (Micro-measurements EA-13-062TV-350) at the center of the front and back surfaces of the specimen. Based on the observations in the previous chapters, masking tape is applied to the edges of the specimen to reduce the twisting effect. Stress-strain data for each specimen are then recorded.

6.2.2 Experimental results and discussion

The stress-strain data obtained from the front and back faces of the six AU4 specimens are shown in Figure 6.2. It is found that the front and back stress-strain responses are not consistent, indicating the presence of specimen twisting, even with the application of masking tape. After taking average of front and back shear strains, the stress-strain data for the six AU4 specimens are coincident, Figure 6.3. After the application of the shear modulus correction factor ($CF=1.19$, from Figure 4.13), the corresponding shear moduli and strengths are shown in Figure 6.4. For the AS4 panel, it is found that the panel thickness is not uniform, Figure 6.1, hence the fiber volume fractions of the six specimens are different. It would be expected that the shear stress-strain data will not be the same due to the inconsistent fiber volume fractions. The stress-strain data for each individual specimens on the front and back faces are shown in Figure 6.5. It is found that the degree of twisting for the AS4 specimens is smaller than that for the AU4 specimens. After taking average of front and back shear strains, the stress-strain data for the six AS4 specimens are not coincident, Figure 6.6. The shear stress-strain data for specimens 2, 3 and 4 are coincident and the shear stress-strain data for specimens 5 and 6 are of different trends. Because the thicknesses of specimens 5 and 6 are 7% less than those of specimens 2,3 and 4, the fiber volume fractions of specimens 5 and 6 would be conversely higher. This can explain the apparent stiffer shear responses of specimens 5 and 6. From this observation, a conclusion can be drawn that the non-homogeneity, such as specimen thickness or fiber volume fraction, of the specimens can cause variation in measured shear moduli. The shear modulus (after application of shear modulus correction factor) and strength for the AS4 specimens are shown in Figure 6.7.

From Figures 6.3 and 6.6, it is shown that the shear modulus and strength of the treated laminate are about 70% higher than those of the untreated laminate while the volume fraction of the treated laminate is only 40% higher than the untreated one. The fracture surface of the AU4 specimen has a broom-like appearance and the fibers are broken into several fragments. The fracture surface of the AS4 specimen shows a combination of splitting and pull-out. Thus, from the experimental observations, it is shown that surface treatment on the fiber improves the adhesion of the fiber to the matrix and provides better shear properties of the composites.

6.3 Cure cycle study

The curing process for fiber reinforced thermosetting resin matrix composite laminate is accomplished by exposing the material to elevated temperatures and pressures for predetermined length of time [32]. The elevated temperatures applied during the cure provide the heat required for initiating and maintaining the chemical reactions (cross-linking) in the resin which cause the desired changes in the molecular structure. The applied pressure provides the force needed to squeeze excess resin out of the material, to consolidate individual plies, and to compress vapor bubbles. Usually the curing process (denoted as the cure cycle) for thermoset composite materials contains multi-step processing, and different cure cycles affect the performance of the finished product significantly. Thermoplastic composites, on the other hand, require higher temperature and higher forming pressures than thermosetting composites with single-step processing. The effect of the cure cycle on the performance of the thermoplastic composites, however, is not well documented in the literature. In this section, Iosipescu shear test is used to evaluate the effect of the consolidation pressure on the shear properties of a thermoplastic composite system (AS4/PES).

6.3.1 Material and specimen details

The thermoplastic composite material was manufactured and supplied by ICI, which employs AS4 graphite fibers in a matrix of polyethersulfone (PES). Three 22-ply unidirectional panels were fabricated under different consolidation pressure. Panel 1, 2 and 3 were consolidated at 3.5, 2.1 and 1.0 MPa (500, 300 and 150 psi), respectively. The laminate was heated in a matched-metal mould under contact pressure to 302°C. Pressure was then applied for 30 minutes and then the laminate was cooled down under the same

pressure. The extensional properties for the AS4/PES were predetermined and were found to be: $E_{11}=41.37$ GPa, $E_{22}= 8.825$ GPa, $\nu_{12}=0.29$. Three 0° specimens from each panel were fabricated.

6.3.2 Experimental results

The normal strains recorded in the individual gages at $\pm 45^\circ$ directions are shown in Figure 6.8. The normal strains at the $\pm 45^\circ$ directions are not equal in magnitude and opposite in sign due to the presence of ϵ_y in the gage section as discussed in Chapters 2 to 5. The shear stress-strain data obtained from front and back faces of the 0° specimens for the three panels are shown in Figure 6.9. It is shown that there is very small deviation in the shear stress-strain curves of the front and back surfaces, which implies that little specimen twisting occurred. The shear moduli for the three laminates are shown in Figure 6.10. The variation of the measured shear moduli for specimens cutting from the same panel is about 8% (in panels 1 and 3), which is caused by the sensitivity of this fiber orientation to the load introduction points. These observations are consistent with the findings from the 0° graphite-epoxy composite specimens.

In Figures 6.10-6.11, it is found that the shear strength slightly decreases when the consolidation pressure increases but the measured shear moduli are essentially the same for the three laminates. From this study, it is shown that the shear properties of the AS4/PES thermoplastic laminate are not sensitive to the consolidation pressure in the cure cycle.

6.4 Summary

Iosipescu shear test was applied to evaluate certain parameters in the composite manufacturing process. It was shown that Iosipescu shear test does differentiate between surface treatments of the fibers. It was shown that a relatively small quantity of the new material is required if the Iosipescu shear test is used. For various material system, such as graphite fibers in thermoset matrix with the thermoplastic additives, and graphite fibers in thermoplastic matrix, consistent shear modulus can be obtained. The Iosipescu shear test has proved to be an accurate and economic tool for parametric studies in the fabrication of composite materials.

The specimen responses, such as twisting in the 90° fiber treated/untreated specimens and variation of measured shear modulus in 0° thermoplastic specimen, are consistent with the previous observations associated with the Iosipescu shear test.

CHAPTER 7. APPLICATION OF IOSIPESCU SHEAR TEST TO WOVEN FABRIC, PARTICULATE COMPOSITES

7.1 Introduction

Woven fabric composites have received increased attention in the recent years due to several advantages over unidirectional composites. For example, in making complicated or curved parts or in process requiring careful positioning of the reinforcement, the more easily handled woven preform is preferred than the unidirectional prepreg. Also, the woven fabric composites provide improved energy absorption characteristics and hence have better impact resistance. Though several analytical models on the elastic behavior of woven fabric composites have been presented [33,34], the experimental data available are relatively sparse. The purpose of this chapter is to investigate experimentally the shear behavior of the uniweave, plain weave and satin weave composites. The whole field moire interferometric and conventional strain gage techniques are applied. From the experimental results, the uniformity and purity of the shear fields for different woven fabric architectures are discussed. The effectiveness of the shear modulus measurement using traditional strain gage technique is also addressed.

Metal particulate reinforced plastics are mechanically strong and tough. The incorporation of short, random metal particles in epoxy resins has led to systems with higher impact strengths, stiffness, fracture toughness and creep performance. In addition to their desirable mechanical properties, the metal particulate composites can be easily machined in less time and at lower cost than metal molds. Due to their special properties, metal particulate composites have gained certain attention in the composite society. But little experimental data are available. In this chapter, the shear behavior of the epoxy based aluminum particulate composites will be investigated using whole field moire interferometric method and strain gage technique. From moire fringe patterns, the uniformity of the shear field is assessed and the validity of the Iosipescu shear test on particulate composites is then evaluated.

7.2 Woven fabric composites

7.2.1 Materials and specimen details

Five graphite-epoxy woven fabric panels were manufactured and supplied by NASA LaRC. The in-plane dimension of the panels is 120mm x 150mm (about 5" x 6"). Weave geometries tested included one uniweave (panel 1), two plain weaves (panels 2 and 3), one 5-harness (panel 4) and one 8-harness satin weaves (panel 5). The fibers in the satin weaves are Celion fibers. One AS4 (panel 2) and one Celion fiber with large tow size (panel 3) are used in plain weaves. For the uniweave material, the AS4 fiber is used. All fabric composites tested were symmetric cross-ply laminates; that is, the warp direction of every ply is oriented in the 0° (1-axis) and 90° (2-axis) directions alternatively. These panels were about 3.8mm thick (0.15"), and subjected to in-plane shear loadings only. A description of these five panels is given in Table 7.1.

Eight specimens were machined from each panel. All specimens are 76mm (3") long and 19mm (0.75") tall with two V-notches on opposite ends of the vertical center line. The dimensions are the same as those described in Figure 1.2b. Two specimens from each panel were instrumented with three-gage stacked rosette (Micro-measurements WA-13-060WR-120) on one face and moire grating on the opposite face and the other six specimens of each panel were instrumented with back-to-back two-gage rosettes (Micro-measurements EA-13-062TV-350). The procedure for moire experiments is the same as that discussed in Section 3.2.

7.2.2 Experimental results

The shear stress-strain data obtained from the strain gaged specimens for the five panels are shown in Figures 7.1-7.5. Shear strains are continuously recorded until saturation in the data acquisition system occurred. Figures 7.1a-7.5a represent the shear stress-strain curves obtained from the front and back surfaces of all six strain gaged specimens. Figures 7.1b-7.5b represent the average shear stress-strain data (taking average of front and back shear strains) of the six strain-gaged specimens. It is found that the averaged shear stress-strain curves from six strain-gaged specimens are mostly coincident for all panels except for panel 3. The averaged in-plane shear moduli and shear strengths are listed in Table 7.2. Typical moire fringe patterns for these five panels are shown in Figures 7.6-7.10. A carrier of rotation was applied to obtain two sets of fringes to render easy data reduction and evaluation of uniformity of strain field in the test section.

Typical shear strain distributions along the notch-root axis for these five panels are shown in Figures 7.12-7.16.

7.2.3 Discussion

Shear stress-strain data

The shear stress-strain data in Figures 7.1-7.5 are nonlinear throughout most the curves. Linear behavior can only be observed for a shear strain less than 0.5%. Thus the shear modulus must be defined very careful. In this chapter, 0.2% tangential shear modulus is used. All fabrics show certain degrees of specimen twisting. After taking average of front and back shear strains, the shear stress-strain curves of six strain-gaged specimens for panels 1, 4 and 5 are very consistent. In panel 2, only one deviation from the general trend of shear stress-strain curves is observed. The derivation was found to be caused by nonuniform specimen thickness. In panel 3 the shear stress-strain data for the six strain-gaged specimens are not consistent before or after taking average of front and back shear strains. The abnormal behavior is attributed to the 12k large sized warp and fill yarns of the fabric. This will be discussed further below.

Moire fringe patterns

In Figures 7.6-7.10, two sets of moire fringe patterns are shown for each specimen. For the first set of the moire fringes, Figures 7.6a&b-7.10a&b, the u-field is adjusted to have minimum fringes such that most of the information is contained in the v-field. For the second set, Figures 7.6c&d-7.10c&d, the u- and v-fields are adjusted to have almost equal amount of fringes. The first set of fringe patterns provides easy data reduction while the second set provides better evaluation of the uniformity of the strain fields. From Figures 7.6b-7.10b, it is noted that the v-field fringe patterns for all panels are not antisymmetrically distributed. This phenomenon is caused by the non-antisymmetric loads resulting from material imperfection or local hardness in the specimen/fixture contact regions. This phenomenon is very commonly observed for all Iosipescu specimens because the fixture only imposes uniform displacement constraints to the specimen and the load points are not defined.

In the u-field, the normal strain ϵ_x is negligible in the test section except at the notch roots for all five fabrics, Figures 7.6a-7.10a. Small ϵ_x are found at the right sides of the top and bottom notch flanks. On the top, ϵ_x is negative and on the bottom ϵ_x is positive. This phenomenon is caused by a combination of very small degree of in-plane and out-of-

plane bending. For all five fabrics, the u -fields are not uniform but contain a zig-zag pattern, especially for panel 5 ($[0/90]_{3s}$, 8HS), Figure 7.10a. The highly irregular zig-zag pattern in the u -field of panel 5 specimen can be attributed to its high yarn density (24 yarns/in). The volume fractions of the fiber bundle and the surrounding resin rich areas are not the same, therefore, high yarn density implies more variations in local volume fraction and stiffness.

The v -displacement fields in Figures 7.6b-7.10b consist of dense, almost vertical fringes in the test section for all panels except for panel 5. The vertical gradient of the fringe contours in this v -displacement field is small for panels 1 to 4. Note that near the notches the terms $\partial u/\partial y$ and $\partial v/\partial x$ do not cancel due to the three-dimensional twisting effect. For panel 5 specimen, the compressive load from the upper inner load points decays into the upper half of the test section and causes a S-shaped v -field fringe pattern in the upper part of the test section. The decay of the compressive loads from the upper inner load points can be seen more clearly in Figure 7.10d.

In Figures 7.6c-7.10c and 7.6d-7.10d, where the u - and v -fields are adjusted to have almost the same amount of fringes, the nonuniformity is observed very clearly. Some high-density fringe bands are noted in the v - and u -fields. This phenomenon is suspected to be caused by nonuniform volume fractions in the fabric. Because the volume fraction of the warp and fill ends is much higher than the volume fraction of the fabric, there will be resin rich regions between the bundles and these resin rich regions will be subjected to large shear strains. If the resin rich regions between the bundles are responsible for the dense fringe bands, it should be possible to predict the amount of the dense fringe bands in the test section from the weave architecture of the fabrics. The fiber bundle densities for panels 1 through 5 are 18, 12.5, 7.5, 18 and 24 yarns/in respectively. Accordingly, across the test section (0.45" in width) there should be about 8, 5, 3, 8 and 10 dense fringe bands for panels 1 to 5. By checking the u -fields of Figures 7.6d-7.10d, it is found that the number of dense fringe bands are as predicted. Therefore, it is concluded that the dense fringe bands are caused by the low shear resistance of the resin rich regions between the fiber bundles.

One consequence of the nonuniform shear field and dense fringe bands is that the measurement of shear strain using strain gage rosette may not be accurate. If the strain gage rosette happens to cover a region composed of one bundle and one resin rich zone such that the volume fraction of the gage section is the same as the volume fraction of the

fabric, then the shear strain measurement can be considered to be approximately accurate. When the gage section cover more than one bundle and one resin rich resin, the measured shear modulus may not be consistent due to the specimen-to-specimen variations in the ratio of number of bundle to number of resin rich zone. If the size of the gage section is smaller than the width of the bundle, large variation in the measured shear modulus will occur. It is shown in Figures 7.8c&d and 7.11a&b that for two different panel 3 specimens, the fringe patterns in the test section could be very different. In Figures 7.8d, fringes in the test section are sparse but dense for regions next to the test section. However, in Figure 7.11b, the dense fringe bands is at the test section. Therefore, at the same applied load, the shear strains obtained from the strain gages in the two specimens are not consistent. It is hence suggested that to measure the shear modulus of high tow sized woven fabric composites, strain gage size should be large enough to cover at least one fabric tow and one resin zone to obtain average strains over the anisotropy scale of the composites.

Shear strain distributions across the notches

The shear strains across the notches, normalized with respect to the average shear strain γ_{avg} , are shown in Figures 7.12-16 for specimens of panels 1 to 5 respectively. The shear strain distributions are not uniform for all five fabrics. For panels 2, 3 and 5, the shear strain distributions are more nonuniform. Thus, the nonuniformity of shear strain distributions not only occurs in the large tow sized fabric (panel 3) or high yarn density fabric (panel 5), but also moderate yarn density and tow sized fabric (panel 2). It was found that the shear strain distribution does not become uniform with increasing applied load. The peak shear strain is not at the center of the specimen.

Due to the nonuniformity of the shear field, shear modulus correction factors could not be applied to strain gage data. For example, in Figures 7.13 and 7.15, the correction factors could be 0.9 for panel 4 or 1.1 for panel 2. However, from Table 7.2 and Figures 7.1-7.5, fairly consistent shear modulus still can be obtained for woven fabrics composites except for large tow sized fabric.

7.3 Particulate composites

An experimental study was conducted to investigate the shear field of an Iosipescu aluminum-epoxy particulate composite specimen. Since the purpose of this section is to

evaluate the the effectiveness of the traditional strain gage technique on the shear modulus measurement of particulate composite, no discussion about the effect of filler size, interfacial adhesion on the shear properties will be given. Moire interferometry was applied to obtain full field displacement fields and uniformity of the shear strain distribution in the test section was then assessed.

7.3.1 Materials and specimen details

The epoxy based aluminum particulate composite was used as potted end support for graphite-epoxy Z-section stiffeners in a compression test to provide for uniform load introduction, prevent end brooming and simulate clamped boundary condition of the stiffener. The material is supplied by NASA LaRC and cut to specimen dimension as shown in Figure 1.2b. The extensional modulus and Poisson ratio were predetermined to be $E=7.752$ GPa and $\nu=0.43$.

7.3.2 Experimental results and discussion

The shear stress-strain data obtained from the strain gaged specimen are shown in Figures 7.17 and 18. The normal strains recorded in the individual gages of the rosette are plotted as a function of the average shear stress in Figure 7.17. It is found that the behavior of the two $\pm 45^\circ$ gages is highly nonlinear and the compressive strain in the $+45^\circ$ gage is only slightly larger than the tensile strain in the -45° gage. From Figure 7.18, it is found that the front and back shear stress-strain curves is only slightly apart indicating that little twisting occurred. The nonlinear behavior occurs when γ_{xy} is larger than 0.15%. Typical u- and v-field moire fringe patterns are shown in Figures 7.19a and b. It is found that the u- and v-fringes are not antisymmetrically distributed. In the u-field, shear strain in the gage section is essentially negligible but are of significant magnitude at the notches. At the right flank of the bottom notch, tensile ϵ_x is observed. In the v-field, the fringes are not straight in the test section and small amount of ϵ_y exists. The existence of ϵ_y is due to the low extensional modulus of the particulate composite. The shear strain distribution across the notches obtained from the moire data reduction is shown in Figure 7.20. It is found that the shear strain distribution is approximately uniform except at the notch regions. The shear strain at the center of the test section is about 0.94 to 1.02 γ_{avg} for all shear strain levels. Under low loading, the shear strain distribution shows more fluctuations. Thus correct shear modulus measurement still can be obtained from the Iosipescu strain gaged specimen. From this experiment, the tangent shear modulus at γ_{xy}

=0.15% was 2.4 GPa. If E and ν values are substituted into $G=E/2(1+\nu)$, a shear modulus $G=2.7$ GPa is obtained.

The failed specimen configuration is shown in Figure 7.21. The specimen failed catastrophically and broke into three pieces. Failure cracks initiated at the notch root-notch flank intersections and propagated across the direction of the maximum tensile stress toward the inner-most load points.

7.4 Summary

Application of Iosipescu shear test to shear modulus measurement of woven fabric composites was presented. It was found that the strain distribution across the notches is not uniform for woven fabrics of all weaves due to nonuniform volume fractions in the specimen. Significant nonuniformity is evidenced by the presence of the fringe bands in the test section. Shear modulus measurement using strain gage technique is not accurate for fabric with large tow size if small strain gages are used.

Strain distribution for epoxy based aluminum particulate composite is approximately uniform in the test section. The shear strain distribution across the notches is sensitive to the loading levels or load proximity effect. The deviation between the shear strain at the gage section and the average shear strain across the notches is about $\pm 5\%$. The measured shear modulus is very close to the calculated shear modulus ($G=E/2(1+\nu)$). Note that little specimen twisting was observed in this epoxy based aluminum particulate composite. On the contrary, large specimen twisting was found in the isotropic aluminum specimen, Figure 5.9a. Thus, for isotropic materials, degree of twisting depends on the extensional stiffness of the material system. In this example, the extensional stiffness of the epoxy based aluminum particulate composite is about a quarter of the extensional stiffness of the aluminum specimen.

CHAPTER 8. EVALUATION OF U-NOTCH IOSIPESCU SPECIMENS

8.1 Introduction

In shear testing of metals, Iosipescu found that if two 90° V-shape sharp notches (with the notch depth ranging from 20% to 25% of the specimen height) were cut at the opposite ends of the center of a beam, the shear stress distribution in the test section would become uniform when two pairs of antisymmetrically load couples are applied to the specimen. The principal stresses are at an angle of $\pm 45^\circ$ to the specimen axes and intersect one another in the test section. Since the sides of the notches are parallel to the direction of normal stresses, stress concentration does not develop. Unfortunately, Iosipescu's idea of shear testing of metals does not apply to the composite materials. For composite materials, it has been shown that the shear stress distribution across the notches is not uniform [10,17-20,25-27] and the nonuniformity depends on the material orthotropic ratio [10,17-20]. There is a significant shear stress concentration near the notch tips for the 0° specimen and at the center of test section for the 90° specimen. The effect of notch parameters (notch depth, notch angle and the notch radius at the notch tip) have been evaluated [5,10,11,18,27]. The range of values of the parameters investigated in these studies was 10-30% of the specimen height for notch depth, 90-130° for notch angle, and 0-2.5mm for notch tip radius. It was found that these three parameters all affect the stress concentrations but the notch tip radius exerts far greater influence on the stress distribution than the notch depth and notch angle.

With the introduction of the notch radius, the normal and shear stress concentrations at the notches are alleviated and the shear stress distribution across the notches becomes more uniform. It has been shown [5] that for a certain material orthotropy, with a certain combination of the values of the parameters, the nonuniformity of the shear stress distribution across the notches can be reduced to a minimum. But the shear stress in the test section is never the same as the applied average shear stress across the whole test section. Thus a correction factor is always needed in order to account for the nonuniformity of the shear field no matter what combination of the notch parameters is used.

Due to the limitation of the V-notch geometry, studies about the effect of notch radius on shear stress field have been performed up to 2.54mm (0.1") radius [18]. Since the notch angle of the V-notch specimen has little effect on the shear stress distribution and application of the shear modulus correction factor is inevitable, one implication is that the notch geometry may be altered and redesigned. An alternative is the U-notch specimen. Because U-notch is easy to cut and does not require special tooling, adoption of the U-notch Iosipescu specimen means cost saving in labor and tooling.

From the results of the numerical analysis of the V-notch Iosipescu shear specimen, it is apparent that most of the applied loads for the imposed uniform displacement constraints are antisymmetrically located in four small regions, Figure 4.5. Experimental observation of the failed specimen also shows evidence of narrow load application regions. Because the influence of the outer load pairs on the shear field in the test section is negligible, it is hence suggested that the specimen length may be further reduced.

In this Chapter, the U-notch Iosipescu shear specimen is proposed and evaluated. U-notch Iosipescu specimens with notch radius $r = 3.175\text{mm}$ (0.125") and specimen lengths of 50mm (2") and 76mm (3") are investigated. Numerical analyses and experiments using moiré interferometric and traditional strain gage techniques are applied.

8.2 3" U-notch specimen

8.2.1 Numerical analysis

The dimensions of the 3" U-notch Iosipescu specimen are shown in Figure 8.1. The test section width is the same as the V-notch specimen. The finite element mesh used in the numerical analysis is shown in Figure 8.2. At regions near the notches, the mesh is refined. This finite element model had 1924 membrane finite elements. The sequence of steps for application of boundary conditions and applied displacements is the same as that described in Chapter 4. After several iterations, the boundary conditions for 0° , 90° and $0^\circ/90^\circ$ graphite-epoxy specimens, as shown in Figure 8.3, are established. The inner load point distance is 7mm for all fiber orientations.

Force distribution on the specimen

The force distributions on the sides of the graphite-epoxy specimen for the three different ply orientations using the finite element models in Figure 8.3 are depicted in Figure 8.4. In comparison with Figure 4.5, it was found that the load introduction regions are essentially the same for the V- and U-notch specimens.

Strain state in the specimen

The shear strains, normalized with respect to average shear strains computed across the test section, are shown in Figure 8.5. It is found that the shear strain concentration near the notches for 0° U-notch specimen is much less than that of the V-notch 0° specimen. The shear strain near the notches and at the center of the test section are 13% larger and 8% smaller than the average shear strain, respectively. For the V-notch 0° specimen, the deviations are 32% and 13%, respectively. Thus the shear strain distribution across the notches for the U-notch 0° specimen is more uniform than that of the V-notch 0° specimen. Conversely, the shear strain concentration at the center of the test section in the 90° U-notch specimen is higher than that of the 90° V-notch specimen. For the $0^\circ/90^\circ$ U-notch specimen, the shear strain distribution is not as uniform as the V-notch specimen. The corresponding shear modulus correction factors are 0.92, 1.25 and 1.08, respectively for 0° , 90° and $0^\circ/90^\circ$ U-notch specimens.

The normal and shear strain contours for 0° , 90° and $0^\circ/90^\circ$ graphite-epoxy specimens are shown in Figures 8.6-8.8. For the 0° specimen, the longitudinal normal strain, ϵ_x , is very small in the test section. The maximum transverse normal and shear strains occur at the inner load points and are approximately of same magnitude. The ϵ_y in the test section is about 14% of the maximum ϵ_y at the inner load points. In two small regions at the left flank of the top notch and the right flank of the bottom notch, ϵ_y is tensile. The magnitudes of the tensile ϵ_y and the corresponding shear strain in these regions are about 32% and 73% of the maximum shear strain in the test section, Figures 8.6b and c. Thus these two regions are potential locations for incipient failure. Adams *et al.* [5] compared three V-notch specimens with notch tip radius ranging from 0.0mm to 0.64mm and 1.27mm, respectively. It was found that the point of maximum shear stress tends to move away from the root of each notch with increasing notch-root radius, in a direction toward the nearest inner loading point. For the U-notch specimen, the region of maximum shear strain near the notches expands further from the test section toward the inner load points as compared to the 0° V-notch specimen. In this analysis, it was found that the shear strain at the right flank of the top notch and at the left flank of the bottom notch is about 11% higher than the maximum shear strain in the test section. The implication of the shift of the

maximum shear near the notches is that shear failure may not necessarily initiate from the minimum cross section.

For the 90° specimen, ϵ_y is small in the load contact regions due to its large transverse stiffness. The ϵ_y in the test section is essentially zero. At the left flank of the top and the right flank of the bottom notches, the longitudinal normal strains are tensile and are about 62% of the maximum shear in the test section. Due to the large radius, the maximum shear strain zones tend to extend to the above mentioned regions. The corresponding shear strains in the regions of tensile ϵ_x are of the same order of magnitude as the maximum shear strain in the test section. The strain contours of the 0°/90° specimen have the characteristics of both the 0° and 90° specimens.

8.2.2 Materials and specimen details

The 3" U-notch Iosipescu specimens were cut from the same panel as the V-notch specimens. They are 20-ply unidirectional and cross-ply, graphite-epoxy specimens with dimensions as shown in Figure 8.1. For each fiber orientation, one specimen was instrumented with a crossed-line diffraction grating on one surface and a stacked three gage rosette (Micro-measurements WK-06-060WR-350) on the other surface. The strain gaged specimens were instrumented with separate two-gage rosette (Micro-measurements EA-13-062TV-350) on each surface of the specimen. The experimental procedure is the same as what described in the Chapters 2 and 3.

8.2.3 Experimental results and discussion

Stress-strain data

Typical shear stress-strain data from the experiments on the strain gaged specimens of three fiber orientation are shown in Figure 8.9. The individual normal strains in the $\pm 45^\circ$ gages are shown in Figure 8.10. For 0° specimen, the tensile strain in the -45° gage is about 69% to 78% of the compression strain in the +45° gage based on specimen-to-specimen variations. For 90° specimen, the two gage readings are equal in magnitude but opposite in sign. The stress-strain behavior is linear until the shear strain exceeds 0.8%. The two $\pm 45^\circ$ gages on the 0°/90° specimen also recorded approximately equal and opposite normal strains and the shear stress-strain behavior is nonlinear.

Moire fringe patterns

Typical moire fringe patterns for 0° , 90° and $0^\circ/90^\circ$ specimens are shown in Figures 8.11-13, respectively. In Figures 8.11a and b, the u-field is adjusted to have the minimum number of fringes and the v-field contains most of the deformation information. The fringes in the v-field are S-shaped, which provide the evidence of the existence of transverse normal strain, ϵ_y , in the 0° specimen test section. In Figures 8.11c and d, where deformation information is equally contained in the u- and v-fields, significant nonuniformity is found in the u-displacement field. These nonuniform fringe distributions may be caused by the randomly distributed resin rich regions (between fiber bundles) in the specimen. For the 0° specimen, because the fibers are in the longitudinal direction, the nonuniformity will be shown in the u-field. Note that some degree of nonuniformity also exists in the V-notch specimens. Due to the rapid change of the cross section in the V-notch sections, most of the the nonuniformity is masked by the large stress gradient in the test section. In the v-field, very dense fringe bands are found at the notch regions neighboring the inner load points. The maximum shear thus moved away from the notch tip in a direction toward the inner load points, which agrees well with the numerical predictions. At the notch regions further from the applied load, large tensile strains ϵ_y are found, an observation which is also consistent with the numerical results.

In Figure 8.12a, significant tensile $\delta u/\delta x$ is observed in the right side of the bottom notch and a lesser amount of tensile $\delta u/\delta x$ is also observed in the left side of the top notch. While the numerical analysis predicts equal magnitude of the tensile ϵ_x in the above mentioned two regions, the inequality in the experimental results indicates that some degree of in-plane bending may occur in the 90° specimen. In Figure 8.12b, the fringes in the test section are straight. Very dense fringe bands are observed. This phenomenon again can be attributed to the existence of resin rich regions in the test section. Because the fibers are in the vertical direction, nonuniformity in the 90° specimen is observed in the v-field fringe pattern. For the $0^\circ/90^\circ$ specimen, the nonuniformity of the displacement fields can be observed in both the u- and v-fields, Figures 8.13.

Shear strain distribution across the notches

The shear strain distributions across the notches obtained from the moire data reduction for 0° , 90° and $0^\circ/90^\circ$ specimens are shown in Figure 8.14. It is found that the shear strain distributions are not symmetric for 0° and $0^\circ/90^\circ$ specimens. For the 0° specimen, at regions near the top notch, there are shear strain concentrations for all load levels, especially at lower applied loads. This effect also occurred in the 3" 0° V-notch specimen. The shear strain concentration at the top notch is as high as 1.38 at a load of

6.5MPa to 1.18 at a load of 33.5MPa, Figure 8.14a. This phenomenon is not predicted in the numerical analysis. It is suspected that the non-symmetric shear strain distribution is caused by non-antisymmetrically distributed applied load. The inner load points at the bottom notch is believed to be farther away than the inner load points at the top notch. From the moire fringe patterns of 0° V- and U-notch specimens, the non-antisymmetrical load application points are evidenced by the unequal fringe densities near the notch flanks. Thus, the closeness of the inner load points at the top notch to the test section may have distorted the shear contour and caused the non-symmetric shear strain distribution across the test section. Due to the U-notch geometry, the distortion is more profound than the V-notch specimen. For the 0°/90° specimen, the shear strain distribution is also not symmetric. But the irregular kink near the center of the specimen is caused by the nonhomogeneity of the material. For the 90° specimen, there is less fluctuation in the shear strain distribution. Because the fibers are in the transverse direction, the effect of non-antisymmetrical load points and material nonhomogeneity to the strain distribution in the test section is negligible.

The correction factors can be obtained from the shear strain distributions across the notches. From Figure 8.14, the shear modulus correction factors are about 0.93, 1.25 and 1.11 for 0°, 90° and 0°/90° specimens, respectively.

8.3 2" U-notch specimen

8.3.1 Numerical analysis

The dimensions for the 2" U-notch specimen are the same as the 3" U-notch specimen except for the specimen length. The finite element mesh for the 2" U-notch specimen in the numerical analyses is shown in Figure 8.15. At the center portion of the specimen, the finite element mesh is the same as the 3" U-notch specimen. This finite element model had 1756 membrane finite elements. The boundary conditions for 0°, 90° and 0°/90° graphite-epoxy specimens are established following the procedure in Chapter 4 and are shown in Figure 8.16. The inner load point distance is 7mm for all fiber orientations.

Force distribution on the specimen

The force distributions on the sides of the graphite-epoxy specimens of the three fiber orientations using the finite element models in Figure 8.16 are depicted in Figure 8.17. The force distributions for the 0° and $0^\circ/90^\circ$ specimens are very similar. Due to the change in specimen length, the force distributions of 3" and 2" U-notch specimens are different.

Strain state in the specimen

The shear strains, normalized with respect to average shear strain across the test section, are shown in Figure 8.18. Similar to the 3" 0° U-notch specimen, the shear strain concentration near the notches for the 2" 0° specimen is much less than that of the 3" 0° V-notch specimen. The shear strain concentration near the notches is 1.3 times the average shear strain, γ_{avg} . At the center, the shear strain is 13% less than the average shear strain while for the 3" U-notch specimen, the deviation is only 8%. The difference between the 3" and 2" U-notch specimens are suspected to be caused by the position of the outer load points. For the 2" specimen, the strain contours are slightly distorted because the outer load points are closer to the notches. Thus the shear strain concentration is higher in the 2" 0° U-notch specimen. For 90° and $0^\circ/90^\circ$ specimens, the shear strain distributions are very similar to those of the 3" U-notch counterparts. The corresponding shear modulus correction factors are 0.87, 1.25 and 1.07, respectively, for 0° , 90° and $0^\circ/90^\circ$ specimens.

The normal and shear strain contours for 0° , 90° and $0^\circ/90^\circ$ graphite-epoxy specimens are shown in Figures 8.19-21. The strain contours for the 2" U-notch specimens are similar to those of the 3" U-notch specimens. The discussions concerning the existence of tensile ϵ_x and ϵ_y in some regions near the notch root in the 3" V- and U-notch 90° , 0° and $0^\circ/90^\circ$ specimens also apply in the 2" U-notch specimens. For the 0° specimen, ϵ_y in the test section is about 14% of the maximum ϵ_y at the inner load points. In the notch regions further from the applied load, the tensile ϵ_y and the corresponding shear strains in these regions are about 25% and 80% of the maximum shear strain in the test section, Figures 8.19b and c. The shear strain at the notch regions neighboring the applied load is about 20% higher than the maximum shear strain in the test section. For the 90° specimen, at the notch regions further from the applied load, the longitudinal normal strain is tensile and is about 72% of the maximum shear in the test section. The corresponding shear strain in the regions of tensile ϵ_x is about 72% of the maximum shear strain in the test section. At these four small regions in the vicinity of the notch root the shear strain is of the same order of magnitude as the maximum shear strain in the test section. If a complex strain state near the notches in the linear analysis exists in the nonlinear range, failure may initiate at those regions and the specimen may fail in mixed mode.

8.3.2 Experimental results and discussion

The 2" U-notch Iosipescu specimens were cut from the same panel as the 3" V- and U-notch specimens. The strain gage instrumentation and moire implementation are the same as those of the 3" specimens. The experimental procedure is the same as that described in the Chapters 2 and 3.

Stress-strain data

Typical shear stress-strain data obtained from the strain gaged specimens for the three fiber orientation are shown in Figure 8.22. It was found that the shear stress-strain curves for 0° , 90° and $0^\circ/90^\circ$ specimens are nonlinear (for $\gamma > 0.4\%$). For the 0° specimen the stress at the first load drop is considered as the shear strength. The individual normal strains in the $\pm 45^\circ$ gages are shown in Figure 8.23. In Figure 8.23a, the tensile strain in the -45° gage is about 63% to 68% of the compressive strain in the $+45^\circ$ gage based on specimen-to-specimen variations. The two $\pm 45^\circ$ gages in the $0^\circ/90^\circ$ specimen also recorded approximately equal and opposite normal strains. Small amounts of twisting are observed for the 0° specimen when the applied load increased.

Moire fringe patterns

Typical moire fringe patterns for 0° , 90° and $0^\circ/90^\circ$ specimens are shown in Figures 8.24-26, respectively. In Figures 8.24a&b-26a&b, the u- and v-fields are adjusted to have approximately equal amount of the fringes. Nonuniformities are found in the u-field for 0° and $0^\circ/90^\circ$ specimens and in the v-field for 90° and $0^\circ/90^\circ$ specimens. For the 0° specimen, the fringes in the v-field are S-shaped. Very dense fringes are found at notch regions neighboring the applied load. Thus the maximum shear moved away from the notch tip toward the inner load points. Tensile ϵ_y is found at regions away from the notch tips. For 90° specimen, tensile ϵ_x is found at the right side of the bottom notch in the u-field.

Shear strain distribution across the notches

The shear strain distributions across the notches obtained from the moire data reduction for 0° , 90° and $0^\circ/90^\circ$ specimens are shown in Figure 8.27. The distributions are similar to the counterparts of the 3" U-notch specimens. The shear strain distributions are not symmetric for 0° and $0^\circ/90^\circ$ specimens. For the 0° specimen, the shear strain concentration is about 1.2 at regions near the top notch. The non-symmetric shear strain

distribution is caused by non-antisymmetrically distributed applied load. For $0^\circ/90^\circ$ specimen, the shear strain distribution is also not uniform reflecting the nonhomogeneity of the specimen. The 90° specimen showed less fluctuation in the shear strain distribution. The corresponding shear modulus correction factors are 0.92, 1.18 and 1.03 for these 0° , 90° and $0^\circ/90^\circ$ moire specimens.

8.4 Summary

Shear modulus

The shear moduli obtained from the 3" V-, U- as well as 2" U-notch AS4-3501-6 graphite-epoxy specimens are shown in Table 8.1. The shear modulus correction factors obtained from numerical analyses and one set of moire specimens are also shown in Table 8.1. Note that the correction factors obtained from different set of moire experiments may be different based on specimen-to-specimen variations. From this comparison, it is found that the deviation of the correction factors from the numerical and experimental results ranges from 5% to 10% for 0° specimens while the deviation for 90° and $0^\circ/90^\circ$ specimens range from 2% to 5%. The large variation for the 0° specimen is caused by uncertainty of load points as discussed in Chapters 4 and 5. After application of correction factors, the shear modulus obtained from 0° specimen is smaller than those of the 90° and $0^\circ/90^\circ$ specimens in all V- and U-notch specimens. The shear moduli obtained from the 2" U-notch specimens for all three fiber orientations are slightly higher than those from the 3" V- and U-notch specimens. For 0° specimen in all V- and U-notch designs, the standard deviation is higher, which is again attributed to the uncertainty of load points for this fiber orientation. In general, the 90° specimens produce more consistent results among these three specimen designs.

Shear strength

The shear strength obtained from the 3" V-, U- and 2" U-notch graphite-epoxy specimens are shown in Table 8.2. Shear strength is interpreted as the stress when the first load-drop occurs in the shear stress-strain curve. Due to the U-notch geometry, very large deformation occurred when the first load drop was observed for the 0° and $0^\circ/90^\circ$ specimens, especially for $0^\circ/90^\circ$ specimens. At the notches, the U-shape is greatly distorted. Thus the strength values obtained from 0° and $0^\circ/90^\circ$ specimens cannot be interpreted as the shear strength of the material. Likewise, the 0° and $0^\circ/90^\circ$ V-notch specimens may distort before the first load-drop occurs. If the distortion in the V-shape

notch is small, it is not visually observable. For the 90° specimens, failure initiated at regions away from the notch-root axis and specimen failed in a mixed mode. Prediction and interpretation of the shear strength is beyond the scope of this research and will not be discussed further.

Supplementary test on thermoplastic composites

In a subsequent test on the AS4/APC-2 cross-ply $([0/90]_{20})$ 3" V-, U- and 2" U-notch specimens, it was found that the shear moduli for 3" V- and U-notch specimens are essentially the same while the modulus obtained from 2" U-notch specimen is slightly higher. The measured shear modulus is shown in Table 8.3. Typical moire fringe patterns for 3" V- and U-notch specimens are shown in Figures 8.28 and 29.

CHAPTER 9. CONCLUSIONS AND FUTURE WORK

9.1 Conclusions

The problems associated with the Iosipescu shear test have been identified and demonstrated experimentally and numerically. For 0° specimens, pure shear is not obtainable in the test section because the compressive strains imposed by the inner load points are transmitted along the fibers into the test section. The strains recorded by the two strain gages at the $\pm 45^\circ$ directions to the longitudinal axis are not equal in magnitude and opposite in sign. Because the normal and shear strain fields in the small *gage section* are uniform, the lack of pure shear for the 0° specimen does not affect the accurate measurement of shear strain.

The shear strain distribution in the *test section* (across the notches) is not uniform for all material systems. Based on the material orthotropy, the distributions are of different shapes. In the calculation of the shear modulus, correction factors must be applied to account for the nonuniform shear strain distribution across the notches. It is not satisfactory to have to use correction factors in material property measurement methods. It is less satisfactory when these correction factors depend upon material properties. Fortunately, the main parameter is the material orthotropy ratio which is readily available, and not the shear modulus which is to be measured. These correction factors also depend upon the size and type of strain gage rosette used, but the variation for gage sizes in the range 1-2mm is less than 3%. Since one of the main purposes of the test is to produce material property data it seems unwise to ignore the issue of correction factors. Values of shear moduli from the 0° and 90° specimens will, otherwise, be 10% too high and 19% too low, respectively, for graphite-epoxy. If such values are used in laminate design a serious over-prediction of properties will occur.

The variation in the measured shear modulus for the 0° specimens is attributed to the sensitivity of the shear strain distribution to the local loading details. The 0° specimen configuration will suffer an intrinsic specimen-to-specimen variability. The 90° specimen does not suffer from the same problems as the 0° specimen. The 90° specimen conforms to the pure shear condition of equal and opposite strains in the $\pm 45^\circ$ gages. It does not show significant sensitivity to the load model used to calculate the correction factor. However, the 90° specimen is prone to twist. Strain gage rosettes must be applied to the

front and back faces of the specimen, and the average shear strain used. This averaging procedure provides an essential value of shear strain for the determination of shear modulus and shear stress-strain data. It does not, however, eliminate the twisting induced shear which can be of the same order as that due to the applied shear force.

In addition to the possible torsional moment, in- and out-of-plane moments can occur for 90° specimens. The presence of the out-of-plane moment is detected by the longitudinal gage (the gage parallel to the x-axis) in the three-gage rosette. The effect of this moment upon the shear strain calculation is negligible. The in-plane moment causes strains of opposite sign in the $\pm 45^\circ$ gages so they are not eliminated in Equation (2.1). It is suggested that strain gages with 30 MILS gage length be used. The possibility of asymmetry in the stress fields for all fiber orientations leads to the recommendation that stacked rosettes be used so that the calculated shear strains are relative to a single location. The sensitivity of the specimen to twisting requires that back-to-back rosettes be used in all composite specimens. It is further recommended that the data acquisition system be arranged to record values on both faces, and not just the average of front and back instrumentation, so that the degree of twisting can be determined.

Application of the Iosipescu shear test in parametric studies of composite manufacturing process has been demonstrated to be accurate and economic. In shear testing of woven fabric composites, it is shown that large variation of the shear stress-strain data will be obtained if the tow size is large. The strain gages applied to the woven fabric composites should be larger than the tow size. Also, stacked rosettes are recommended. It was found that the behavior of the epoxy based aluminum particulate composite is very similar to the its isotropic base material - the epoxy. For both woven fabric and particulate composites, consistent shear modulus measurements can be obtained.

Numerical and experimental evaluations of the U-notch specimens have shown that the strain distributions for the 2" and 3" specimens are of no significant difference. It was found that the shear strain distribution across the notches for the 2" and 3" U-notch 0° specimens is more uniform than that of the V-notch 0° specimen. The maximum shear in the test section shifts toward the load points. A complex strain state was found in the vicinity of the notches. For 90° specimens, the shear strain distribution across the notches is of same pattern for both U- and V-notch specimens except that the strain concentration at the center of the test section is larger for the U-notch specimens. Consistent shear moduli

can be obtained for these three specimen geometries. Thus the U-notch design can be a substitute to the current V-notch design in the shear modulus measurement.

Strength measurements for the Iosipescu specimens could be a problem for both V- and U-notch designs. Because of the notch design, tensile normal strains are present in the vicinity of the notches. Though the application of the notch root radius reduces the stress/strain concentrations near the notches for the 0° specimens, it also shifts the maximum shear from the test section toward the inner load points and produces a complex stress/strain state in the vicinity of the notches. The complex stress/strain state near the notches and the twisting effect are responsible for the low shear strength obtained from the 90° specimens. After taking into account the degree of twisting and applying the necessary corrections, the apparent strength for the 90° specimen is still an underestimate due to its mixed-mode failure. The apparent strength obtained from the 0° specimens is also questionable. Because failure never initiates from the minimum cross section, the 0° specimens may failed in shear, tensile or combined modes.

9.2 Future work

Investigation of the failure strength of the Iosipescu composite specimens will continue. The 3" and 2" U-notch specimens have proved to be a valid design for shear modulus measurement. It is hence suggested the notch geometry can be further altered and the specimen length and thickness could be reduced. Application of the Iosipescu shear test to the shear modulus measurement of SMC composite materials will be evaluated. Possible modification of the Wyoming fixture to eliminate specimen twisting will be studied.

REFERENCES

References

1. Rosen, B.W., "A Simple Procedure for Experimental Determination of the Longitudinal Shear Modulus of Unidirectional Composites," *Journal of Composite Materials*, 6 : 552-554 (1972).
2. "Standard Practice for Inplane Shear Stress-Strain Response of Unidirectional Reinforced Plastics," D3518-76, *1991 Annual Book of ASTM Standard*, Vol. 15.03, American Society for Testing and Materials, 1991.
3. Pindera, M. J. and Herakovich, C. T., "Shear Characterization of Unidirectional Composites with the Off-Axis Tension Test," *Experimental Mechanics*, 26 (1) : 103-112 (1986).
4. Whitney, J. M., Stansbarger, D. L. and Howell, H. B., "Analysis of the Rail Shear Test-Application and Limitations," *Journal of Composite Materials*, 5 : 24-34 (1971).
5. Adams, D. F. and Walrath, D. E., "Further Development of the Iosipescu Shear Test Method," *Experimental Mechanics*, 27 (2) : 113-119 (1987).
6. Iosipescu, N., "New Accurate Procedure for Single Shear Testing of Metals," *Journal of Materials*, 2 (3) : 537-566 (1967).
7. Arcan, M., Hashin, Z. and Voloshin, A., "A Method to Produce Uniform Plane-Stress States with Applications to Fiber Reinforced Materials," *Experimental Mechanics*, 18 (4) : 141-146 (1978).
8. Slepetz, J. M., Zegeski, T. F., and Novello, R., "In-Plane Shear Test for Composite Materials," AMMRC TR 78-30, Army Materials and Mechanics Research Center, July 1978.
9. Walrath, D.E. and Adams, D. F., "The Iosipescu Shear Test As Applied to Composite Materials," *Experimental Mechanics*, 23 (1) : 105-110 (1983).
10. Walrath, D.E. and Adams, D. F., "Analysis of the Stress State in an Iosipescu Shear Test Specimen," Report UWME-DR-301-101-1, Department of Mechanical Engineering, University of Wyoming, (June 1983).
11. Adams, D. F. and Walrath, D. E., "Current Status of the Iosipescu Shear Test Method," *Journal of Composite Materials*, 21 (6) : 494-507 (1987).
12. Abdallah, M. G. and Gascoigne, H. E., "The Influence of Test Fixture Design of Iosipescu Shear Test for Fiber Composite Material," *Test Methods for Design Allowables for Fibrous Composites: 2nd Vol.*, ASTM STP 1003, C. C. Chamis, Ed., pp. 231-260 (1989).
13. Wilson, D.W., "Evaluation of the V-notched Beam Shear Test Through an Interlaboratory Study", *Journal of Composites Technology and Research*, 12 (3) : 131-138 (1990).
14. Ho, H., Tsai, M.Y., Morton, J. and Farley, G.L., "A Comparison of Popular Shear Test Methods for Composite Materials," proceedings of ICCM VIII, Hawaii, July, 1991.

15. Sullivan, John L., "The Use of Iosipescu Specimens," *Experimental Mechanics*, 28 (3) : 326-328 (1988).
16. Lee, S. and Munro, M., "Evaluation of Testing Techniques for the Iosipescu Shear Test for Advanced Composite Materials," *Journal of Composite Materials*, 24 : 419-440 (1990).
17. Pindera, M. J., Choksi, G., Hidde, J. S. and Herakovich, C. T., "A Methodology for Accurate Shear Characterization of Unidirectional Composites," *Journal of Composite Materials*, 21 (12) : 1164-1184 (1987).
18. Spigel, B. S., "An Experimental and Analytical Investigation of the Iosipescu Shear Test for Composite Materials," Master's Thesis, Old Dominion University, Virginia. (Aug. 1984)
19. Broughton, W. R., Kumosa, M. and Hull, D., "Analysis of the Iosipescu Shear Test as Applied to Unidirectional Carbon-Fiber Reinforced Composites," *Composite Science and Technology*, 38 : 299-325 (1990).
20. Kumosa, M. and Hull, D., "FEM Analysis of Mixed Mode Fracture in the Iosipescu Shear Test," Proceedings of the Sixth International Conference On Composite Materials/Second European Conference on Composite Materials, Elsevier Applied Science, Matthews, F. L., Buskell, N. R. C., Hodgkinson, J. M. and Morton, J., Eds., Vol. 3, pp. 243-253 (1987).
21. Guild, J., "The Interference Systems of Crossed Diffraction Gratings; Theory of Moire Fringes," Oxford at the Clarendon Press, (1956).
22. Post, D., "Developments in Moire Interferometry," *Optical Engineering*, 21 (3): 458-467 (1982).
23. Czarnek, R., "Moire Interferometry," *Structural Testing, Society of Experimental Mechanic*", 30 (2) : 195-200 (June 1990).
24. Morton, J., Post, D., Han, B. and Tsai, M.Y., "A Localized Hybrid Method of Stress Analysis," *Experimental Mechanics*, 30 (2) : 195-200 (June 1990).
25. Barnes, J. A., Kumosa, M. and Hull, D., "Theoretical and Experimental Evaluation of the Iosipescu Shear Test," *Composites Science and Technology*, 28 : 251-268 (1987).
26. Pindera, M. J., Ifju, P. and Post, D., "Iosipescu Shear Characterization of Polymeric and Metal Matrix Composites," *Experimental Mechanics*, 30 (1) : 101-108 (1990).
27. Sullivan, J. L., Kao, B.G. and Van Oene, H., "Shear Properties and a Stress Analysis Obtained from Vinyl-ester Iosipescu Specimen," *Experimental Mechanics*, 24 (3): 223-232 (1984).
28. Tsai, S. W. , "Composite Design," 4th edition, Appendix B, p B-2 (1988).
29. Sullivan, J., Private communication.
30. Timoshenko, S.P. and Goodier, J.N., "Theory of Elasticity," 3rd. ed., McGraw-Hill (1979).

31. Swanson, S. R., Messick, M. and Toombes, G. R., "Comparison of Torsional Tube and Iosipescu In-plane Shear Test Results for A Carbon Fiber-Reinforced Epoxy Composite," *Composites*, 2 (3) : 220-224 (1985).
32. Loos, A. C., Springer, G. S., "Curing of Epoxy Matrix Composites," *Journal of Composite Materials*, 17 : 135-169 (1983).
33. Ishikawa, T. and Chou, T. W., "Stiffness and Strength Behavior of Woven Fabric Composites," *Journal of Material Science*, 17 : 3211-3200 (1982).
34. Ishikawa, T. and Chou, T. W., "Nonlinear Behavior of Woven Fabric Composites," *Journal of Composite Materials*, 17 : 399-413 (1983).

TABLE AND FIGURE CAPTIONS

Table 4.1 Mechanical property for numerical analysis.

Table 7.1 Fabric architecture.

Table 7.2 Averaged in-plane shear moduli and shear strengths for woven fabric composite materials.

Table 8.1 Measured in-plane shear moduli from AS4-3501-6 notched specimens.

Table 8.2 Averaged in-plane shear strengths from AS4-3501-6 notched specimens.

Table 8.3 Measured in-plane shear moduli from AS4/APC-2 notched specimens.

Fig.1.1 (a) Wyoming fixture (W1) and (b) original Iosipescu specimen.

Fig.1.2 (a) Modified Wyoming fixture (W2) and (b) modified Iosipescu specimen.

Fig.1.3 Normalized values of in-plane shear moduli obtained from Iosipescu shear test on AS4/3501-6. Values are normalized with respect to $G^*_{12} = 5.12$ GPa, the average obtained from $\pm 45^\circ$ tension and 10° off-axis tests [14]. The ranges shown in the figure are moduli of repeatability [13] or denote one standard deviation.

Fig.2.1a Strain vs. stress for typical 0° graphite-epoxy specimen. Gages are aligned at $\pm 45^\circ$ and 0° directions.

Fig.2.1b Strain vs. stress for typical 90° graphite-epoxy specimen. Gages are aligned at $\pm 45^\circ$ and 0° directions.

Fig.2.1c Strain vs. stress for typical $0^\circ/90^\circ$ graphite-epoxy specimen. Gages are aligned at $\pm 45^\circ$ and 0° directions.

Fig.2.2 Schematic diagram of pure shear (a) in x-y coordinate, (b) in principal direction and (c) Mohr's circle representation.

Fig.2.3 Shear stress-strain data and failure modes for typical 0° , 90° and $0^\circ/90^\circ$ graphite-epoxy specimens.

Fig.3.1 (a) optical set-up of moire interferometry, (b) Two-beam interferometry.

Fig.3.2 (a) u-field, (b) v-field moire fringe patterns for the 0° graphite-epoxy Iosipescu specimen at an applied load of 667 N.

Fig.3.3 (a) u-field, (b) v-field moire fringe patterns for the 90° graphite-epoxy Iosipescu specimen at an applied load of 1112 N.

Fig.3.4 (a) u-field, (b) v-field moire fringe patterns for the $0^\circ/90^\circ$ graphite-epoxy Iosipescu specimen at an applied load of 1334 N.

Fig.3.5 Normalized shear strain distributions across the notches obtained from manual data reduction of moire fringe patterns for (a) 0° , (b) 90° , (c) $0^\circ/90^\circ$ graphite-epoxy Iosipescu specimens.

Fig.3.6 Shear stress-strain data obtained from moire (front face) and gages (back face) for (a) 0° , (b) 90° , (c) $0^\circ/90^\circ$ graphite-epoxy Iosipescu specimens.

Fig.3.7 Moire fringe patterns for (a) u-displacement field, (b) v-displacement field. Reproduced fringe patterns for (c) u-displacement field, (d) v-displacement field (showing every 5th fringe) from the localized hybrid analysis. The data correspond to the 0° specimen at an applied load of 1334N.

Fig.3.8 Moire fringe patterns for (a) u-displacement field, (b) v-displacement field. Reproduced fringe patterns for (c) u-displacement field, (d) v-displacement field (showing every 5th fringe) from the localized hybrid

analysis. The data correspond to the $0^\circ/90^\circ$ specimen at an applied load of 1334N.

- Fig.3.9 Moire fringe patterns for (a) u-displacement field, (b) v-displacement field. Reproduced fringe patterns for (c) u-displacement field, (d) v-displacement field (showing every 3rd fringe) from the localized hybrid analysis. The data correspond to the 90° specimen at an applied load of 1112N.
- Fig.3.10 (a) Deformed shape, contours of (b) ϵ_x , (c) ϵ_y , (d) γ_{xy} obtained from a localized hybrid analysis of a 0° specimen at an applied load of 1334N
- Fig.3.11 (a) Deformed shape, contours of (b) ϵ_x , (c) ϵ_y , (d) γ_{xy} obtained from a localized hybrid analysis of a 90° specimen at an applied load of 1112N
- Fig.3.12 (a) Deformed shape, contours of (b) ϵ_x , (c) ϵ_y , (d) γ_{xy} obtained from a localized hybrid analysis of a $0^\circ/90^\circ$ specimen at an applied load of 1334N
- Fig.3.13 Comparisons of shear strain data across the notches obtained from manual data reduction of moire fringe patterns and the localized hybrid analysis for (a) 0° (at an applied load of 1334N), (b) 90° (at an applied load of 1112N), (c) $0^\circ/90^\circ$ (at an applied load of 1334N) graphite-epoxy Iosipescu specimens.
- Fig.3.14 Comparisons of shear strain data along the longitudinal axis obtained from manual data reduction of moire fringe patterns and the localized hybrid analysis for (a) 0° (at an applied load of 1334N), (b) 90° (at an applied load of 1112N), (c) $0^\circ/90^\circ$ (at an applied load of 1334N) graphite-epoxy Iosipescu specimens.
- Fig.4.1 Deformation characteristics of Iosipescu shear specimen.
- Fig.4.2 Finite element model of Iosipescu specimen.
- Fig.4.3 Initial displacement (applied and constrained) distribution on Iosipescu specimen.
- Fig.4.4 Finite element models for Iosipescu specimen tested in modified Wyoming fixture, (a) 0° specimen, (b) 90° specimen, (c) $0^\circ/90^\circ$ specimen.
- Fig.4.5 Distributed loads on the specimen sides due to imposition of uniform displacement for (a) 0° , (b) 90° , (c) $0^\circ/90^\circ$ specimens.
- Fig.4.6 Normal and shear strains along the notch axis, normalized with respect to average shear strain, for (a) graphite-epoxy, (b) Kevlar-epoxy, (c) glass-epoxy 0° specimen.
- Fig.4.7 Normal and shear strains along the notch axis, normalized with respect to average shear strain, for (a) graphite-epoxy, (b) Kevlar-epoxy, (c) glass-epoxy 90° specimen.
- Fig.4.8 Normal and shear strains along the notch axis, normalized with respect to average shear strain, for (a) graphite-epoxy, (b) Kevlar-epoxy, (c) glass-epoxy $0^\circ/90^\circ$ specimen.

- Fig.4.9 Typical shear strain contours for (a) 0° , (b) 90° , (c) $0^\circ/90^\circ$ graphite-epoxy Iosipescu specimens.
- Fig.4.10 Typical transverse normal strain contours for (a) 0° , (b) 90° , (c) $0^\circ/90^\circ$ graphite-epoxy Iosipescu specimens.
- Fig.4.11 Typical longitudinal normal strain contours for (a) 0° , (b) 90° , (c) $0^\circ/90^\circ$ graphite-epoxy Iosipescu specimens.
- Fig.4.12 Shear strain distribution along the notch axis for (a) 0° , (b) 90° , (c) $0^\circ/90^\circ$ graphite-epoxy, Kevlar-epoxy and glass-epoxy specimens.
- Fig.4.13 Correction factor vs. material orthotropic ratio.
- Fig.4.14 Normalized strains of $\pm 45^\circ$ gages from finite element analysis for (a) 0° , (b) 90° , (c) $0^\circ/90^\circ$ graphite-epoxy Iosipescu specimen.
- Fig.4.15 Normalized strains of $\pm 45^\circ$ gages from finite element analysis for (a) 0° , (b) 90° , (c) $0^\circ/90^\circ$ Kevlar-epoxy Iosipescu specimen.
- Fig.4.16 Normalized strains of $\pm 45^\circ$ gages from finite element analysis for (a) 0° , (b) 90° , (c) $0^\circ/90^\circ$ glass-epoxy Iosipescu specimen.
- Fig.4.17 Models for load-point effect analysis.
- Fig.4.18 Load point effect on the shear strain distribution along the notch axis for 0° graphite-epoxy specimen. Load cases are shown in Fig.4.17.
- Fig.4.19 Load point effect on the shear strain distribution along the notch axis for 90° graphite-epoxy specimen. Load cases are shown in Fig.4.17.
- Fig.5.1 One dimensional mechanics of the Iosipescu shear specimen --force and moment equilibrium models.
- Fig.5.2 Free body diagram and Mohr's circle representation of strain state of an element in the gage section of (a) 90° specimen, (b) 0° specimen.
- Fig.5.3 Schematic diagram of complementary shear: (a) 0° specimen, (b) 90° specimen, (c) $0^\circ/90^\circ$ specimen.
- Fig.5.4 Three dimensional representation of the free body diagram of the Iosipescu specimen.
- Fig.5.5 Effect of load eccentricity upon the shear stresses.
- Fig.5.6a Shear stress-strain data for 90° graphite-epoxy specimen loaded in different orientations which were obtained by rotating the specimen about the x,y and z axis.
- Fig.5.6b Average of front and back surface shear strains as a function of shear stress for 90° graphite-epoxy specimen.

- Fig.5.7a Shear stress-strain data for 0° graphite-epoxy specimen loaded in different orientations which were obtained by rotating the specimen about the x,y and z axis.
- Fig.5.7b Average of front and back surface shear strains as a function of shear stress for 0° graphite-epoxy specimen.
- Fig.5.8a Shear stress-strain data for $0^\circ/90^\circ$ graphite-epoxy specimen loaded in different orientations which were obtained by rotating the specimen about the x,y and z axis.
- Fig.5.8b Average of front and back surface shear strains as a function of shear stress for $0^\circ/90^\circ$ graphite-epoxy specimen.
- Fig.5.8c Shear stress-strain data for $0^\circ/90^\circ$ graphite-epoxy specimen with soft shim, when loaded in different orientations which were obtained by rotating the specimen about the x,y and z axis.
- Fig.5.9a Shear stress-strain data for aluminum specimen loaded in different orientations which were obtained by rotating the specimen about the x,y and z axis.
- Fig.5.9b Average of front and back surface shear strains as a function of shear stress for an aluminum specimen.
- Fig.5.10 Calculated G_{12} for three graphite-epoxy 0° and 90° specimens, before and after application of correction factors. The areas shown shaded represent the ranges of values due to the uncertainty in the finite element calculated correction factors.
- Fig.6.1 Panel size and specimen positions for AU4/BMIPES and AS4/BMIPES composite materials.
- Fig.6.2 Shear stress-strain data from front and back faces of six AU4/BMIPES specimens.
- Fig.6.3 Average of front and back shear stress-strain data of six AU4/BMIPES specimens.
- Fig.6.4 (a) G_{12} , (b) S_{12} of six AU4/BMIPES specimens.
- Fig.6.5 Shear stress-strain data from front and back faces of six AS4/BMIPES specimens.
- Fig.6.6 Average of front and back shear stress-strain data of six AS4/BMIPES specimens.
- Fig.6.7 (a) G_{12} , (b) S_{12} of six AS4/BMIPES specimens.
- Fig.6.8 Strain vs. stress for typical 0° graphite-PES specimen cured at (a) 3.45MPa (500 psi), (b) 2.07MPa (300psi), (c) 1.03MPa (150psi). Gages are aligned at $\pm 45^\circ$ and 0° directions.
- Fig.6.9 Shear stress-strain data for 0° graphite-PES specimens cured at (a) 3.45MPa (500 psi), (b) 2.07MPa (300psi), (c) 1.03MPa (150psi).
- Fig.6.10 Shear moduli for 0° graphite-PES specimens cured at (a) 3.45MPa (500psi), (b) 2.07MPa (300psi), (c) 1.03MPa (150psi).

Fig.6.11 Shear strength for 0° graphite-PES specimens cured at (a) 3.45MPa (500psi), (b) 2.07MPa (300psi), (c) 1.03MPa (150psi).

Fig.7.1 (a) Shear stress-strain data from front and back faces, (b) average of front and back shear stress-strain data of the uniweave [0/90]_{7s} specimens.

Fig.7.2 (a) Shear stress-strain data from front and back faces, (b) average of front and back shear stress-strain data of the plain weave [0/90]_{6s} specimens.

Fig.7.3 (a) Shear stress-strain data from front and back faces, (b) average of front and back shear stress-strain data of the plain weave [0/90]_{2s} specimens.

Fig.7.4 (a) Shear stress-strain data from front and back faces, (b) average of front and back shear stress-strain data of the 5HS [0/90]_{4s} specimens.

Fig.7.5 (a) Shear stress-strain data from front and back faces, (b) average of front and back shear stress-strain data of the 8HS [0/90]_{3s} specimens.

Fig.7.6a&b Typical moire fringe patterns of the uniweave [0/90]_{7s} specimen at an applied load of 1312N. (a) u-field, (b) v-field. (c) u-field (half density).

Fig.7.6c&d Typical moire fringe patterns of the uniweave [0/90]_{7s} specimen at an applied load of 1770N. (c) u-field (half density), (d) v-field (half density).

Fig.7.7a&b Typical moire fringe patterns of the plain weave [0/90]_{6s} specimen at an applied load of 854N. (a) u-field, (b) v-field.

Fig.7.7c&d Typical moire fringe patterns of the plain weave [0/90]_{6s} specimen at an applied load of 796N. (c) u-field (half density), (d) v-field (half density).

Fig.7.8a&b Typical moire fringe patterns of the plain weave [0/90]_{2s} specimen at an applied load of 961N. (a) u-field, (b)v-field, (c) u-field (half density).

Fig.7.8c&d Typical moire fringe patterns of the plain weave [0/90]_{2s} specimen at an applied load of 961N. (c) u-field (half density), (d) v-field (half density).

Fig.7.9a&b Typical moire fringe patterns of the 5HS [0/90]_{4s} specimen at an applied load of 1316N. (a) u-field, (b)v-field, (c) u-field (half density).

Fig.7.9c&d Typical moire fringe patterns of the 5HS [0/90]_{4s} specimen at an applied load of 1463N. (c) u-field (half density), (d) v-field (half density).

Fig.7.10a&b Typical moire fringe patterns of the 8HS [0/90]_{3s} specimen at an applied load of 1170N. (a) u-field, (b)v-field, (c) u-field (half density).

Fig.7.10c&d Typical moire fringe patterns of the 8HS [0/90]_{3s} specimen at an applied load of 1601N. (c) u-field (half density), (d) v-field (half density).

Fig.7.11 Supplement moire fringe patterns of the plain weave [0/90]_{2s} specimen at an applied load of 1059N. (a) u-field (half density), (b) v-field (half density).

Fig.7.12 Shear strains across the notches, normalized with respect to the average shear strain, for uniweave [0/90]_{7s} specimens.

- Fig.7.13 Shear strains across the notches, normalized with respect to the average shear strain, for plain weave $[0/90]_{6S}$ specimens.
- Fig.7.14 Shear strains across the notches, normalized with respect to the average shear strain, for plain weave $[0/90]_{2S}$ specimens.
- Fig.7.15 Shear strains across the notches, normalized with respect to the average shear strain, for 5HS $[0/90]_{4S}$ specimens.
- Fig.7.16 Shear strains across the notches, normalized with respect to the average shear strain, for 8HS $[0/90]_{3S}$ specimens.
- Fig.7.17 Strain vs. stress for typical epoxy based aluminum particulate composite specimen. Gages are aligned at $\pm 45^\circ$ and 0° directions.
- Fig.7.18 Average of front and back shear stress-strain data of epoxy based aluminum particulate composite specimens.
- Fig.7.19 Moire fringe patterns of the epoxy based aluminum particulate composite specimen at an applied load of 476N. (a) u-field, (b) v-field.
- Fig.7.20 Shear strains across the notches, normalized with respect to the average shear strain, for epoxy-based aluminum particulate composite.
- Fig.7.21 Failed specimen configuration for epoxy based aluminum particulate composite specimen.
- Fig.8.1 Dimensions of 3" U-notch Iosipescu specimen.
- Fig.8.2 Finite element mesh for 3" U-notch specimen.
- Fig.8.3 Finite element models for 3" U-notch Iosipescu specimen tested in modified Wyoming fixture, (a) 0° specimen, (b) 90° specimen, (c) $0^\circ/90^\circ$ specimen.
- Fig.8.4 Distributed loads on the specimen sides due to imposition of uniform displacement for (a) 0° , (b) 90° , (c) $0^\circ/90^\circ$ 3" U-notch specimens.
- Fig.8.5 Shear strains, normalized with respect to average γ_{xy} , along the notch axis for (a) 0° , (b) 90° , (c) $0^\circ/90^\circ$ graphite-epoxy 3" U-notch specimens.
- Fig.8.6 (a) ϵ_x , (b) ϵ_y , (c) γ_{xy} strain contours, obtained from finite element analysis, for 3" U-notch 0° graphite-epoxy Iosipescu specimens.
- Fig.8.7 (a) ϵ_x , (b) ϵ_y , (c) γ_{xy} strain contours, obtained from finite element analysis, for 3" U-notch 90° graphite-epoxy Iosipescu specimens.
- Fig.8.8 (a) ϵ_x , (b) ϵ_y , (c) γ_{xy} strain contours, obtained from finite element analysis, for 3" U-notch $0^\circ/90^\circ$ graphite-epoxy Iosipescu specimens.
- Fig.8.9 Shear stress-strain data and failure modes for typical 3" U-notch 0° , 90° and $0^\circ/90^\circ$ graphite-epoxy specimens.

- Fig.8.10 Strain vs. stress for typical 3" U-notch (a) 0°, (b) 90°, (c) 0°/90° graphite-epoxy specimen. Gages are aligned at $\pm 45^\circ$ and 0° directions.
- Fig.8.11a&b Typical moire fringe patterns of the 3" 0° U-notch specimen at an applied load of 214N. (a) u-field, (b)v-field.
- Fig.8.11c&d Typical moire fringe patterns of the 3" 0° U-notch specimen at an applied load of 1094N. (c) u-field (half density), (d) v-field (half density).
- Fig.8.12a&b Typical moire fringe patterns of the 3" 90° U-notch specimen at an applied load of 640N. (a) u-field, (b)v-field.
- Fig.8.13a&b Typical moire fringe patterns of the 3" 0°/90° U-notch specimen at an applied load of 382N. (a) u-field, (b)v-field.
- Fig.8.13c&d Typical moire fringe patterns of the 3" 0°/90° U-notch specimen at an applied load of 1748N. (c) u-field (half density), (d) v-field (half density).
- Fig.8.14 Shear strain distribution, normalized with respect to the average shear strain, across the notches for (a) 0°, (b) 90°, (c) 0°/90° 3" U-notch Iosipescu specimens.
- Fig.8.15 Finite element mesh for 2" U-notch specimen.
- Fig.8.16 Finite element models for 2" U-notch Iosipescu specimen tested in modified Wyoming fixture, (a) 0° specimen, (b) 90° specimen, (c) 0°/90° specimen.
- Fig.8.17 Distributed loads on the specimen sides due to imposition of uniform displacement for (a) 0°, (b) 90°, (c) 0°/90° 2" U-notch specimens.
- Fig.8.18 Shear strains, normalized with respect to average γ_{xy} , along the notch axis for (a) 0°, (b) 90°, (c) 0°/90° graphite-epoxy 2" U-notch specimens.
- Fig.8.19 (a) ϵ_x , (b) ϵ_y , (c) γ_{xy} strain contours, obtained from finite element analysis, for 2" U-notch 0° graphite-epoxy Iosipescu specimens.
- Fig.8.20 (a) ϵ_x , (b) ϵ_y , (c) γ_{xy} strain contours, obtained from finite element analysis, for 2" U-notch 90° graphite-epoxy Iosipescu specimens.
- Fig.8.21 (a) ϵ_x , (b) ϵ_y , (c) γ_{xy} strain contours, obtained from finite element analysis, for 2" U-notch 0°/90° graphite-epoxy Iosipescu specimens.
- Fig.8.22 Shear stress-strain data and failure modes for typical 2" U-notch 0°, 90° and 0°/90° graphite-epoxy specimens.
- Fig.8.23 Strain vs. stress for typical 2" U-notch (a) 0°, (b) 90°, (c) 0°/90° graphite-epoxy specimen. Gages are aligned at $\pm 45^\circ$ and 0° directions.
- Fig.8.24 Typical moire fringe patterns of the 2" 0° U-notch specimen at an applied load of 1099N. (a) u-field (half density), (b) v-field (half density).
- Fig.8.25 Typical moire fringe patterns of the 2" 90° U-notch specimen at an applied load of 1050N. (a) u-field (half density), (b) v-field (half density).

- Fig.8.26 Typical moire fringe patterns of the 2" $0^{\circ}/90^{\circ}$ U-notch specimen at an applied load of 1005N. (a) u-field (half density), (b) v-field (half density).
- Fig.8.27 Shear strain distribution, normalized with respect to the average shear strain, across the notches for (a) 0° , (b) 90° , (c) $0^{\circ}/90^{\circ}$ 2" U-notch Iosipescu specimens.
- Fig.8.28 Typical moire fringe patterns of the 3" $0^{\circ}/90^{\circ}$ V-notch AS4/APC-2 specimen at an applied load of 1410N. (a) u-field (half density), (b) v-field (half density).
- Fig.8.29 Typical moire fringe patterns of the 3" $0^{\circ}/90^{\circ}$ U-notch AS4/APC-2 specimen at an applied load of 2535N. (a) u-field (half density), (b) v-field (half density).

TABLES AND FIGURES

Table 4.1 Mechanical property for numerical analysis.

Material*	E_{11}/E_{22}	G_{12} (GPa)	ν_{12}
epoxy	1.00	1.11**	0.35
steel	1.00	116.28**	0.29
glass-epoxy	4.67	4.14	0.26
Kevlar-epoxy	13.6	2.30	0.34
graphite-epoxy	15.4	7.10	0.30

* - Data were obtained from Tsai[28].

** - Calculated using $G = E/2(1 + \nu)$

Table 7.1 Fabric architecture.

Panel Number	Layup	Weave Designation	Weave Architecture Warp yarns/in x Fill yarns/in	Yarn Description	Fiber Volume Fraction (%)
110190	[0/90] _{7s}	Uniweave*	18	3k AS4	55.4
101890	[0/90] _{6s}	Plain Weave	12.5 x 12.5	3k Celion	55.5
092790	[0/90] _{2s}	Plain Weave	7.5 x 7.5	12k AS4	52.2
112590	[0/90] _{4s}	5 Harness Satin	18.0 x 18.0	3k Celion	59.6
100290	[0/90] _{3s}	8 Harness Satin	24.0 x 24.0	3k Celion	51.0

* Uniweave - Approximately 97 % of the yarns are oriented in warp direction.
A fine denier glass yarn is used in fill direction, 8 yarns/in.

Table 7.2 Averaged in-plane shear moduli and shear strengths for woven fabric composite materials.

Panel Number	Avg. G_{12} (GPa)	G_{12} Standard Deviation(GPa)	Avg. S_{12} (MPa)	S_{12} Standard Deviation(MPa)	Normalized G_{12} (GPa) (vf=51%)
110190	5.33	0.174	136.20	9.99	4.91
101890	4.96	0.251	140.64	4.11	4.56
092790	4.05	0.343	100.04	2.60	3.96
112590	4.69	0.181	141.59	2.71	4.01
100290	4.23	0.058	125.65	3.74	4.23

Table 8.1 Measured in-plane shear moduli from AS4/3501-6 notched Iosipescu specimen.

	Average G_{12} * (GPa/Msi)	Standard deviation (GPa/Msi)	Correction factor (from FEA)	Correction factor (from one moire experiment)	G_{12} * x C.F. (from FEA)
3" V-notch specimen					
0°	5.016 / 0.727	0.241 / 0.035	0.87	0.91	4.364
90°	4.068 / 0.590	0.069 / 0.001	1.19	1.19	4.841
0°/90°	4.254 / 0.617	0.143 / 0.021	1.03	1.13	4.382
3" U-notch specimen					
0°	4.568 / 0.662	0.142 / 0.021	0.92	0.92	4.203
90°	3.620 / 0.525	0.077 / 0.013	1.25	1.25	4.525
0°/90°	4.158 / 0.603	0.032 / 0.006	1.08	1.11	4.491
2" U-notch specimen					
0°	5.316 / 0.771	0.198 / 0.029	0.87	0.92	4.625
90°	4.043 / 0.586	0.126 / 0.018	1.25	1.18	5.054
0°/90°	4.654 / 0.675	0.146 / 0.021	1.07	1.03	4.980

Table 8.2 Measured in-plane shear strengths from AS4/3501-6 notched Iosipescu specimens.

	Average S_{12} (MPa/ksi)	Standard deviation (MPa/ksi)
3" V-notch specimen		
0°	71.22 / 10.33	4.21 / 0.61
90°	36.54 / 5.30	7.63 / 1.11
0°/90°	78.95 / 11.45	4.83 / 0.70
3" U-notch specimen		
0°	86.36 / 12.52	8.02 / 1.16
90°	43.67 / 6.33	3.97 / 0.58
0°/90°	134.91 / 19.57	4.89 / 0.71
2" U-notch specimen		
0°	60.45 / 8.77	7.25 / 1.05
90°	37.70 / 5.47	8.88 / 1.29
0°/90°	87.39 / 12.68	1.32 / 0.19

Table 8.3 Averaged in-plane shear moduli from AS4/APC-2 notched Iosipescu specimen.

AS4/APC-2 0°/90° specimen	Average G_{12} * (GPa/Msi)	Standard deviation s* (GPa/Msi)
3" V-notch	4.995 / 0.724	0.249 / 0.036
3" U-notch	5.019 / 0.728	0.189 / 0.027
2" U-notch	5.075 / 0.736	0.138 / 0.020

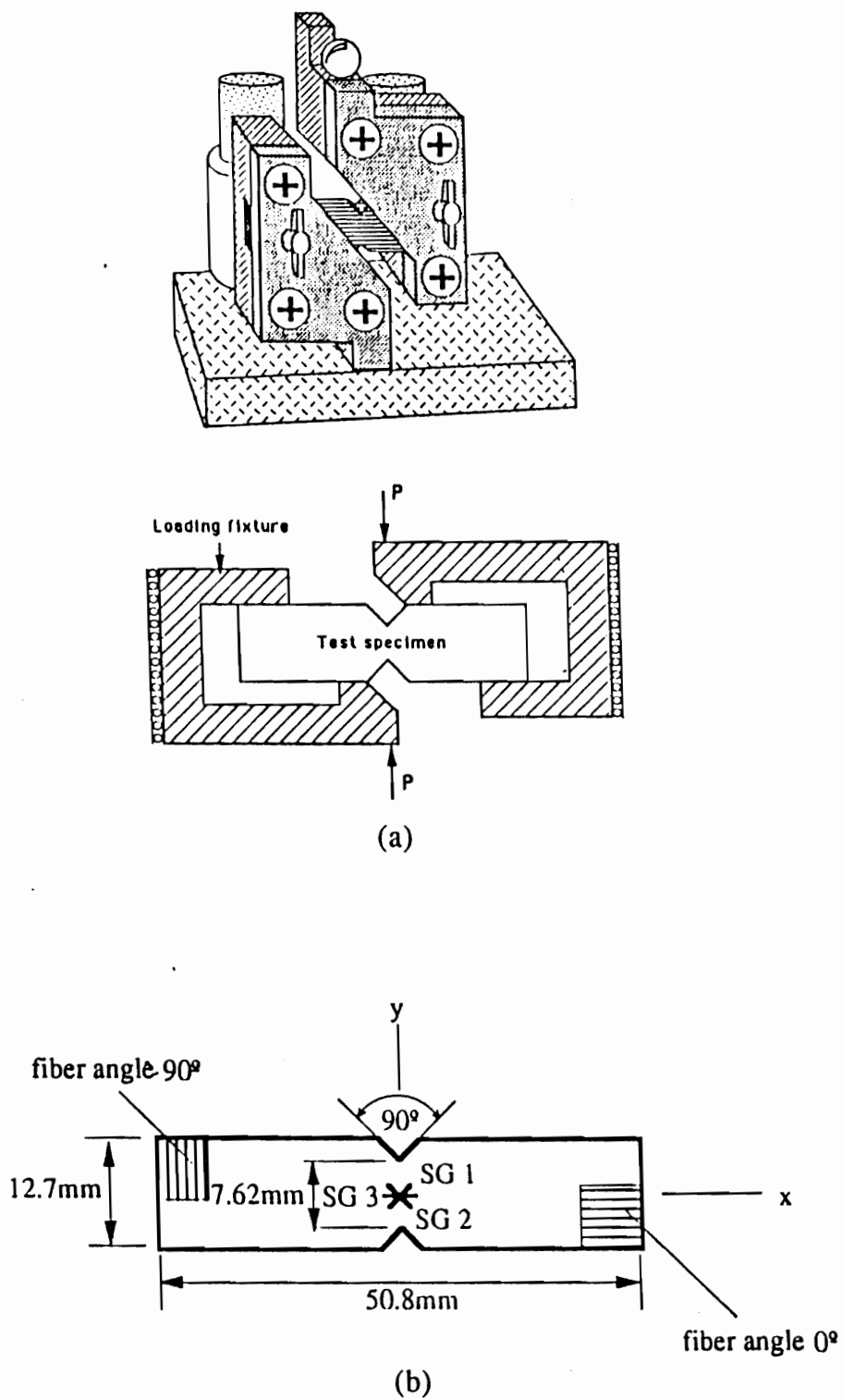


Fig.1.1 (a) Wyoming fixture (W1) and (b) original Iosipescu specimen.

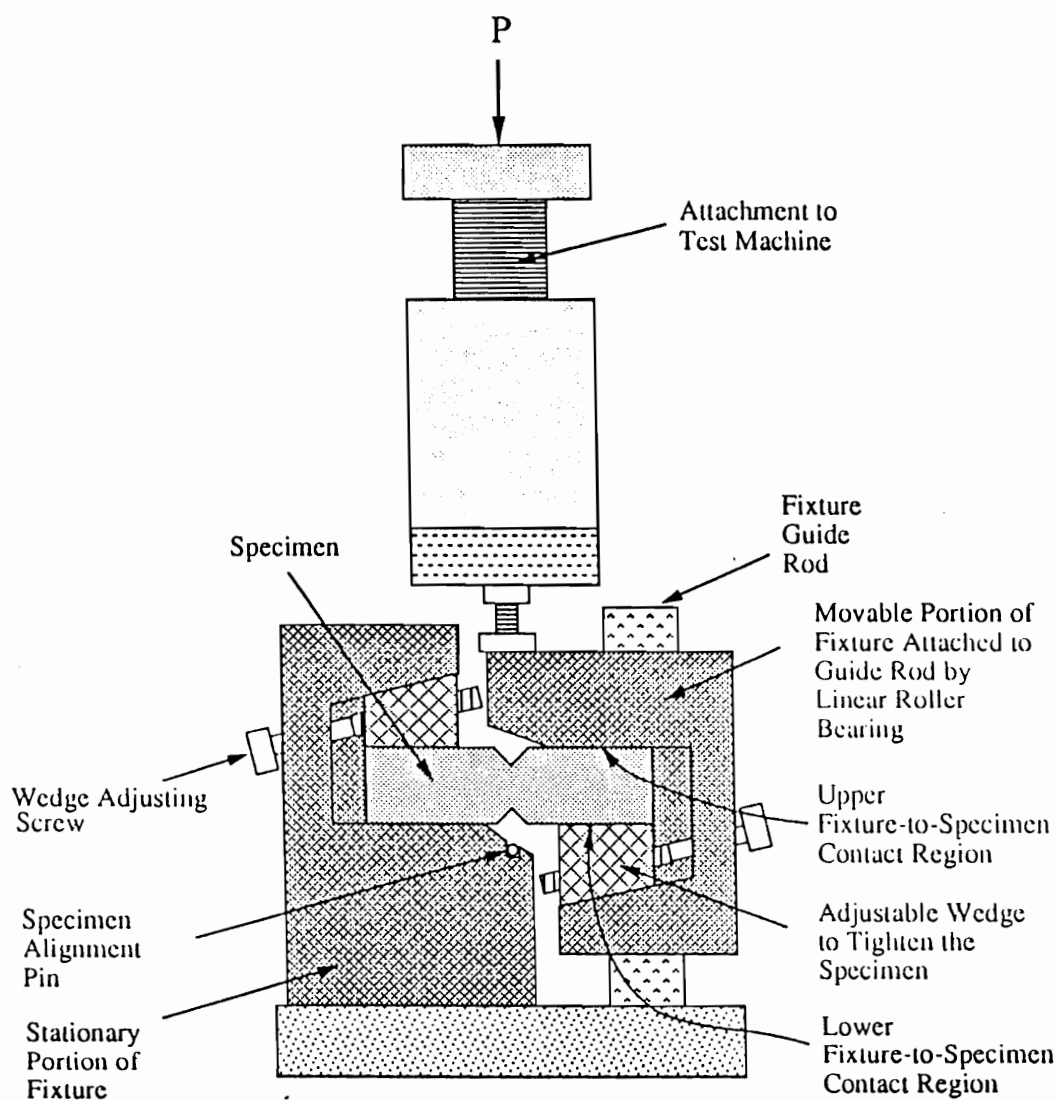


Fig.1.2a Modified Wyoming fixture (W2).

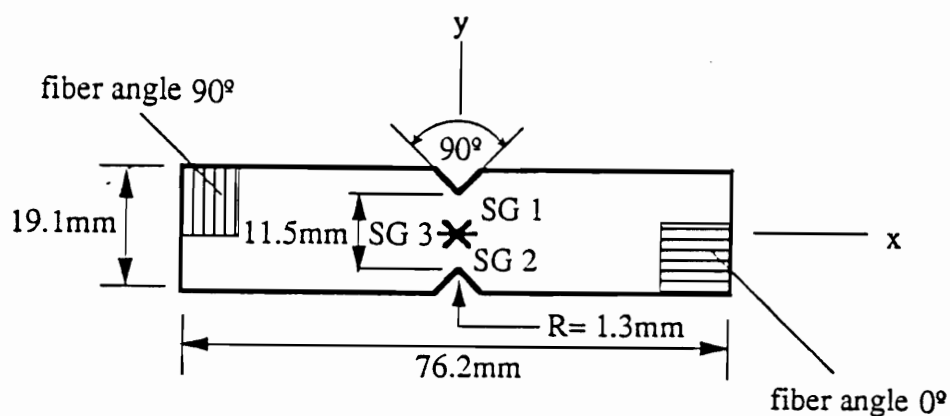
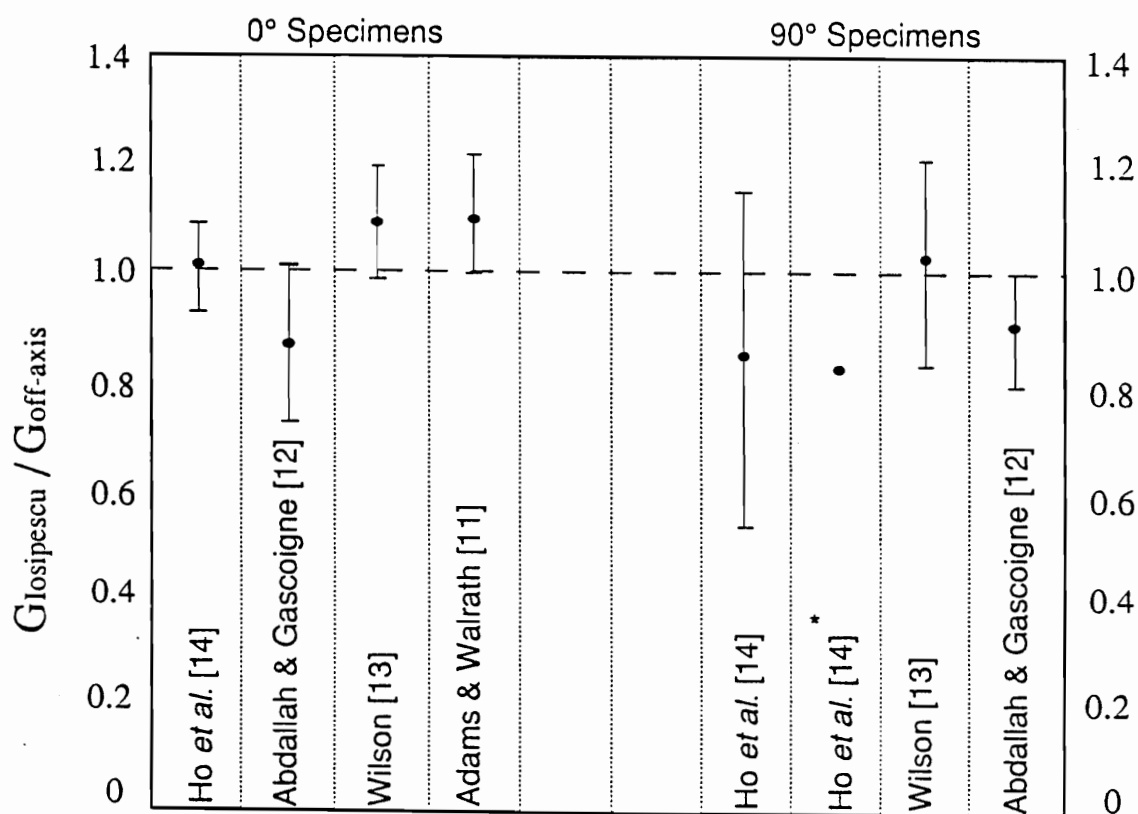


Fig.1.2b Modified Iosipescu specimen.



* Average of front and back shear moduli

Fig.1.3 Normalized values of in-plane shear moduli obtained from Iosipescu shear test on AS4/3501-6. Values are normalized with respect to $G^*_{12} = 5.12$ GPa, the average obtained from $\pm 45^\circ$ tension and 10° off-axis tests [14]. The ranges shown in the figure are moduli of repeatability [13] or denote one standard deviation.

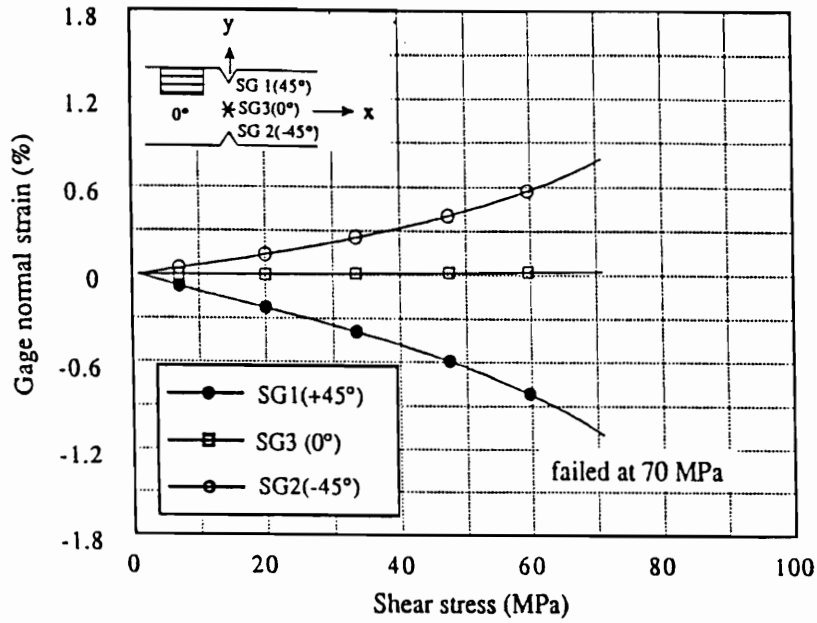


Fig.2.1a Strain vs. stress for typical 0° graphite-epoxy specimen. Gages are aligned at $\pm 45^\circ$ and 0° directions.

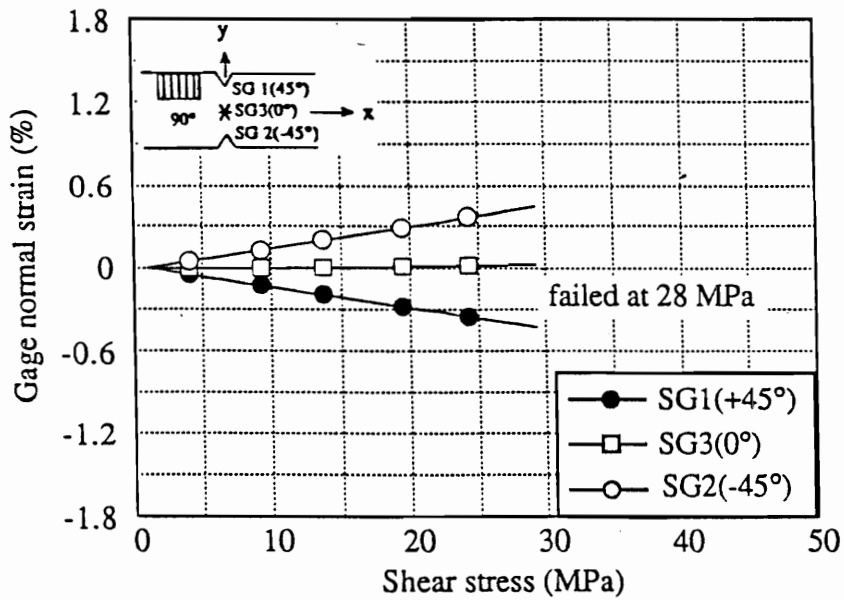


Fig.2.1b Strain vs. stress for typical 90° graphite-epoxy specimen. Gages are aligned at $\pm 45^\circ$ and 0° directions.

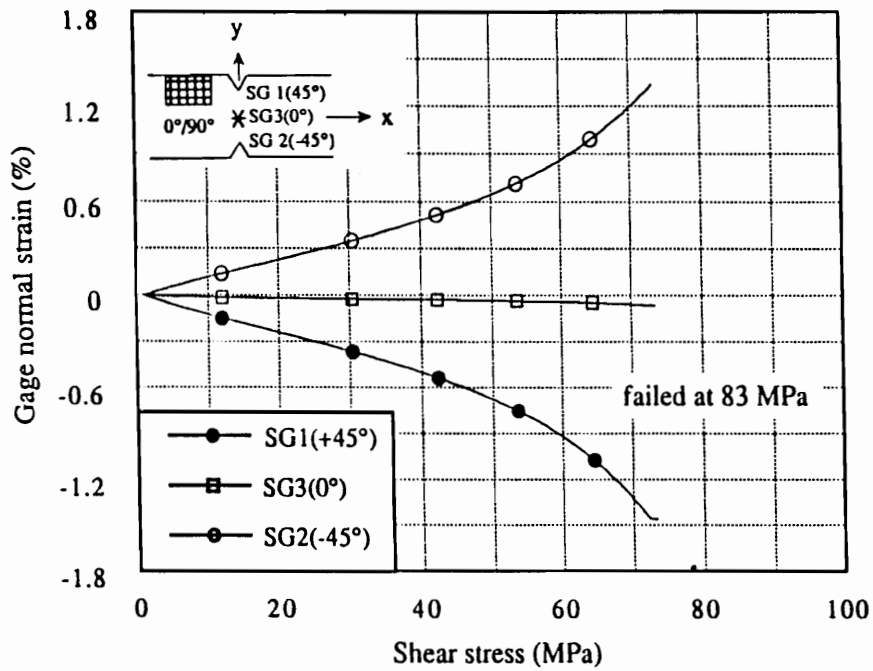


Fig.2.1c Strain vs. stress for typical $0^\circ/90^\circ$ graphite-epoxy specimen. Gages are aligned at $\pm 45^\circ$ and 0° directions.

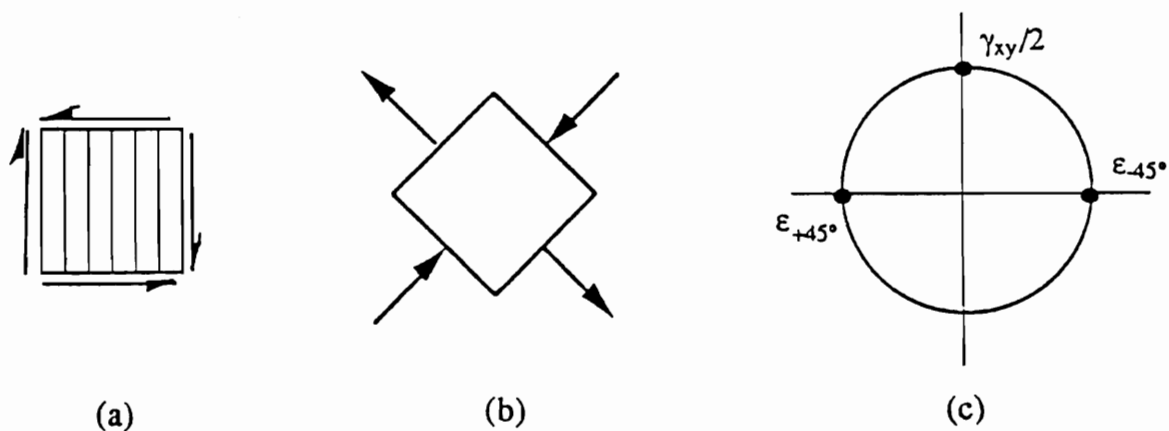


Fig.2.2 Schematic diagram of pure shear (a) in x-y coordinate, (b) in principal direction and (c) Mohr's circle representation.

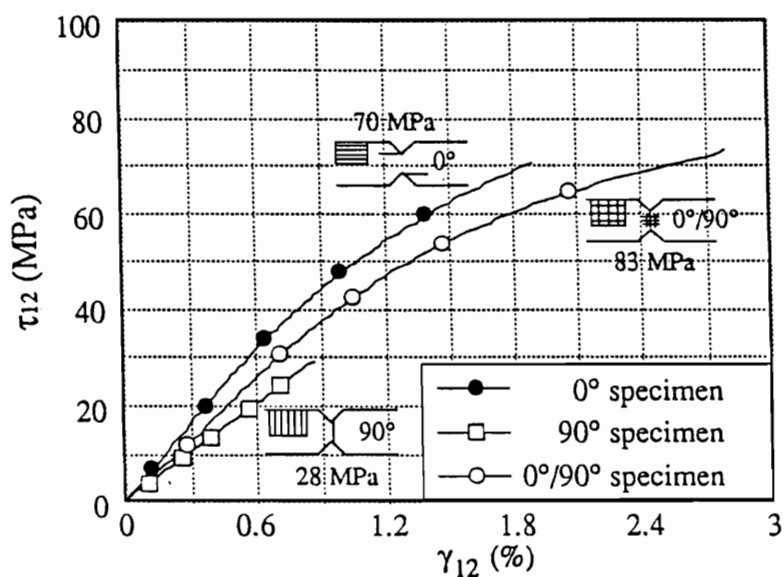
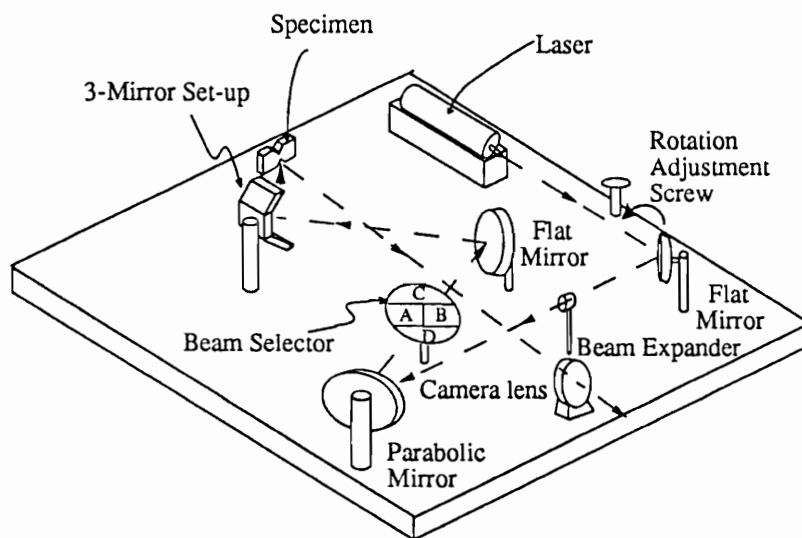
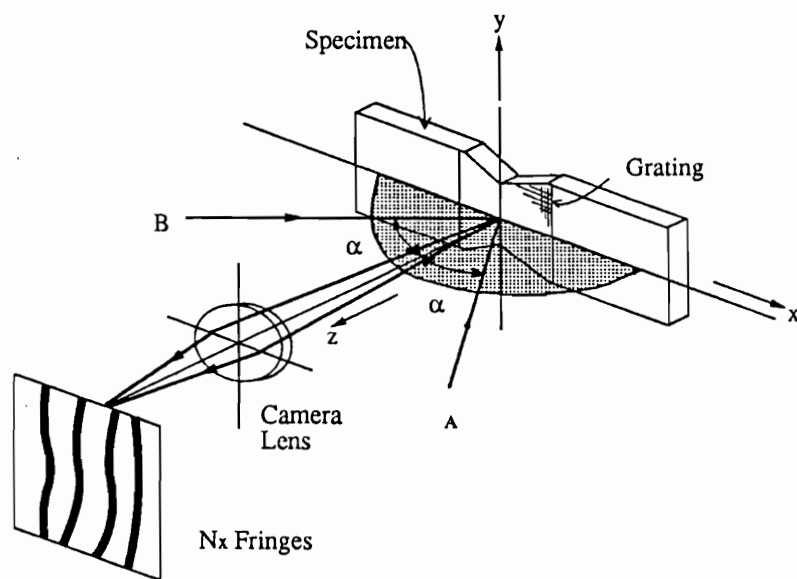


Fig.2.3 Shear stress-strain data and failure modes for typical 0° , 90° and $0^\circ/90^\circ$ graphite-epoxy specimens.

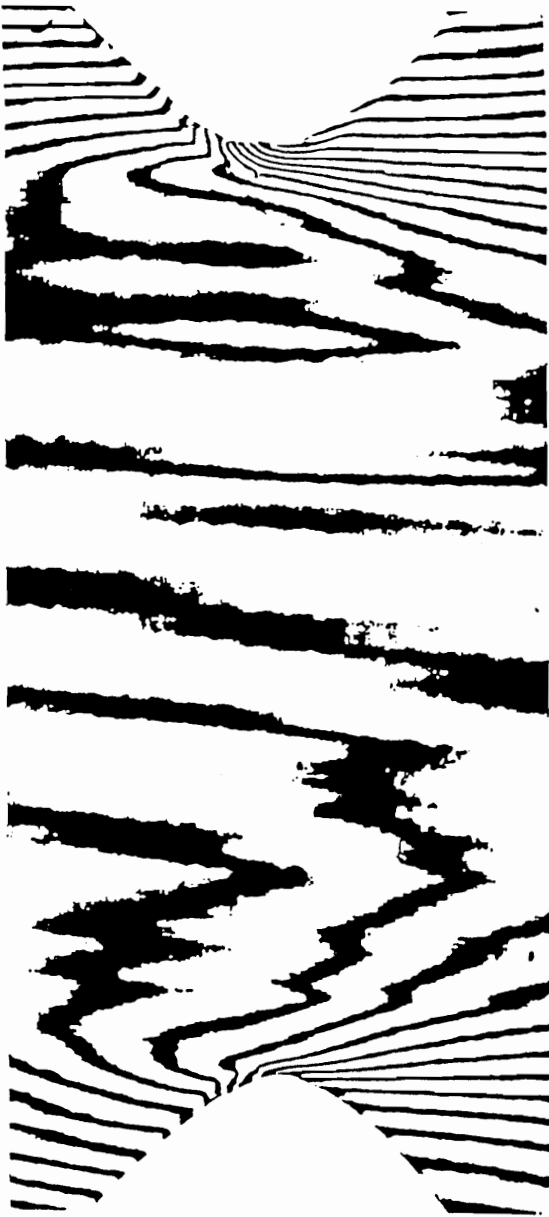


(a)

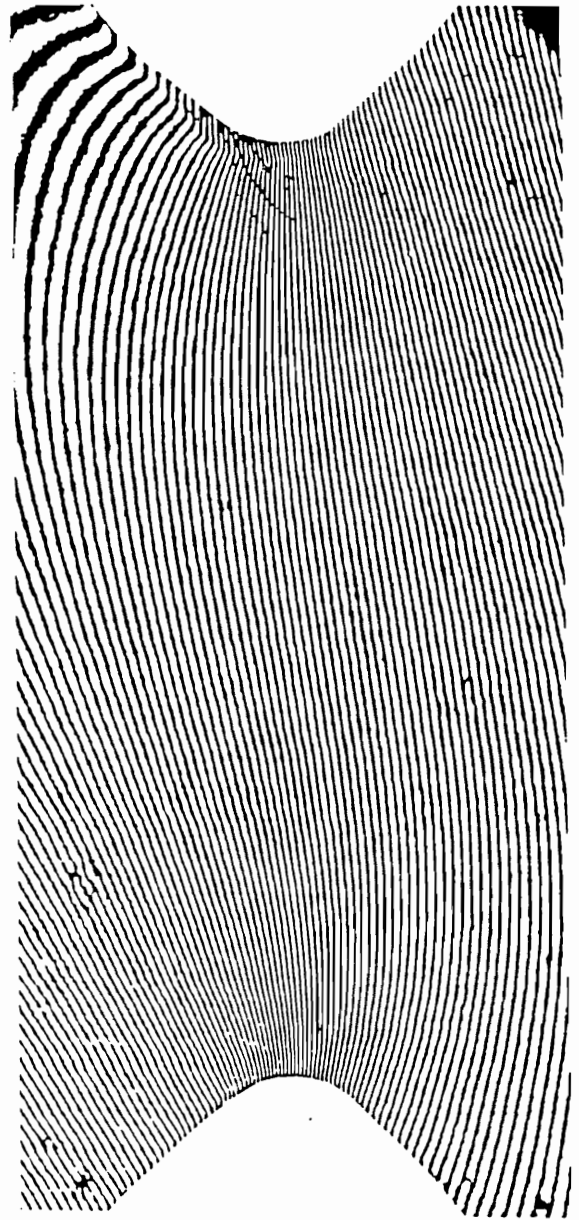


(b)

Fig.3.1 (a) optical set-up of moiré interferometry, (b) Two-beam interferometry.



(a)



(b)

Fig.3.2 (a) u-field, (b) v-field moiré fringe patterns for the 0° graphite-epoxy Iosipescu specimen at an applied load of 667 N.

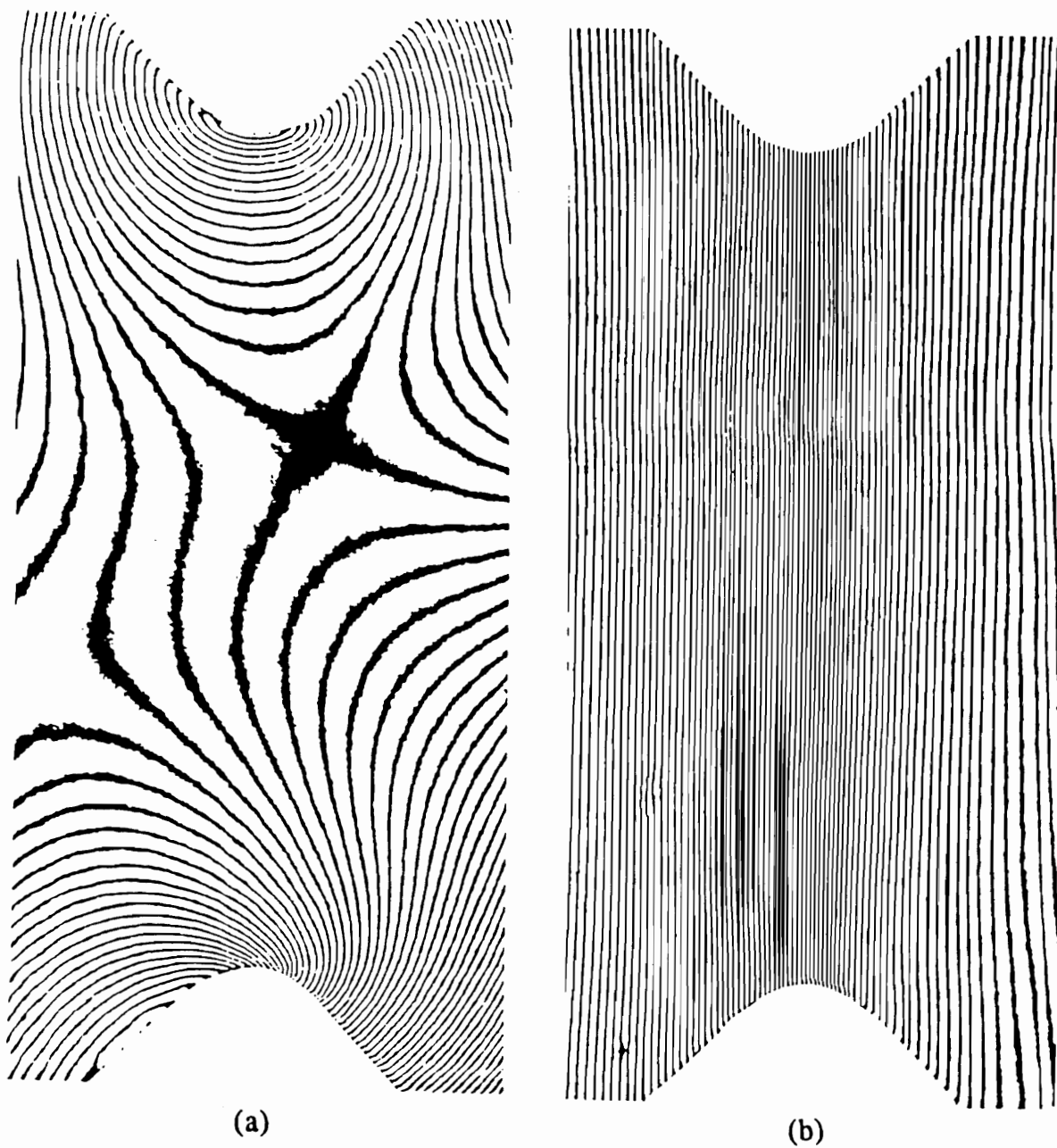


Fig.3.3 (a) u-field, (b) v-field moiré fringe patterns for the 90° graphite-epoxy Iosipescu specimen at an applied load of 1112 N.

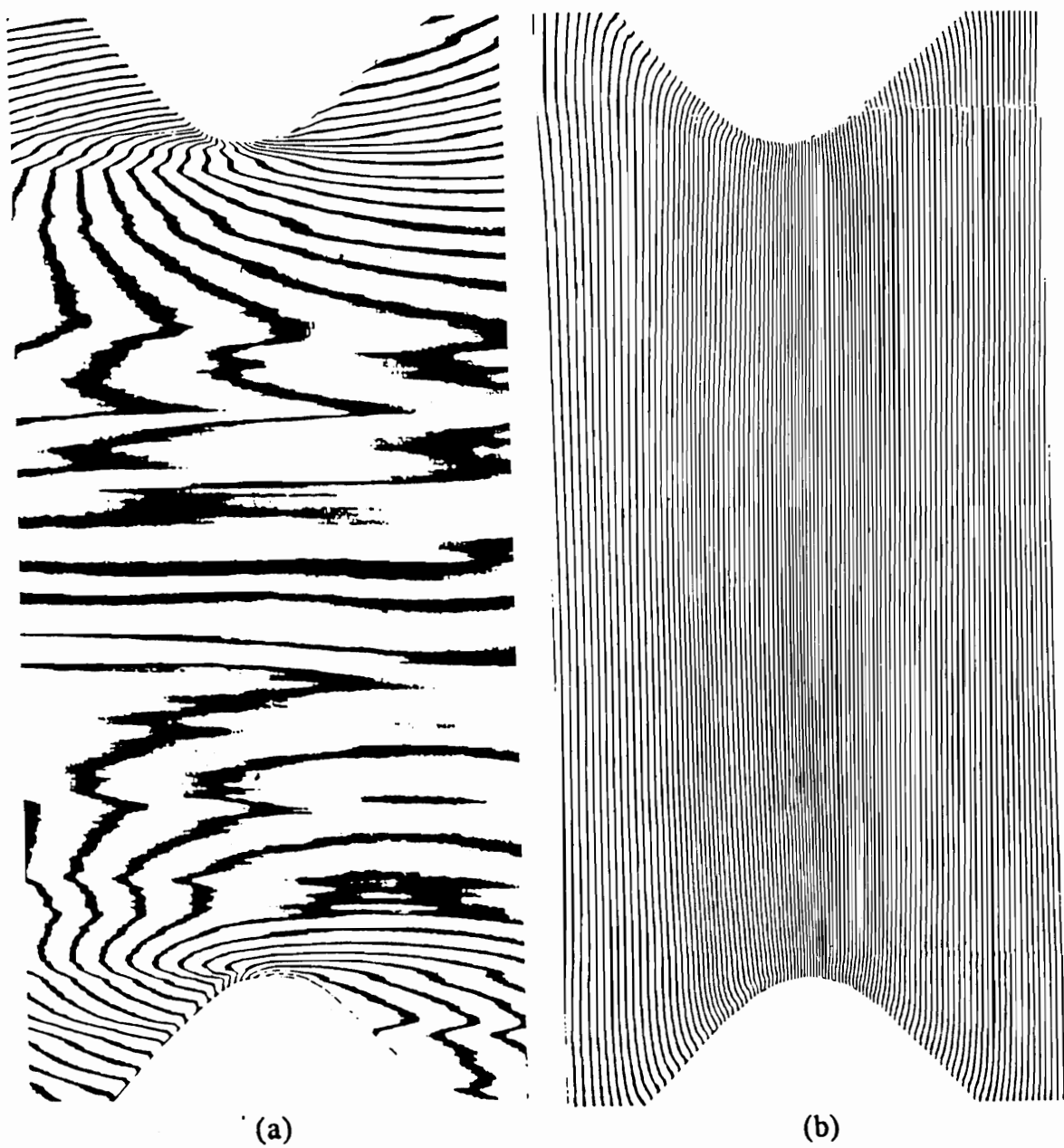


Fig.3.4 (a) u-field, (b) v-field moiré fringe patterns for the $0^{\circ}/90^{\circ}$ graphite-epoxy Iosipescu specimen at an applied load of 1334 N.

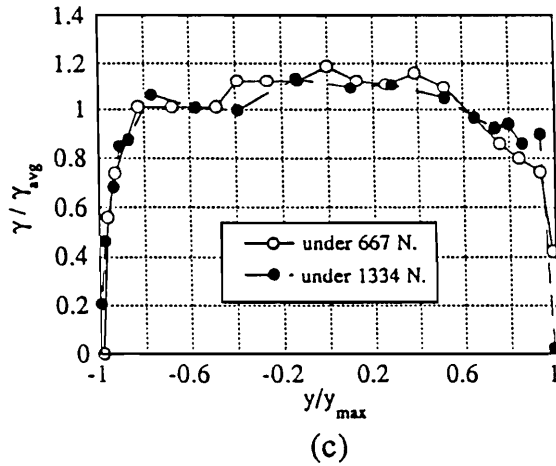
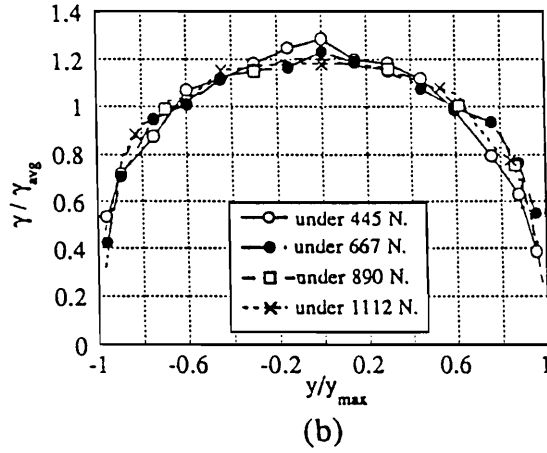
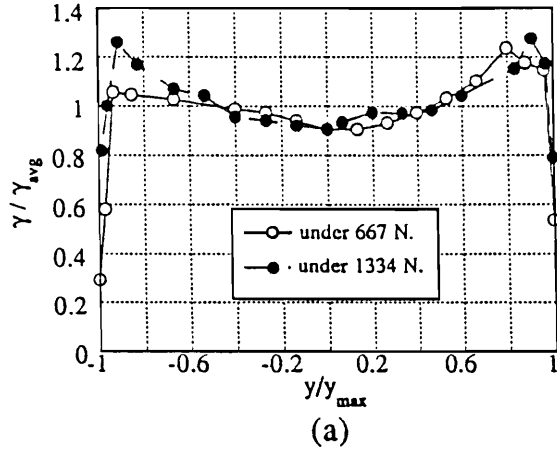


Fig.3.5 Normalized shear strain distributions across the notches obtained from manual data reduction of moiré fringe patterns for (a) 0° , (b) 90° , (c) $0^\circ/90^\circ$ graphite-epoxy Iosipescu specimens.

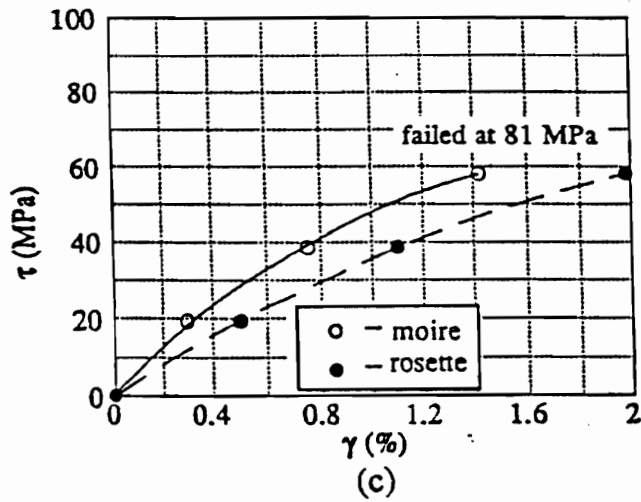
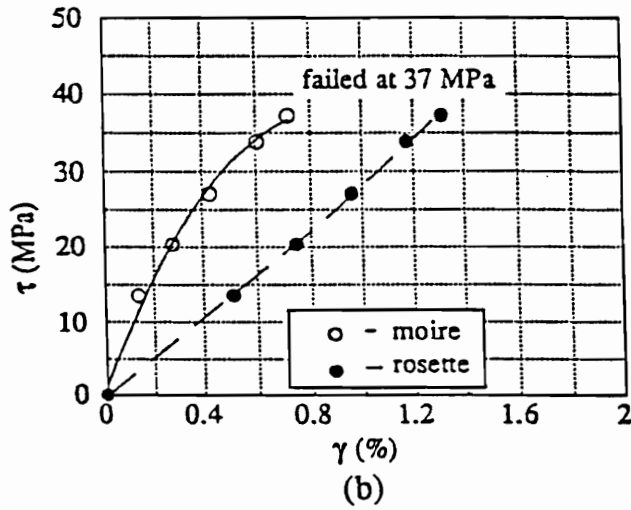
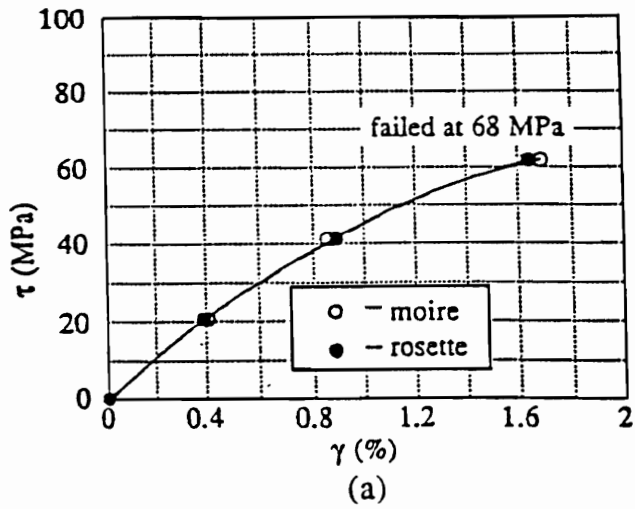


Fig.3.6 Shear stress-strain data obtained from moiré (front face) and gages (back face) for (a) 0°, (b) 90°, (c) 0°/90° graphite-epoxy Iosipescu specimens.

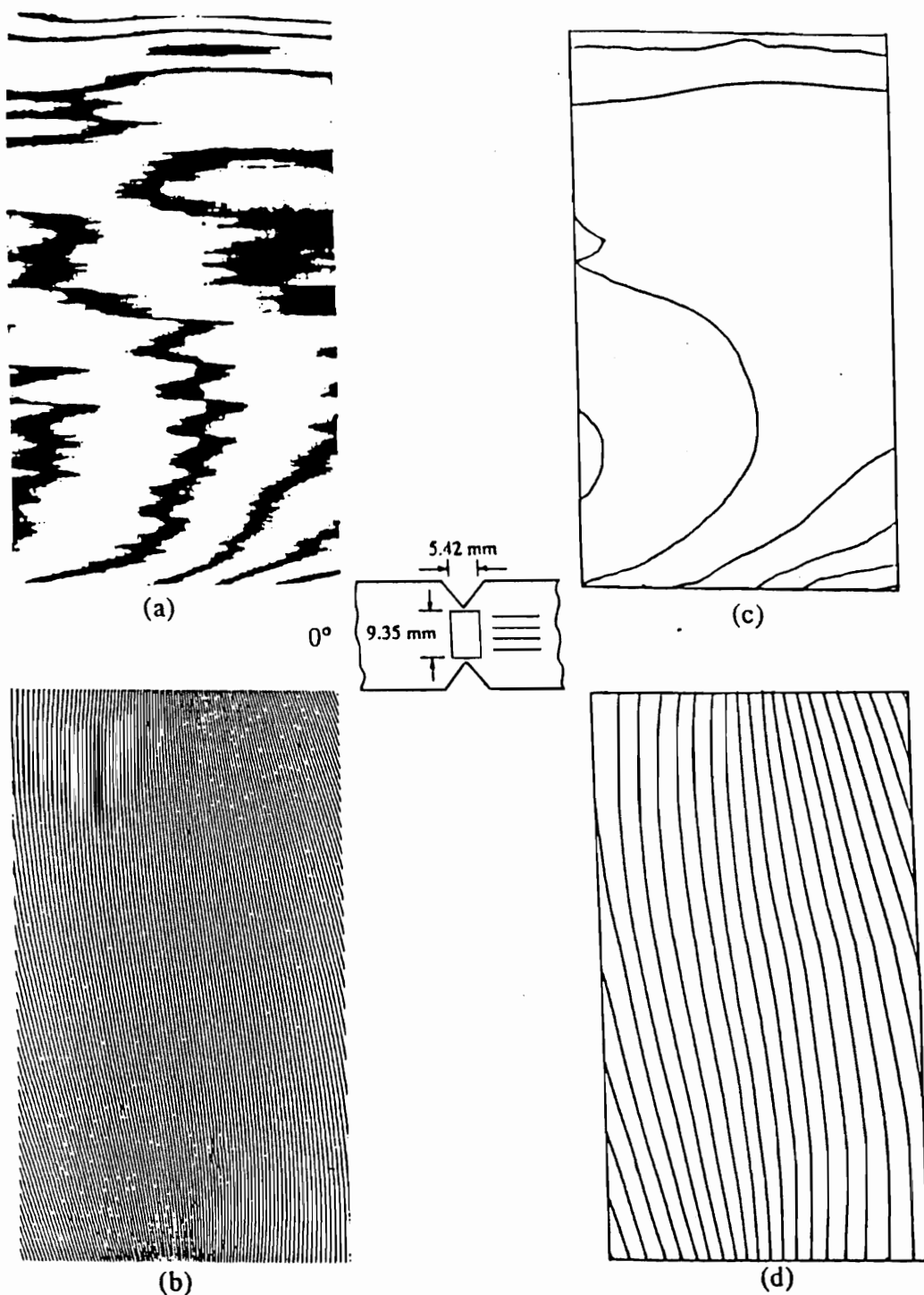


Fig.3.7 Moiré fringe patterns for (a) u-displacement field, (b) v-displacement field. Reproduced fringe patterns for (c) u-displacement field, (d) v-displacement field (showing every 5th fringe) from the localized hybrid analysis. The data correspond to the 0° specimen at an applied load of 1334N.

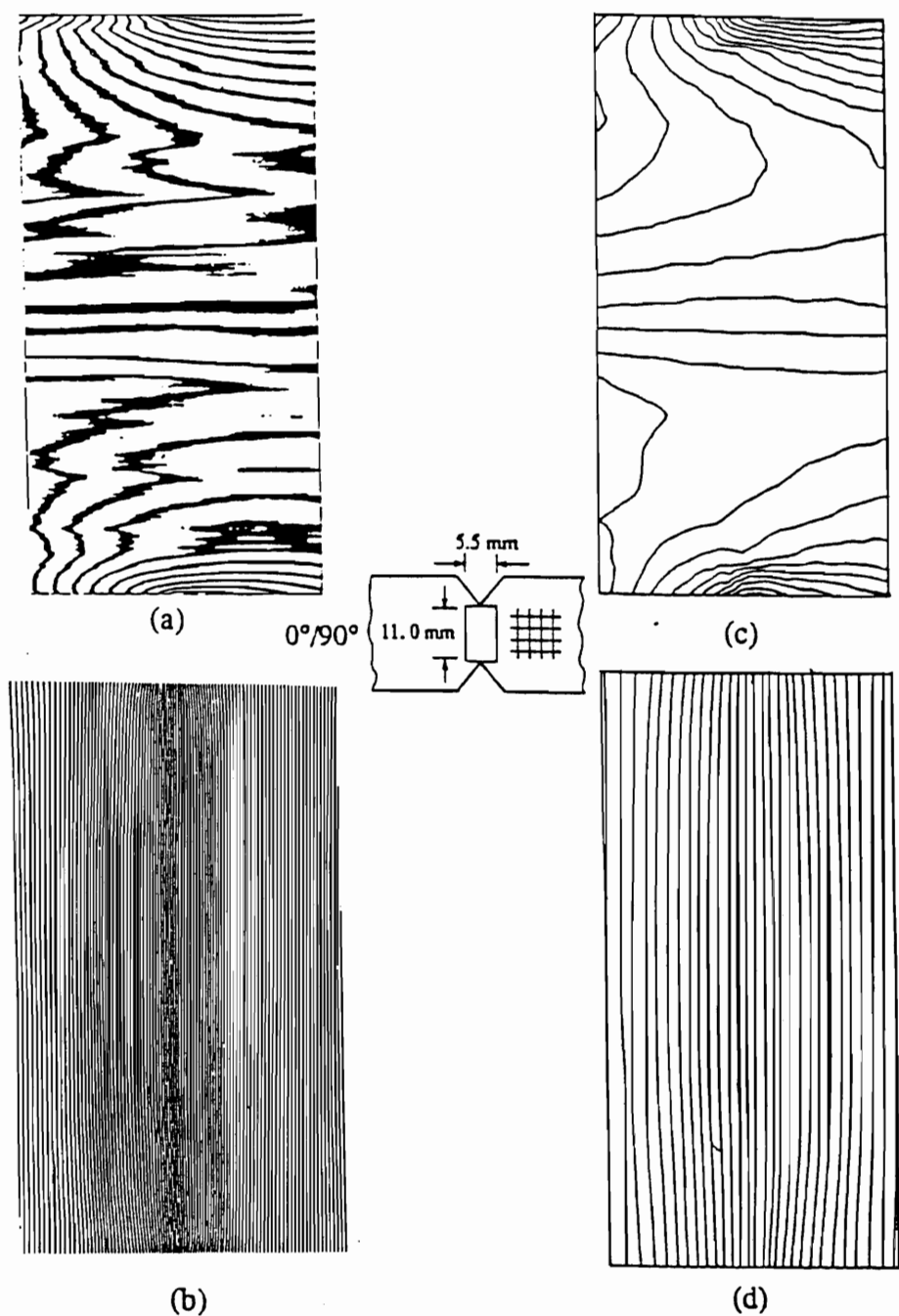


Fig.3.8 Moiré fringe patterns for (a) u-displacement field, (b) v-displacement field. Reproduced fringe patterns for (c) u-displacement field, (d) v-displacement field (showing every 5th fringe) from the localized hybrid analysis. The data correspond to the $0^\circ/90^\circ$ specimen at an applied load of 1334N.

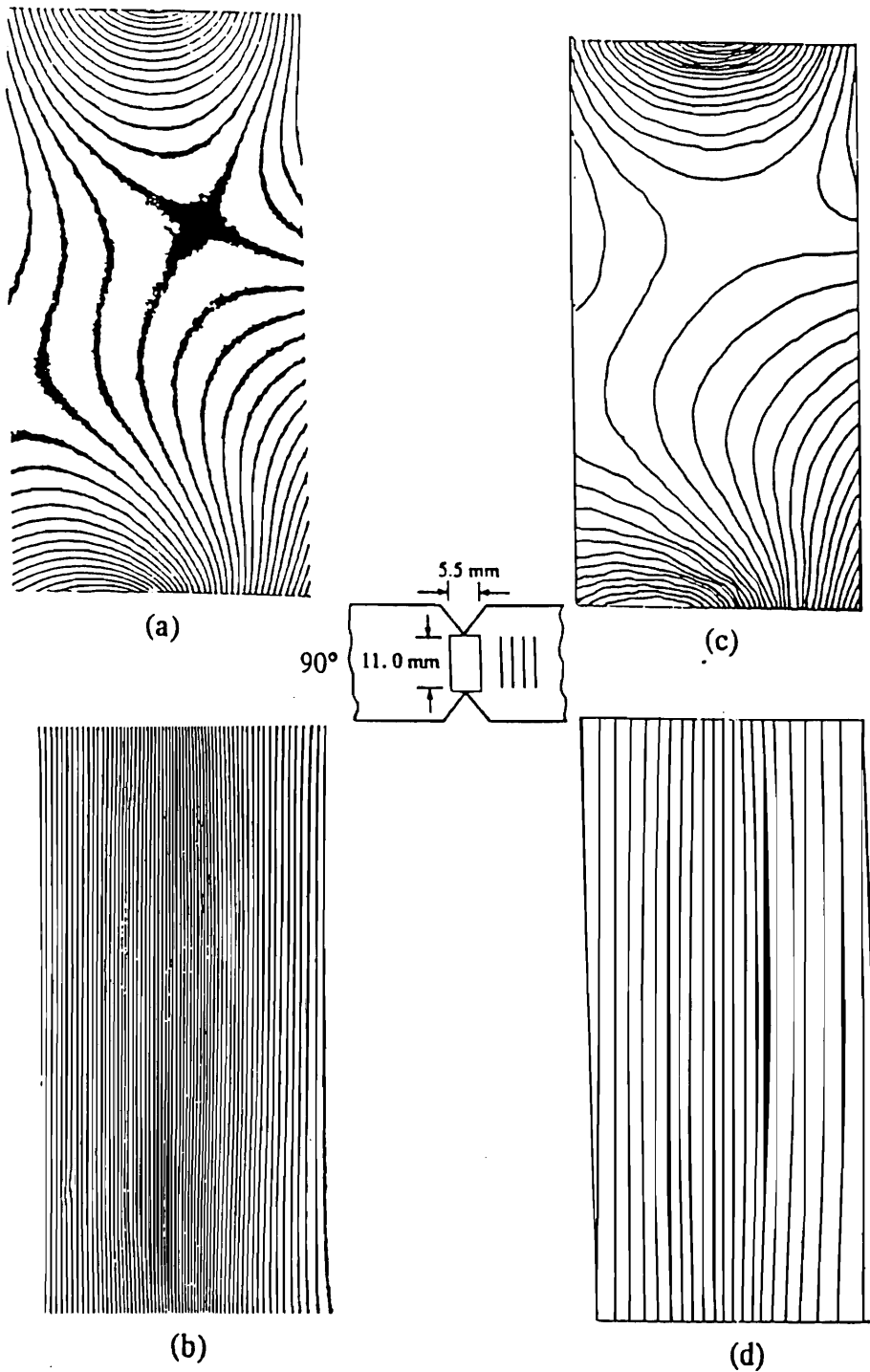


Fig.3.9 Moiré fringe patterns for (a) u-displacement field, (b) v-displacement field. Reproduced fringe patterns for (c) u-displacement field, (d) v-displacement field (showing every 3rd fringe) from the localized hybrid analysis. The data correspond to the 90° specimen at an applied load of 1112N.

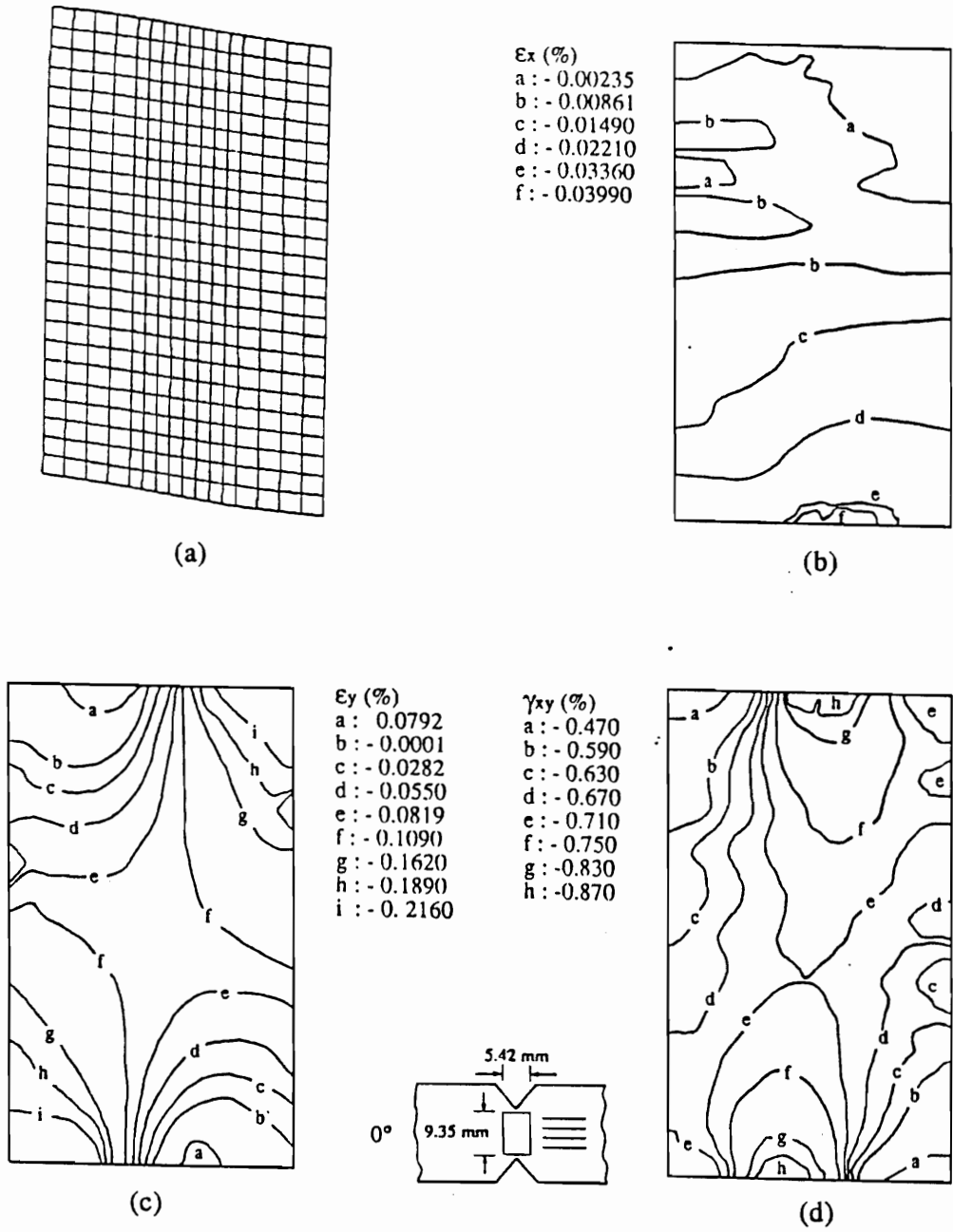


Fig.3.10 (a) Deformed shape, contours of (b) ϵ_x , (c) ϵ_y , (d) γ_{xy} obtained from a localized hybrid analysis of a 0° specimen at an applied load of 1334N

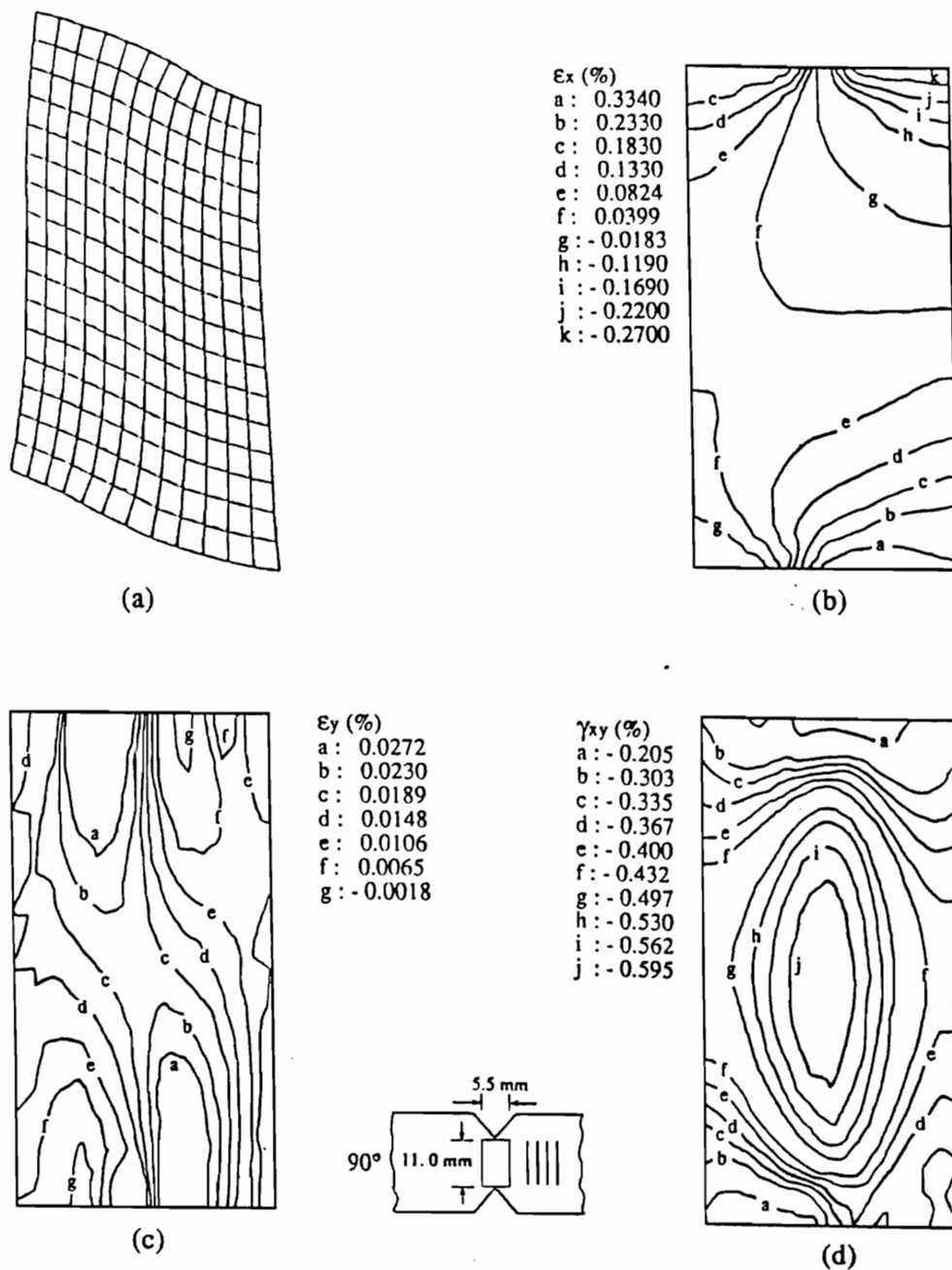


Fig.3.11 (a) Deformed shape, contours of (b) ϵ_x , (c) ϵ_y , (d) γ_{xy} obtained from a localized hybrid analysis of a 90° specimen at an applied load of 1112N

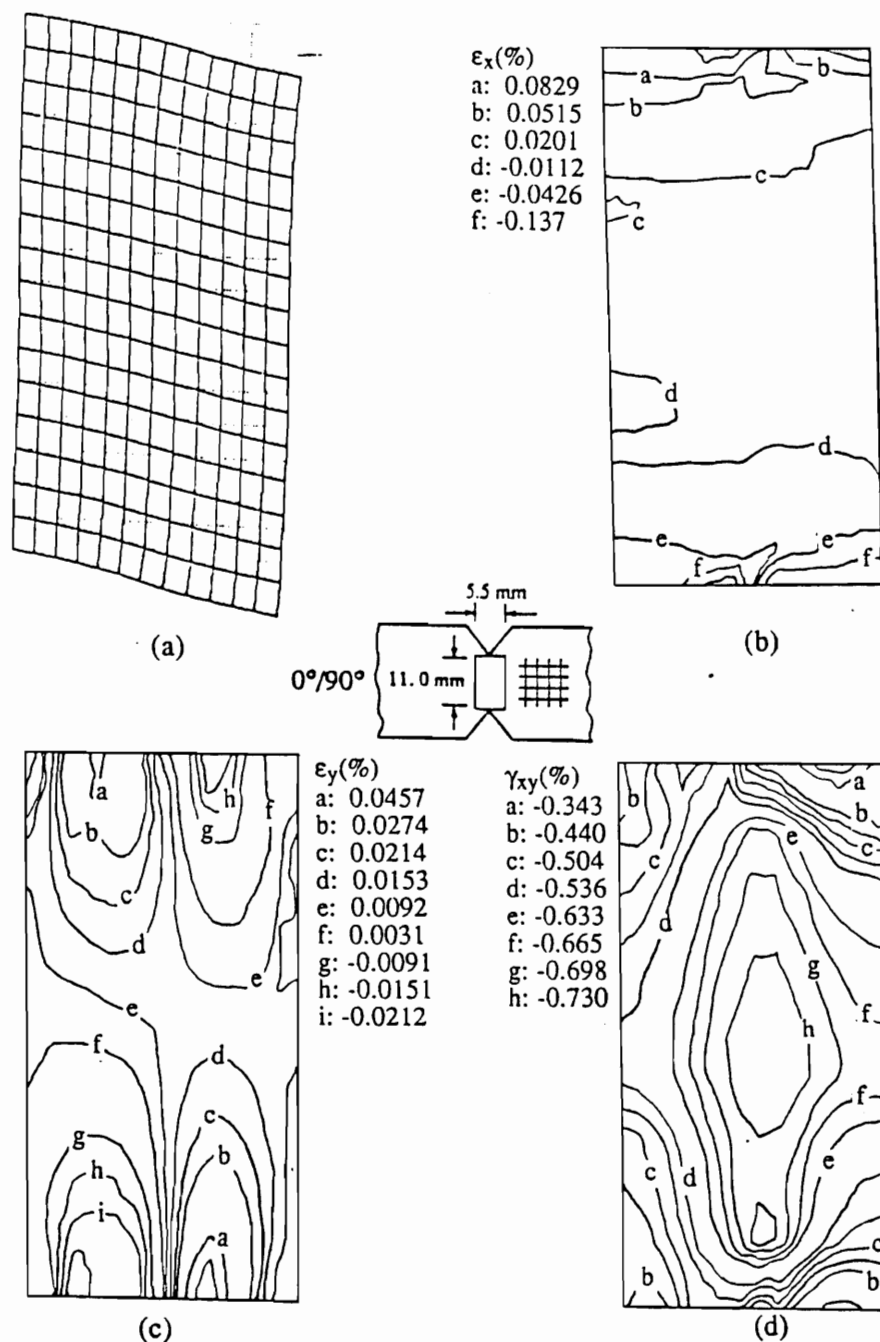


Fig.3.12 (a) Deformed shape, contours of (b) ϵ_x , (c) ϵ_y , (d) γ_{xy} obtained from a localized hybrid analysis of a 0°/90° specimen at an applied load of 1334N

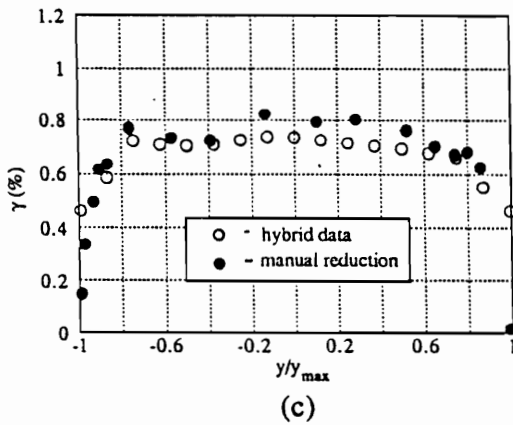
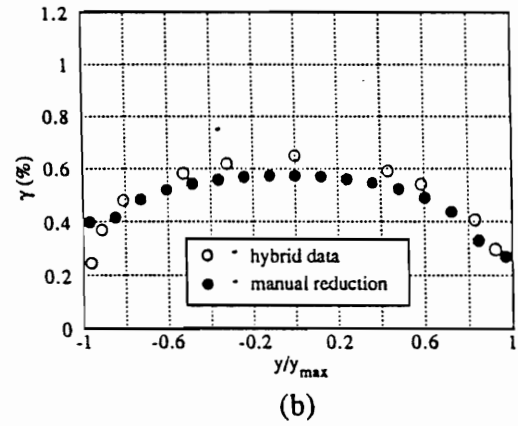
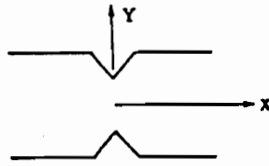
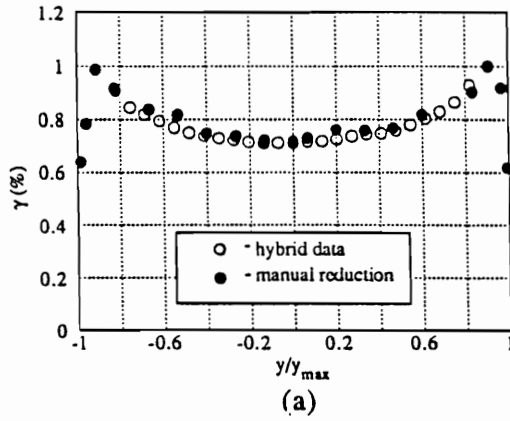


Fig.3.13 Comparisons of shear strain data across the notches obtained from manual data reduction of moire fringe patterns and the localized hybrid analysis for (a) 0° (at an applied load of 1334N), (b) 90° (at an applied load of 1112N), (c) $0^\circ/90^\circ$ (at an applied load of 1334N) graphite-epoxy Iosipescu specimens.

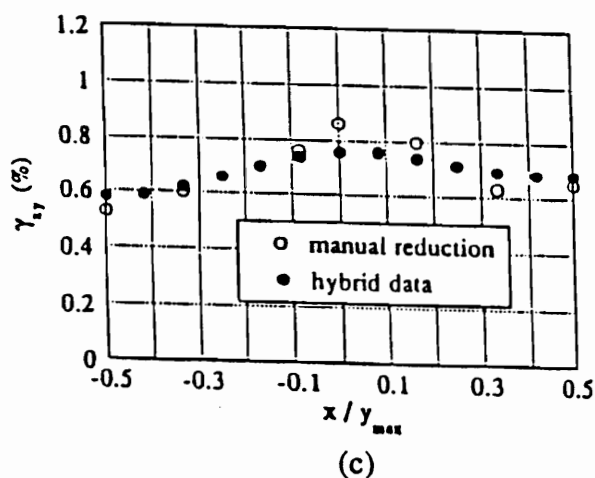
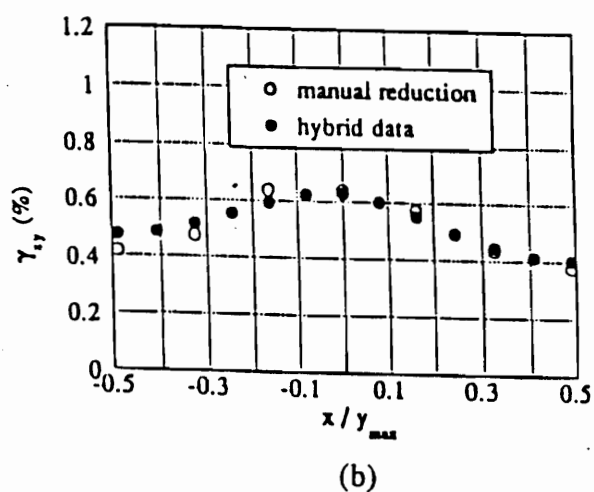
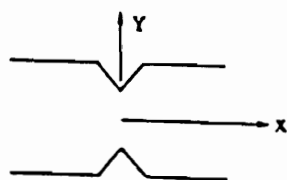
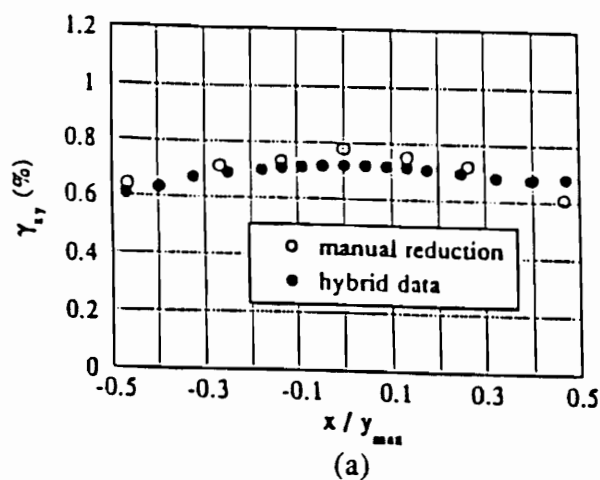


Fig.3.14 Comparisons of shear strain data along the longitudinal axis obtained from manual data reduction of moire fringe patterns and the localized hybrid analysis for (a) 0° (at an applied load of 1334N), (b) 90° (at an applied load of 1112N), (c) $0^\circ/90^\circ$ (at an applied load of 1334N) graphite-epoxy Iosipescu specimens.

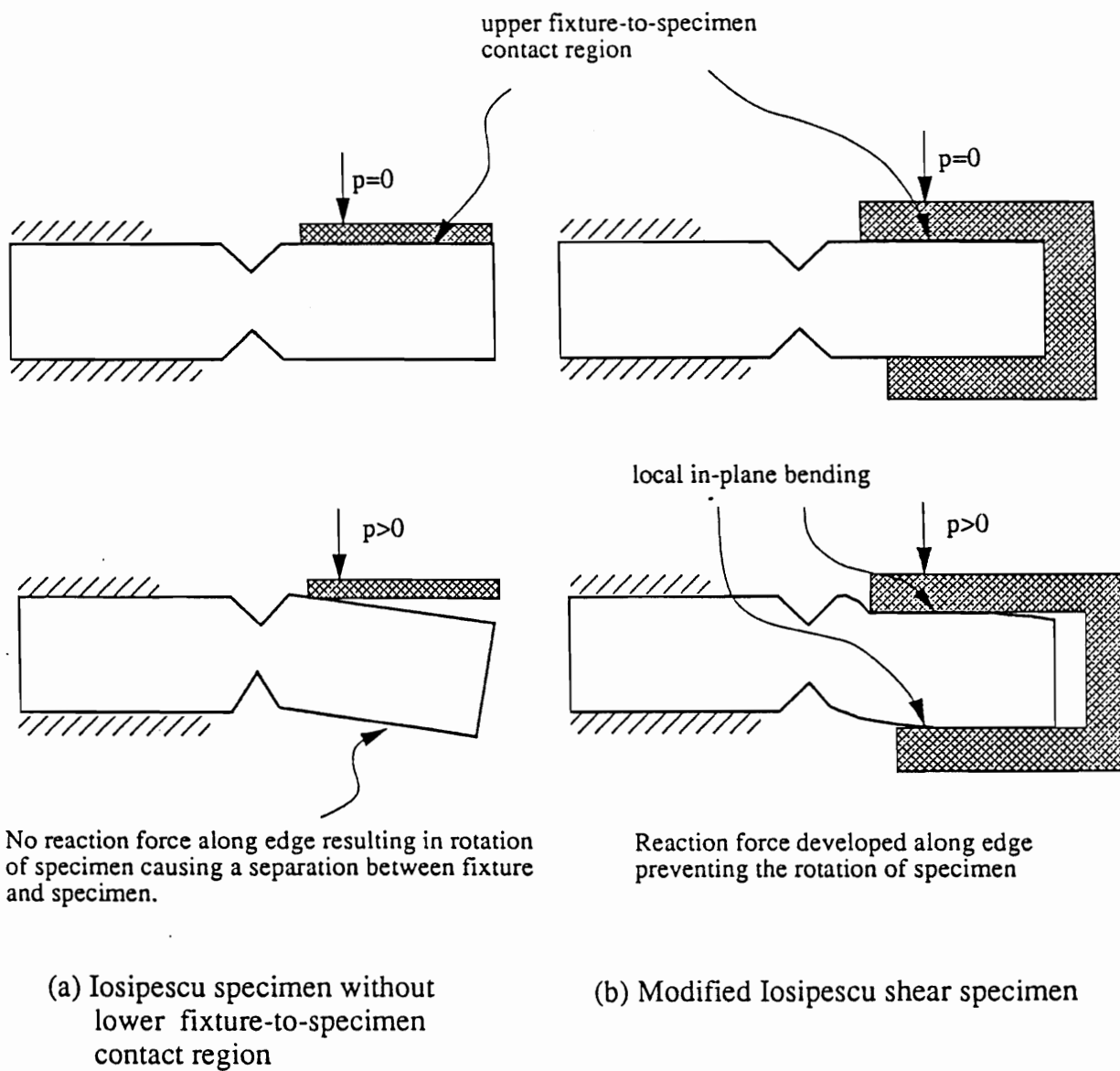


Fig.4.1 Deformation characteristics of Iosipescu shear specimen.

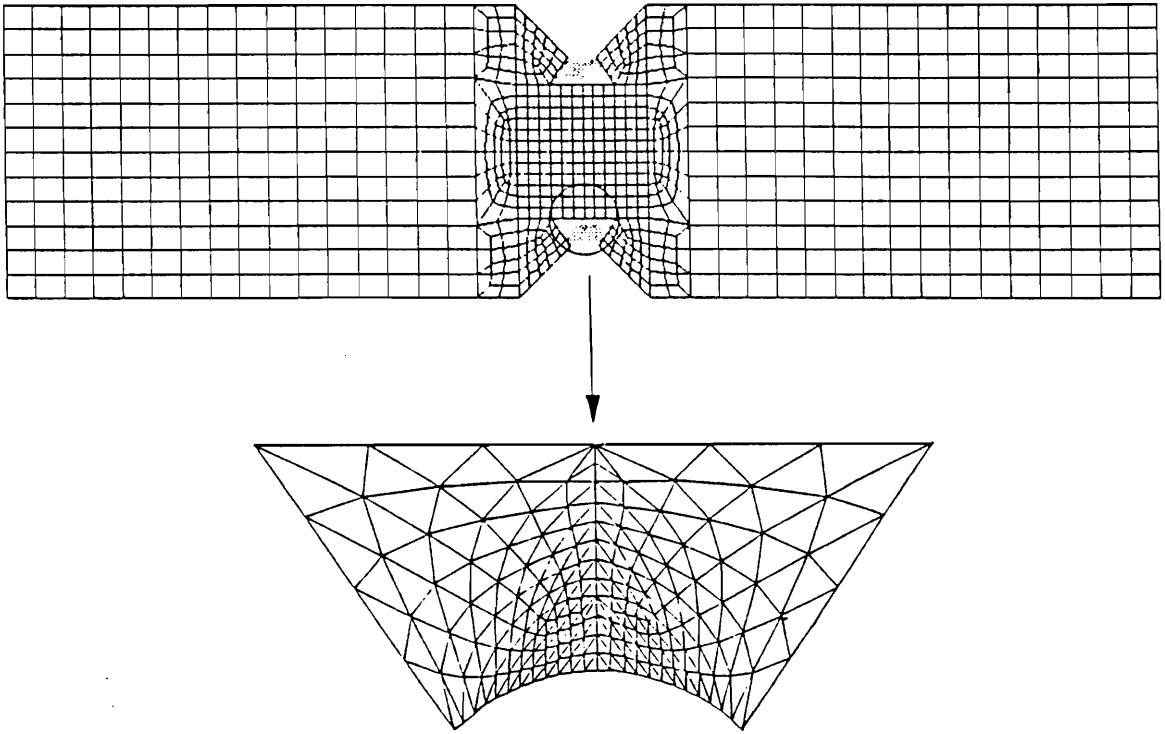


Fig.4.2. Finite element model of Iosipescu specimen.

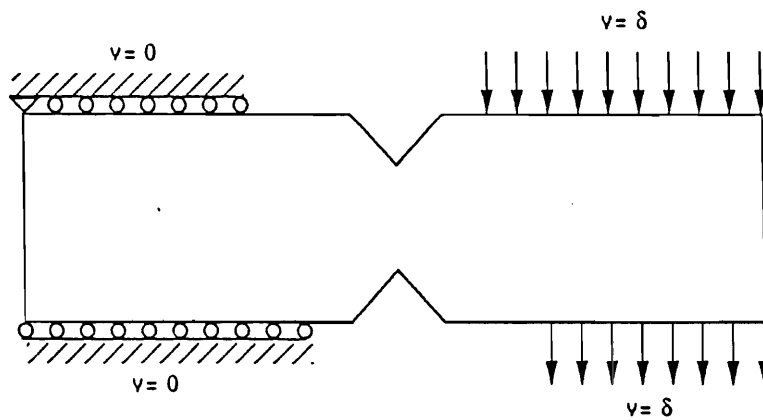


Fig.4.3 Initial displacement (applied and constrained) distribution on Iosipescu specimen.

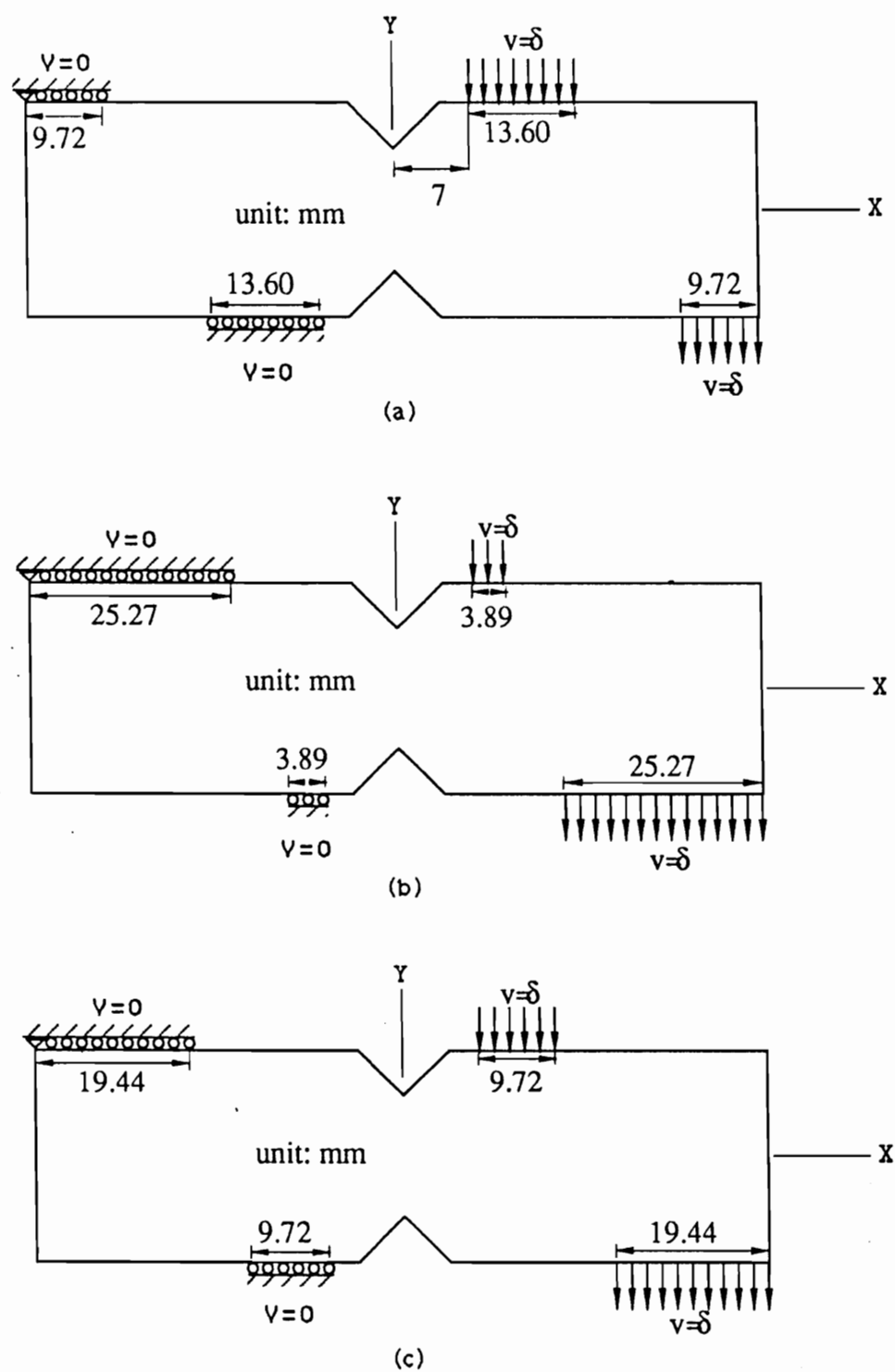
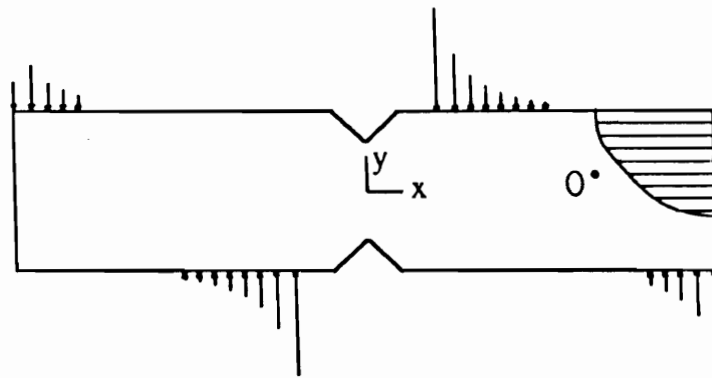
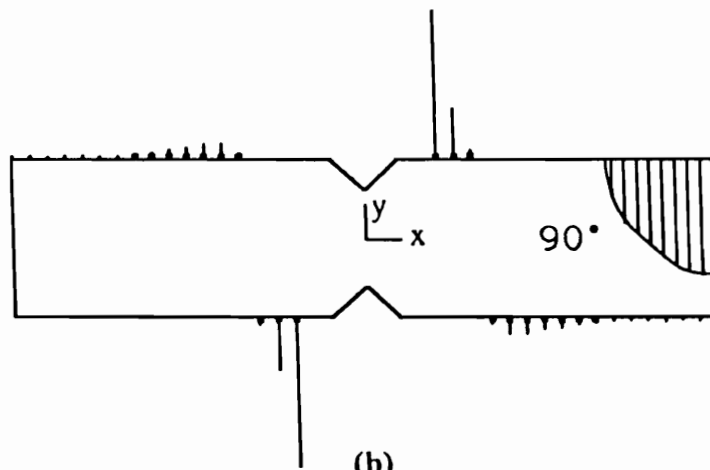


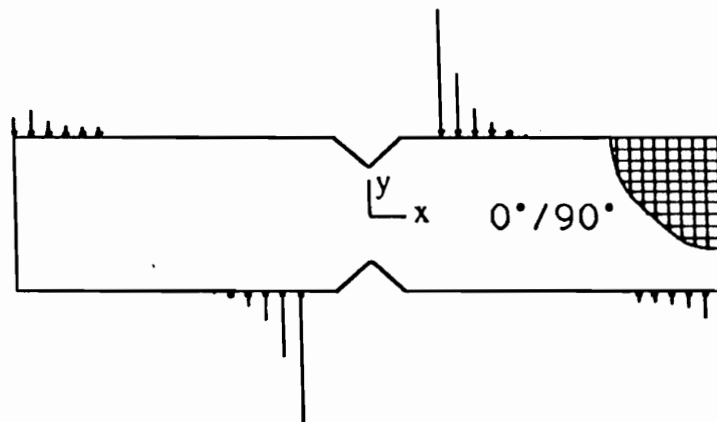
Fig.4.4 Finite element models for Iosipescu specimen tested in modified Wyoming fixture, (a) 0° specimen, (b) 90° specimen, (c) 0°/90° specimen.



(a)



(b)



(c)

Fig.4.5 Distributed loads on the specimen sides due to imposition of uniform displacement for (a) 0° , (b) 90° , (c) $0^\circ/90^\circ$ specimens.

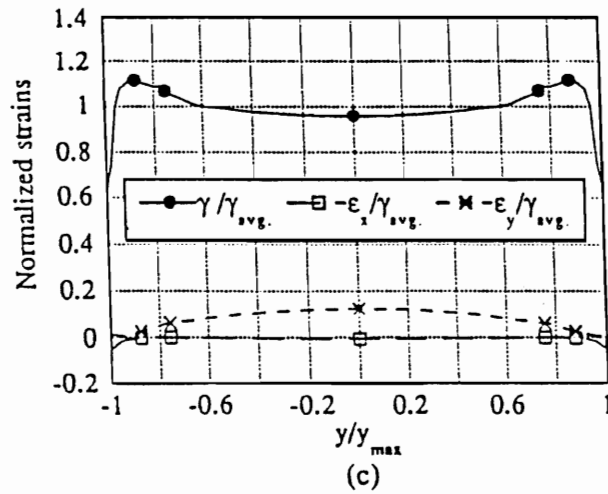
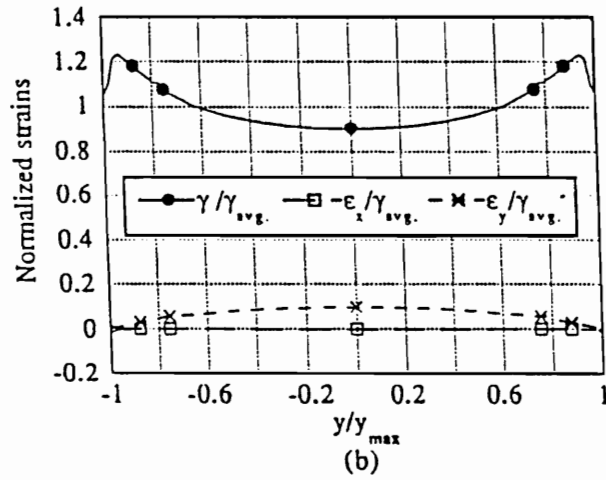
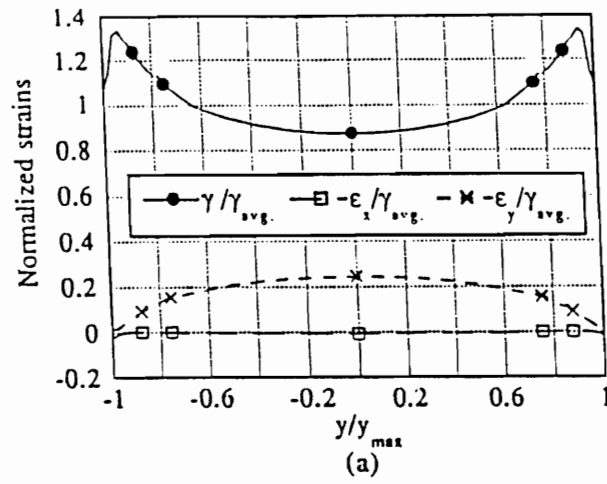


Fig.4.6 Normal and shear strains along the notch axis, normalized with respect to average shear strain, for (a) graphite-epoxy, (b) Kevlar-epoxy, (c) glass-epoxy 0° specimen.

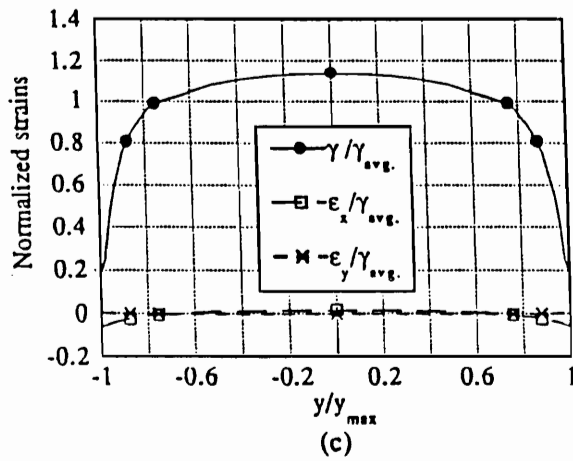
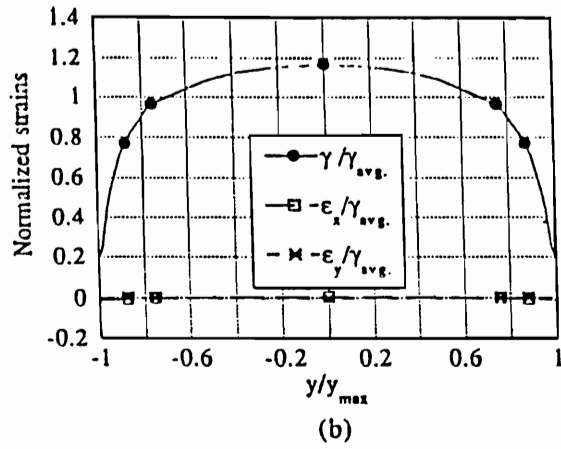
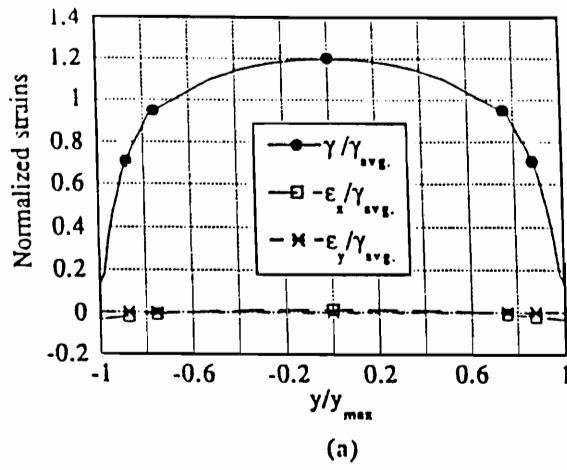


Fig.4.7 Normal and shear strains along the notch axis, normalized with respect to average shear strain, for (a) graphite-epoxy, (b) Kevlar-epoxy, (c) glass-epoxy 90° specimen.

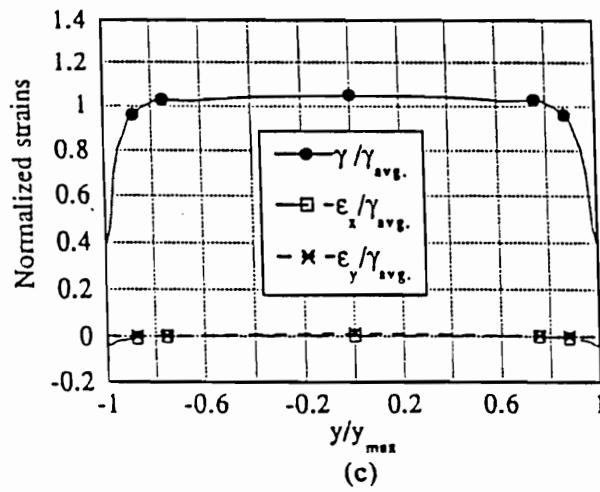
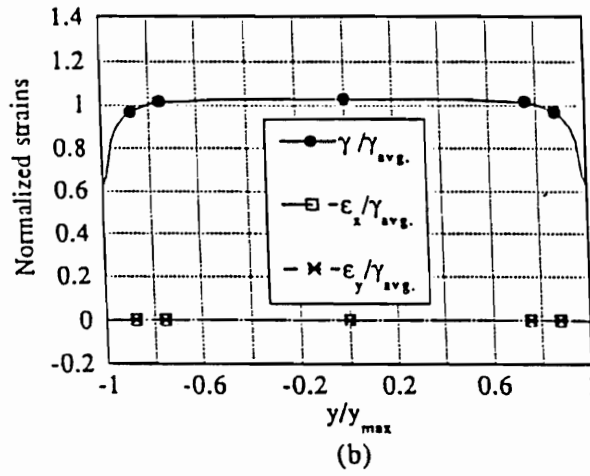
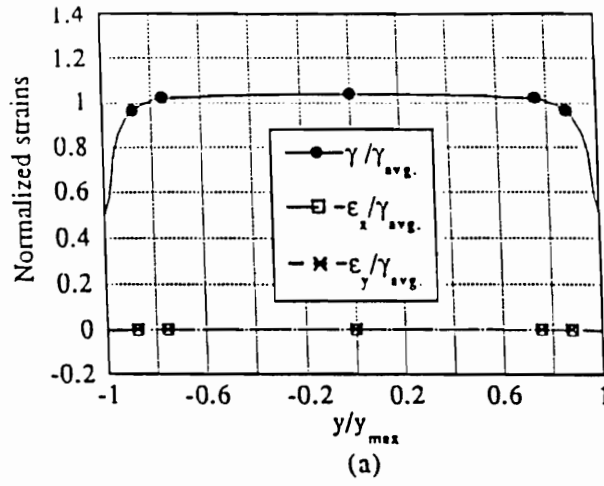


Fig.4.8 Normal and shear strains along the notch axis, normalized with respect to average shear strain, for (a) graphite-epoxy, (b) Kevlar-epoxy, (c) glass-epoxy $0^\circ/90^\circ$ specimen.

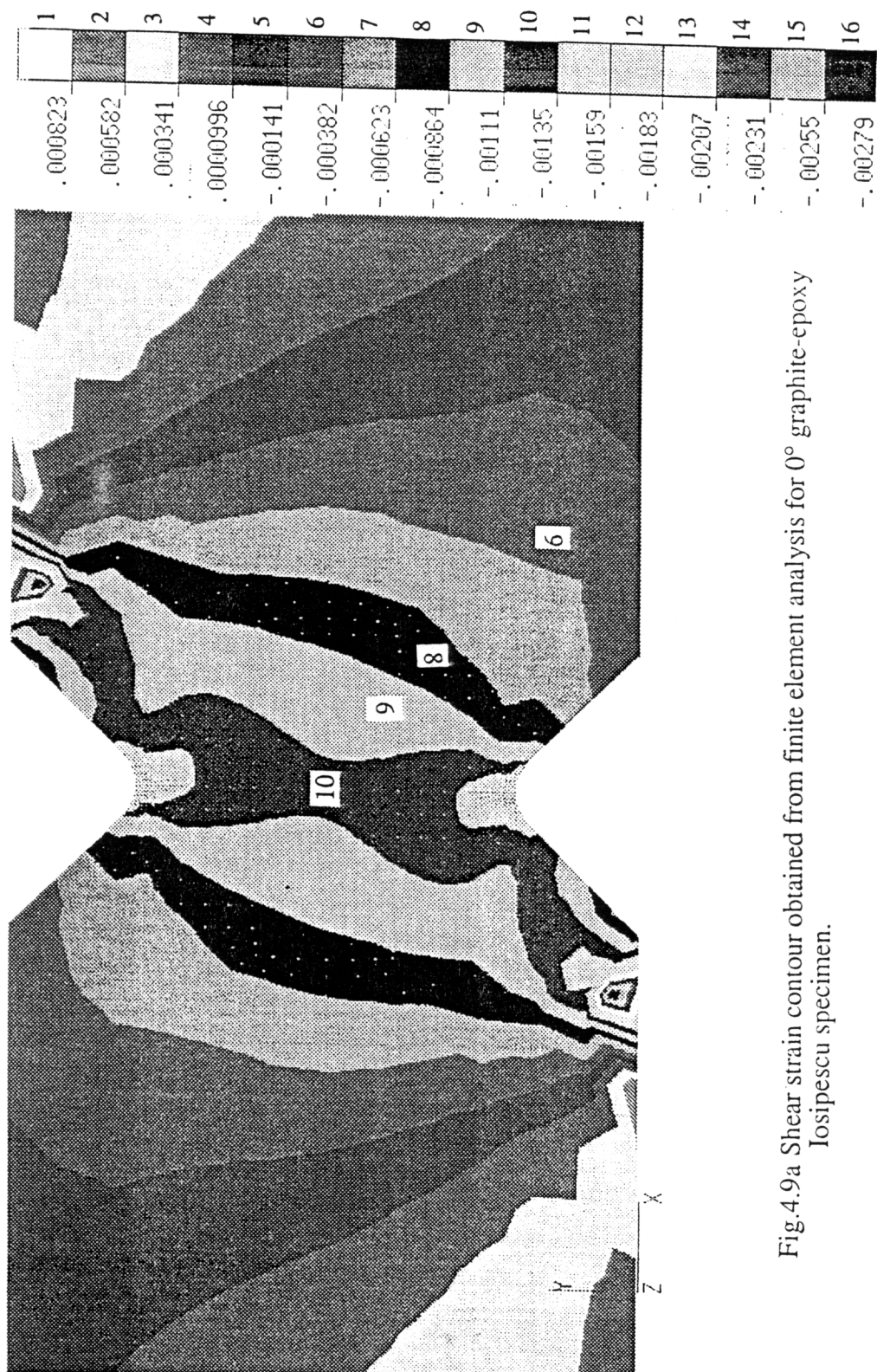


Fig.4.9a Shear strain contour obtained from finite element analysis for 0° graphite-epoxy Iosipescu specimen.

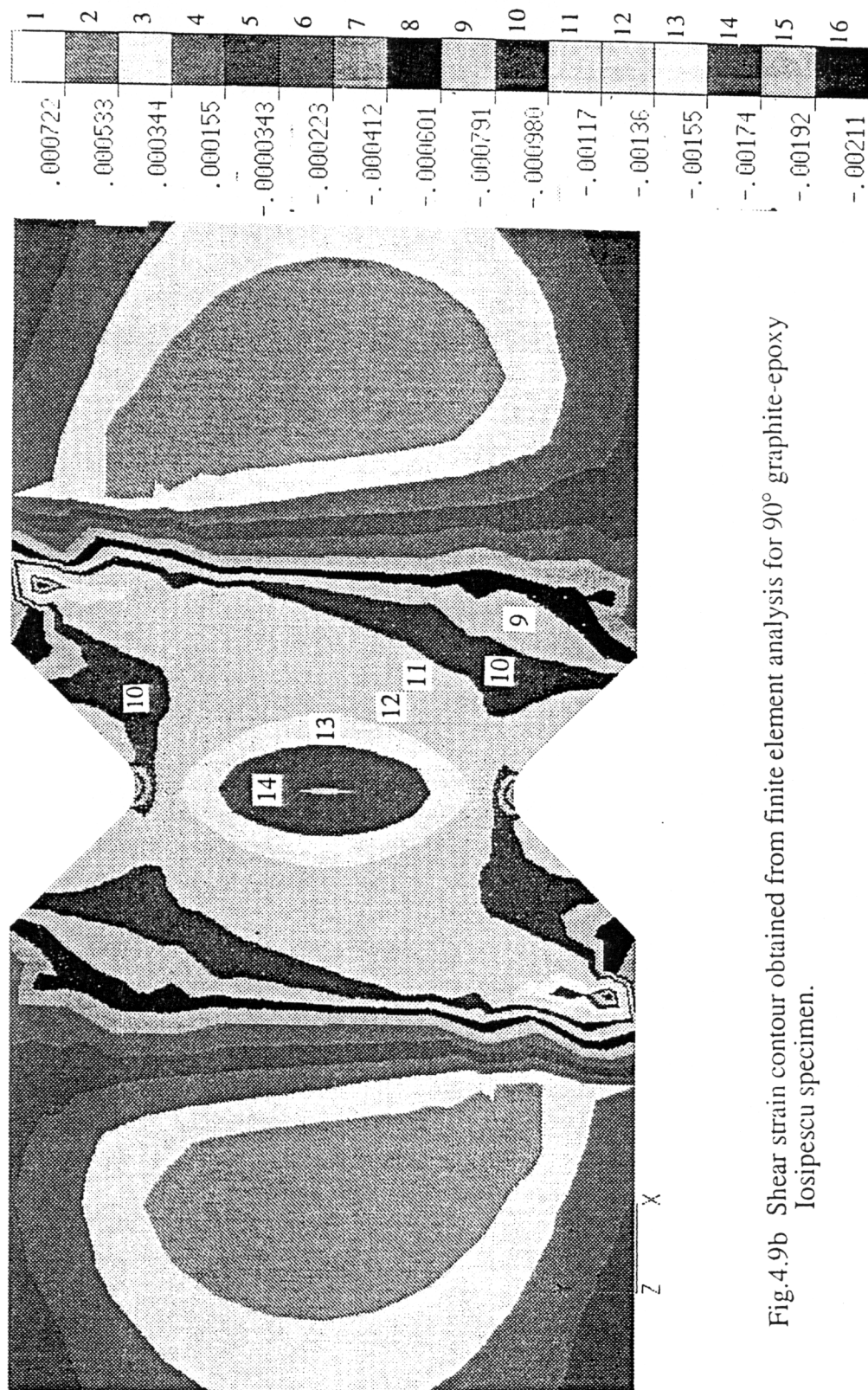


Fig.4.9b Shear strain contour obtained from finite element analysis for 90° graphite-epoxy Iosipescu specimen.

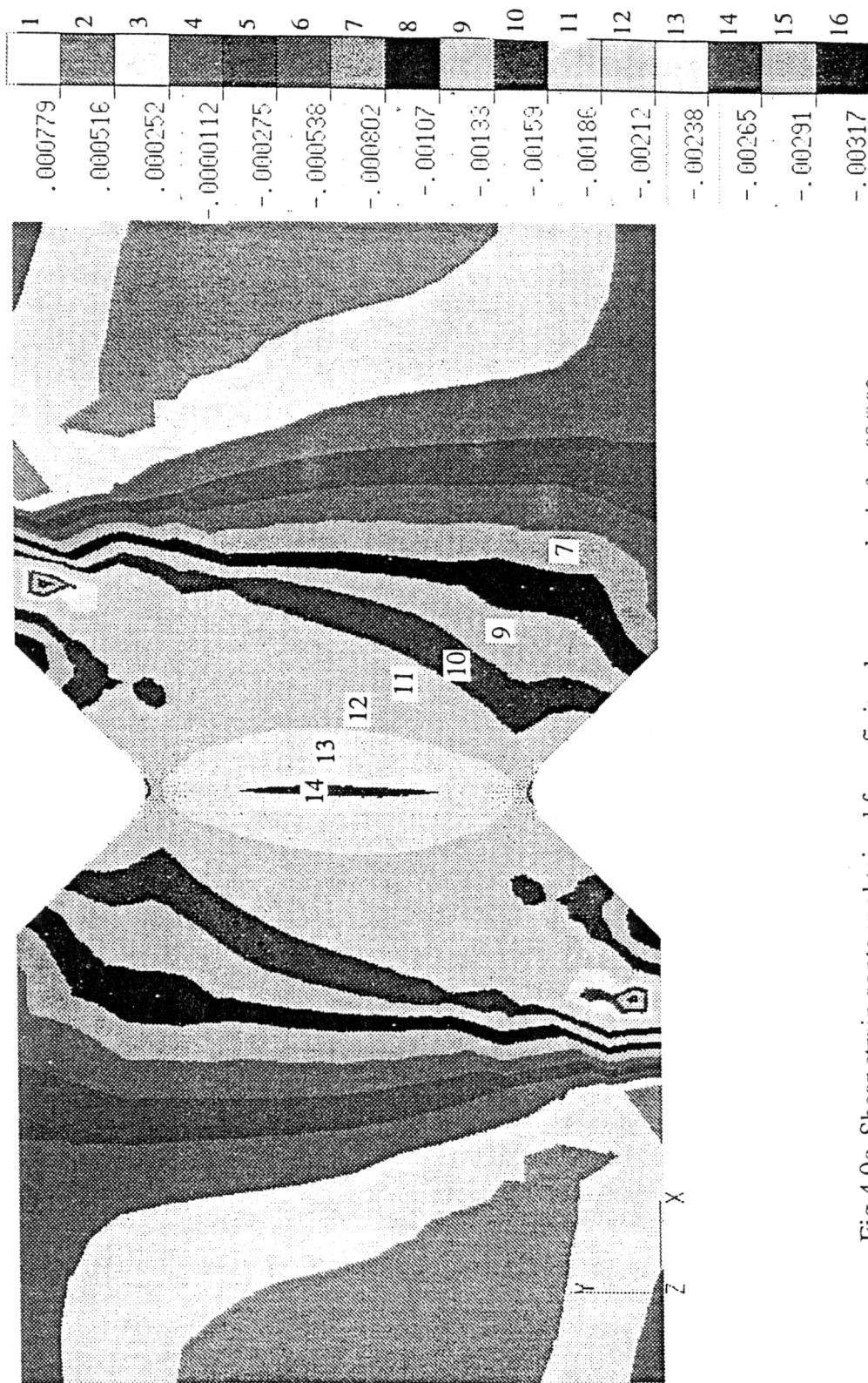


Fig.4.9c Shear strain contour obtained from finite element analysis for $0^\circ/90^\circ$ graphite-epoxy Iosipescu specimen.

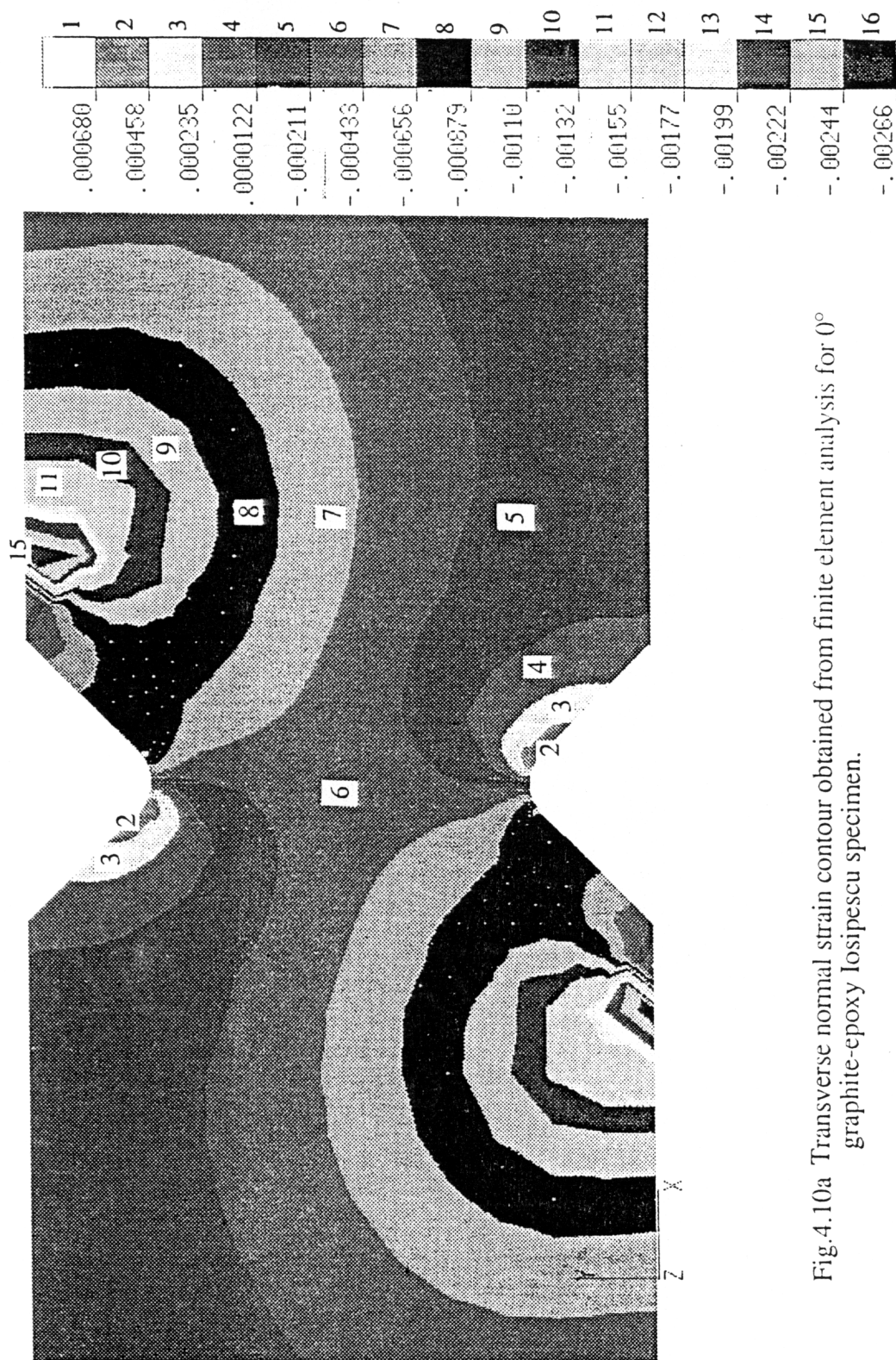


Fig.4.10a Transverse normal strain contour obtained from finite element analysis for 0° graphite-epoxy Iosipescu specimen.

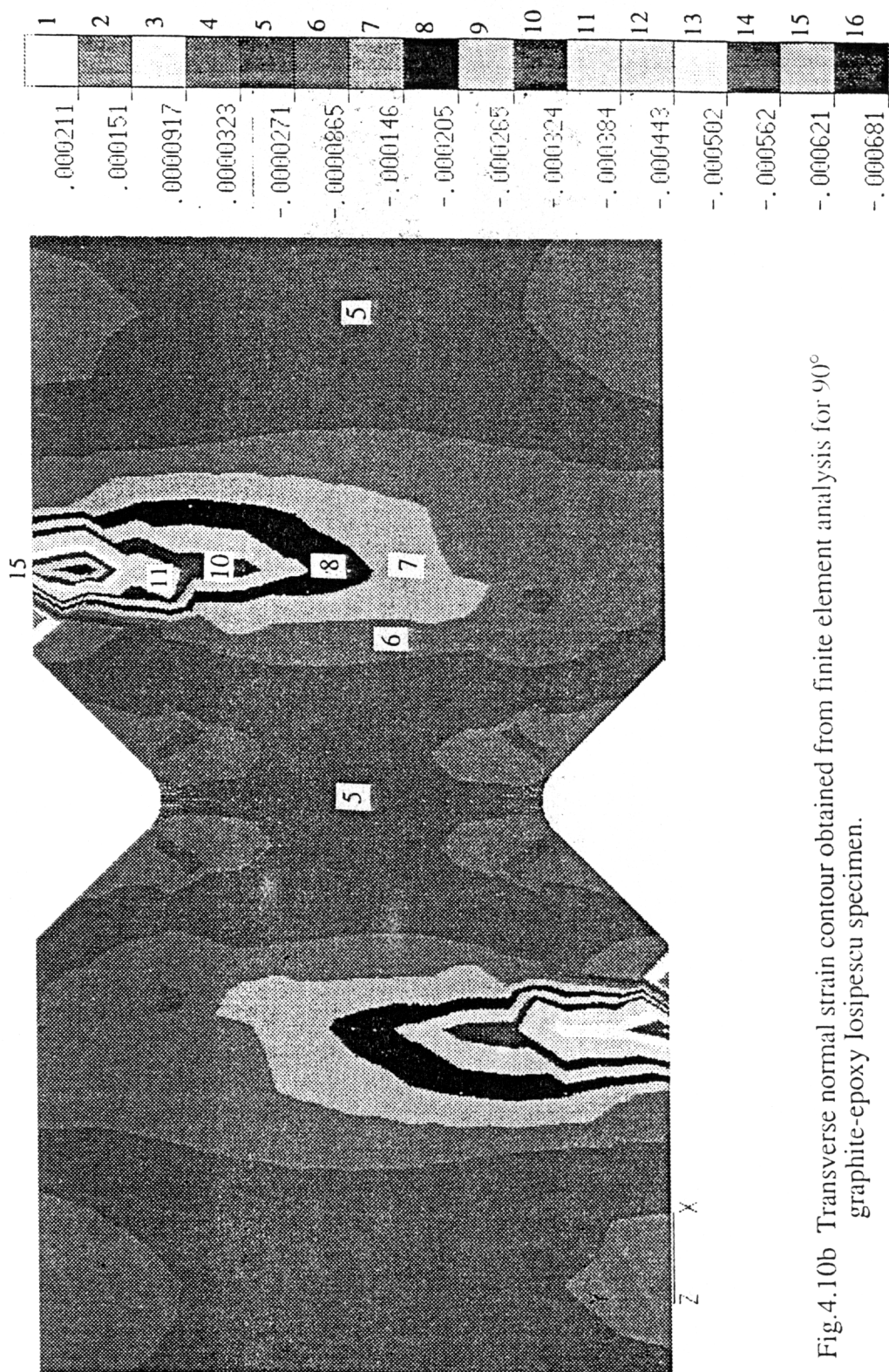


Fig.4.10b Transverse normal strain contour obtained from finite element analysis for 90° graphite-epoxy Iosipescu specimen.

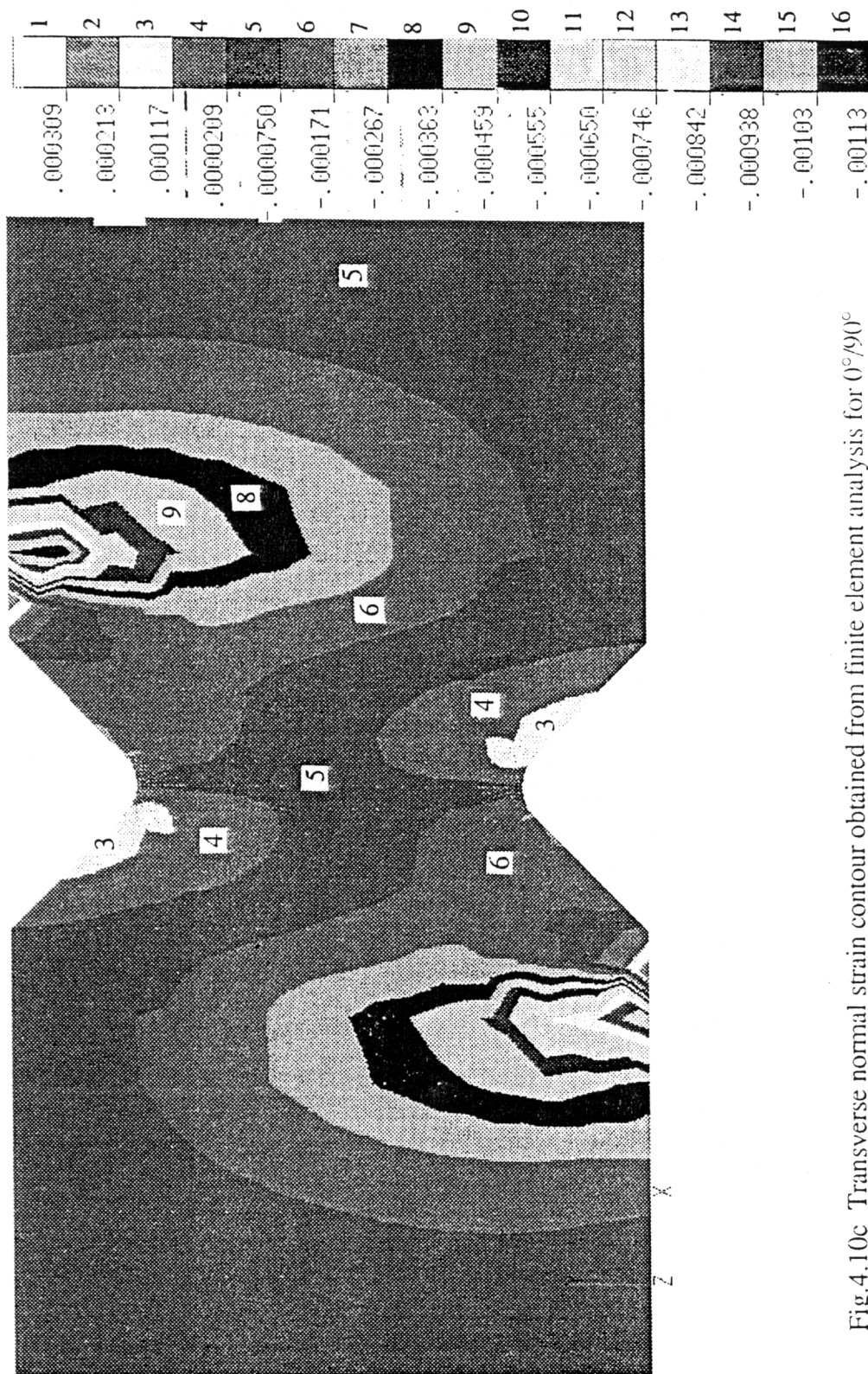


Fig.4.10c Transverse normal strain contour obtained from finite element analysis for 0°/90° graphite-epoxy Iosipescu specimen.

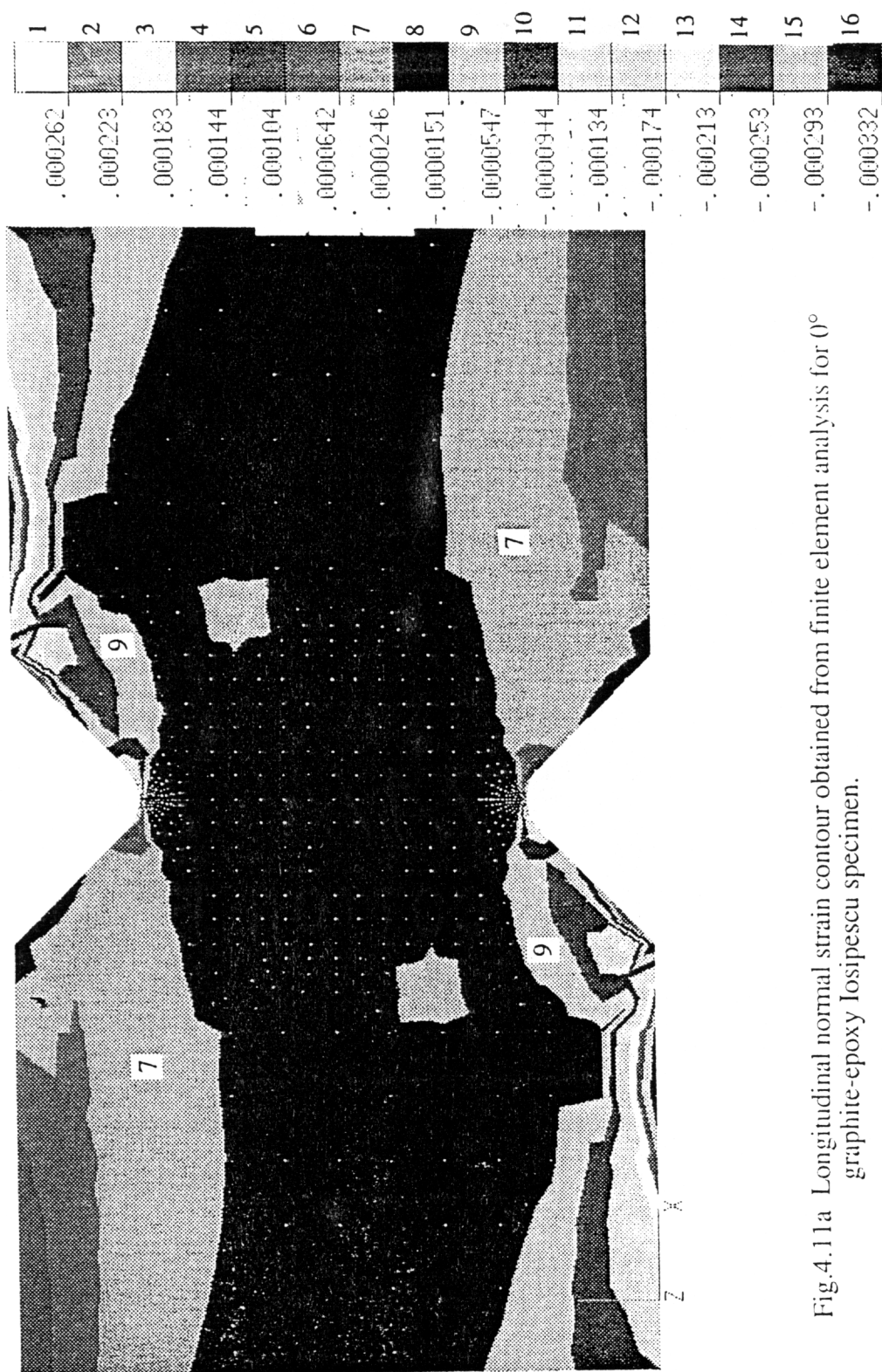


Fig.4.11a Longitudinal normal strain contour obtained from finite element analysis for 0° graphite-epoxy Iosipescu specimen.

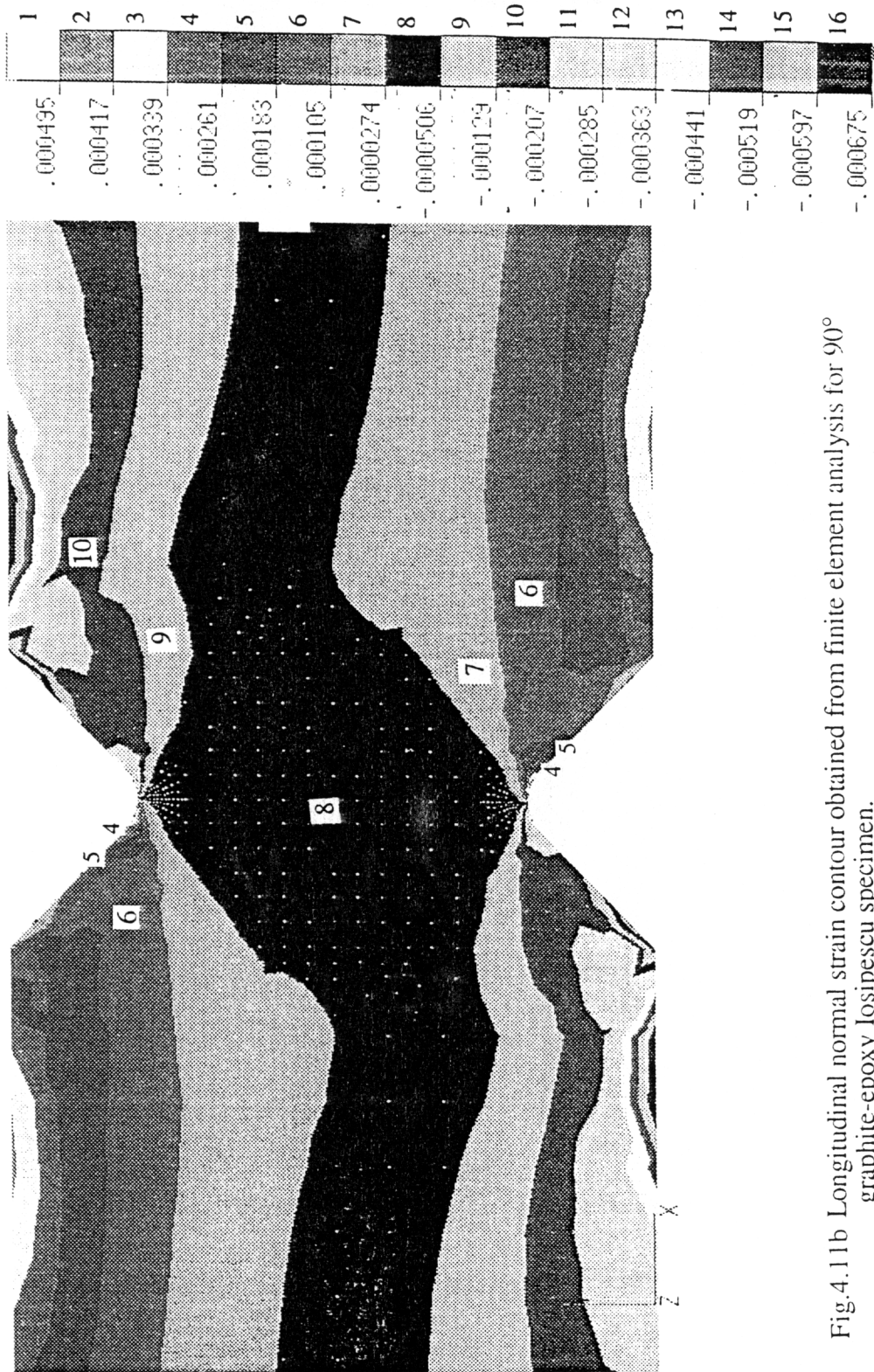


Fig.4.11b Longitudinal normal strain contour obtained from finite element analysis for 90° graphite-epoxy Iosipescu specimen.

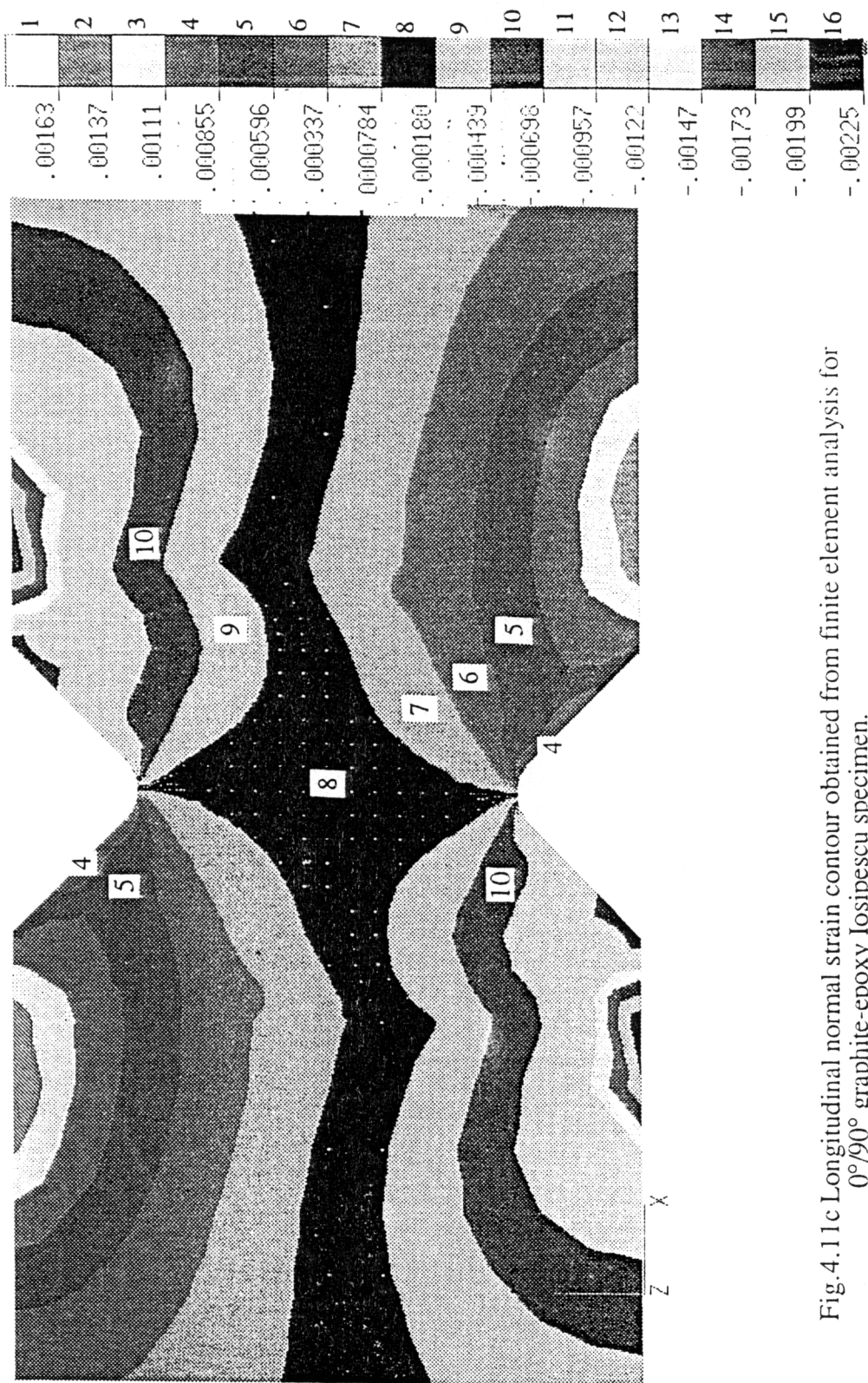
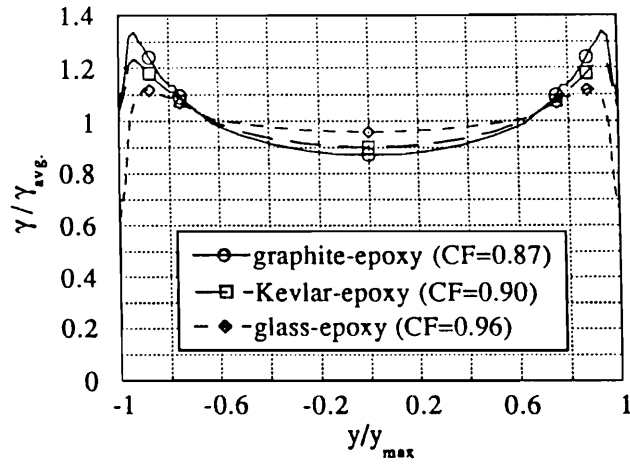
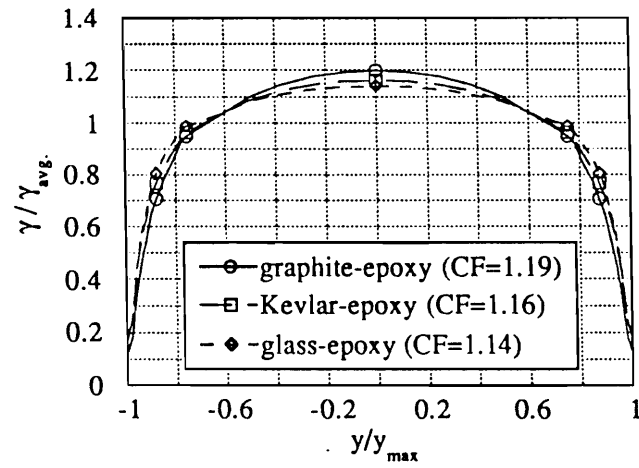


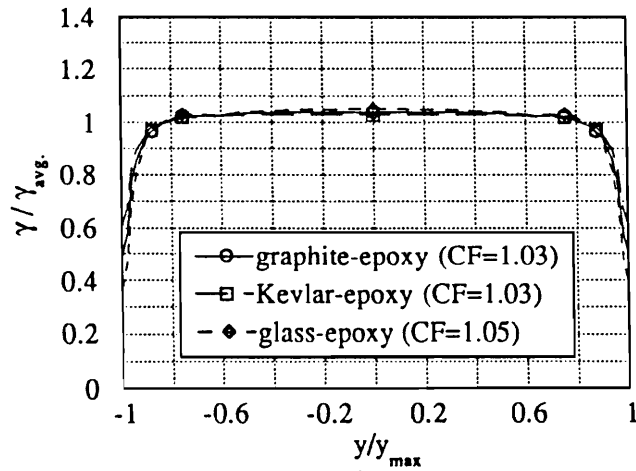
Fig.4.11c Longitudinal normal strain contour obtained from finite element analysis for $0^{\circ}/90^{\circ}$ graphite-epoxy Iosipescu specimen.



(a)



(b)



(c)

Fig.4.12 Shear strain distribution along the notch axis for (a) 0°, (b) 90°, (c) 0°/90° graphite-epoxy, Kevlar-epoxy and glass-epoxy specimens.

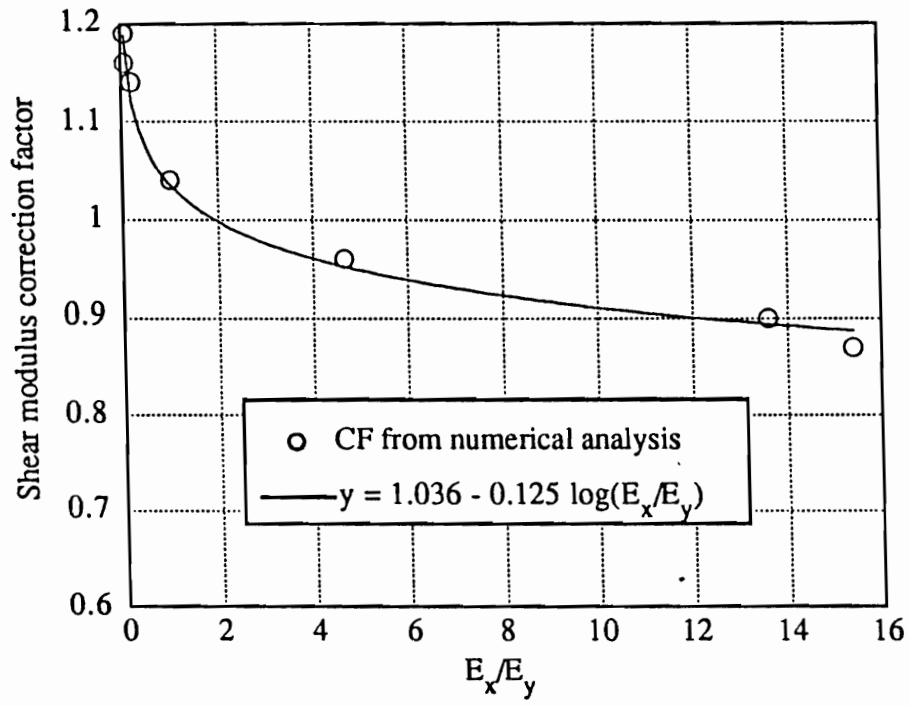


Fig.4.13 Correction factor vs. material orthotropic ratio.

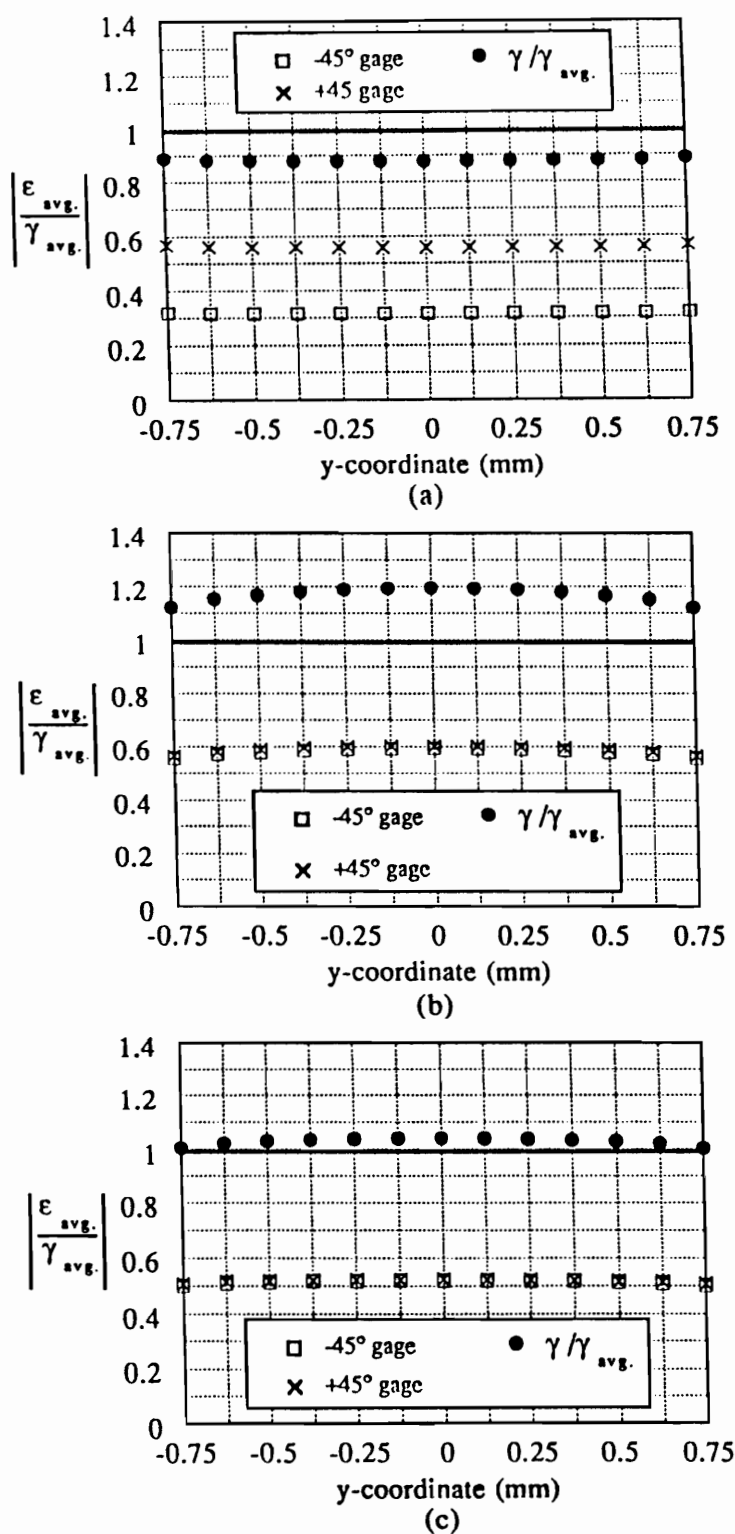
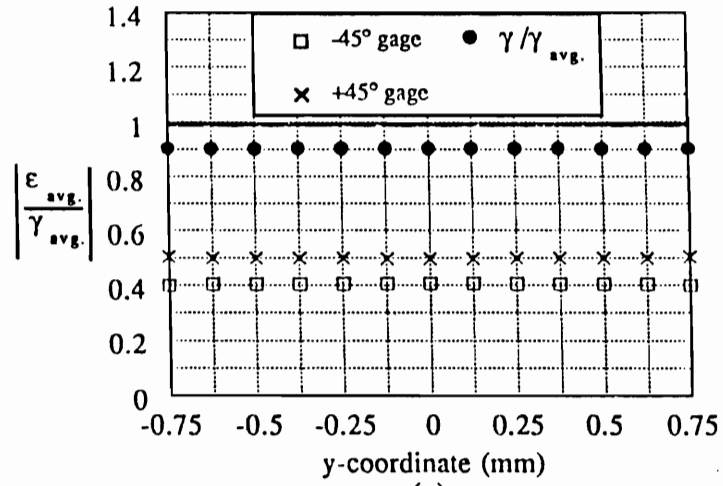
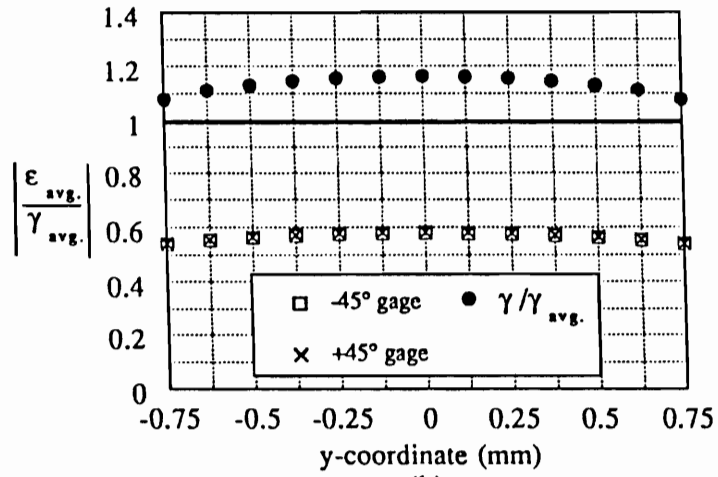


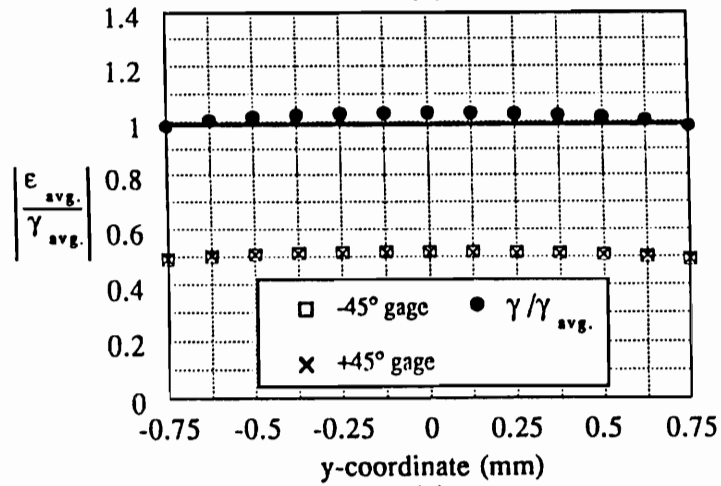
Fig.4.14 Normalized strains of $\pm 45^\circ$ gages from finite element analysis for (a) 0° , (b) 90° , (c) $0^\circ/90^\circ$ graphite-epoxy Iosipescu specimen.



(a)



(b)



(c)

Fig.4.15 Normalized strains of $\pm 45^\circ$ gages from finite element analysis for (a) 0° , (b) 90° , (c) $0^\circ/90^\circ$ Kevlar-epoxy Iosipescu specimen.

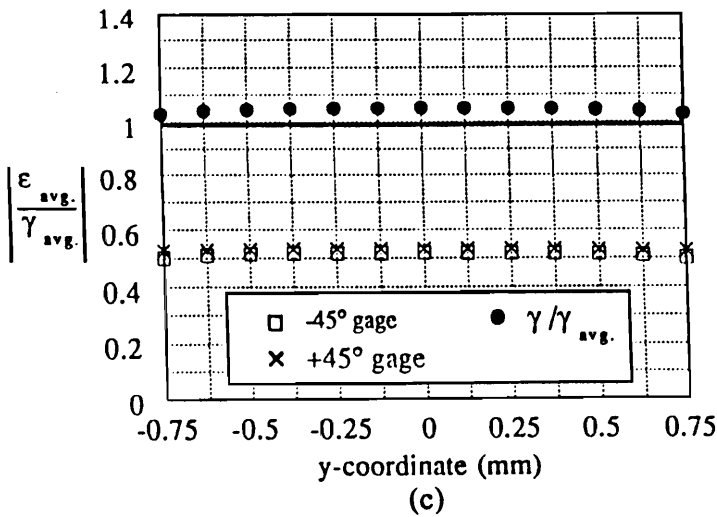
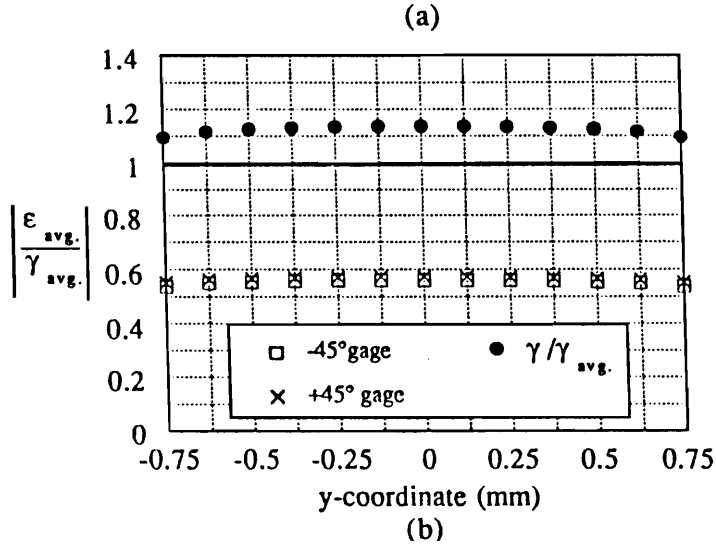
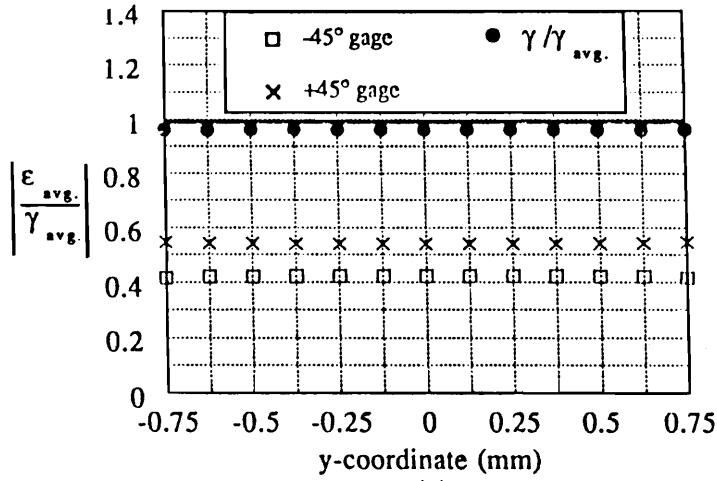
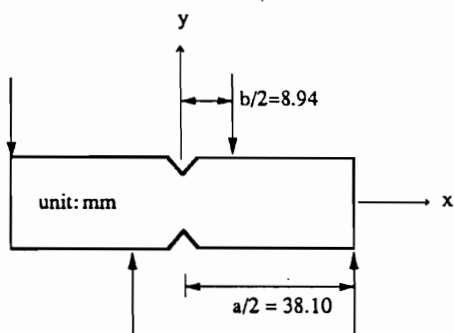
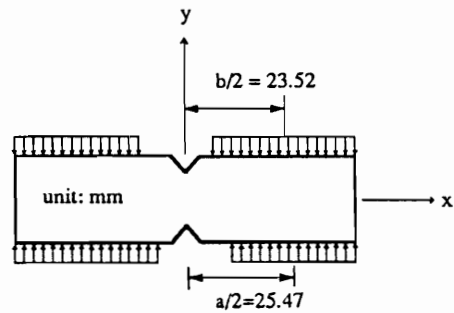


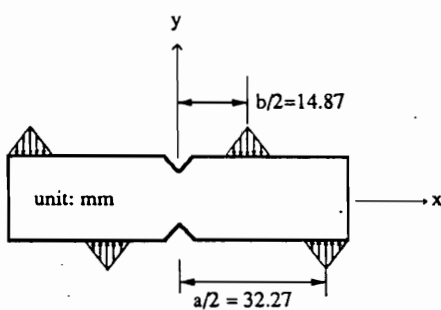
Fig.4.16 Normalized strains of $\pm 45^\circ$ gages from finite element analysis for (a) 0° , (b) 90° , (c) $0^\circ/90^\circ$ glass-epoxy Iosipescu specimen.



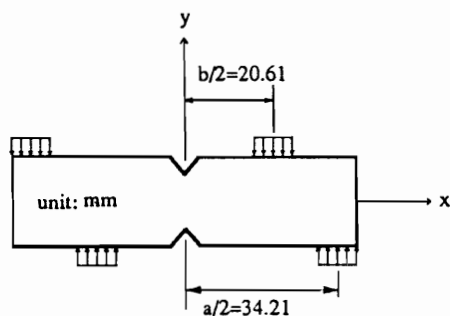
case 1



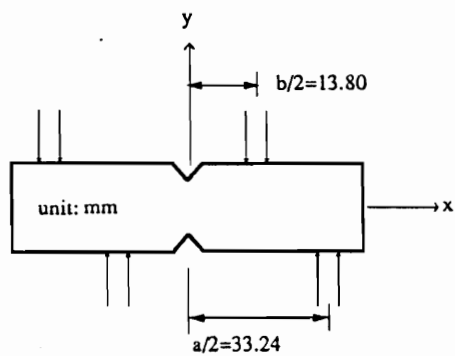
case 2



case 3



case 4



case 5

Fig.4.17 Models for load-point effect analysis.

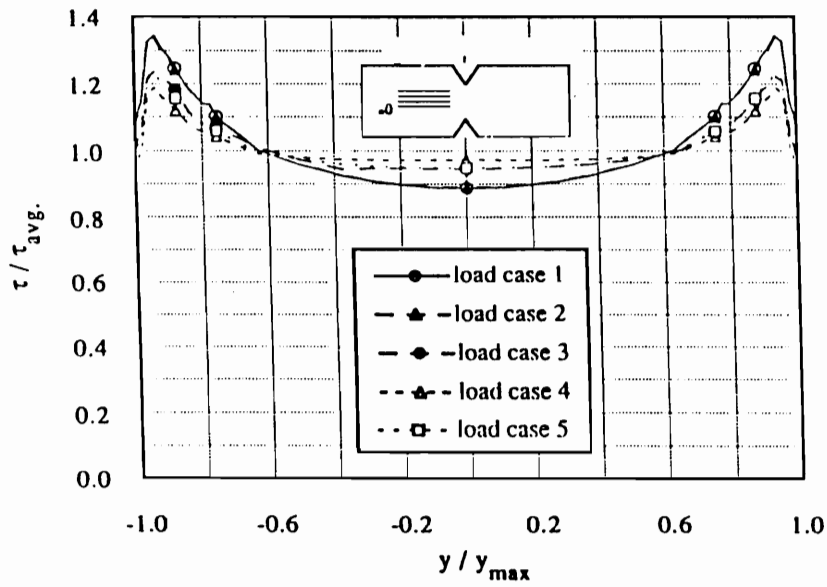


Fig.4.18 Load point effect on the shear strain distribution along the notch axis for 0° graphite-epoxy specimen. Load cases are shown in Fig.4.17

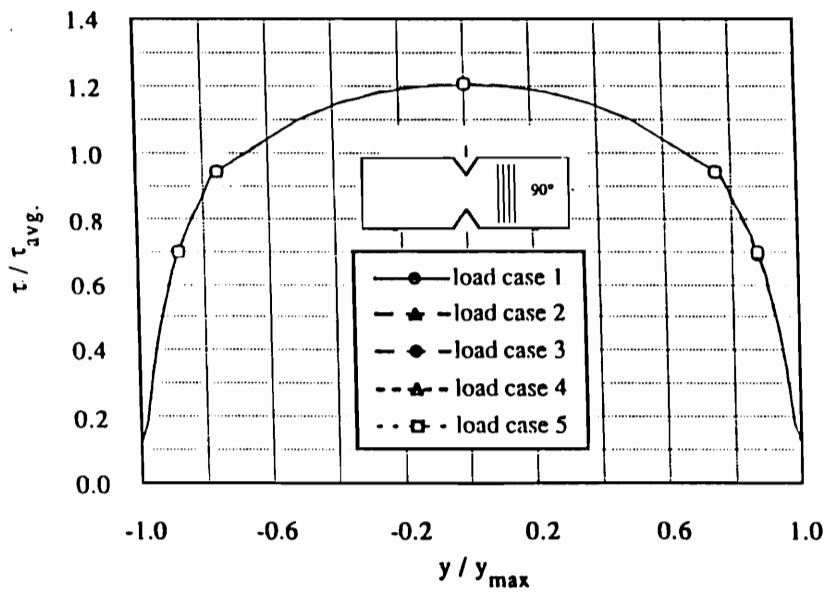


Fig.4.19 Load point effect on the shear strain distribution along the notch axis for 90° graphite-epoxy specimen. Load cases are shown in Fig.4.17.

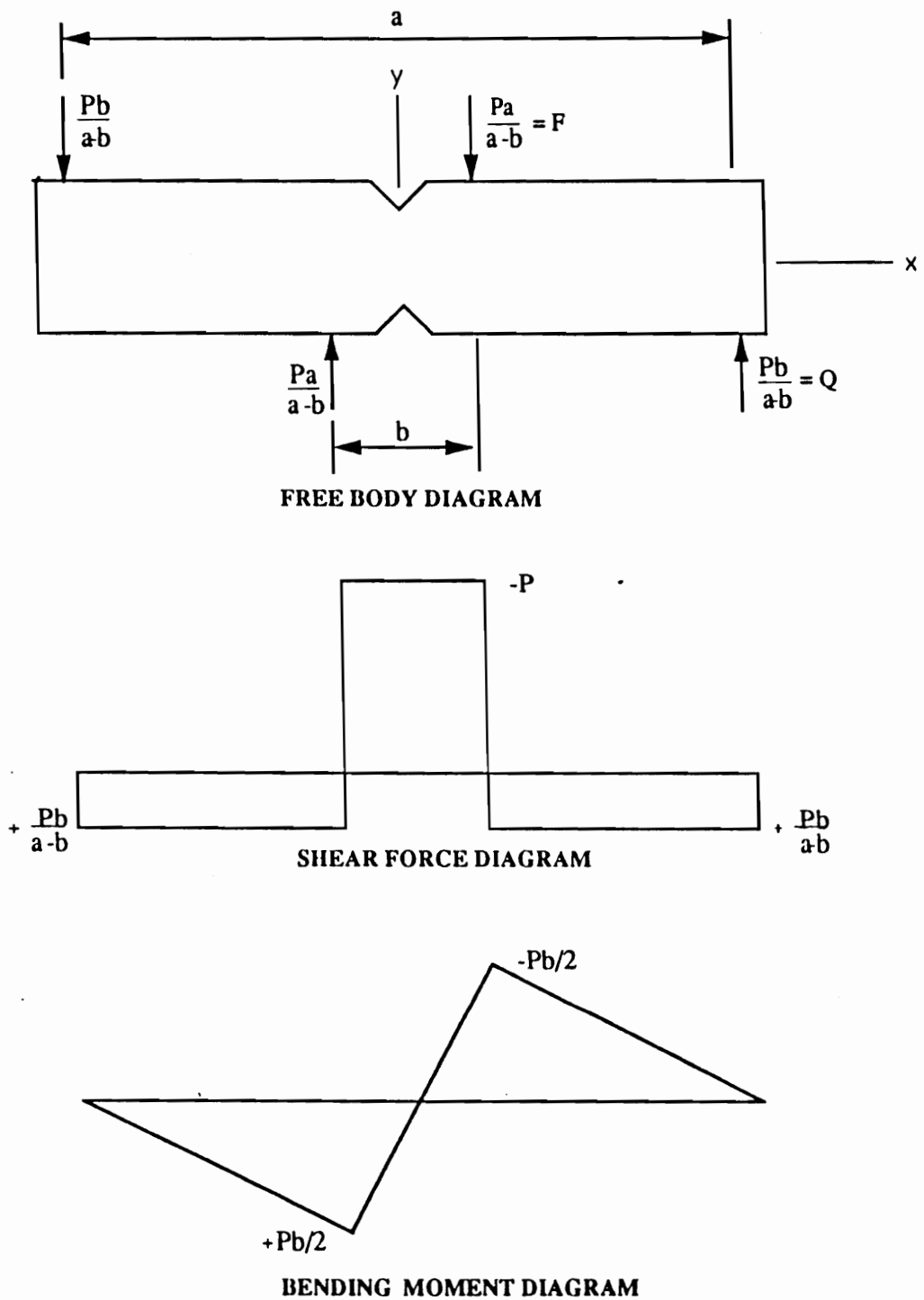


Fig.5.1 One dimensional mechanics of the Iosipescu shear specimen --force and moment equilibrium models.

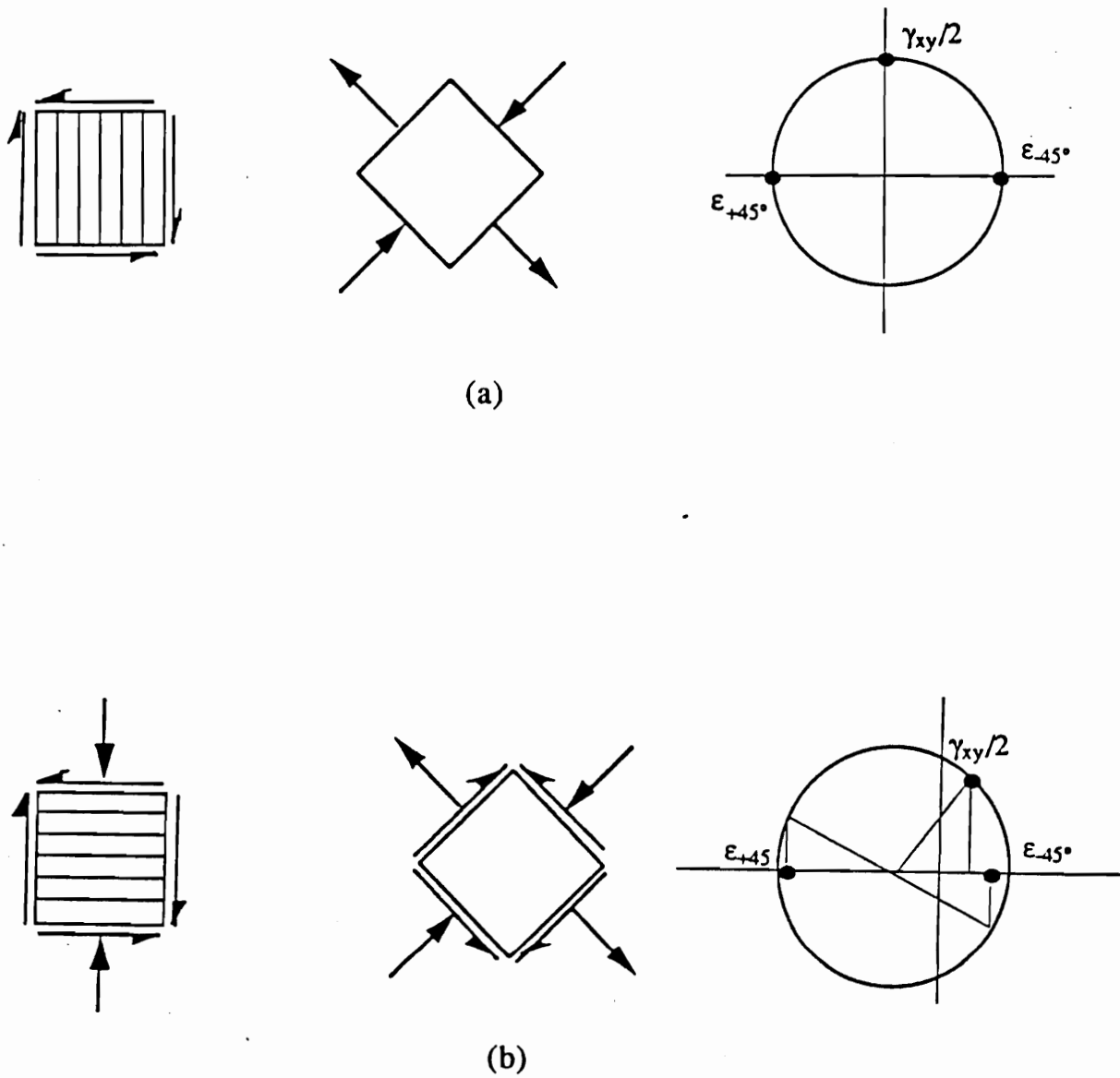


Fig.5.2 Free body diagram and Mohr's circle representation of strain state of an element in the gage section of (a) 90° specimen, (b) 0° specimen.

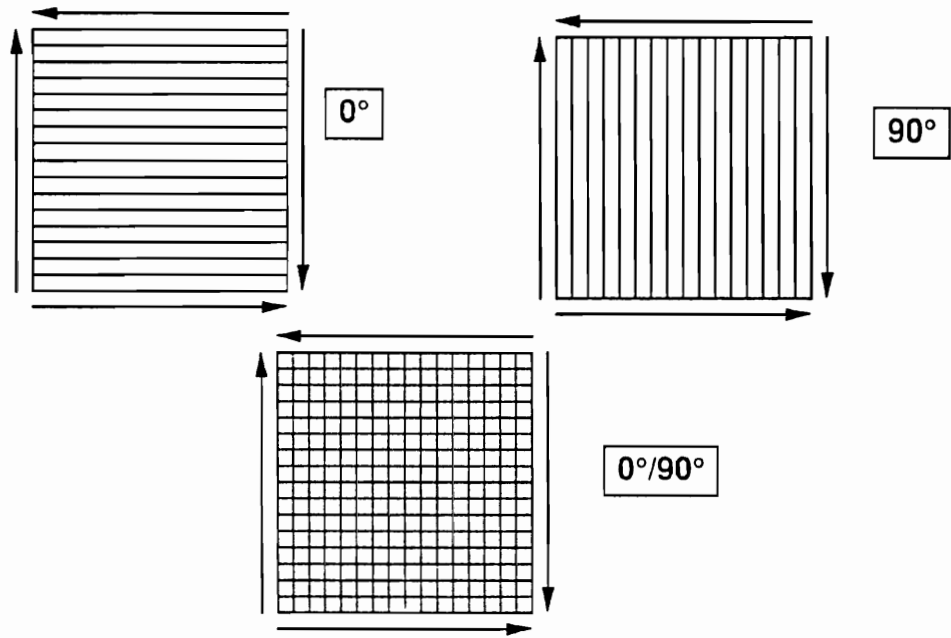


Fig.5.3 Schematic diagram of complementary shear: (a) 0° specimen, (b) 90° specimen, (c) $0^\circ/90^\circ$ specimen.

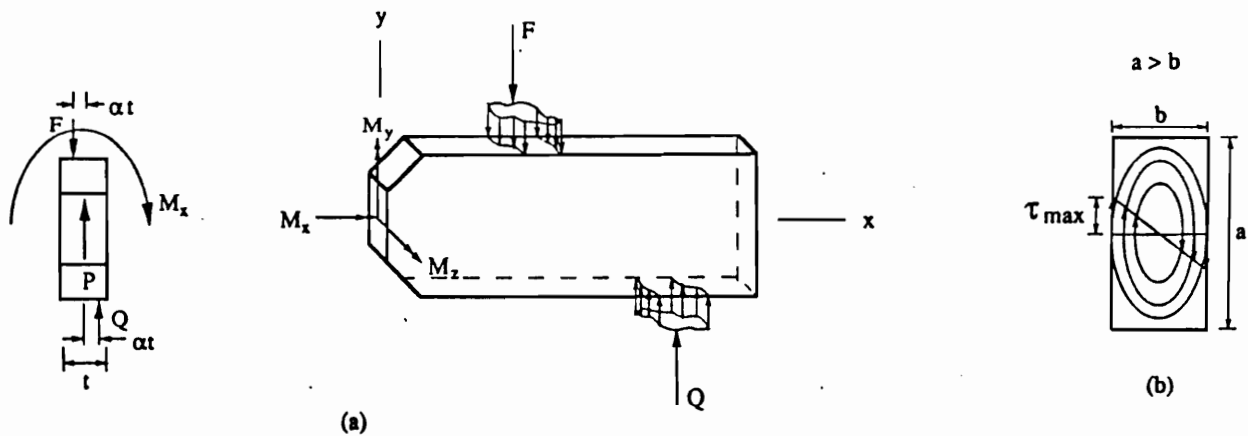


Fig.5.4 (a) Three dimensional representation of the free body diagram of the Iosipescu specimen, (b) the qualitative shear flow contours on the y-z plane due to the twisting moment, M_x .

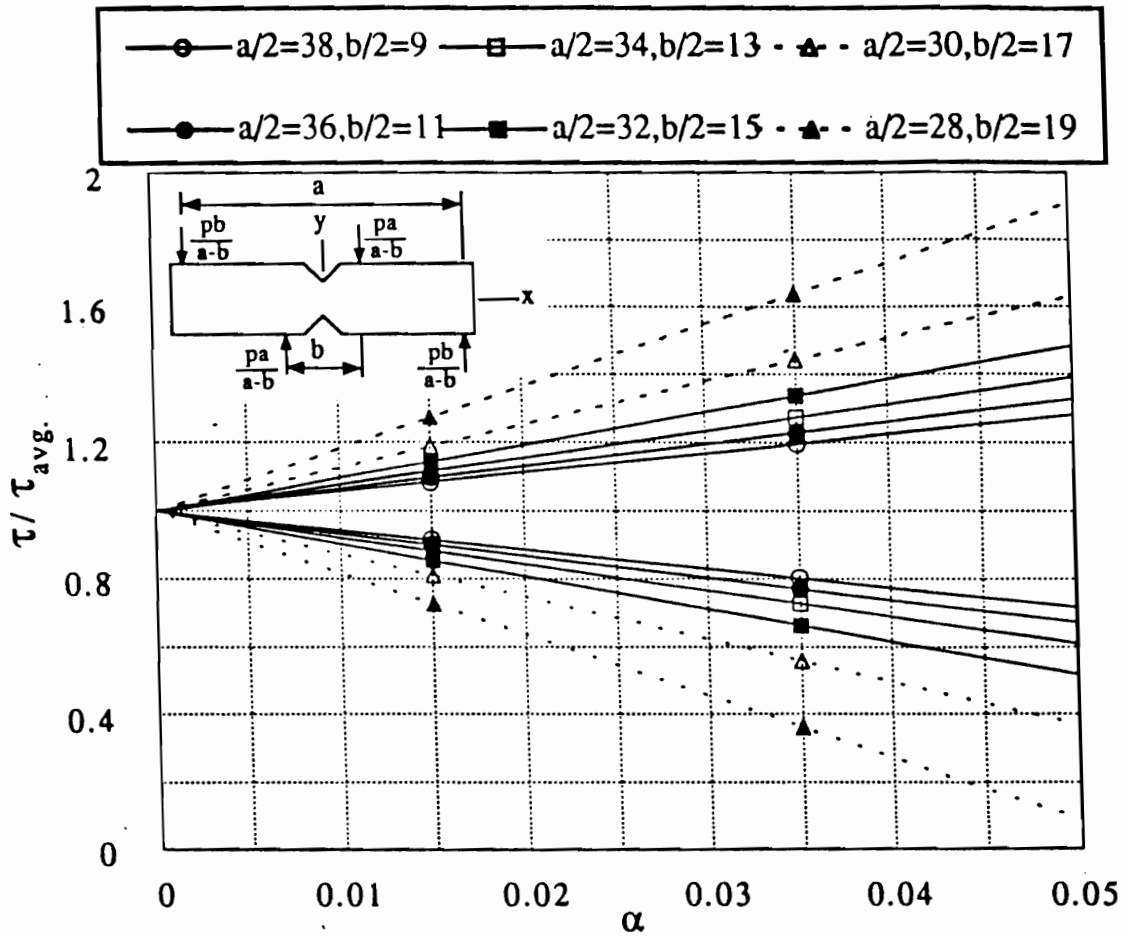


Fig.5.5 Effect of load eccentricity upon the shear stresses.

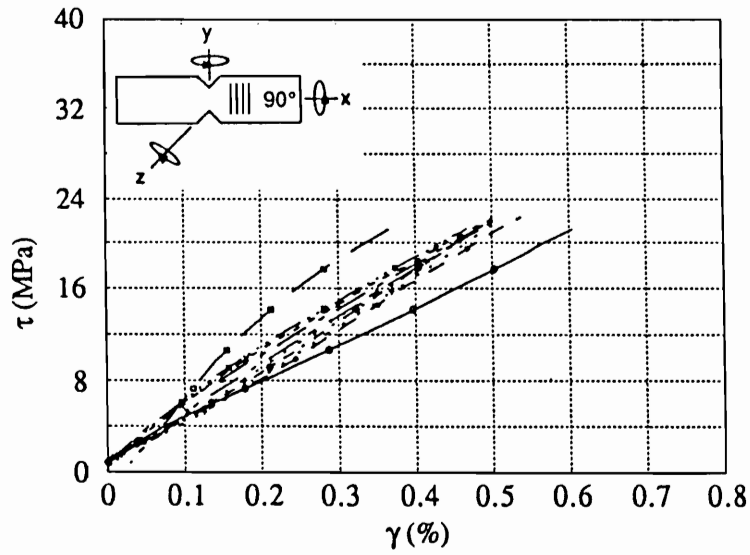


Fig.5.6a Shear stress-strain data for 90° graphite-epoxy specimen loaded in different orientations which were obtained by rotating the specimen about the x,y and z axis.

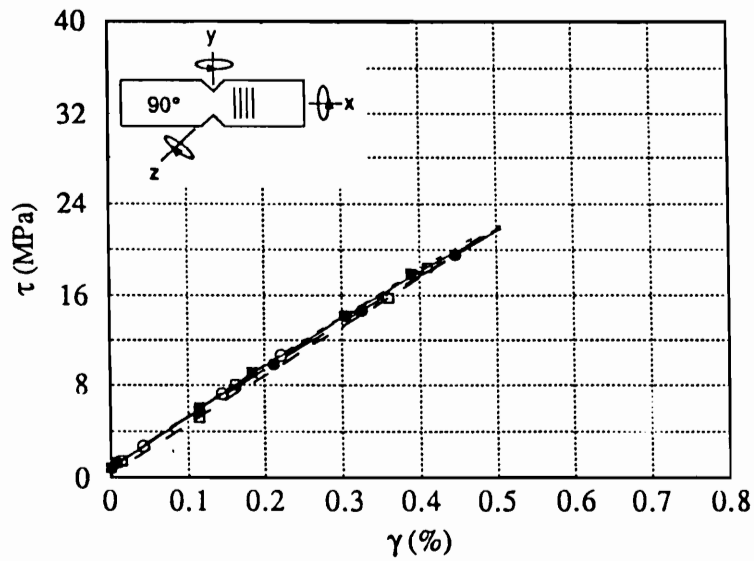


Fig.5.6b Average of front and back surface shear strains as a function of shear stress for 90° graphite-epoxy specimen.

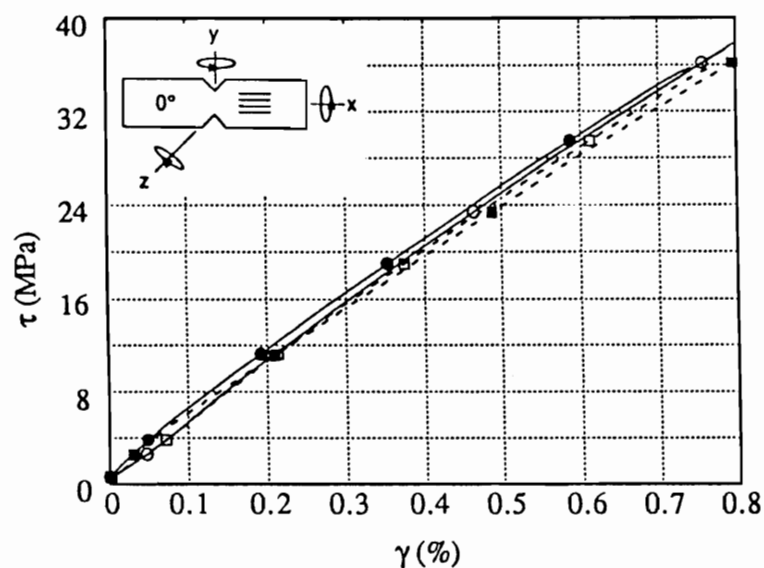


Fig.5.7a Shear stress-strain data for 0° graphite-epoxy specimen loaded in different orientations which were obtained by rotating the specimen about the x,y and z axis.

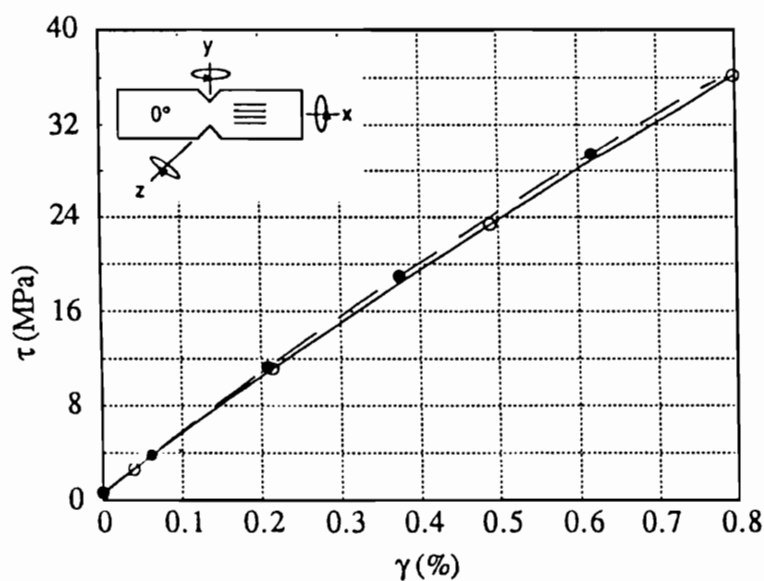


Fig.5.7b Average of front and back surface shear strains as a function of shear stress for 0° graphite-epoxy specimen.

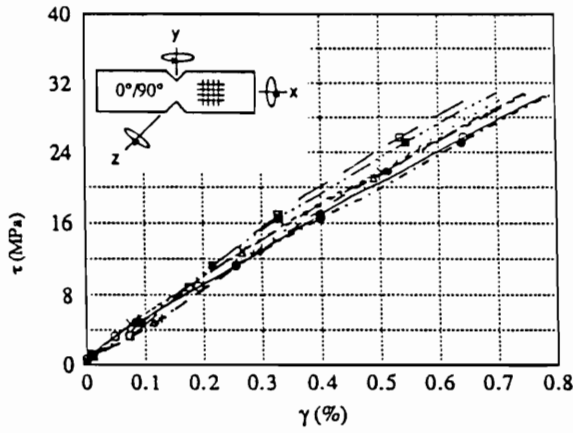


Fig.5.8a

Shear stress-strain data for $0^\circ/90^\circ$ graphite-epoxy specimen loaded in different orientations which were obtained by rotating the specimen about the x,y and z axis.

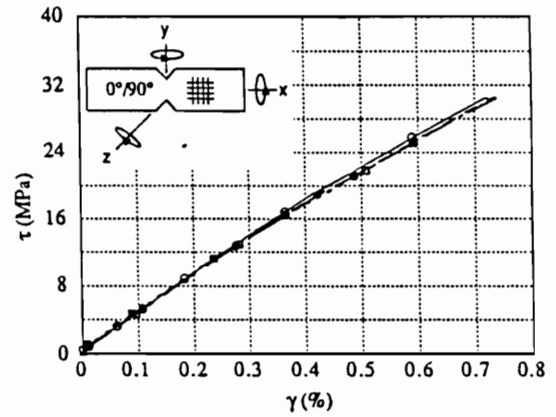


Fig.5.8b Average of front and back surface shear strains as a function of shear stress for $0^\circ/90^\circ$ graphite-epoxy specimen.

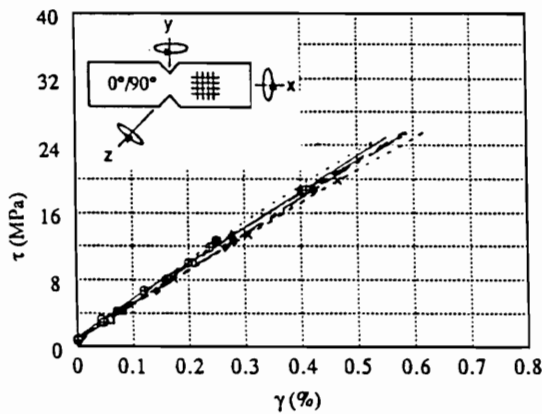


Fig.5.8c Shear stress-strain data for $0^\circ/90^\circ$ graphite-epoxy specimen with soft shim, when loaded in different orientations which were obtained by rotating the specimen about the x,y and z axis.

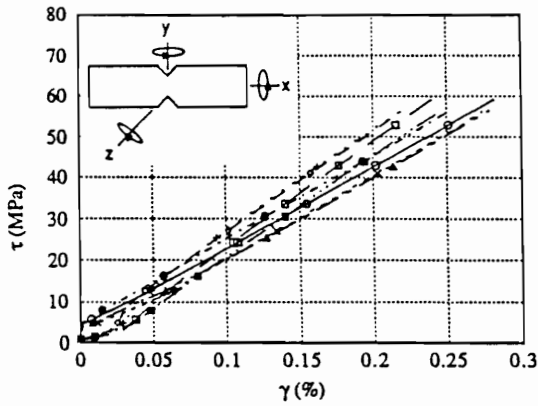


Fig.5.9a
Shear stress-strain data for aluminum specimen loaded in different orientations which were obtained by rotating the specimen about the x,y and z axis.

Fig.5.9b
Average of front and back surface shear strains as a function of shear stress for an aluminum specimen.

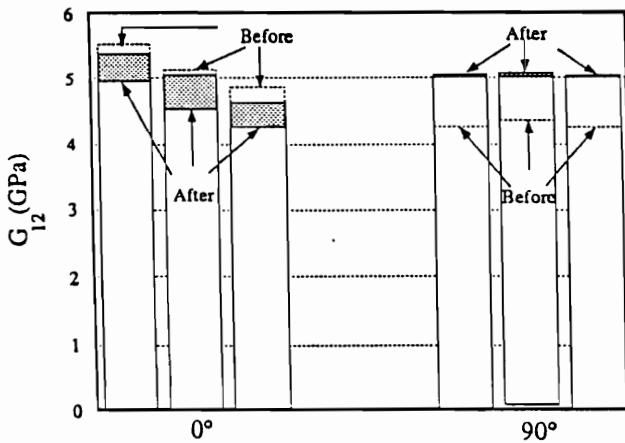
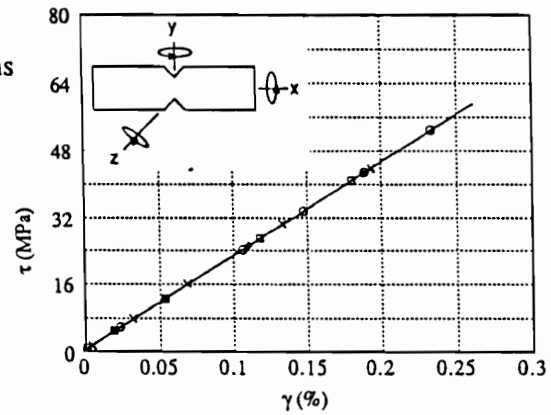


Fig.5.10
Calculated G_{12} for three graphite-epoxy 0° and 90° specimens, before and after application of correction factors. The areas shown shaded represent the ranges of values due to the uncertainty in the finite element calculated correction factors.

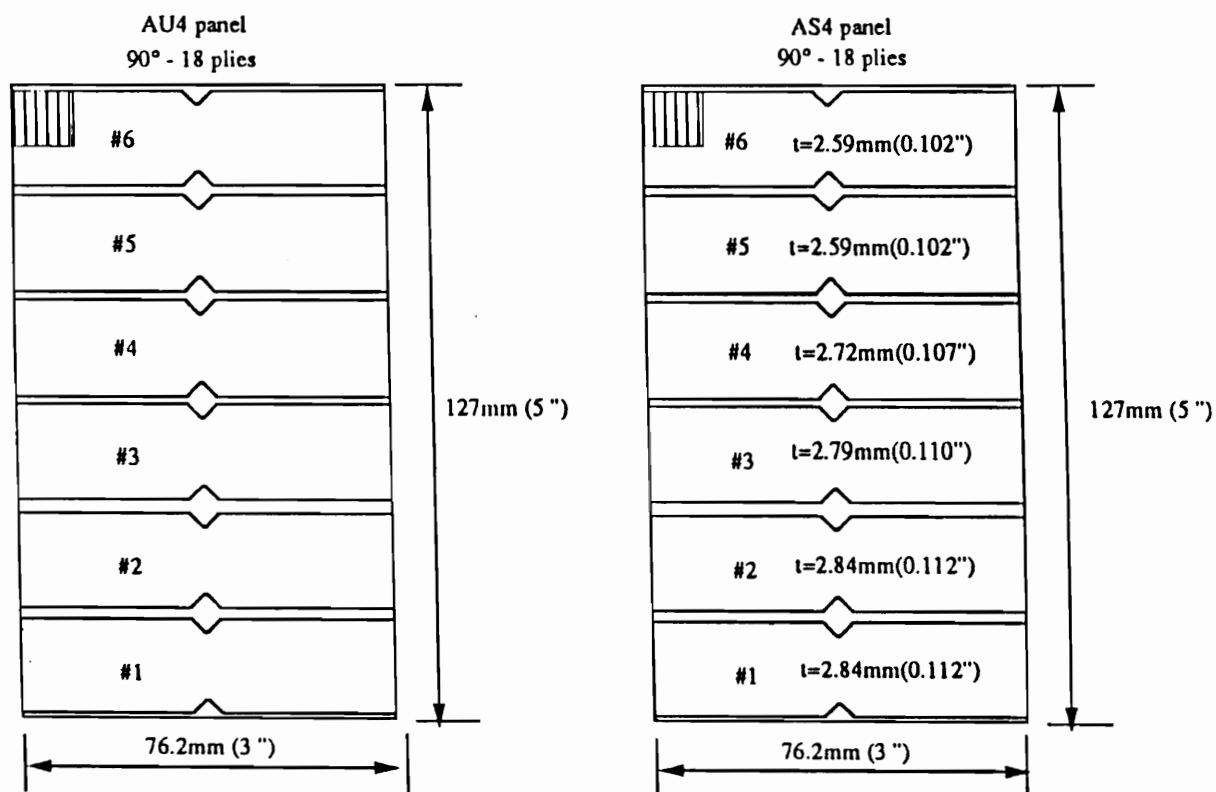


Fig.6.1 Panel size and specimen positions for AU4/BMIPES and AS4/BMIPES composite materials.

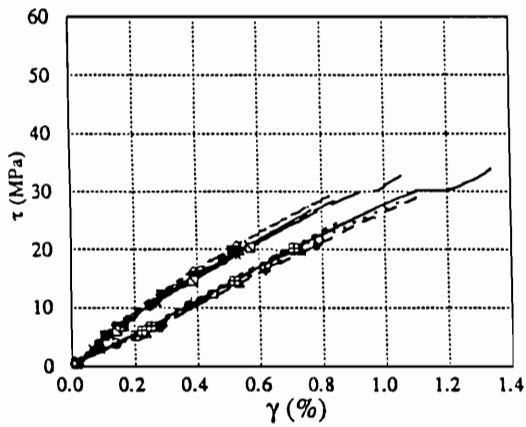


Fig.6.2
Shear stress-strain data from front and back
faces of six AU4/BMIPES specimens.

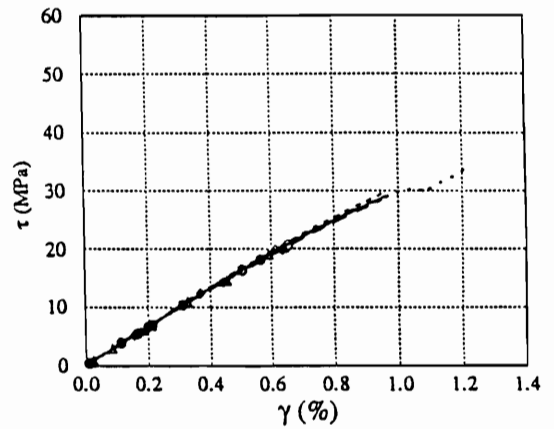


Fig.6.3
Average of front and back shear stress-strain
data of six AU4/BMIPES specimens.

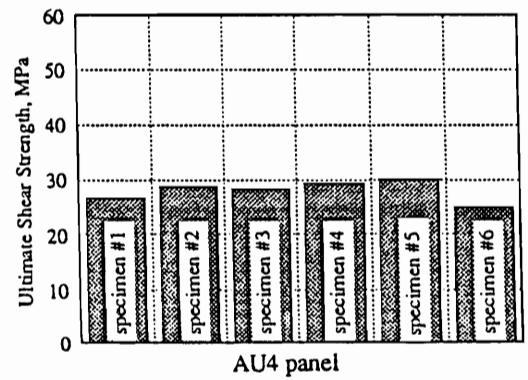
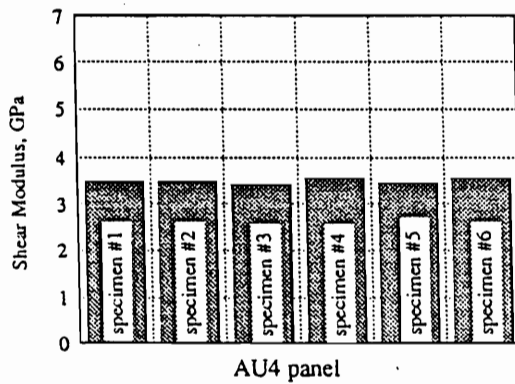


Fig.6.4 (a) G_{12} , (b) S_{12} of six AU4/BMIPES specimens.

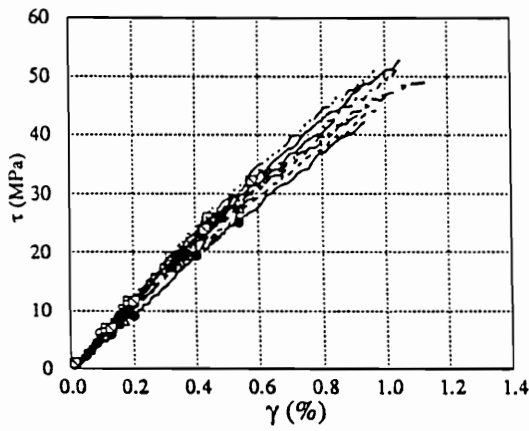


Fig. 6.5 Shear stress-strain data from front and back faces of six AS4/BMIPES specimens.

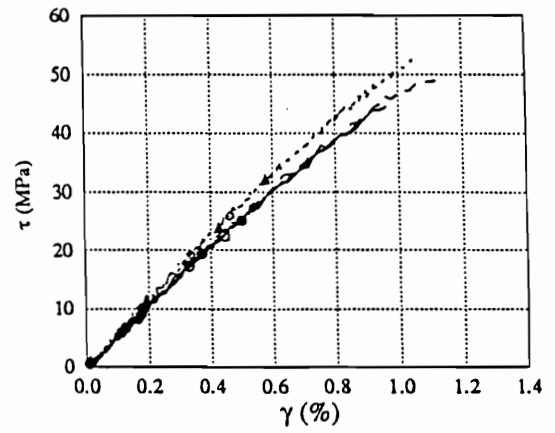


Fig. 6.6 Average of front and back shear stress-strain data of six AS4/BMIPES specimens.

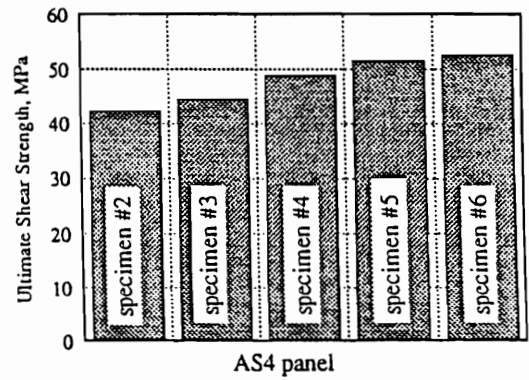
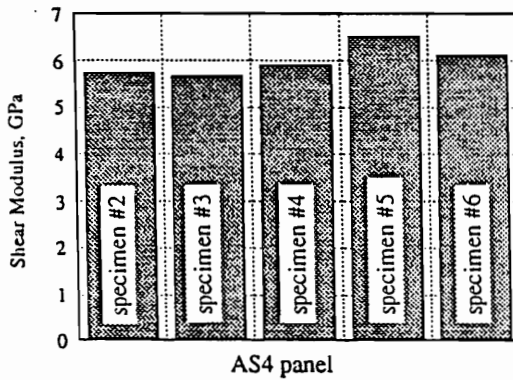


Fig. 6.7 (a) G_{12} , (b) S_{12} of six AS4/BMIPES specimens.

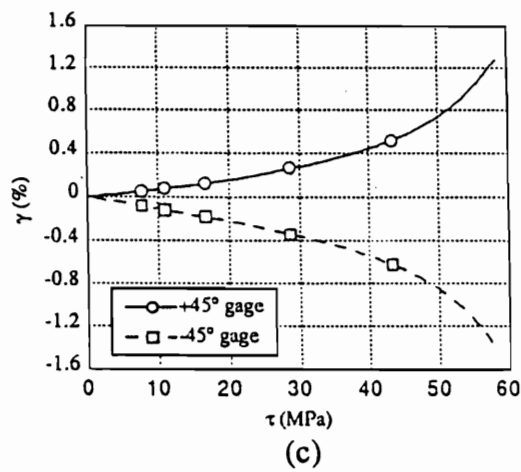
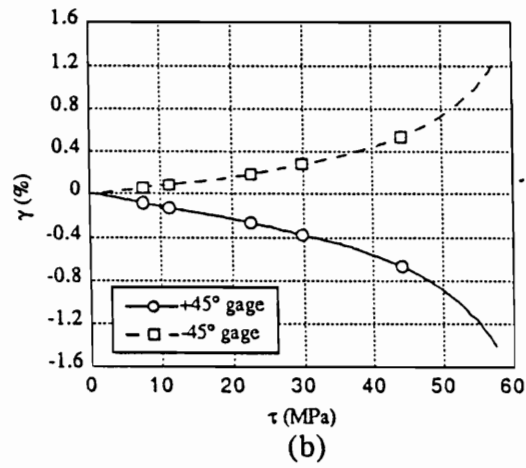
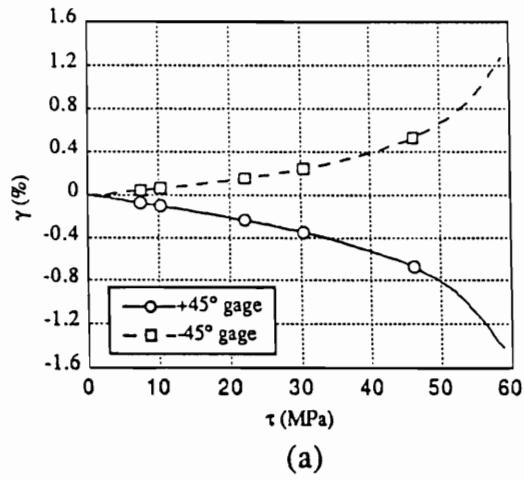


Fig.6.8 Strain vs. stress for typical 0° graphite-PES specimen cured at (a) 3.45MPa (500 psi), (b) 2.07MPa (300psi), (c) 1.03MPa (150psi). Gages are aligned at $\pm 45^\circ$ and 0° directions.

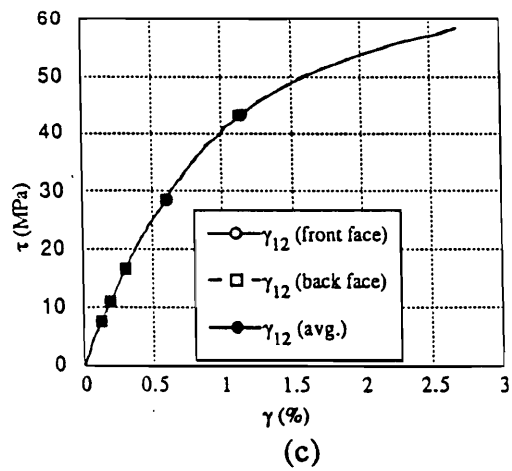
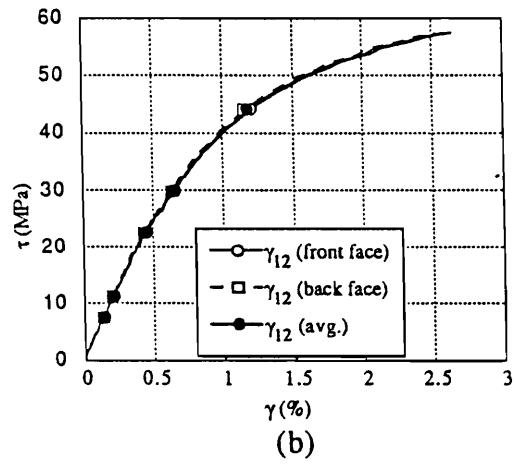
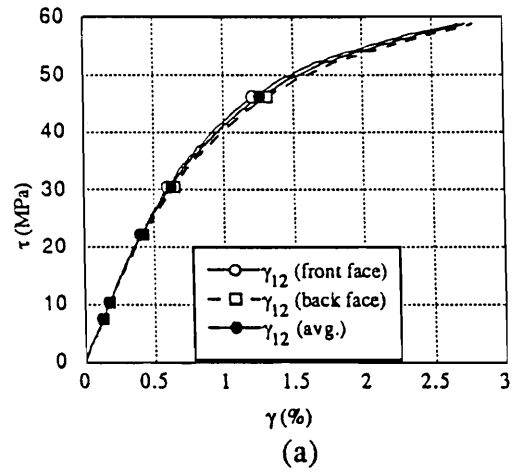


Fig.6.9 Shear stress-strain data for 0° graphite-PES specimens cured at (a) 3.45MPa (500 psi), (b) 2.07MPa (300psi), (c) 1.03MPa (150psi).

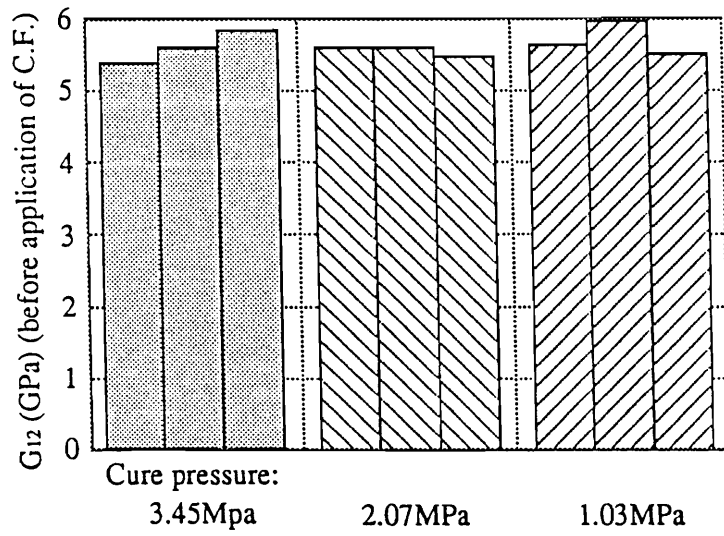


Fig.6.10 Shear moduli for 0° graphite-PES specimens cured at (a) 3.45MPa (500psi), (b) 2.07MPa (300psi), (c) 1.03MPa (150psi).

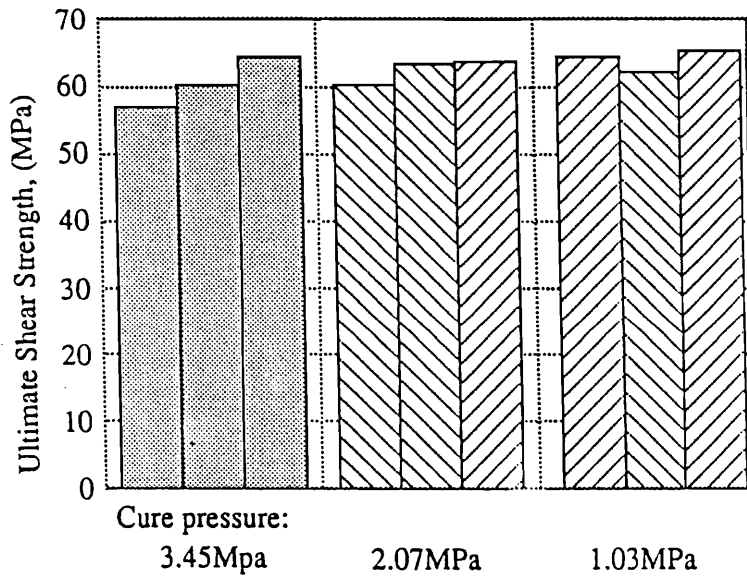


Fig.6.11 Shear strength for 0° graphite-PES specimens cured at (a) 3.45MPa (500psi), (b) 2.07MPa (300psi), (c) 1.03MPa (150psi).

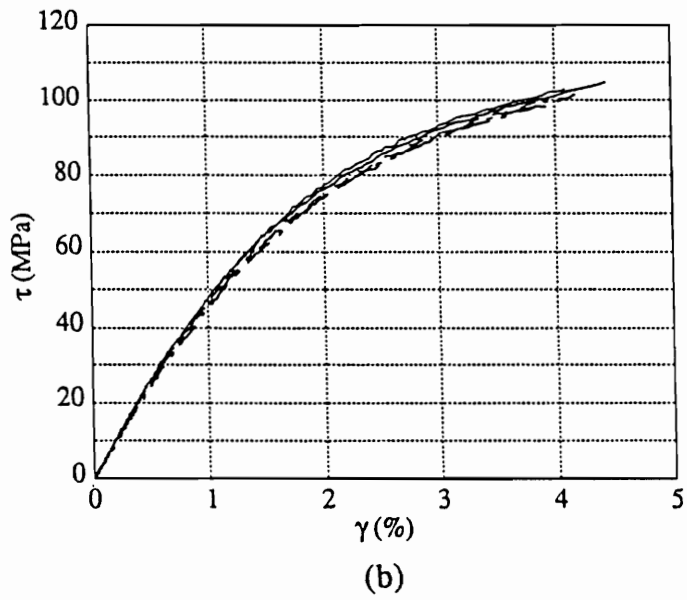
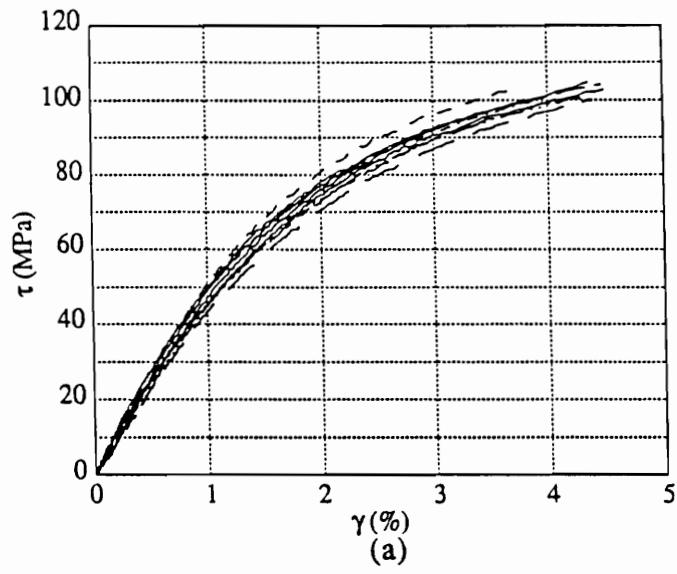


Fig.7.1 (a) Shear stress-strain data from front and back faces, (b) average of front and back shear stress-strain data of the uniweave $[0/90]_{7s}$ specimens.

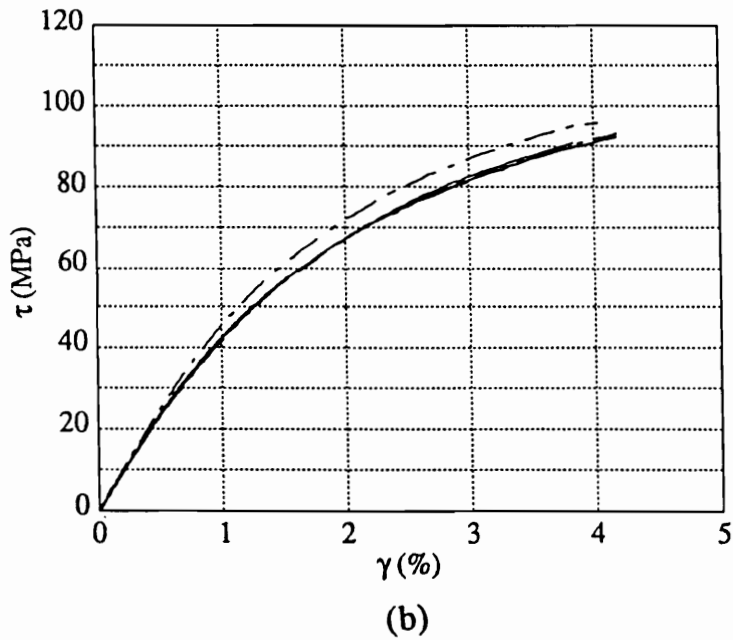
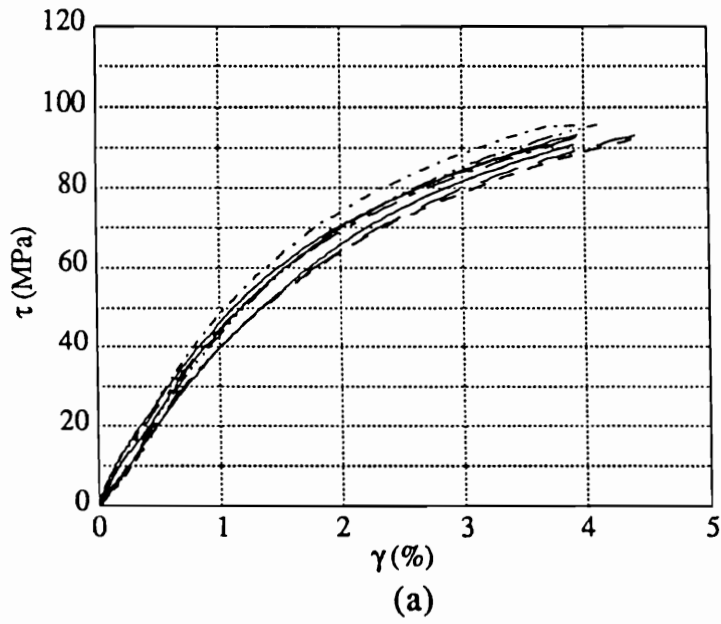


Fig.7.2 (a) Shear stress-strain data from front and back faces, (b) average of front and back shear stress-strain data of the plain weave $[0/90]_{6s}$ specimens.

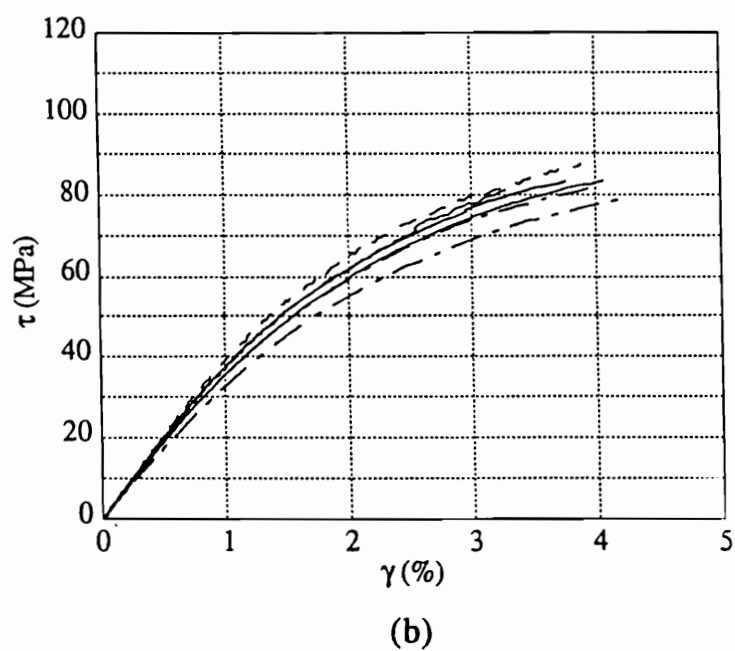
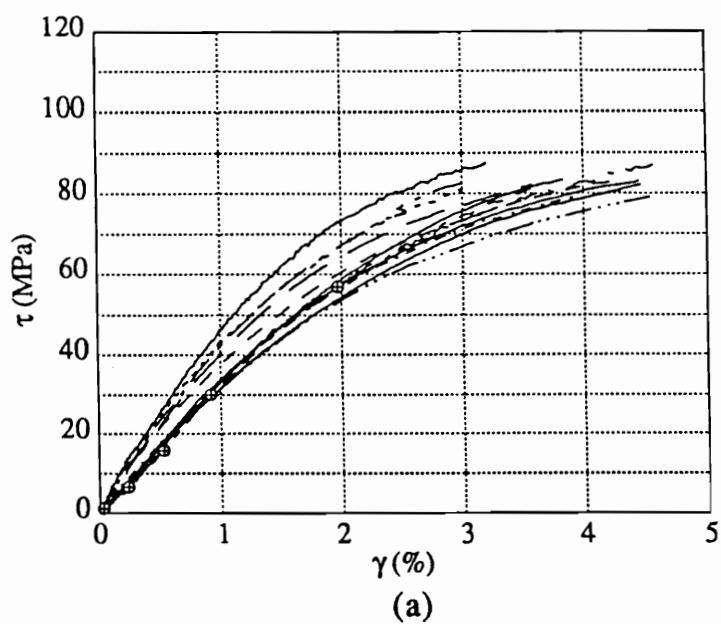


Fig.7.3 (a) Shear stress-strain data from front and back faces, (b) average of front and back shear stress-strain data of the plain weave $[0/90]_{2s}$ specimens.

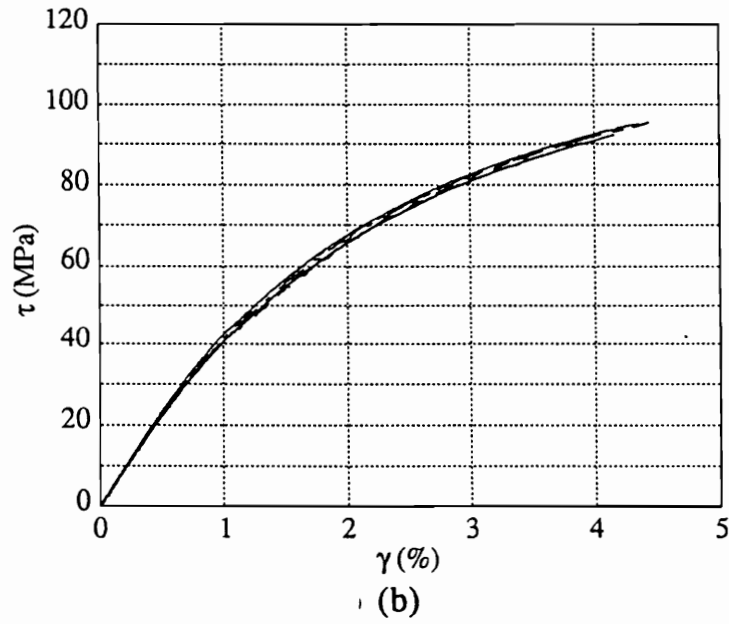
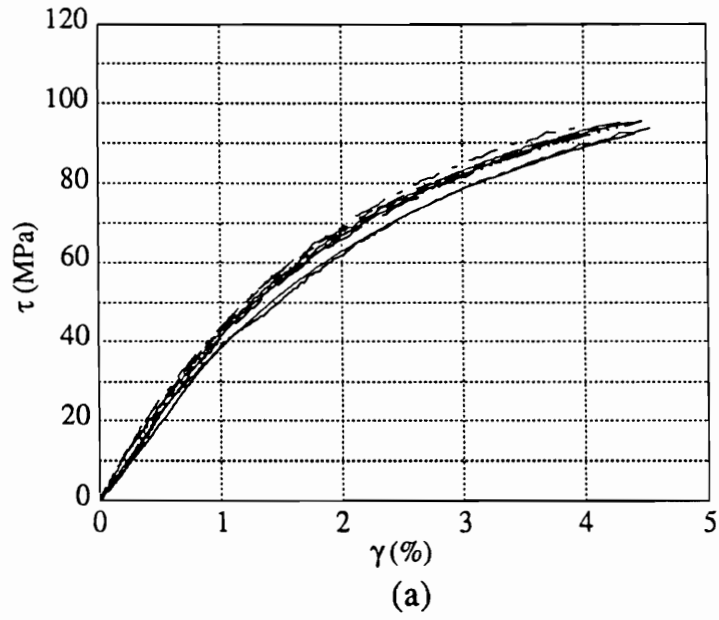


Fig.7.4 (a) Shear stress-strain data from front and back faces, (b) average of front and back shear stress-strain data of the 5HS $[0/90]_{4s}$ specimens.

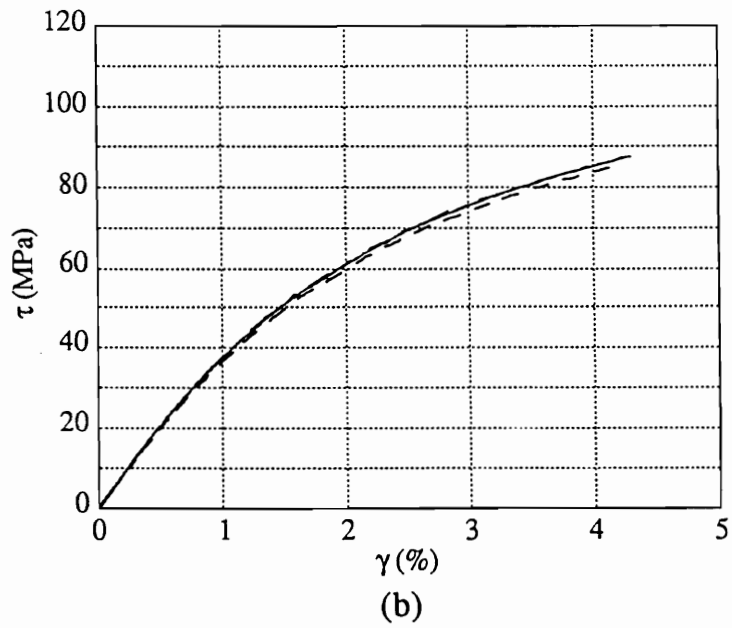
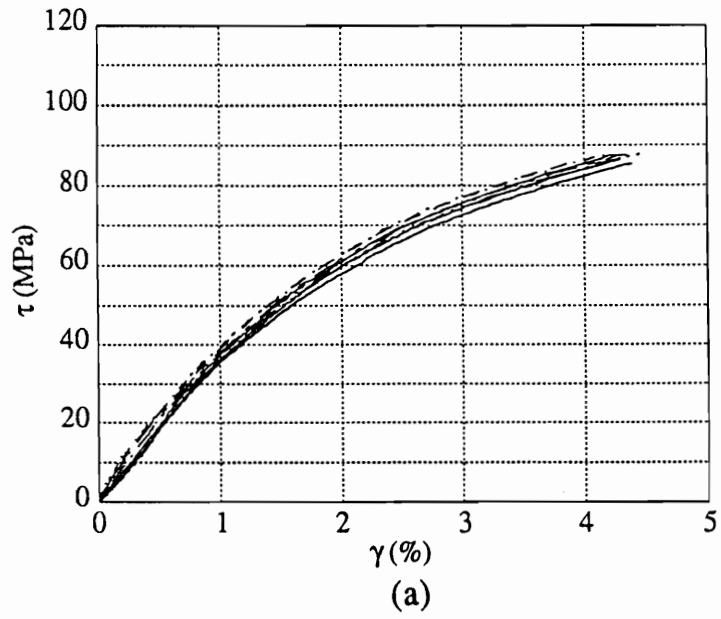


Fig.7.5 (a) Shear stress-strain data from front and back faces, (b) average of front and back shear stress-strain data of the 8HS $[0/90]_{3s}$ specimens.

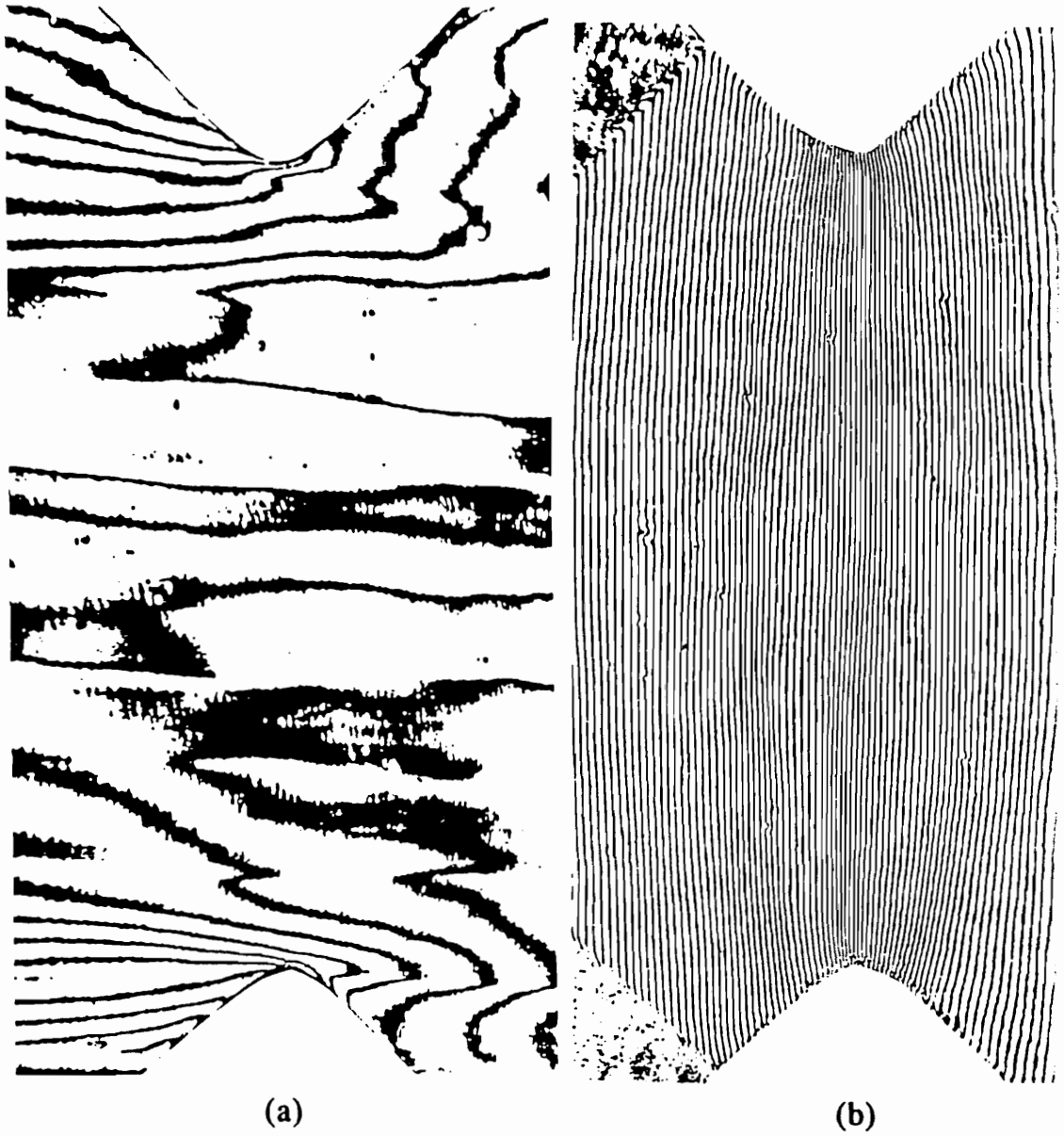


Fig.7.6a&b Typical moiré fringe patterns of the uniweave $[0/90]_{7s}$ specimen at an applied load of 1312N. (a) u-field, (b) v-field.

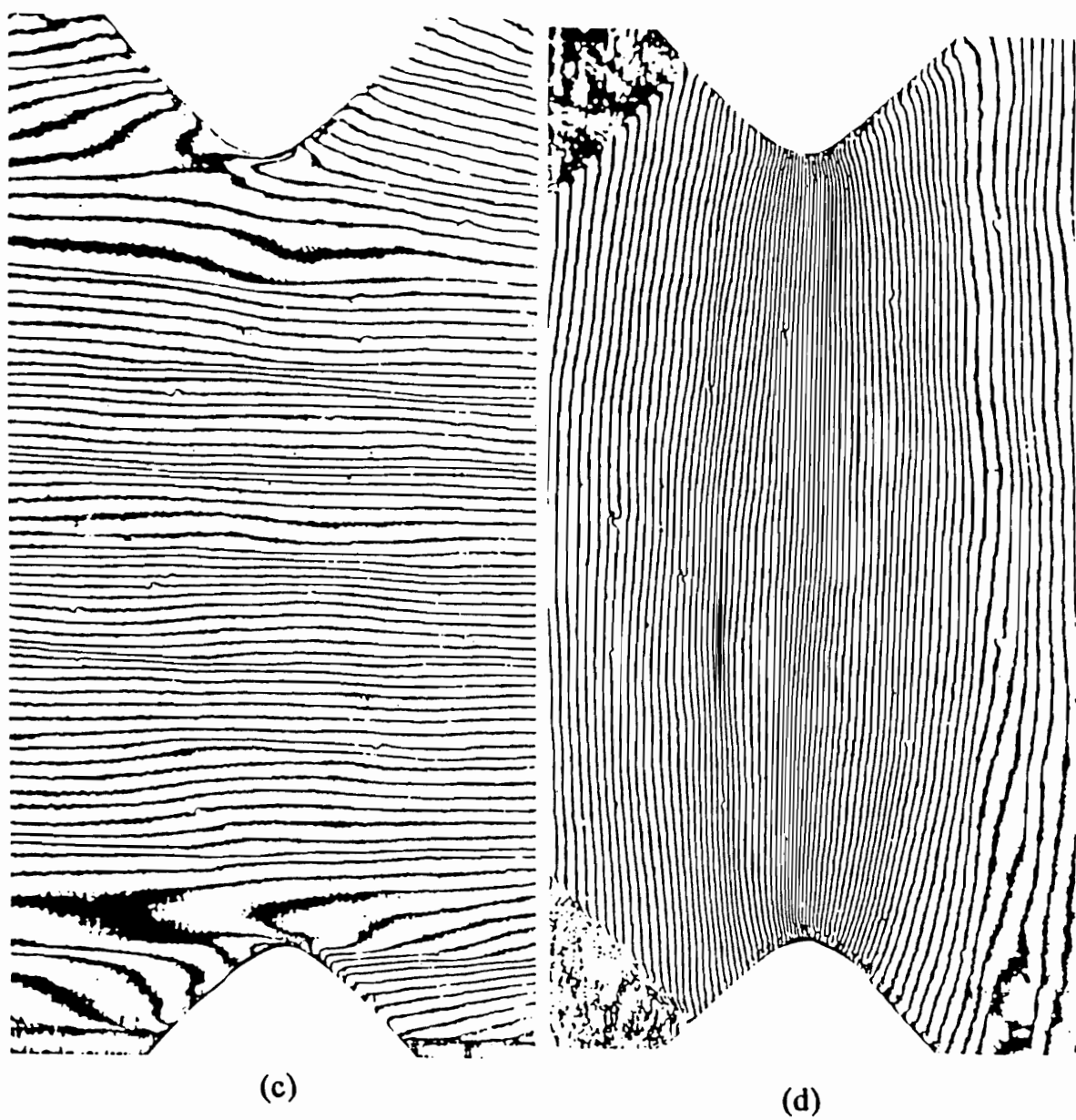


Fig.7.6c&d Typical moiré fringe patterns of the uniweave $[0/90]_{7s}$ specimen at an applied load of 1770N. (c) u-field (half density), (d) v-field (half density).

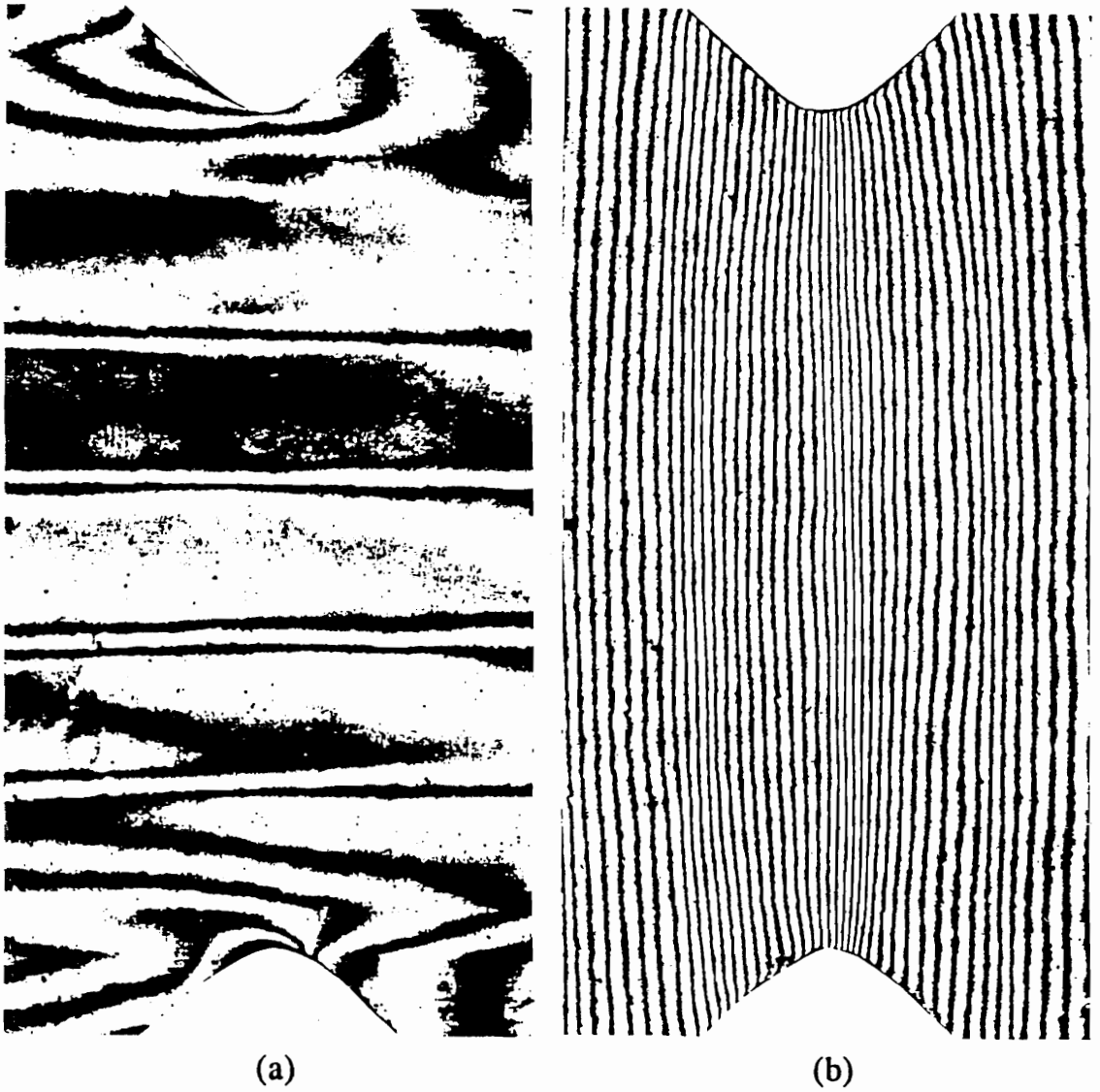


Fig.7.7a&b Typical moiré fringe patterns of the plain weave $[0/90]_{6s}$ specimen at an applied load of 854N. (a) u-field, (b) v-field.

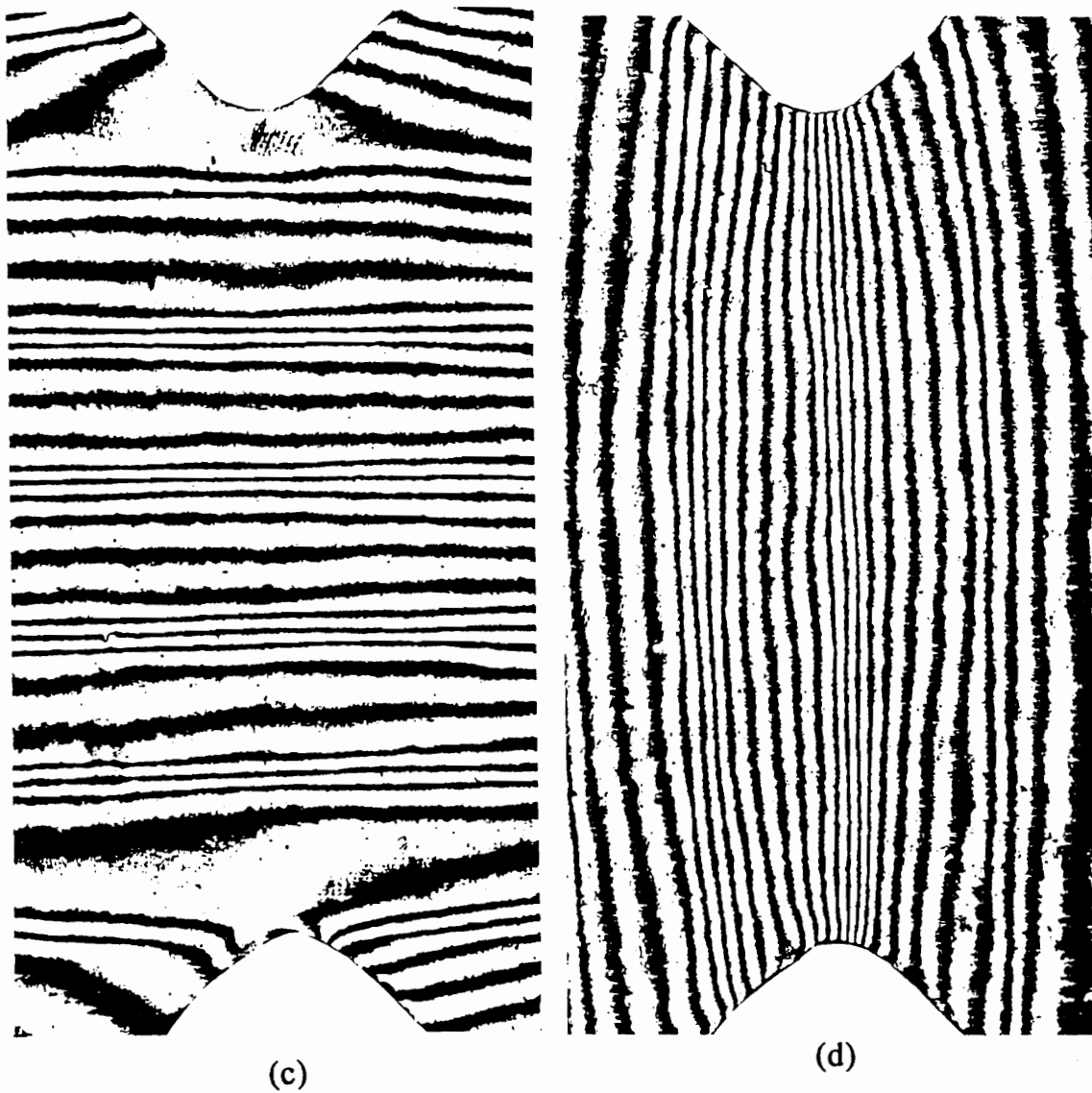


Fig.7.7c&d Typical moiré fringe patterns of the plain weave $[0/90]_{6S}$ specimen at an applied load of 796N. (c) u-field (half density), (d) v-field (half density).

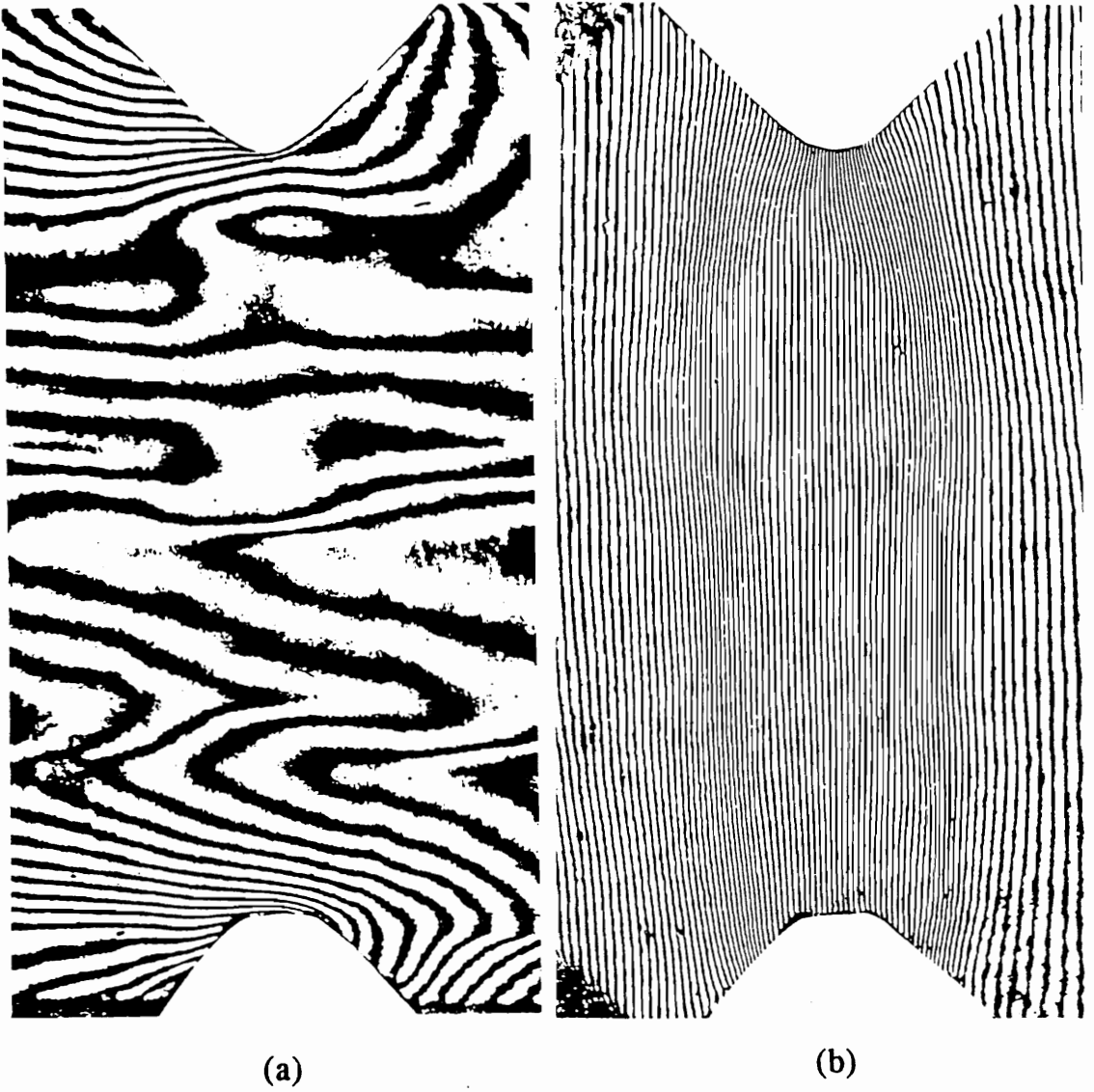


Fig.7.8a&b Typical moiré fringe patterns of the plain weave $[0/90]_{2s}$ specimen at an applied load of 961N. (a) u-field, (b) v-field.

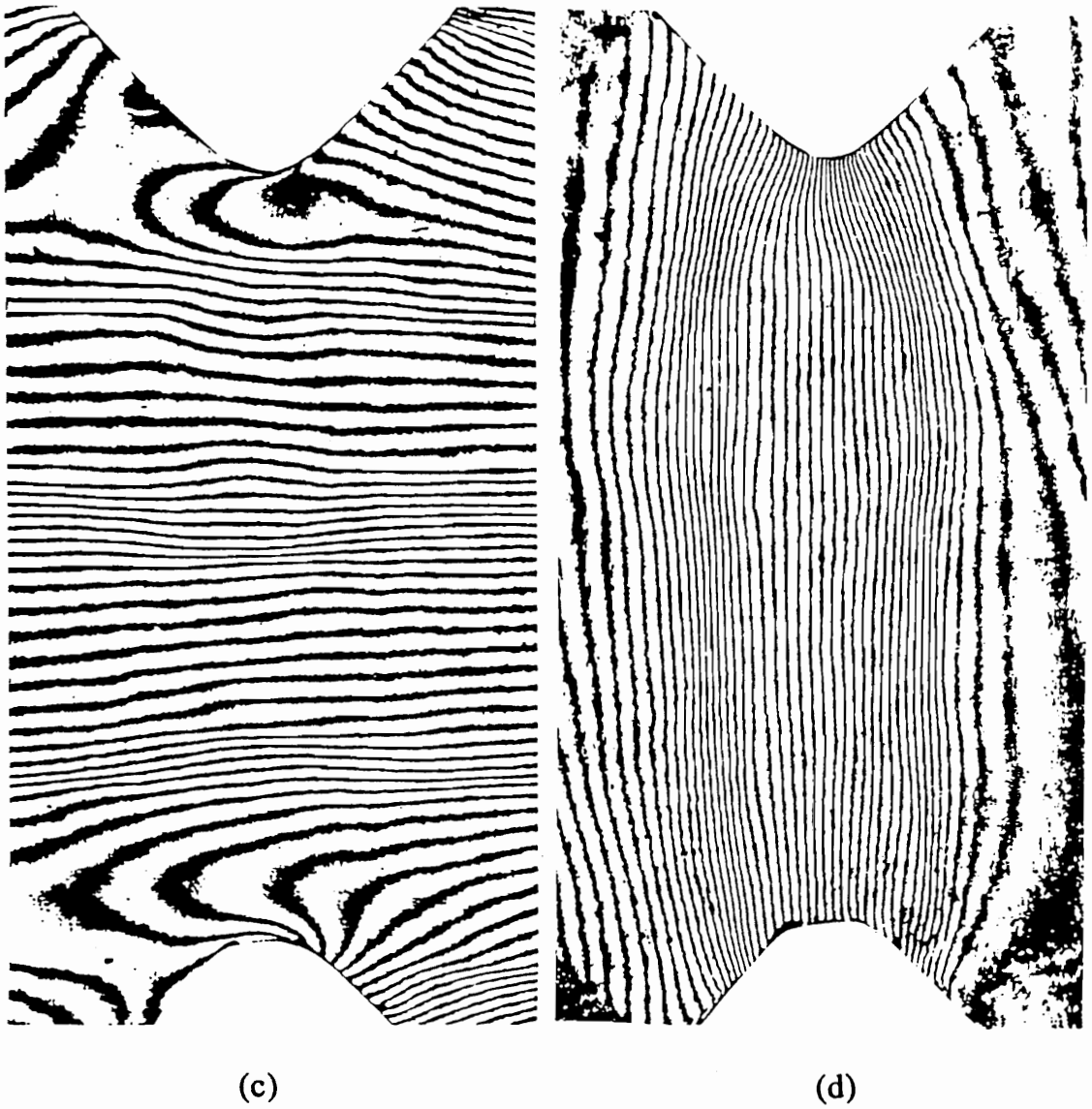


Fig.7.8c&d Typical moiré fringe patterns of the plain weave [0/90]_{2s} specimen at an applied load of 961N. (c) u-field (half density), (d) v-field (half density).

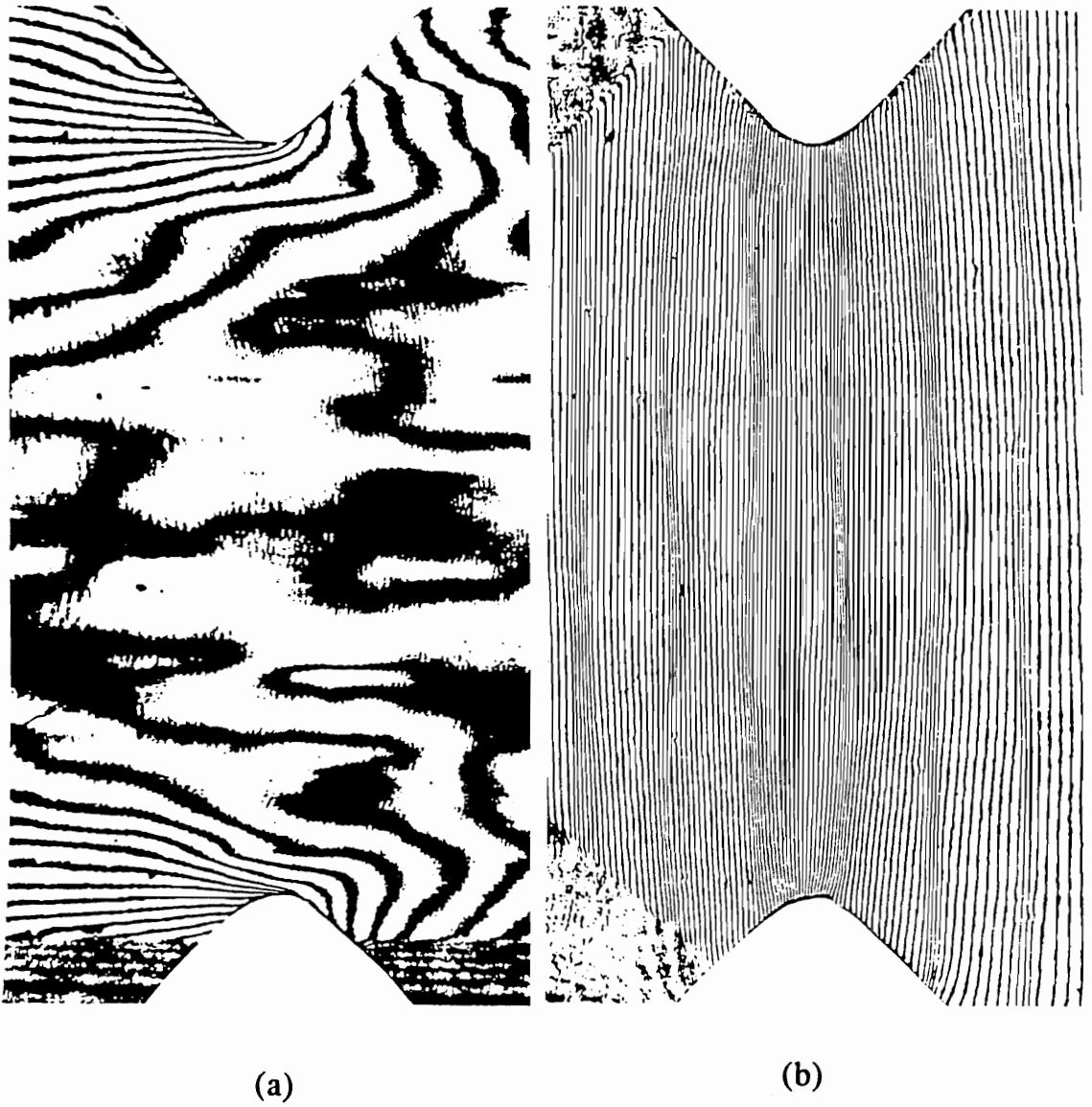
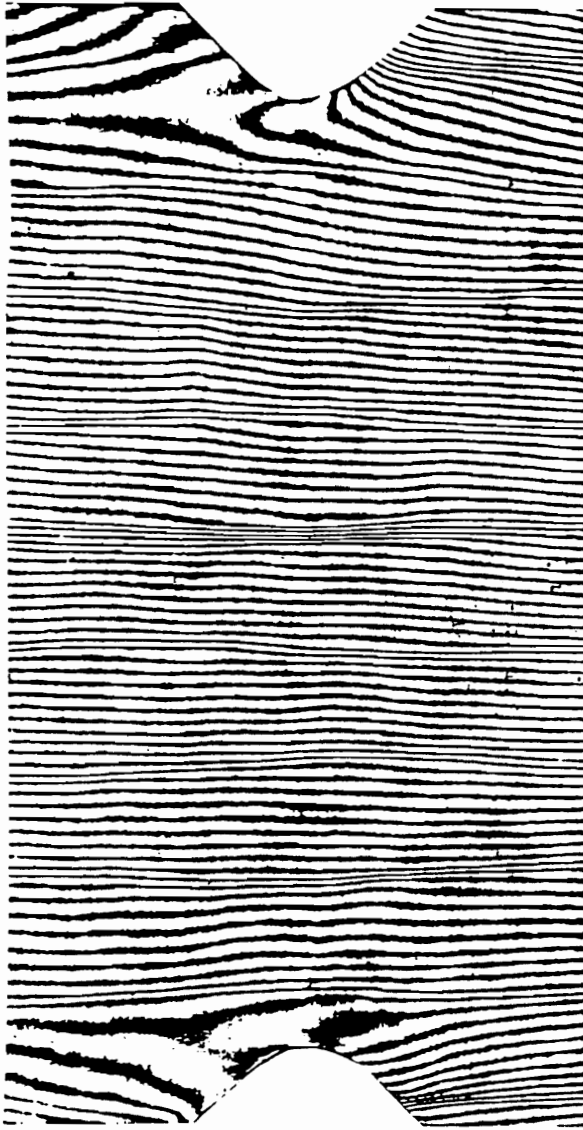
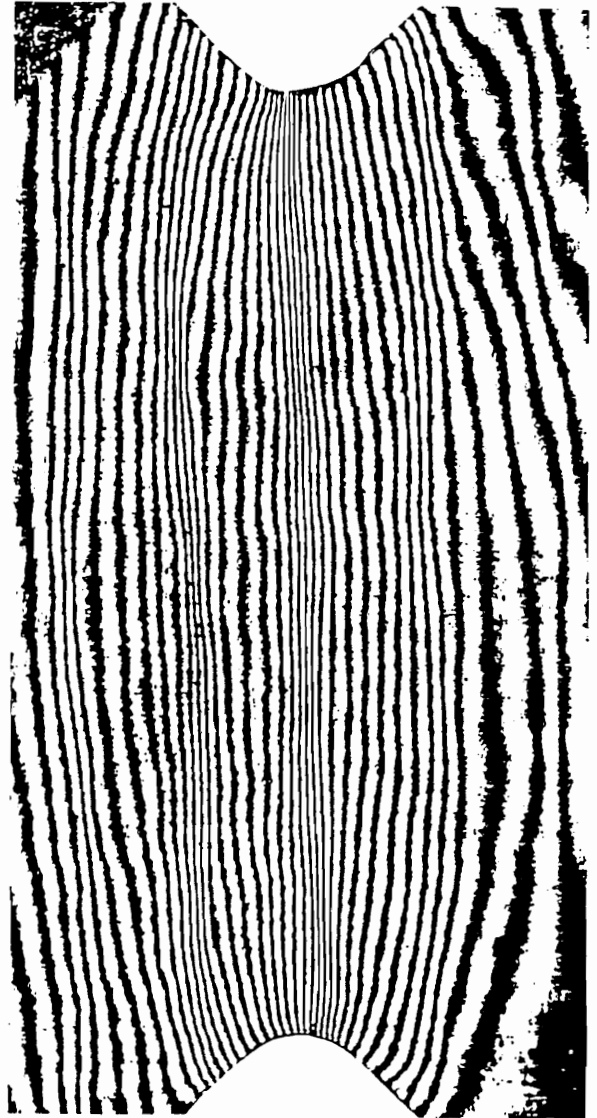


Fig.7.9a&b Typical moiré fringe patterns of the 5HS $[0/90]_4s$ specimen at an applied load of 1316N. (a) u-field, (b)v-field.



(c)

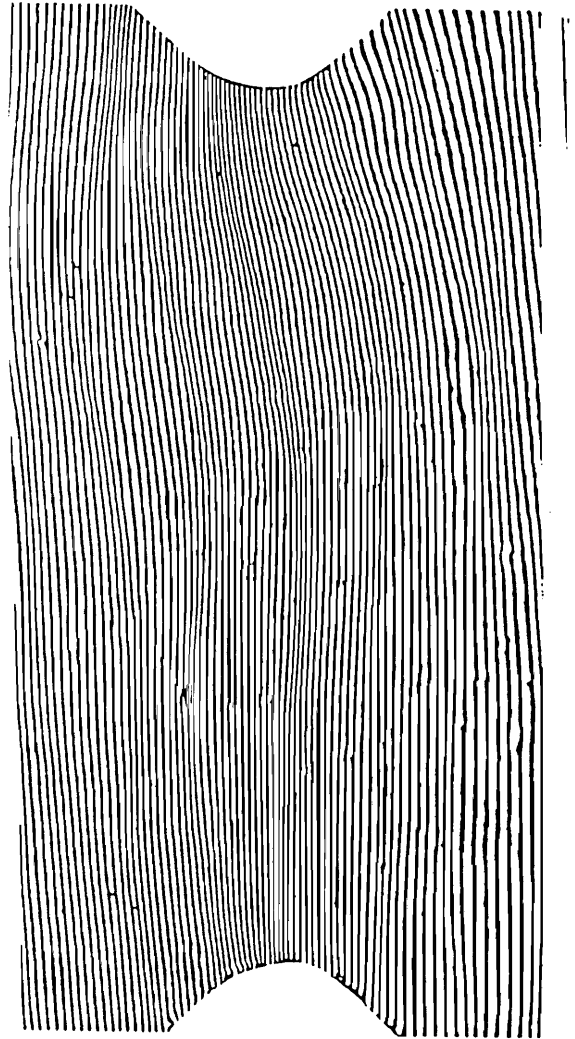


(d)

Fig.7.9c&d Typical moire fringe patterns of the 5HS $[0/90]_{4s}$ specimen at an applied load of 1463N. (c) u-field (half density), (d) v-field (half density).



(a)



(b)

Fig.7.10a&b Typical moire fringe patterns of the 8HS $[0/90]_{3s}$ specimen at an applied load of 1170N. (a) u-field, (b)v-field.

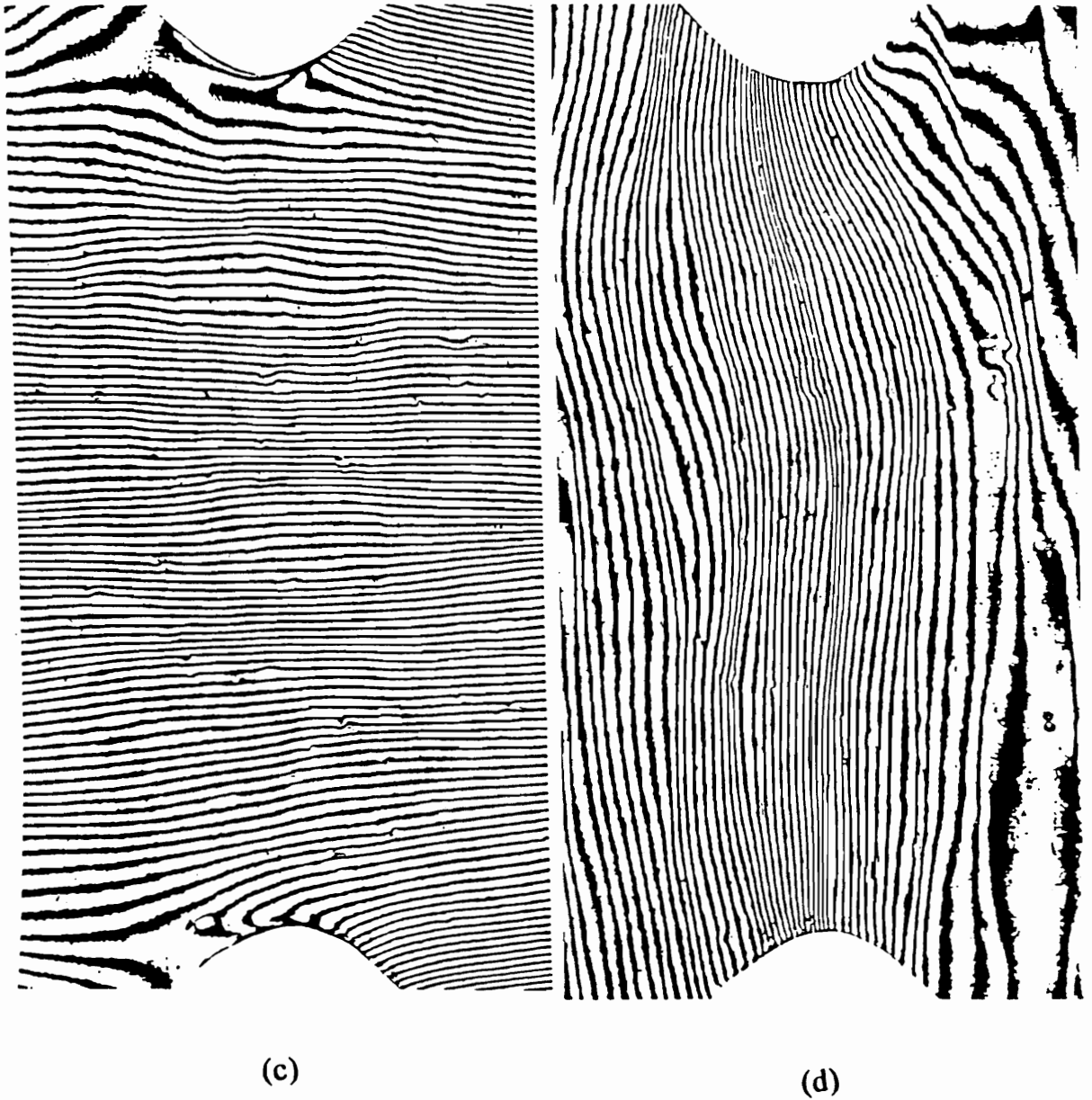


Fig.7.10c&d Typical moiré fringe patterns of the 8HS $[0/90]_{3s}$ specimen at an applied load of 1601N. (c) u-field (half density), (d) v-field (half density).

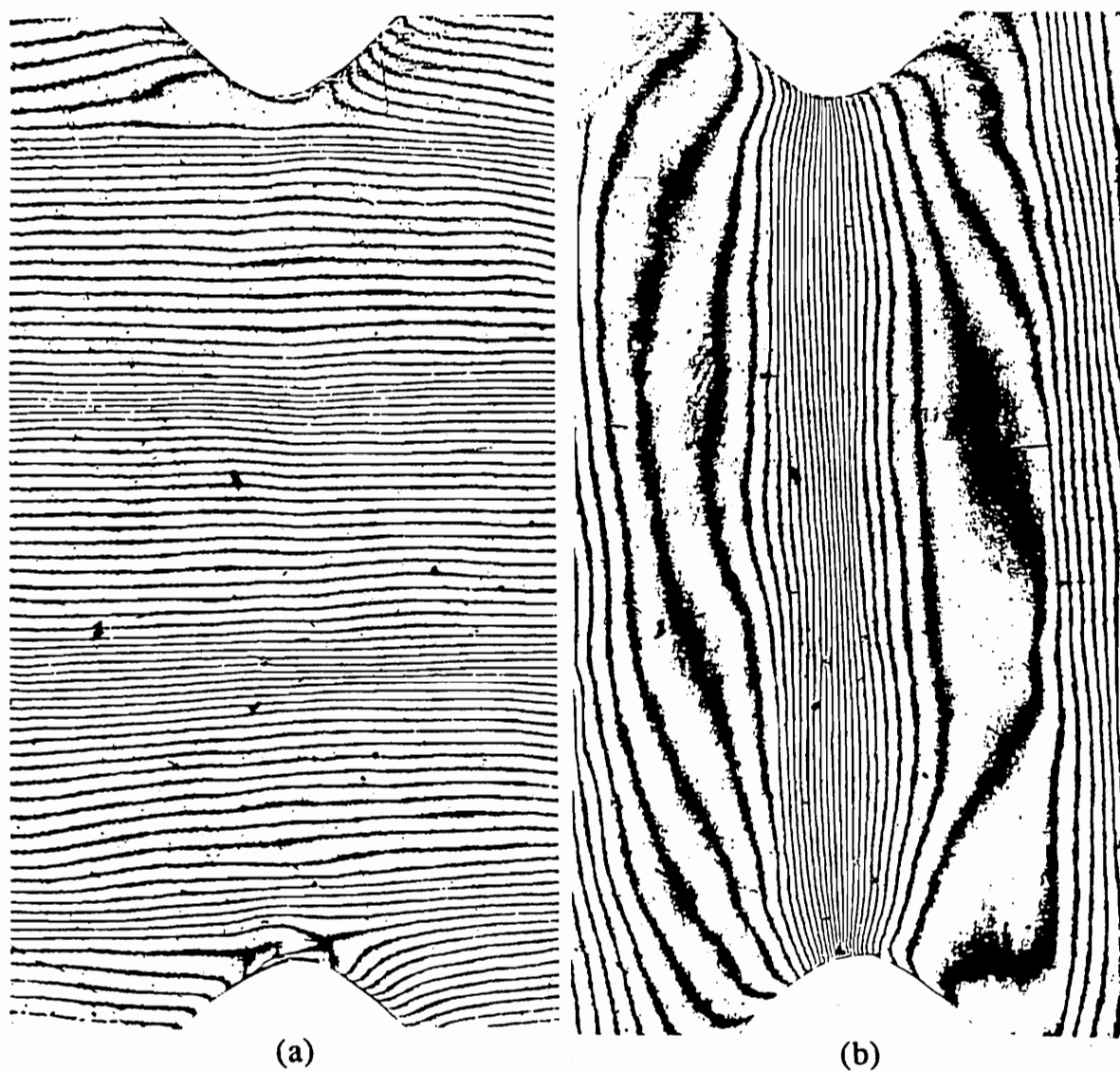


Fig.7.11 Supplement moiré fringe patterns of the plain weave $[0/90]_{2s}$ specimen at an applied load of 1059N. (a) u-field (half density), (b) v-field (half density).

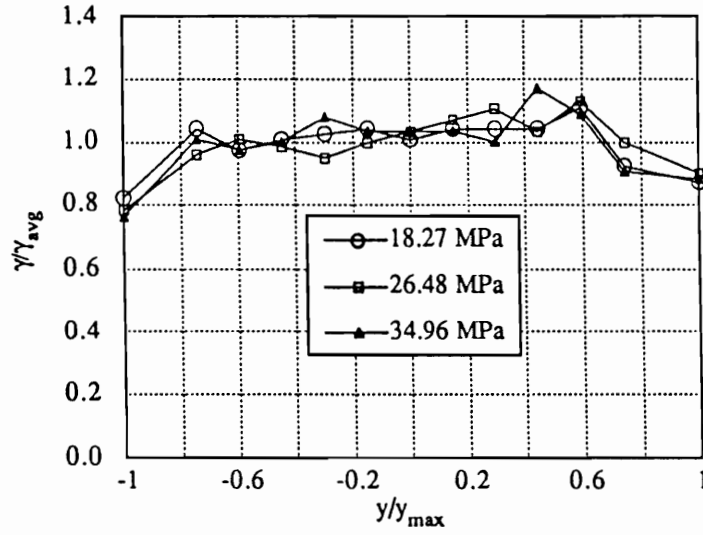


Fig.7.12 Shear strains across the notches, normalized with respect to the average shear strain, for uniweave $[0/90]_{7s}$ specimens.

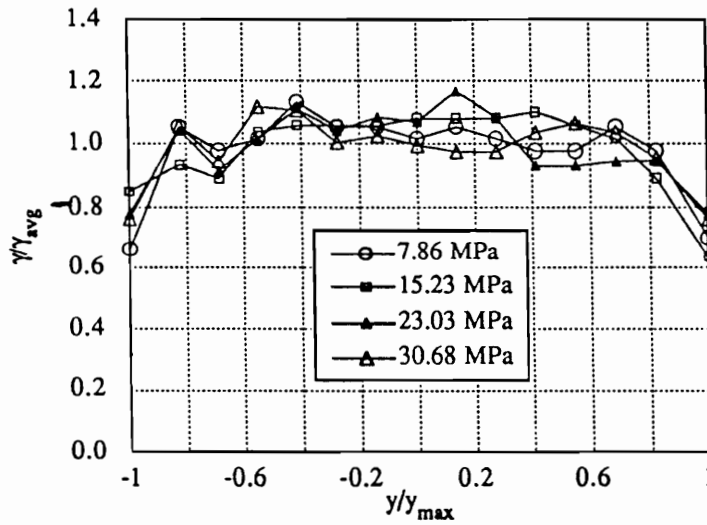


Fig.7.13 Shear strains across the notches, normalized with respect to the average shear strain, for plain weave $[0/90]_{6s}$ specimens.

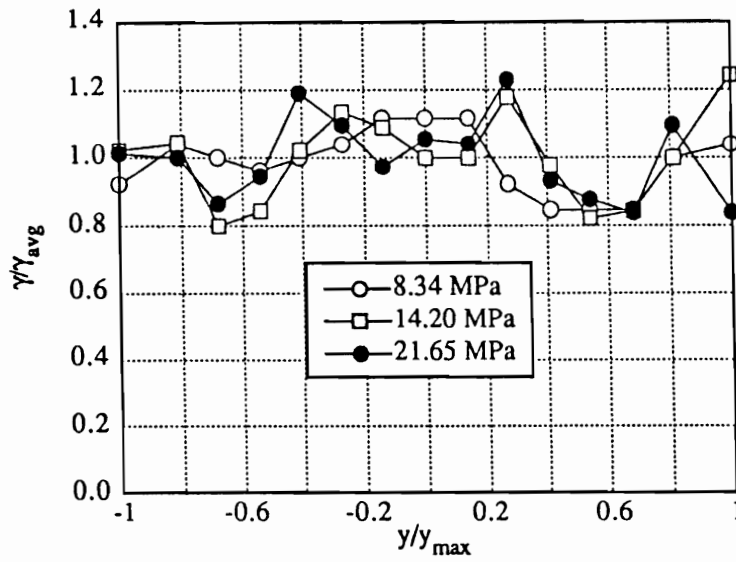


Fig.7.14 Shear strains across the notches, normalized with respect to the average shear strain, for plain weave $[0/90]_{2s}$ specimens.

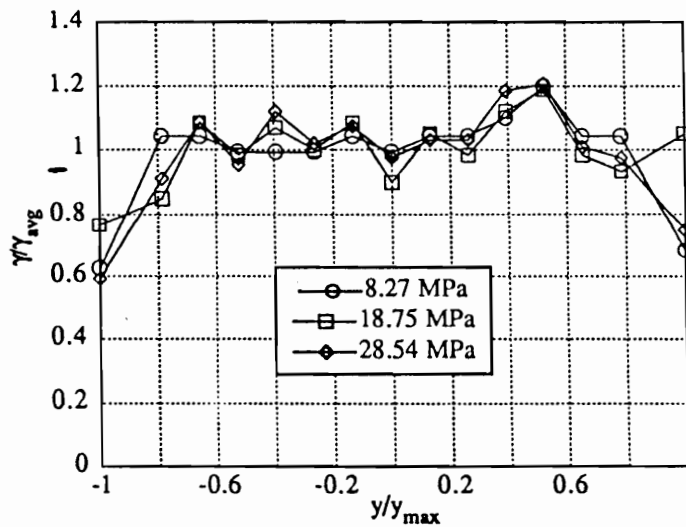


Fig.7.15 Shear strains across the notches, normalized with respect to the average shear strain, for 5HS $[0/90]_{4s}$ specimens.

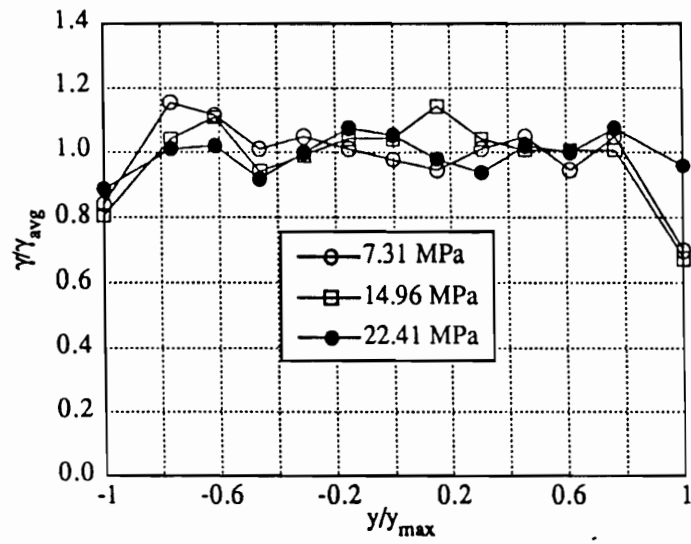


Fig.7.16 Shear strains across the notches, normalized with respect to the average shear strain, for 8HS [0/90]_{3s} specimens.

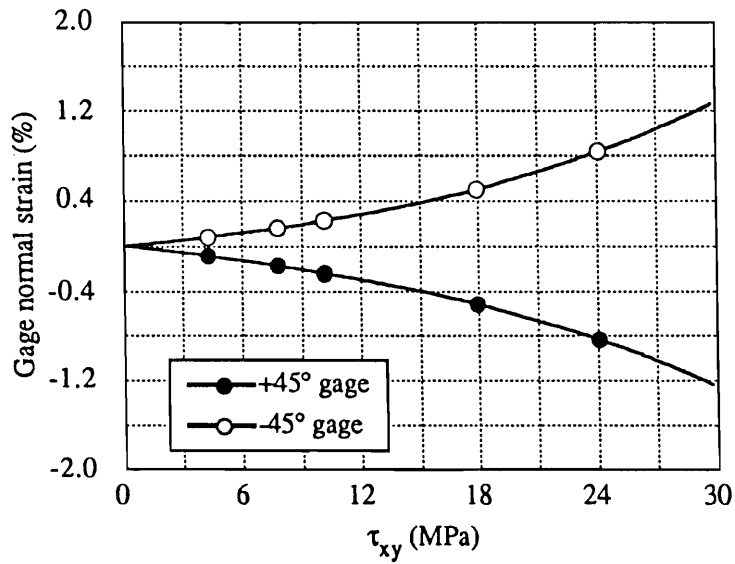


Fig.7.17 Strain vs. stress for typical epoxy based aluminum particulate composite specimen. Gages are aligned at $\pm 45^\circ$ and 0° directions.

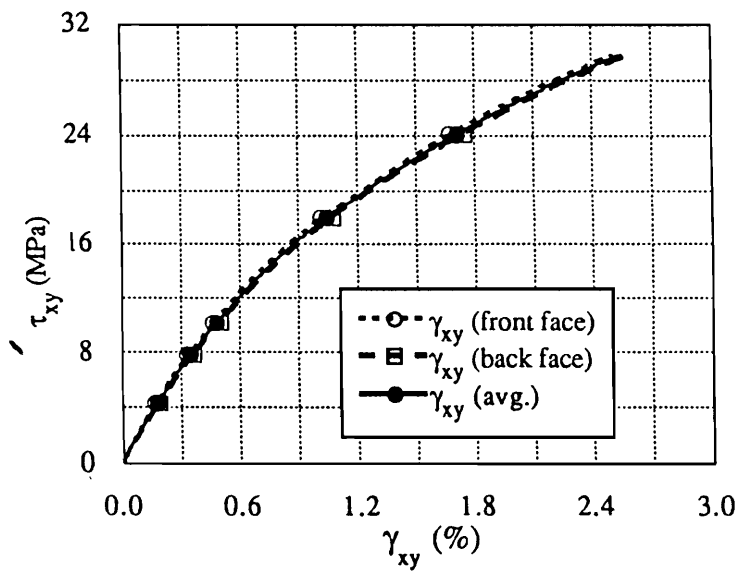


Fig.7.18 Average of front and back shear stress-strain data of epoxy based aluminum particulate composite specimens.

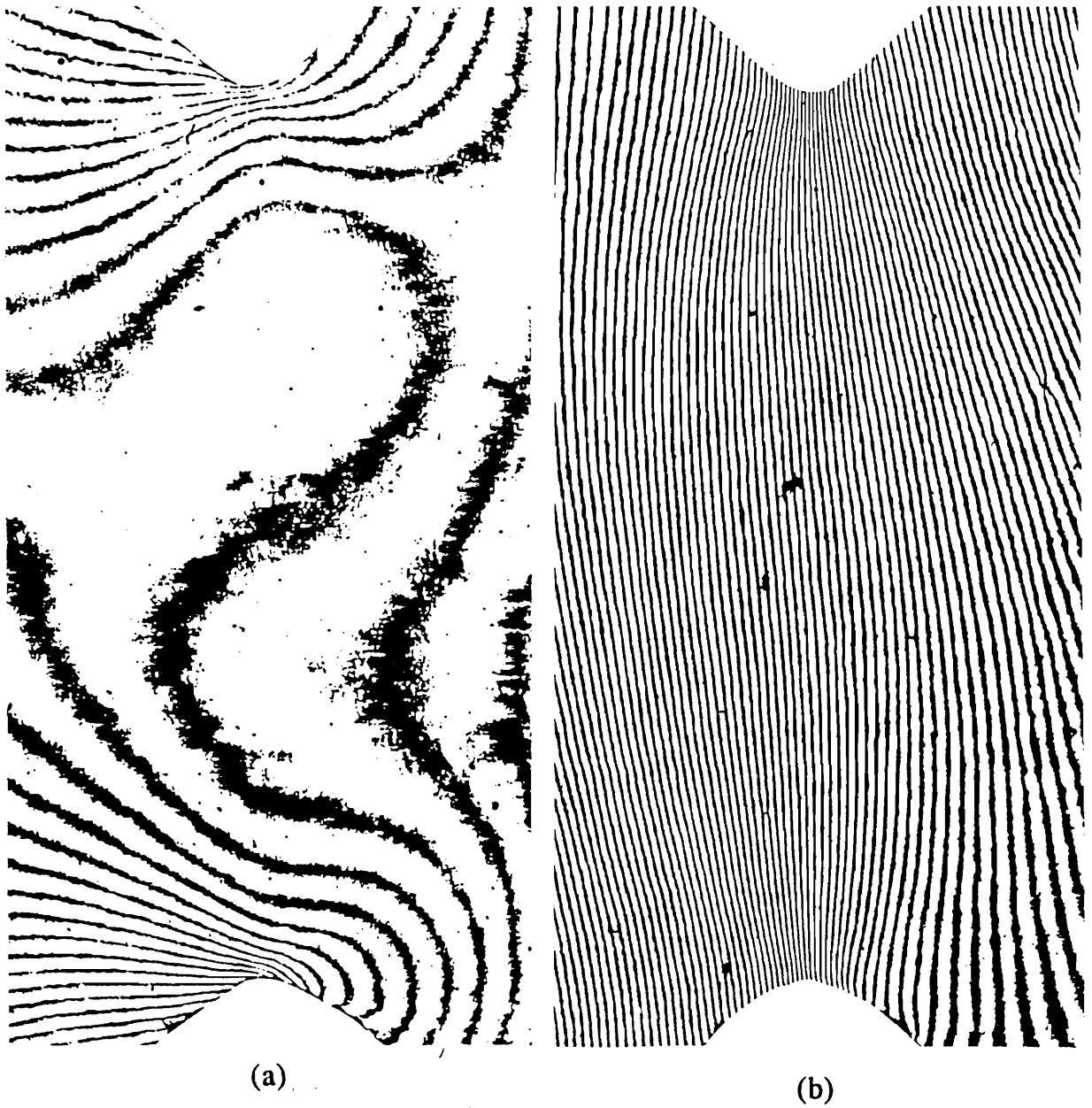


Fig.7.19 Moiré fringe patterns of the epoxy based aluminum particulate composite specimen at an applied load of 476N. (a) u-field, (b) v-field.

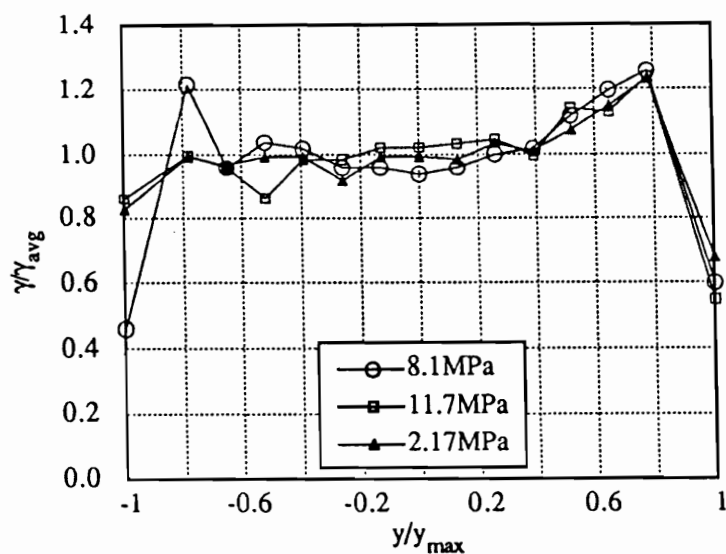


Fig.7.20 Shear strains across the notches, normalized with respect to the average shear strain, for epoxy-based aluminum particulate composite.

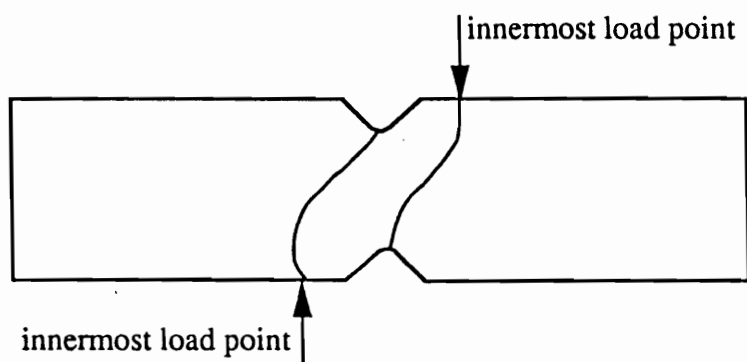


Fig.7.21 Failed specimen configuration for epoxy based aluminum particulate composite specimen.

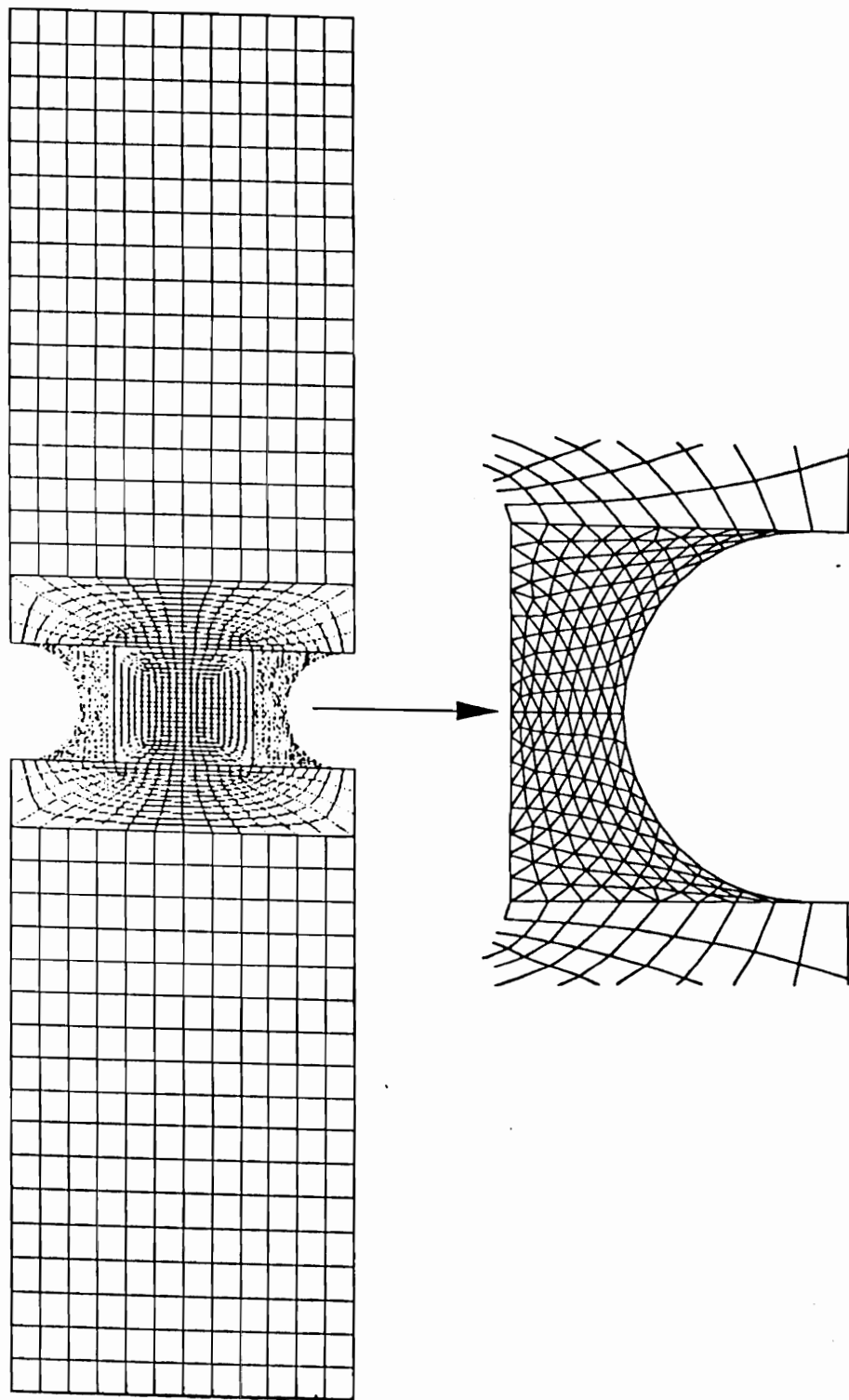


Fig.8.2 Finite element mesh for 3" U-notch specimen.

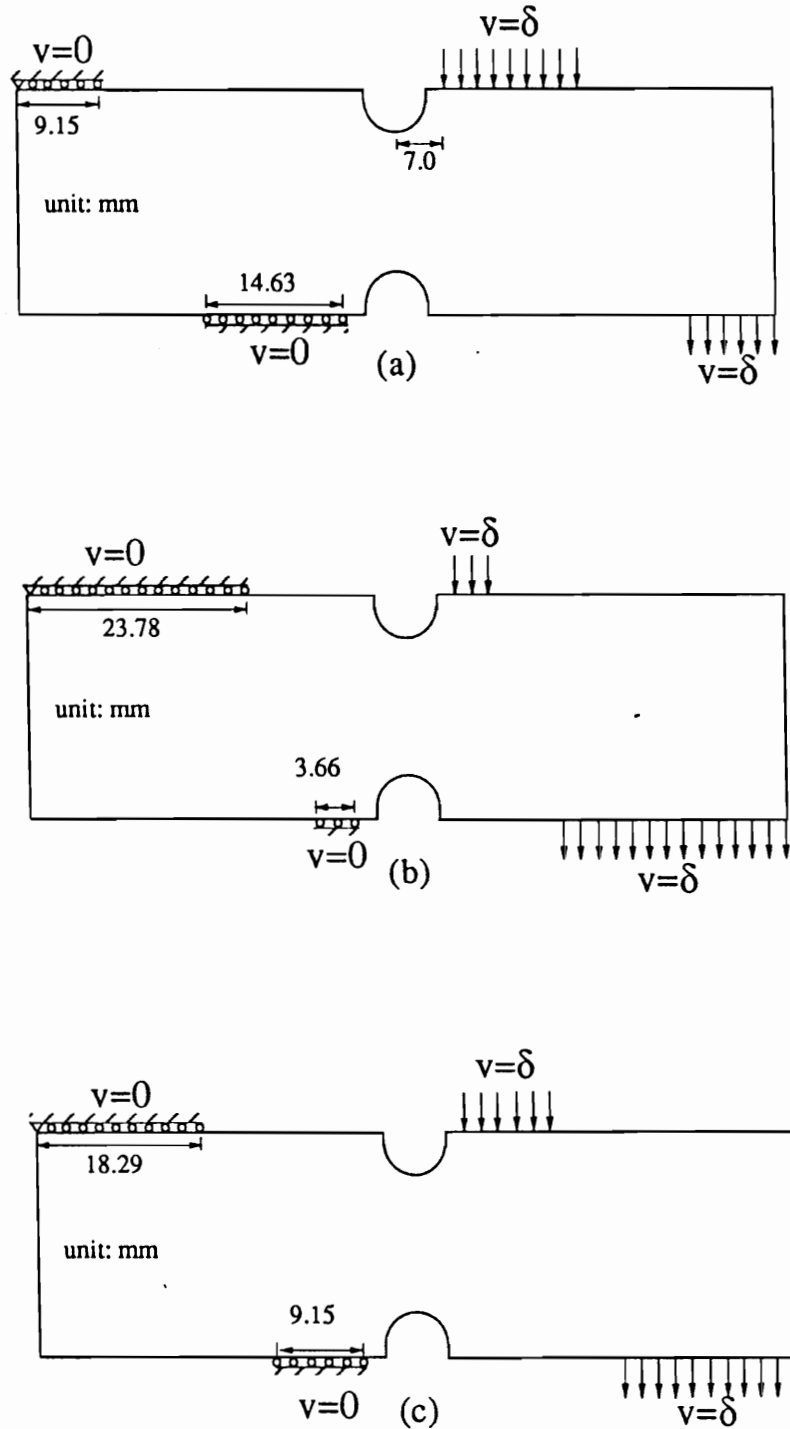


Fig.8.3 Finite element models for 3" U-notch Iosipescu specimen tested in modified Wyoming fixture, (a) 0° specimen, (b) 90° specimen, (c) $0^\circ/90^\circ$ specimen.

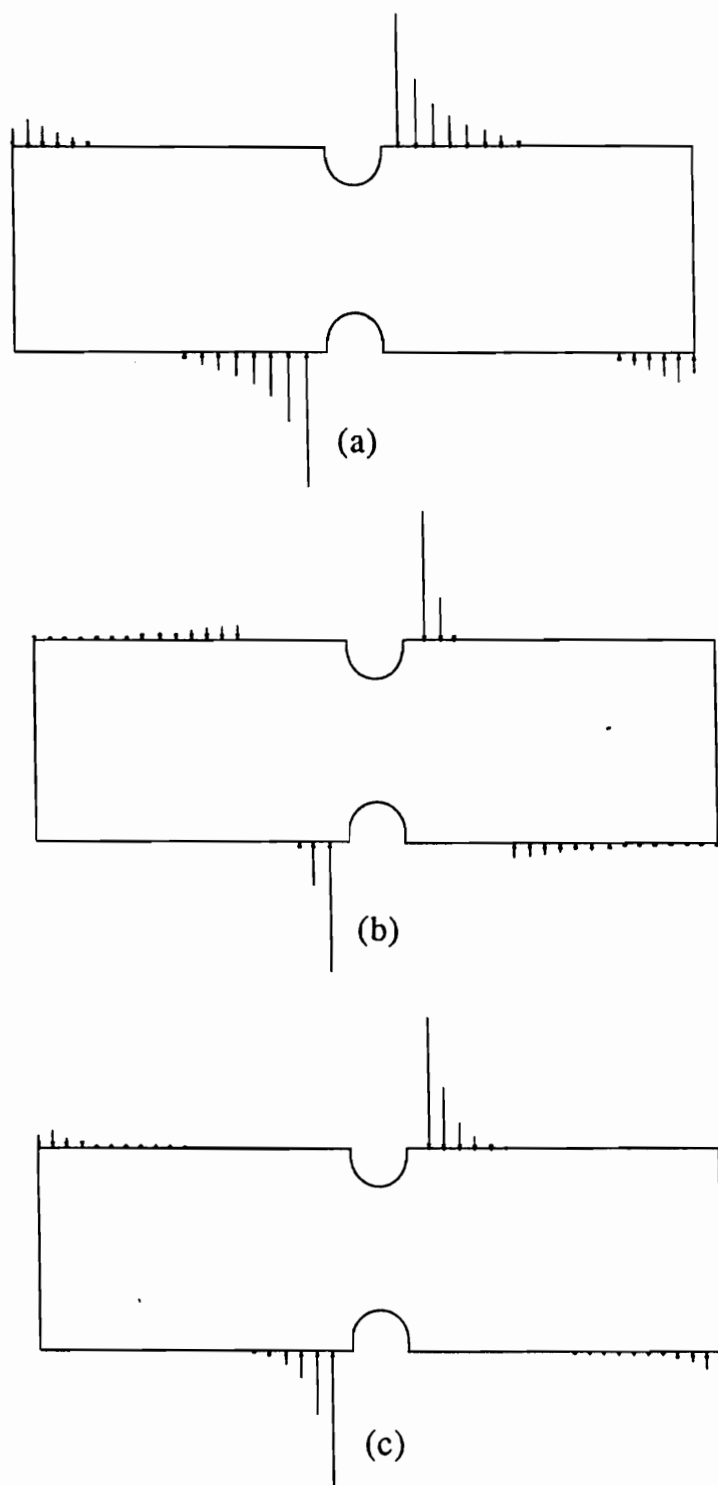
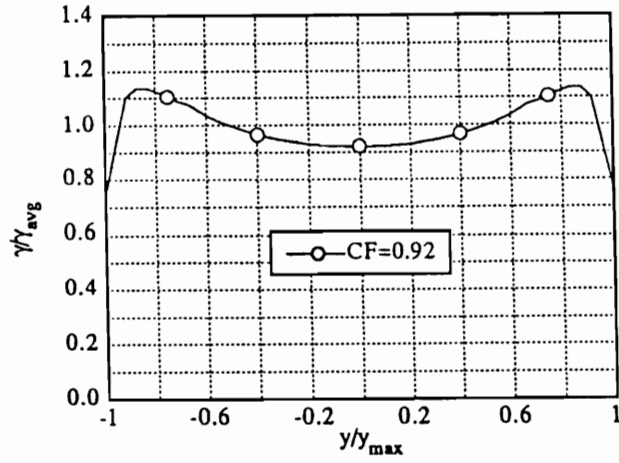
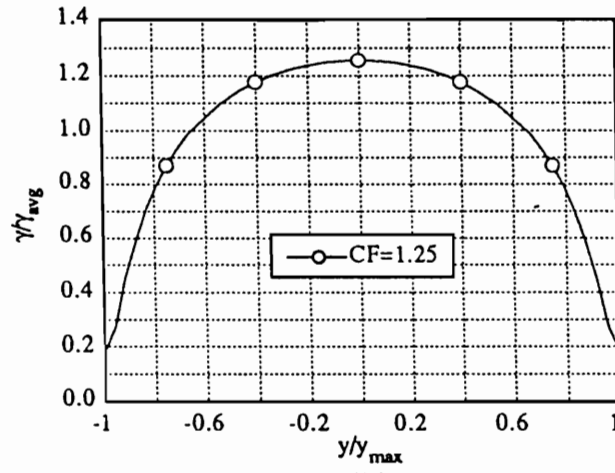


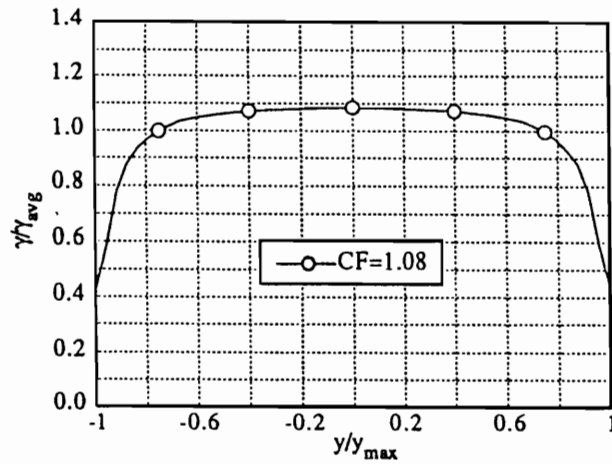
Fig.8.4 Distributed loads on the specimen sides due to imposition of uniform displacement for (a) 0°, (b) 90°, (c) 0°/90° 3" U-notch specimens.



(a)



(b)



(c)

Fig.8.5 Shear strains, normalized with respect to average γ_{xy} , along the notch axis for (a) 0° , (b) 90° , (c) $0^\circ/90^\circ$ graphite-epoxy 3" U-notch specimens.

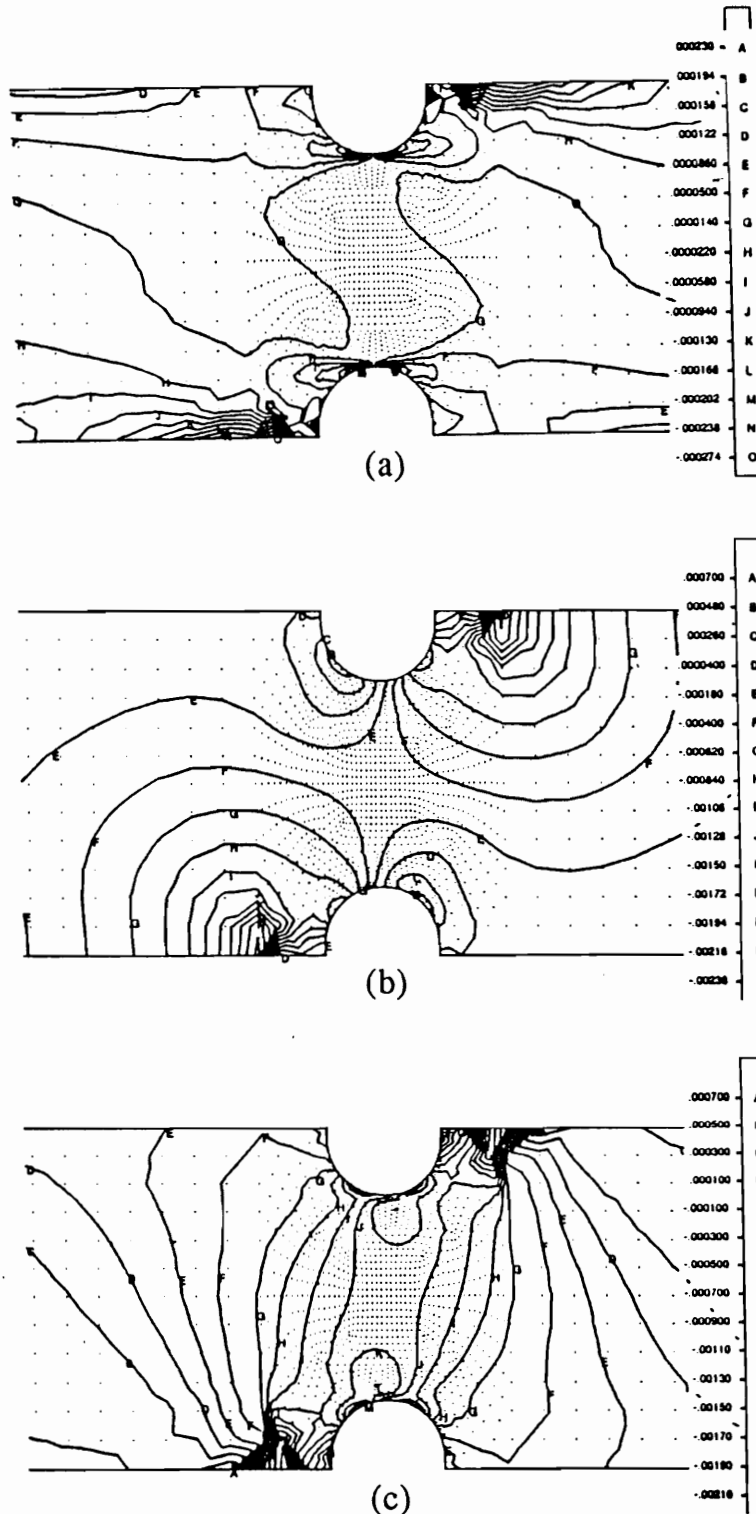


Fig.8.6 (a) ϵ_x , (b) ϵ_y , (c) γ_{xy} strain contours, obtained from finite element analysis, for 3" U-notch 0° graphite-epoxy Iosipescu specimens.

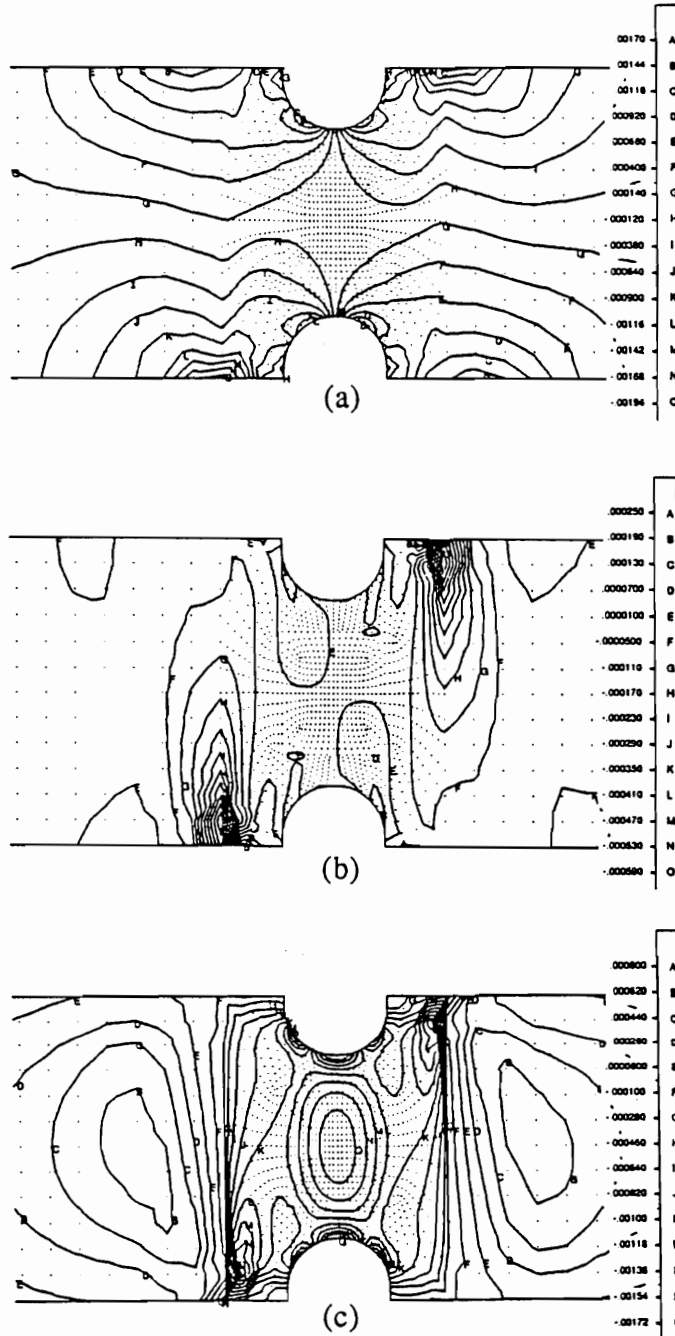


Fig.8.7 (a) ϵ_x , (b) ϵ_y , (c) γ_{xy} strain contours, obtained from finite element analysis, for 3" U-notch 90° graphite-epoxy Iosipescu specimens.

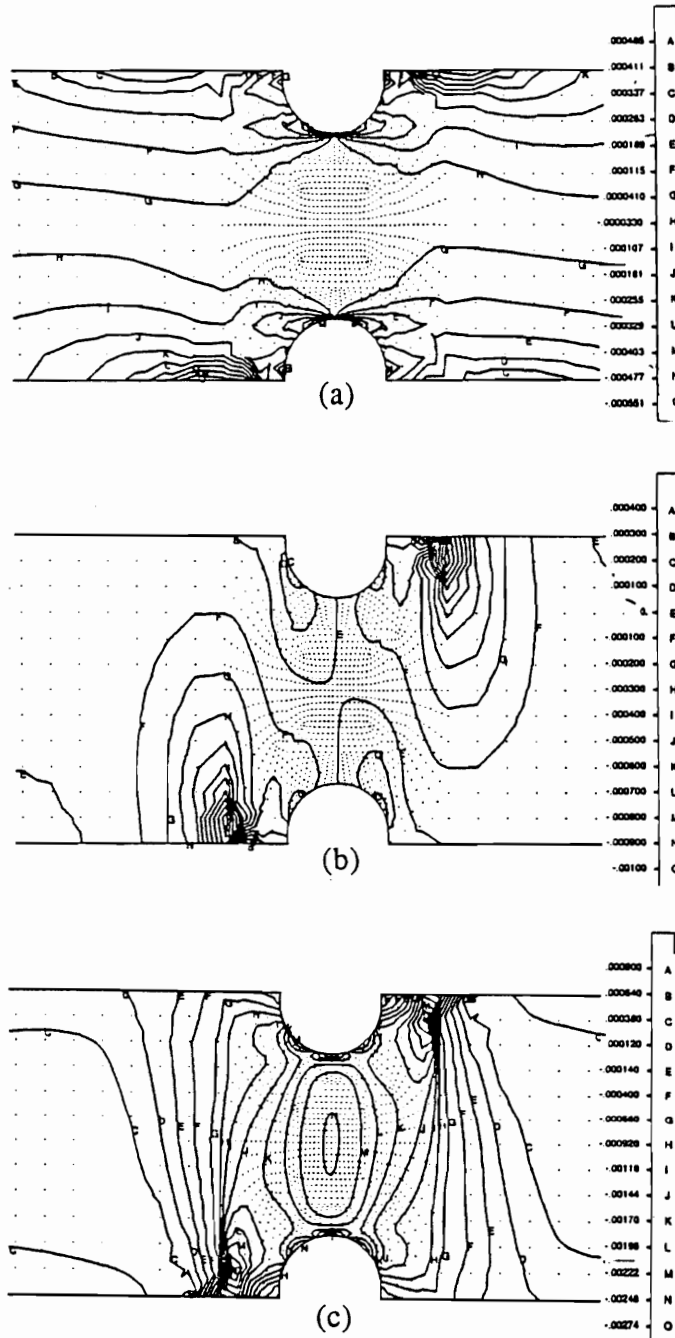


Fig.8.8 (a) ϵ_x , (b) ϵ_y , (c) γ_{xy} strain contours, obtained from finite element analysis, for 3" U-notch $0^\circ/90^\circ$ graphite-epoxy Iosipescu specimens.

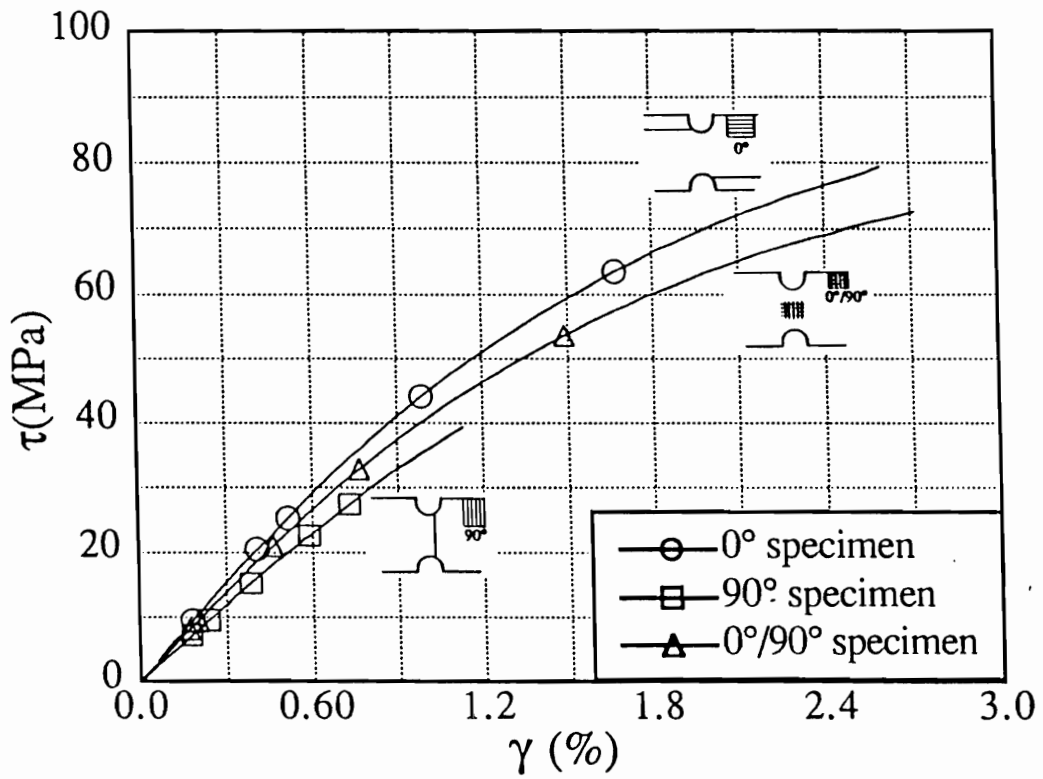


Fig.8.9 Shear stress-strain data and failure modes for typical 3" U-notch 0°, 90° and 0°/90° graphite-epoxy specimens.

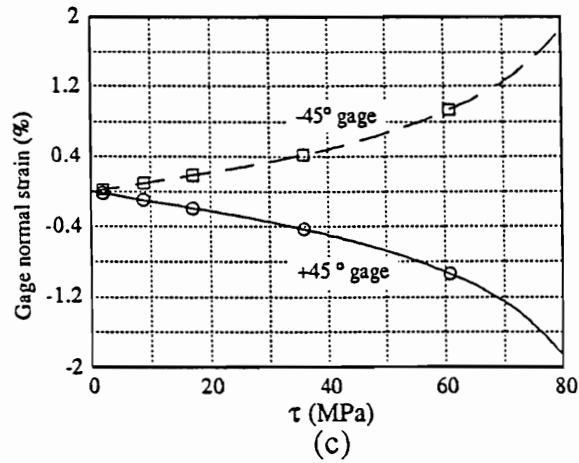
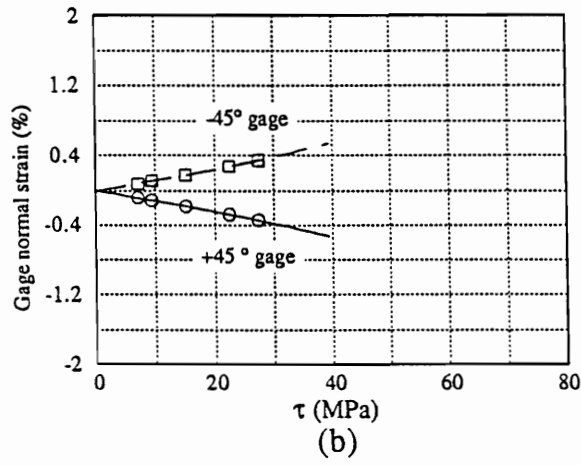
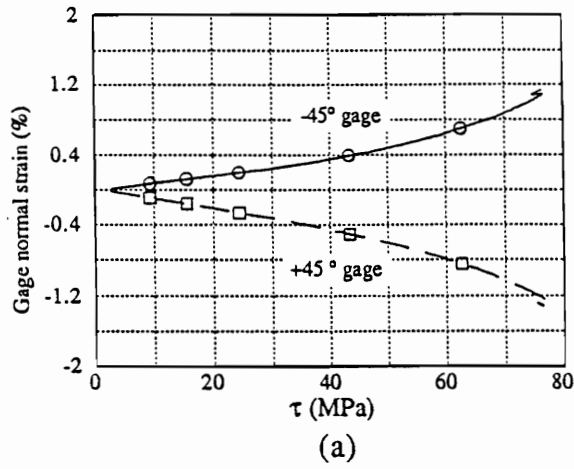


Fig.8.10 Strain vs. stress for typical 3" U-notch (a) 0°, (b) 90°, (c) 0°/90° graphite-epoxy specimen. Gages are aligned at $\pm 45^\circ$ and 0° directions.

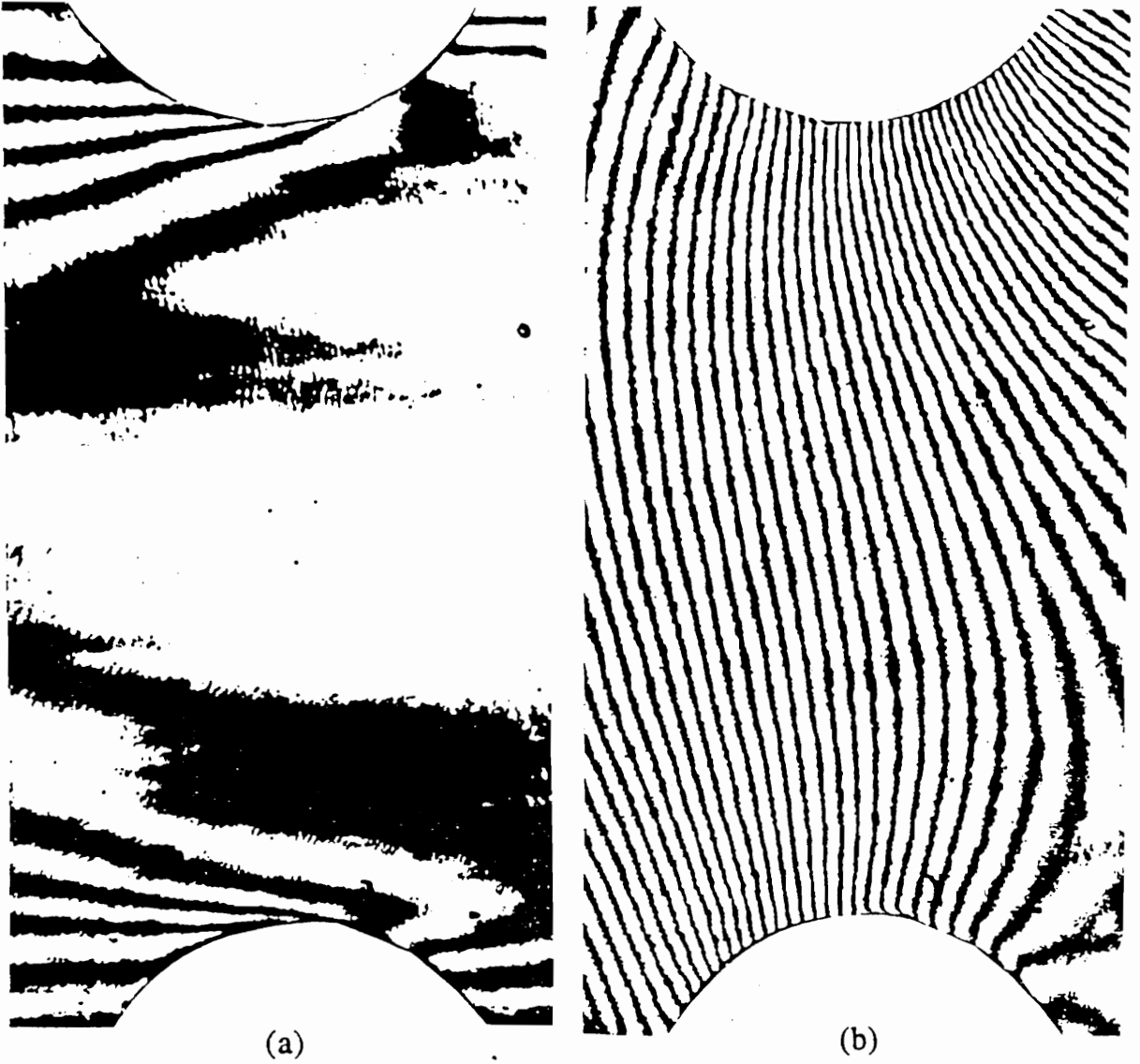
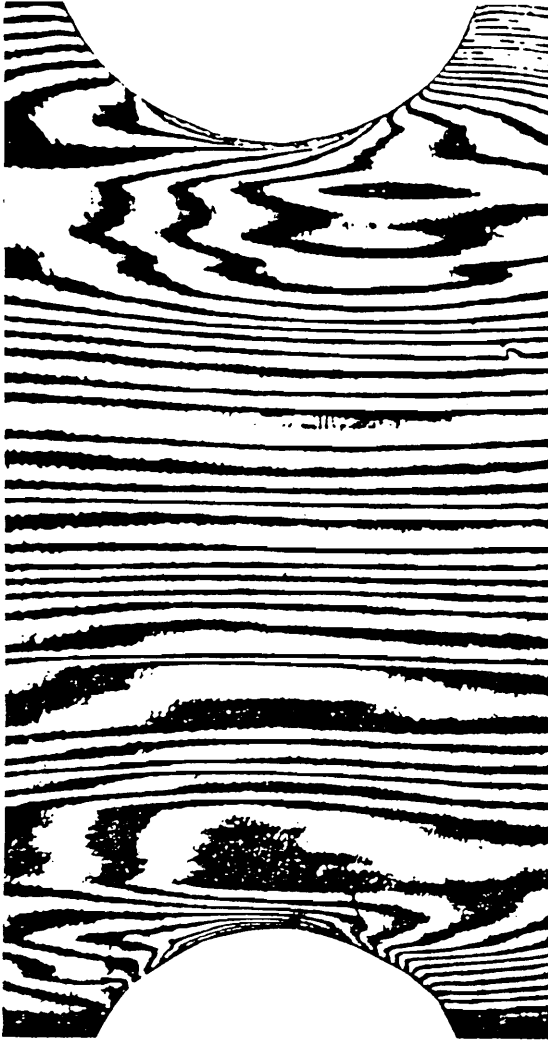
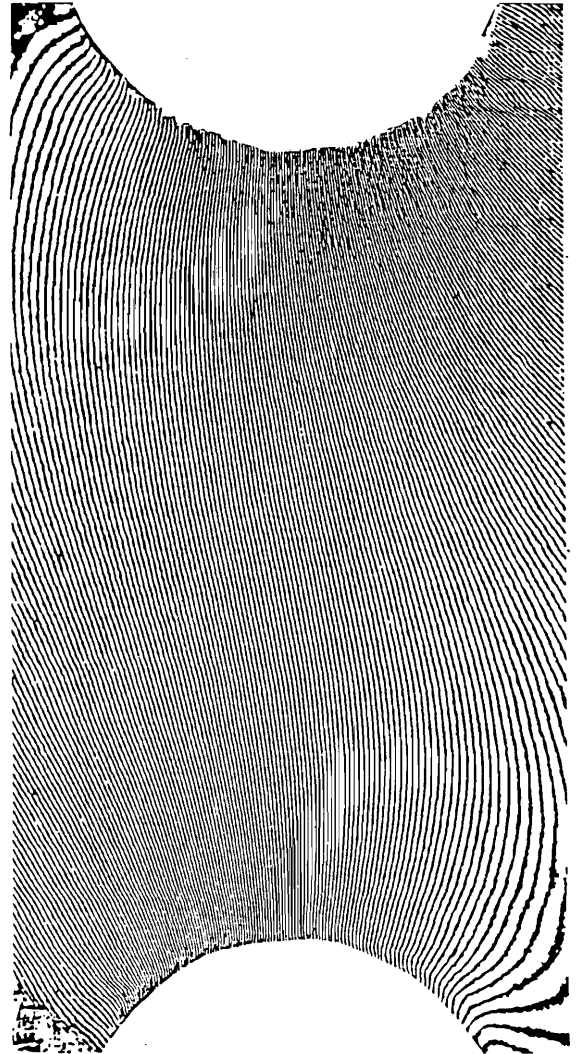


Fig.8.11a&b Typical moire fringe patterns of the 3" 0° U-notch specimen at an applied load of 214N. (a) u-field, (b)v-field.



(c)



(d)

Fig.8.11c&d Typical moire fringe patterns of the 3" 0° U-notch specimen at an applied load of 1094N. (c) u-field (half density), (d) v-field (half density).

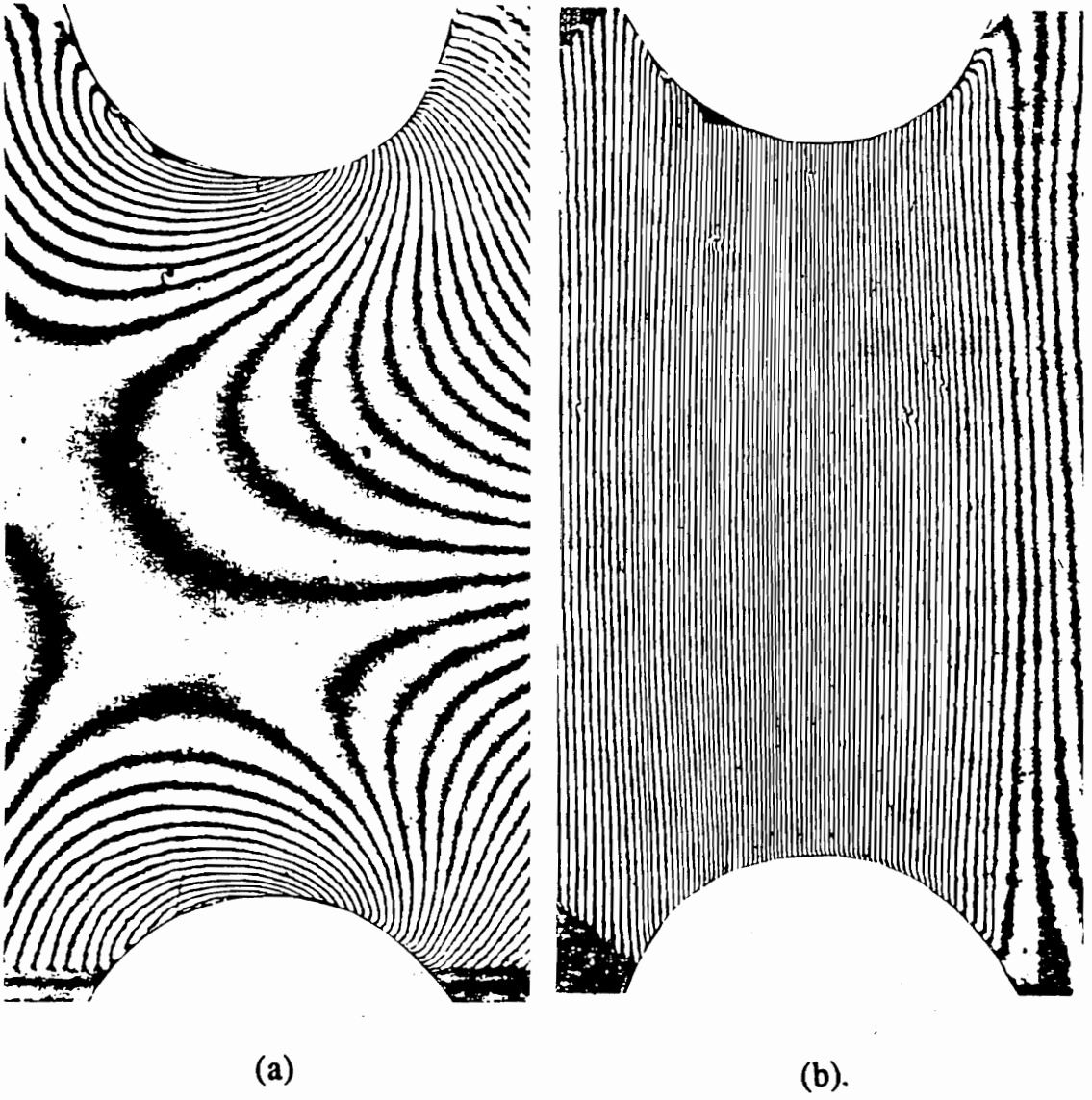


Fig.8.12a&b Typical moiré fringe patterns of the 3" 90° U-notch specimen at an applied load of 640N. (a) u-field, (b)v-field.

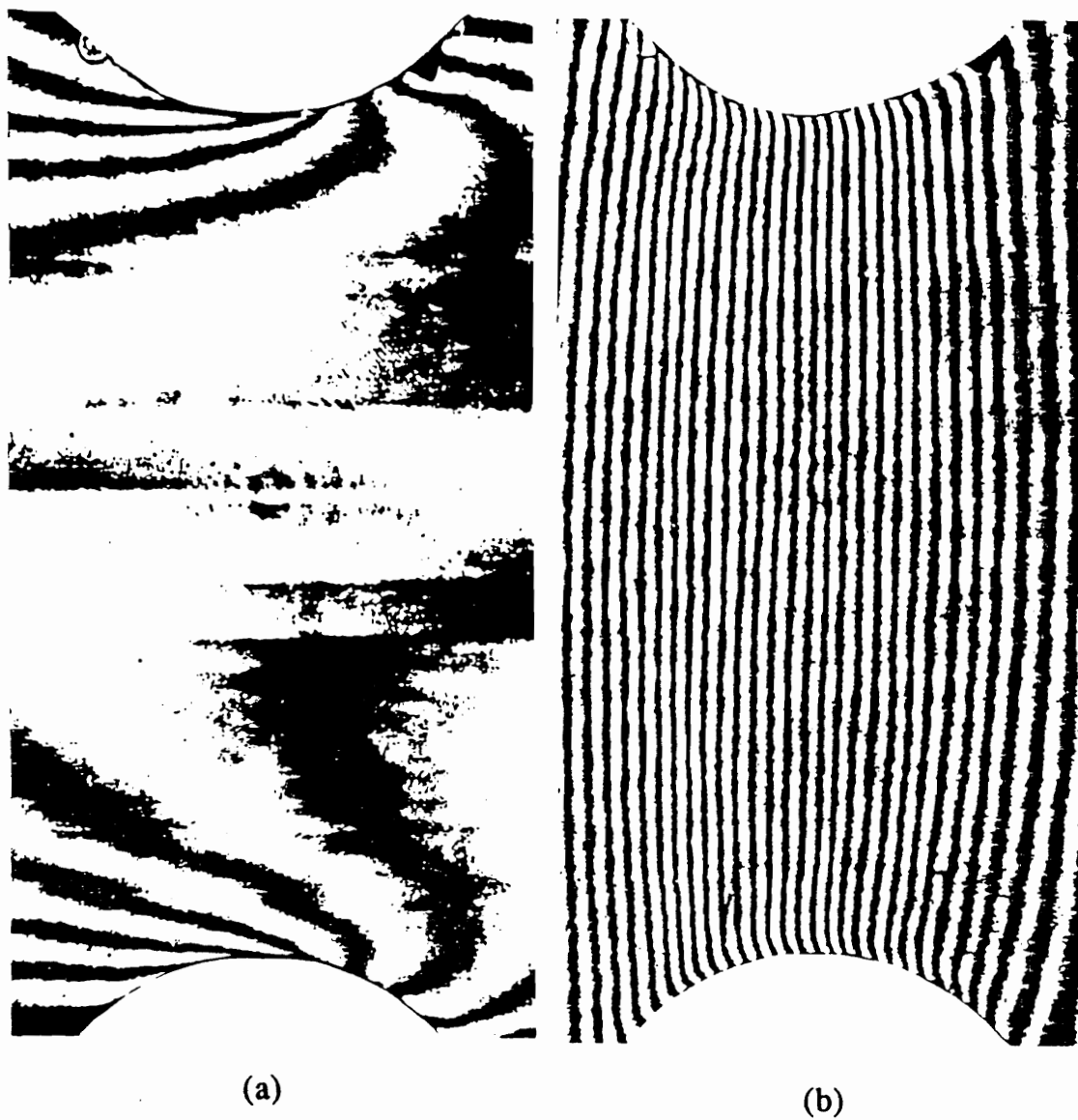
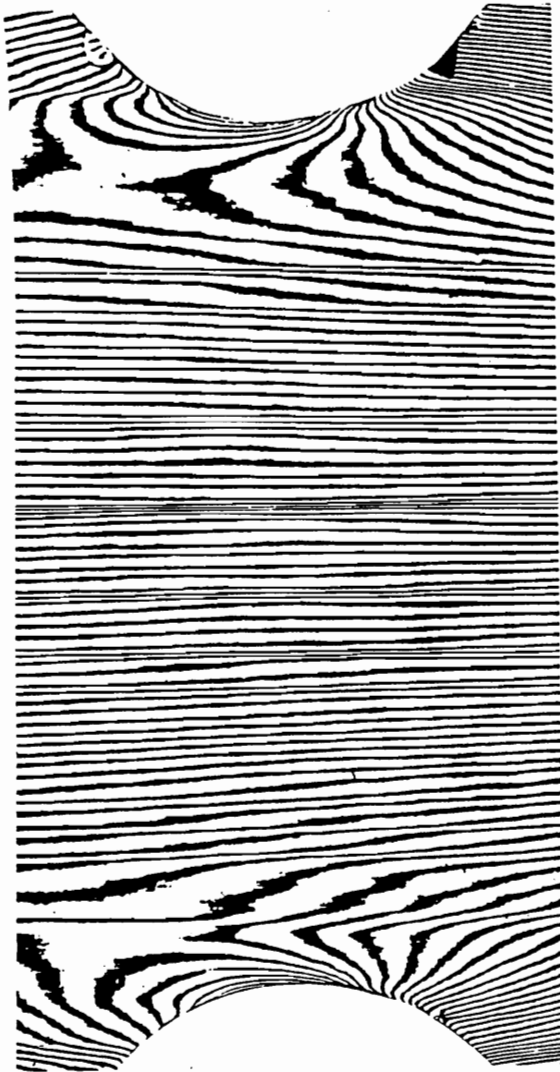
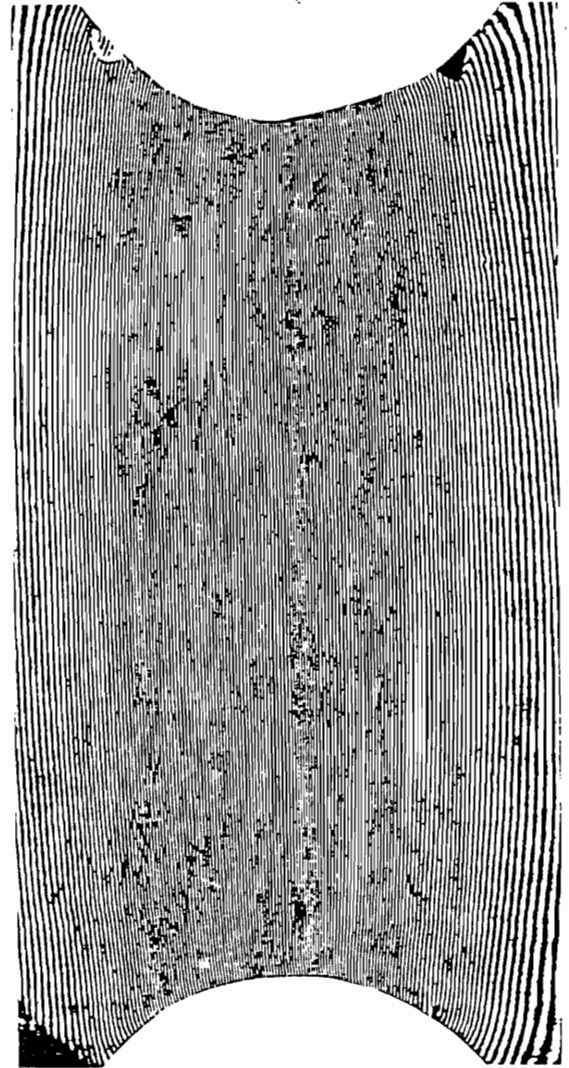


Fig.8.13a&b Typical moiré fringe patterns of the 3" 0°/90° U-notch specimen at an applied load of 382N. (a) u-field, (b)v-field.



(c)



(d)

Fig.8.13c&d Typical moire fringe patterns of the 3" $0^{\circ}/90^{\circ}$ U-notch specimen at an applied load of 1748N. (c) u-field (half density), (d) v-field (half density).

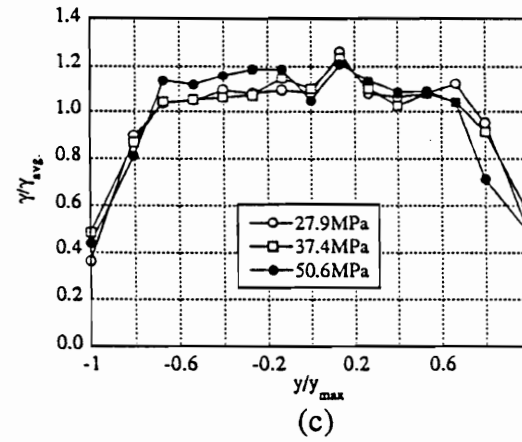
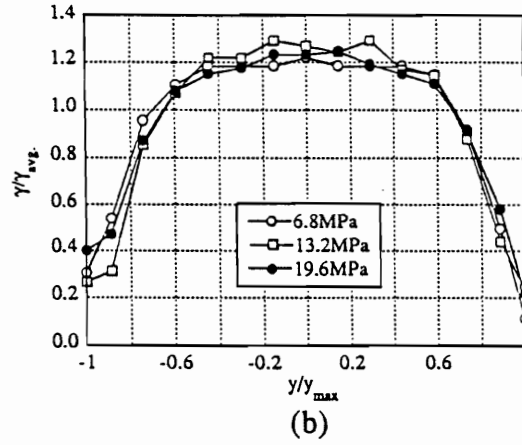
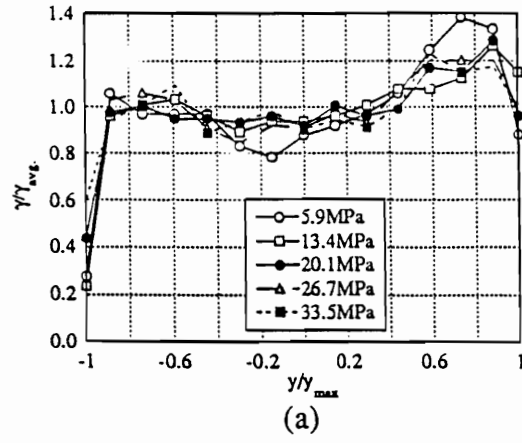


Fig.8.14 Shear strain distribution, normalized with respect to the average shear strain, across the notches for (a) 0°, (b) 90°, (c) 0°/90° 3'' U-notch Iosipescu specimens.

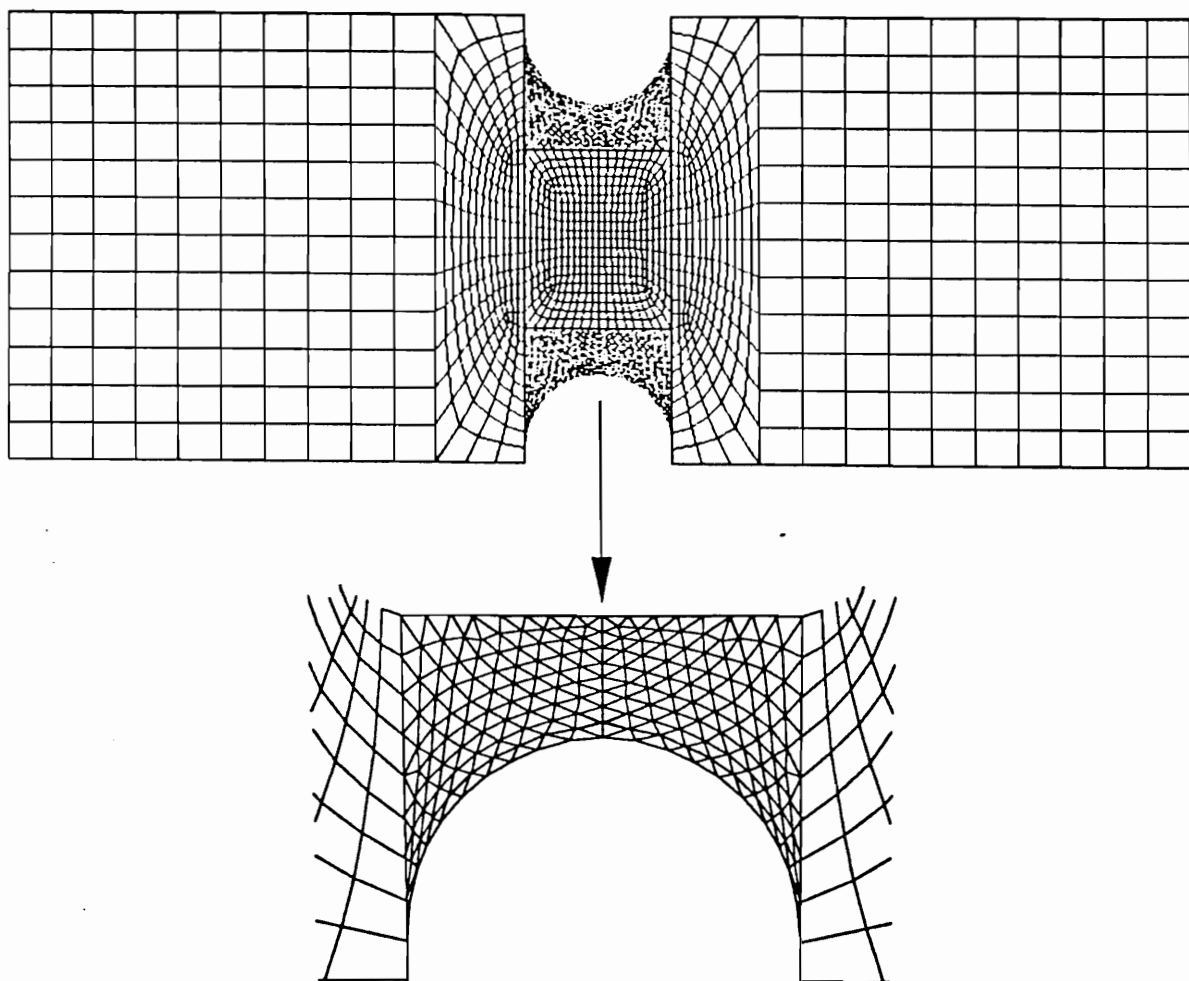


Fig.8.15 Finite element mesh for 2" U-notch specimen.

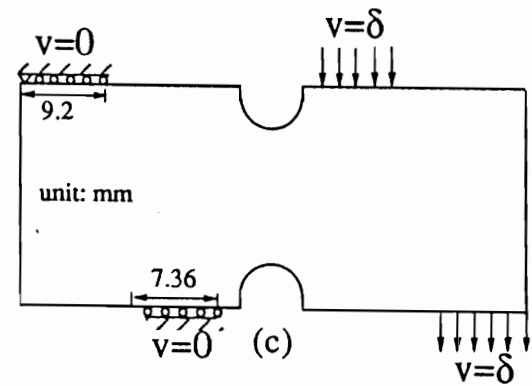
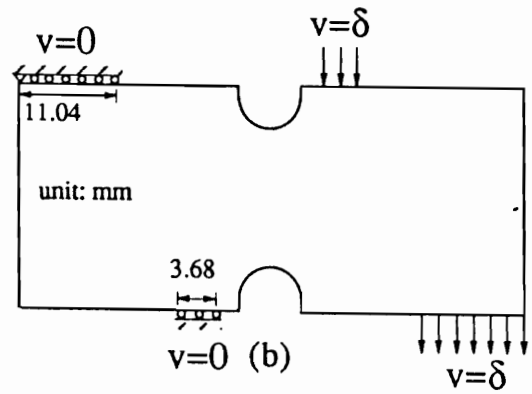
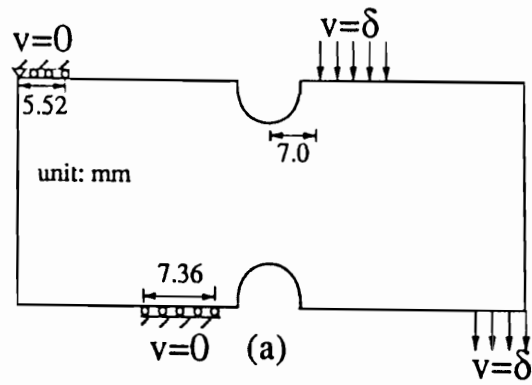


Fig.8.16 Finite element models for 2" U-notch Iosipescu specimen tested in modified Wyoming fixture, (a) 0° specimen, (b) 90° specimen, (c) 0°/90° specimen.

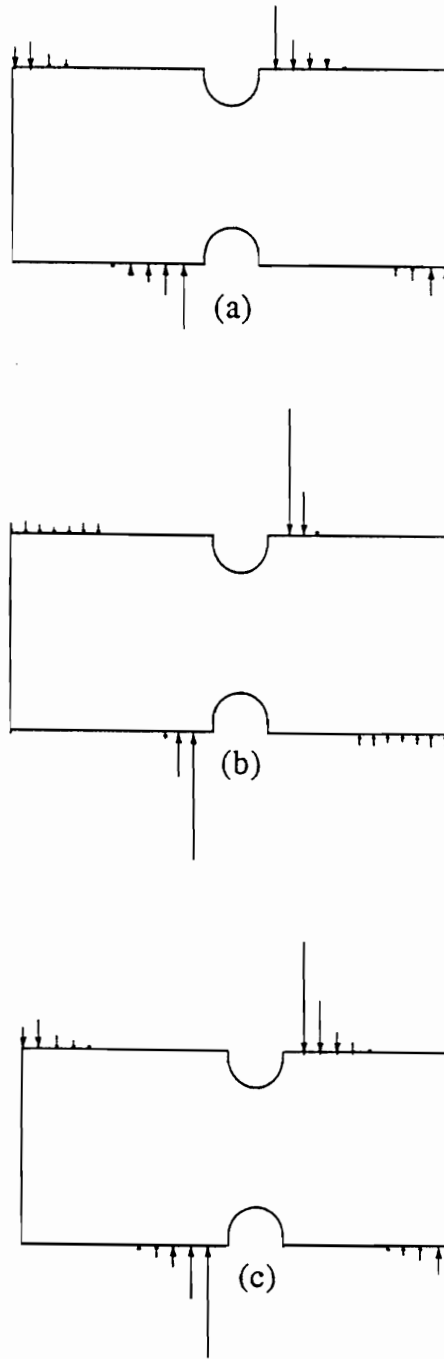


Fig.8.17 Distributed loads on the specimen sides due to imposition of uniform displacement for (a) 0°, (b) 90°, (c) 0°/90° 2" U-notch specimens.

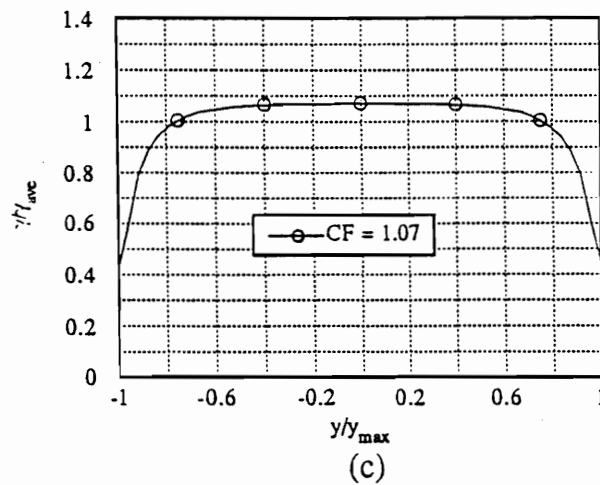
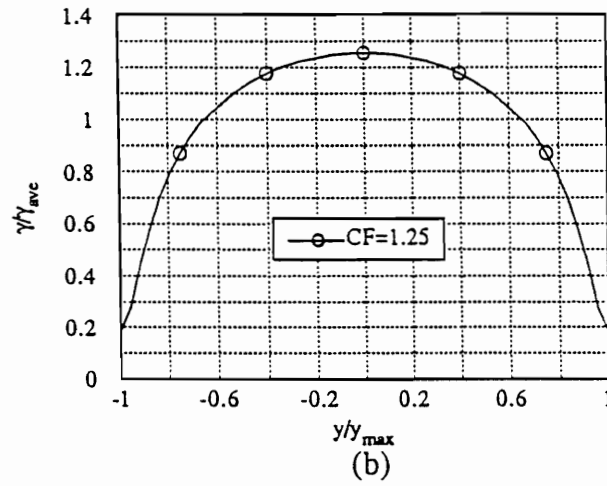
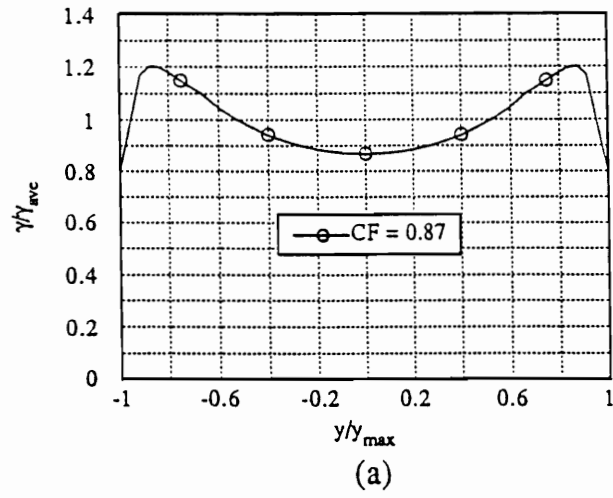


Fig.8.18 Shear strains, normalized with respect to average γ_{xy} , along the notch axis for (a) 0° , (b) 90° , (c) $0^\circ/90^\circ$ graphite-epoxy 2" U-notch specimens.

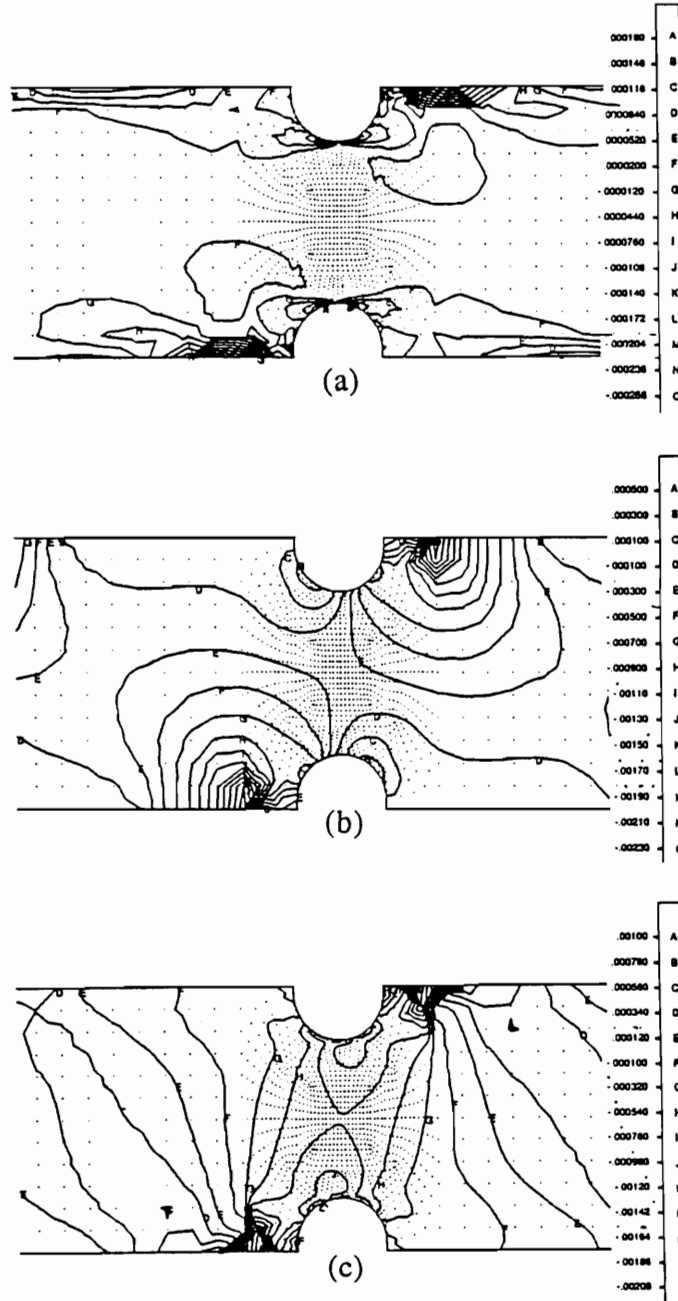


Fig.8.19 (a) ϵ_x , (b) ϵ_y , (c) γ_{xy} strain contours, obtained from finite element analysis, for 2" U-notch 0° graphite-epoxy Iosipescu specimens.

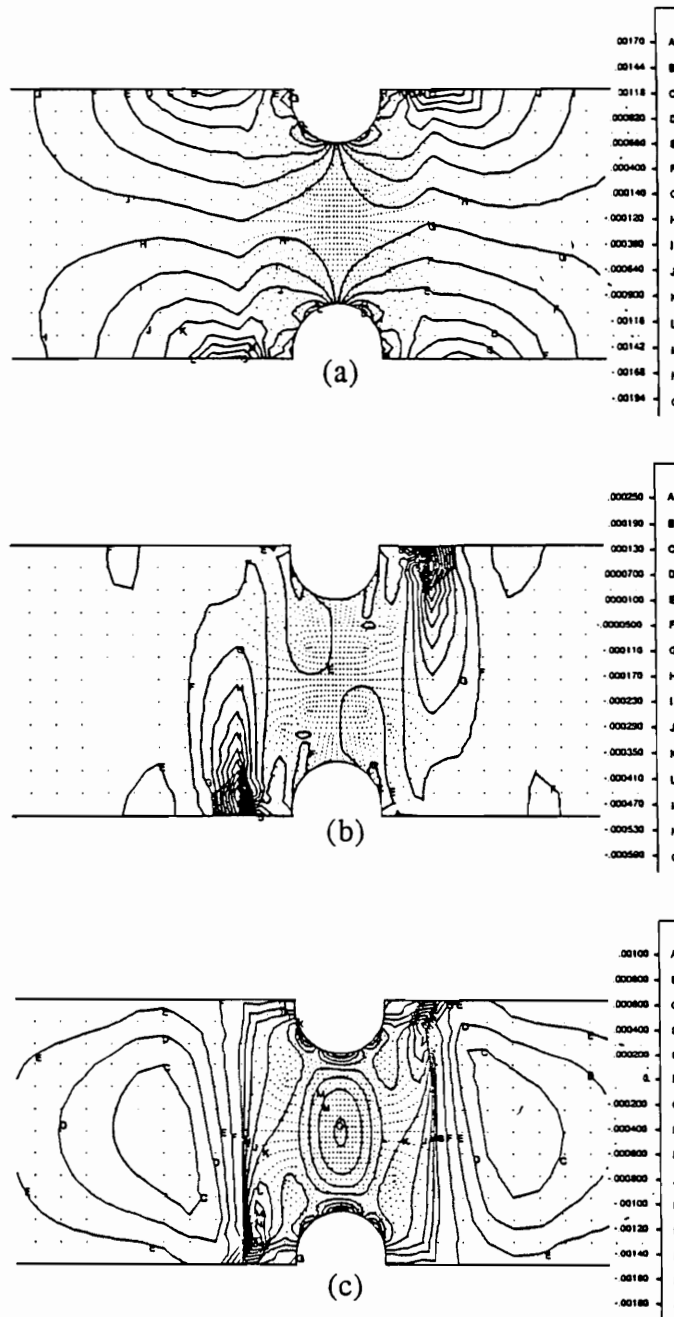


Fig.8.20 (a) ϵ_x , (b) ϵ_y , (c) γ_{xy} strain contours, obtained from finite element analysis, for 2" U-notch 90° graphite-epoxy Iosipescu specimens.

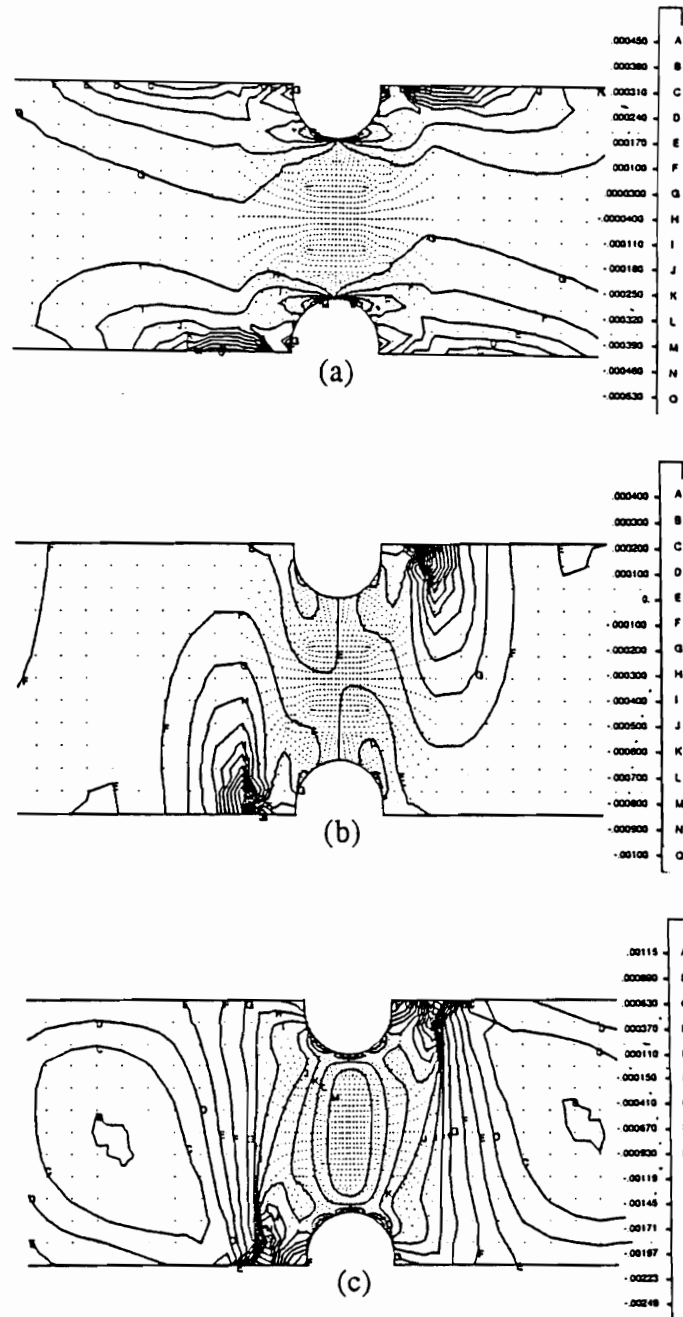


Fig.8.21 (a) ϵ_x , (b) ϵ_y , (c) γ_{xy} strain contours, obtained from finite element analysis, for 2" U-notch 0°/90° graphite-epoxy Iosipescu specimens.

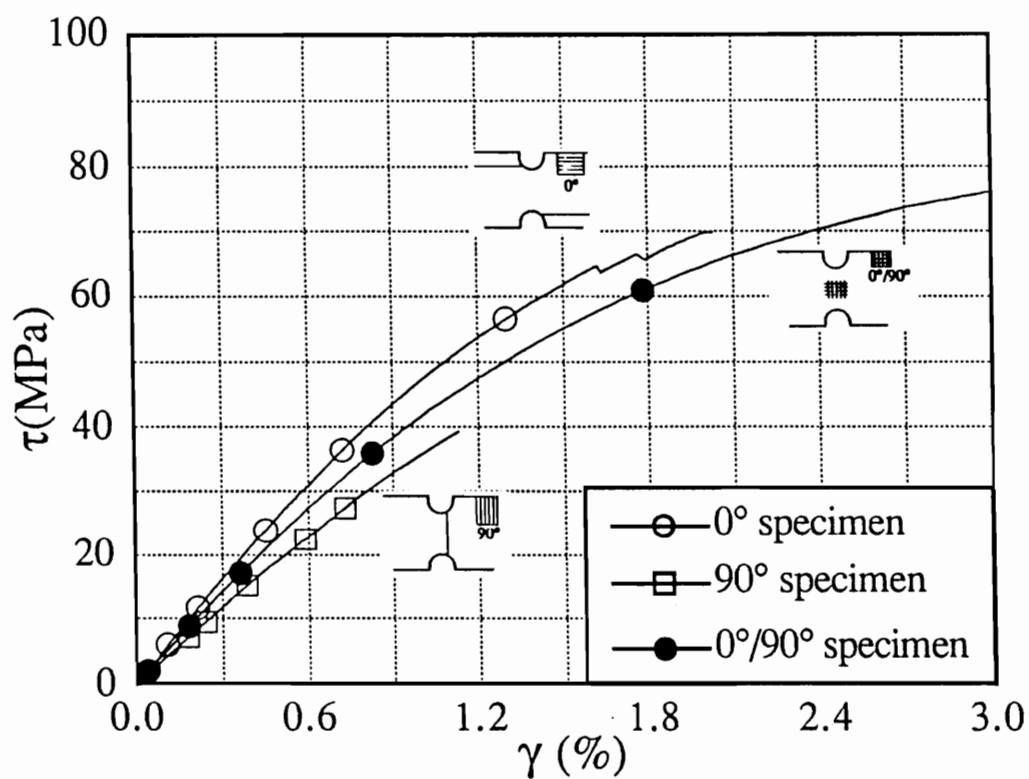


Fig.8.22 Shear stress-strain data and failure modes for typical 2" U-notch 0°, 90° and 0°/90° graphite-epoxy specimens.

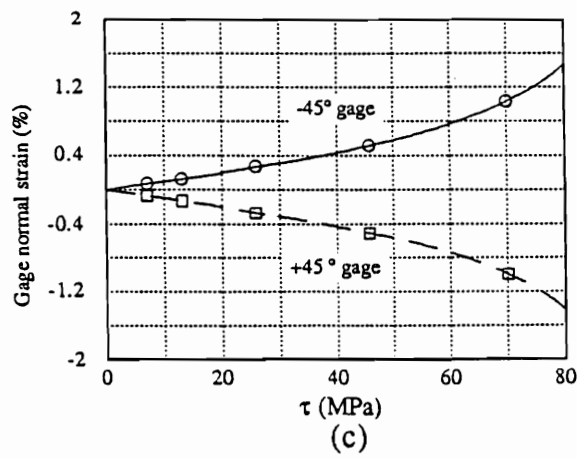
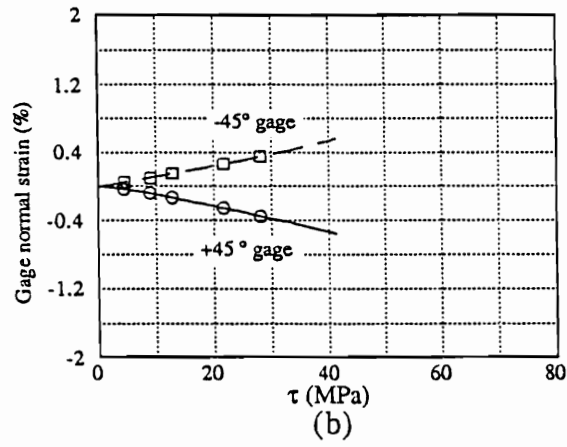
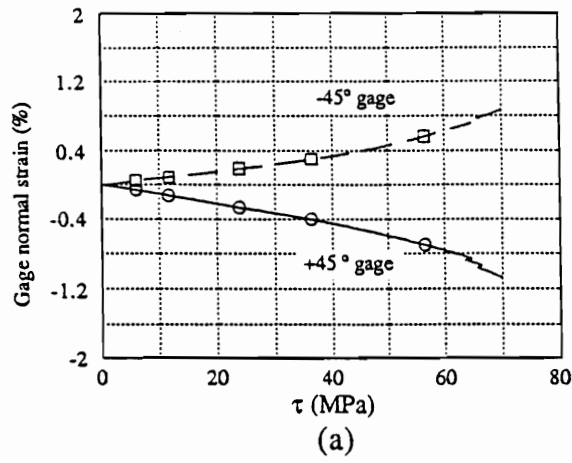


Fig.8.23 Strain vs. stress for typical 2" U-notch (a) 0°, (b) 90°, (c) 0°/90° graphite-epoxy specimen. Gages are aligned at $\pm 45^\circ$ and 0° directions.

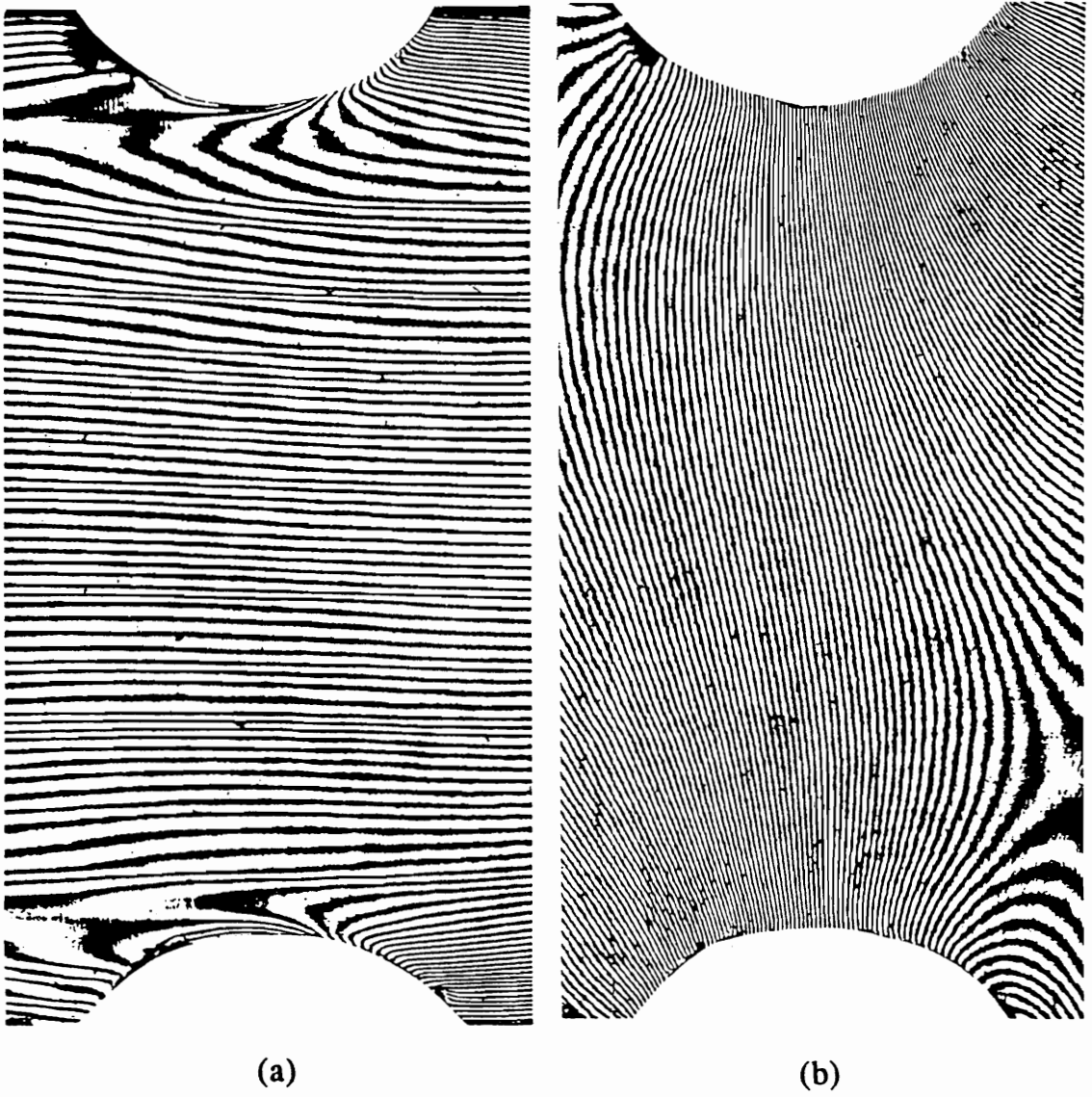


Fig.8.24 Typical moiré fringe patterns of the 2" 0° U-notch specimen at an applied load of 1099N. (a) u-field (half density), (b) v-field (half density).

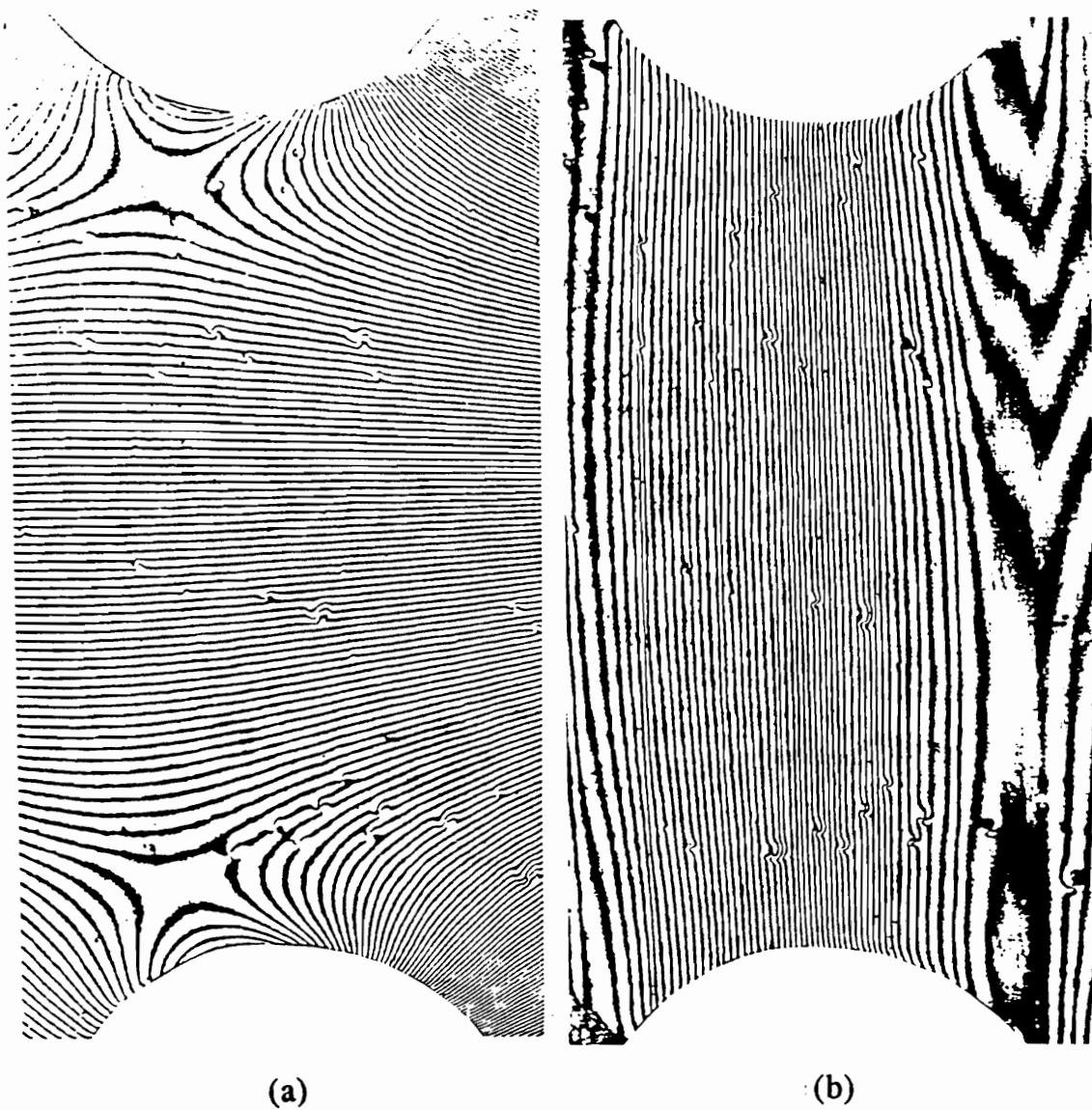


Fig.8.25 Typical moiré fringe patterns of the 2" 90° U-notch specimen at an applied load of 1050N. (a) u-field (half density), (b) v-field (half density).

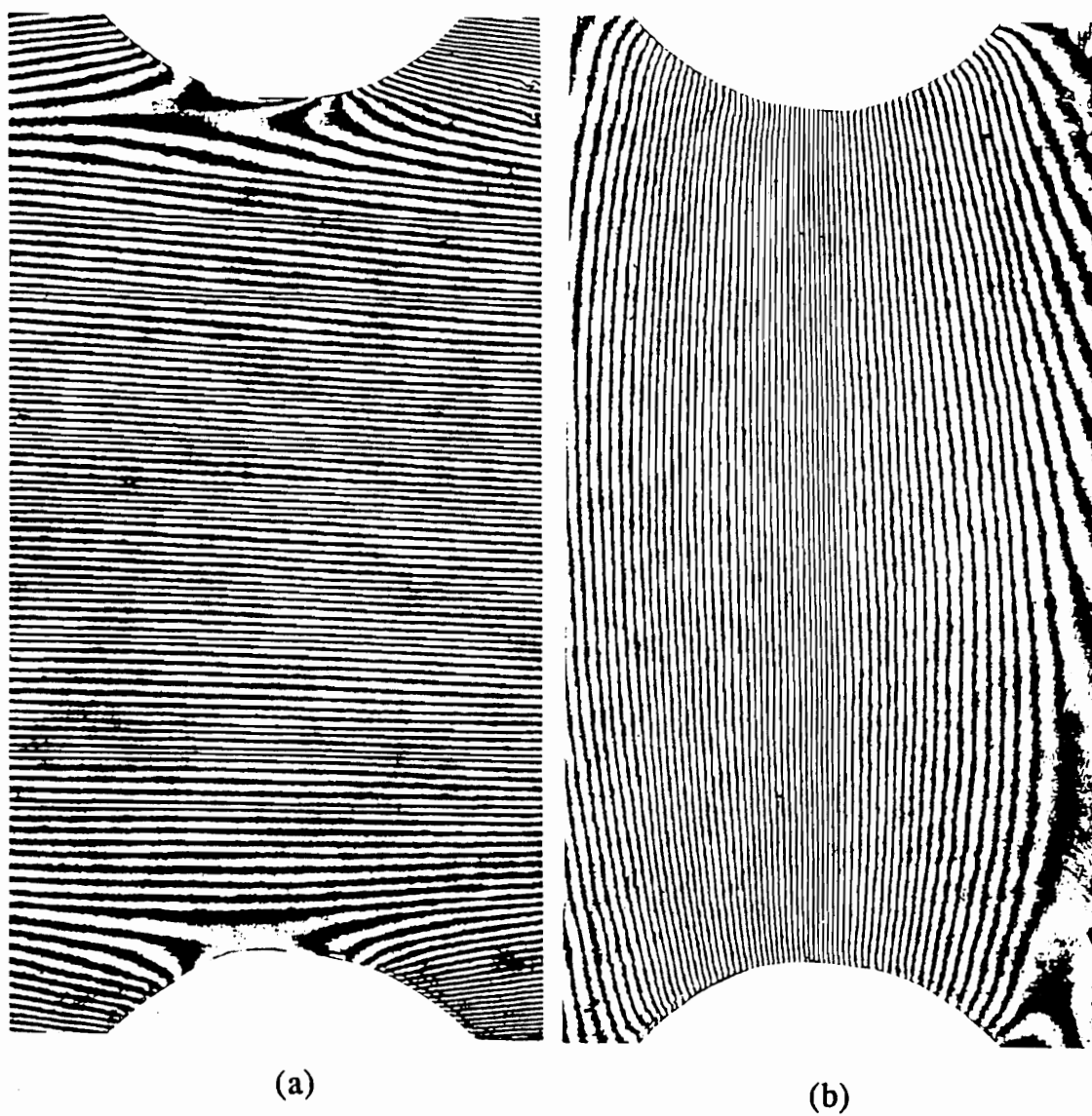


Fig.8.26 Typical moiré fringe patterns of the 2" $0^{\circ}/90^{\circ}$ U-notch specimen at an applied load of 1005N. (a) u-field (half density), (b) v-field (half density).

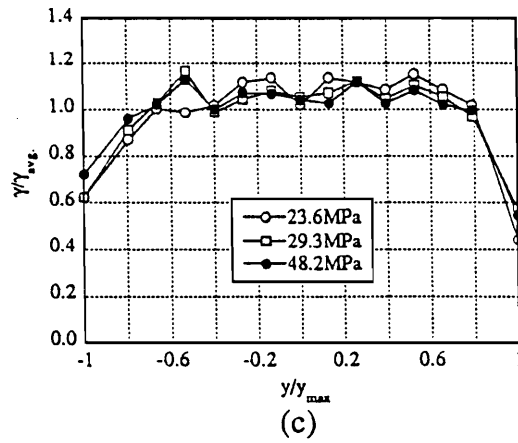
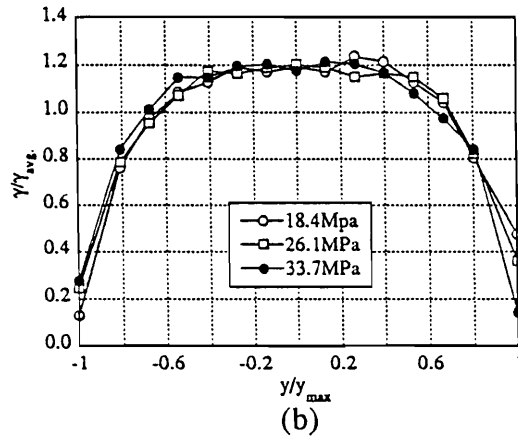
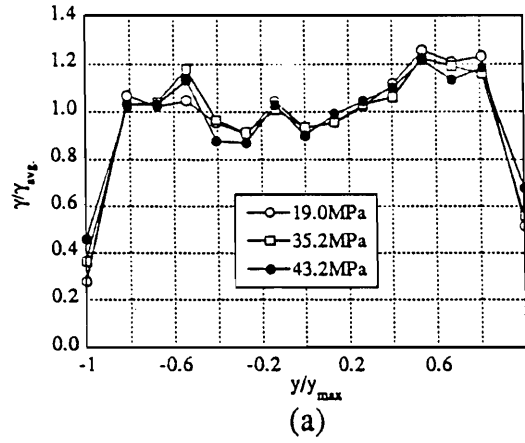


Fig.8.27 Shear strain distribution, normalized with respect to the average shear strain, across the notches for (a) 0° , (b) 90° , (c) $0^\circ/90^\circ 2^\circ$ U-notch Iosipescu specimens.

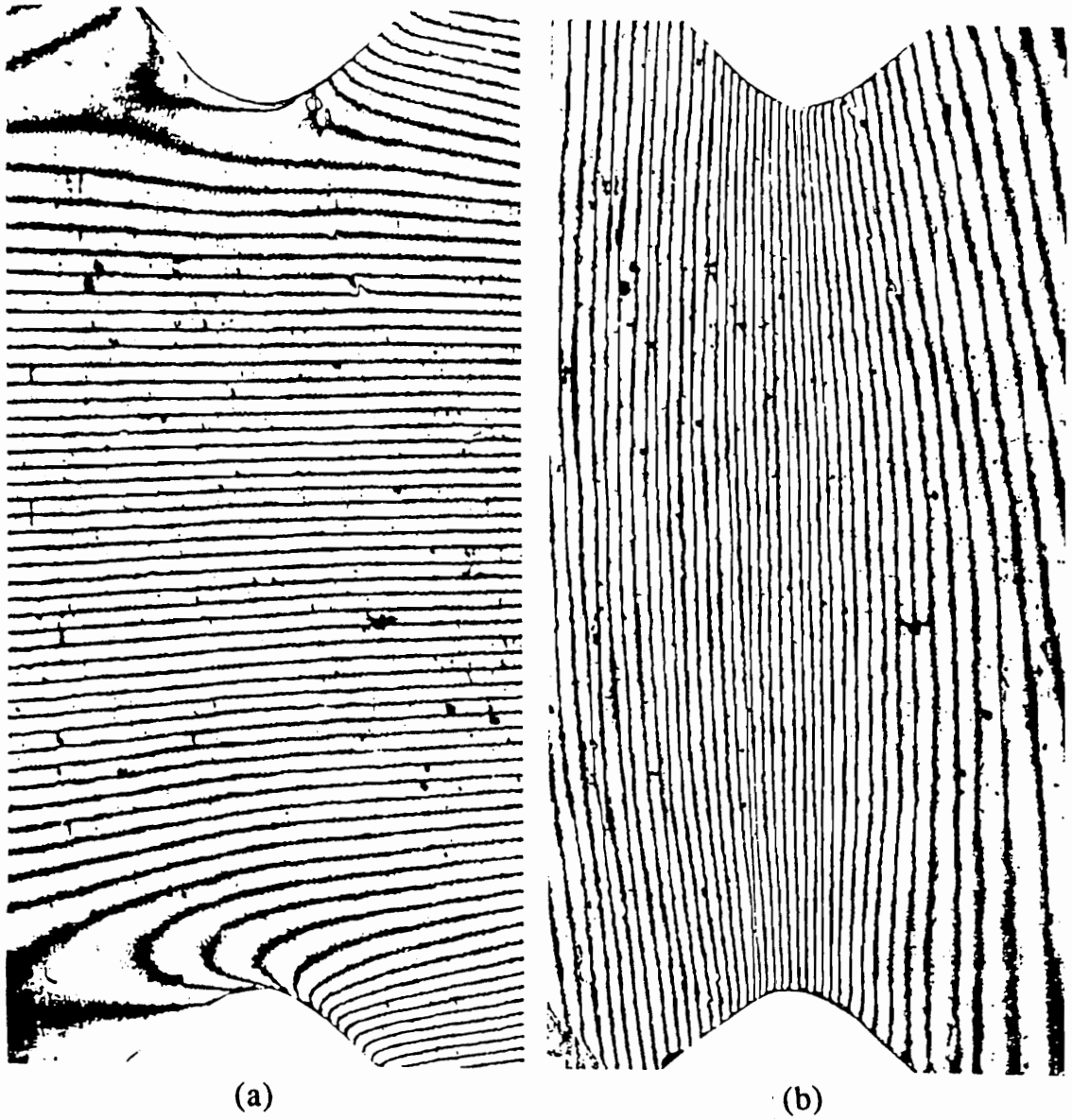


Fig.8.28 Typical moiré fringe patterns of the 3" $0^{\circ}/90^{\circ}$ V-notch AS4/APC-2 specimen at an applied load of 1410N. (a) u-field (half density), (b) v-field (half density).

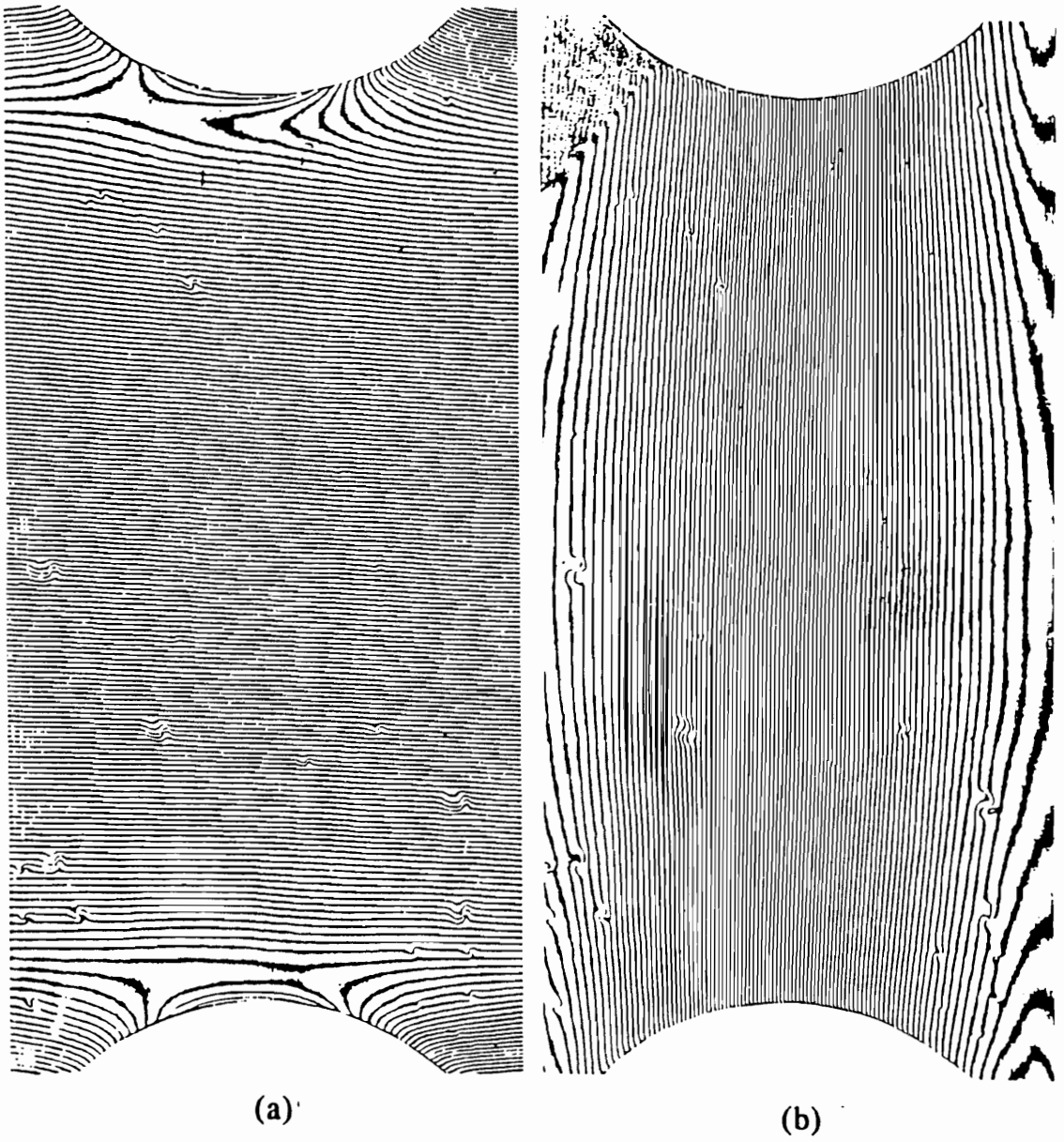


Fig.8.29 Typical moiré fringe patterns of the 3" 0°/90° U-notch AS4/APC-2 specimen at an applied load of 2535N. (a) u-field (half density), (b) v-field (half density).

VITA

Henjen Ho was born in September 11, 1955 in Chiayi, Taiwan. In May 1978, he received a Bachelor of Science degree in Mechanical Engineering at National Taiwan University, Taipei, Taiwan. He then served in the Army as a second lieutenant officer for two years. After military service, he worked in Sanyang Honda motorcycle manufacturing plant at Taipei. From May 1981 to November 1983, he worked as a mechanical engineer at Office of Nuclear Power Project, Taiwan Power Company. He came to the States in January 1984 and entered graduate studies at University of Texas at Arlington. In December 1985 he received a Master of Science degree in Mechanical Engineering. After working in a local home appliance manufacturing plant in Arlington, Texas for six months, he entered the Ph.D. program at the Department of Engineering Science and Mechanics at Virginia Polytechnic Institute and State University in January, 1987.

